5704

Strange Particle Production in $\bar{p}p$ Interactions at 12 GeV/c

by

Judith Anne Chaff

A thesis submitted for the degree of Doctor of Philosophy of the University of London.

Department of Physics

Imperial College

London SW7

August 1979

Abstract

This thesis describes the first physics experiment to be performed using the Big European Bubble Chamber at CERN. The discovery of the ψ particle in 1974, and its interpretation as a meson composed of a charmed quark and anti-quark left open the question of the existence of mesons with one charmed quark (or anti-quark) together with an ordinary (p, n, or λ type) anti-quark (or quark). A proposal was made to look for such charmed mesons and possible charmed baryons using an antiproton beam, at a momentum of 12 GeV/c, incident in the hydrogen-filled bubble chamber. Final states containing at least one strange particle (a predicted charm signature) were scanned, and all such events were then measured. The difficulties encountered in these processes, using a new large bubble chamber with its unusual spherical optics, are described in detail.

A study of neutral strange particle inclusive physics is presented and details of a search for narrow resonances are also given. An investigation of a narrow, 4.5 standard deviation peak in the 6-prong channel was made, but it is not thought to be the result of charmed particle production. Upper limits for the production cross sections times branching ratios for the charmed particles discovered in 1976 are given for various channels, and a search for directly produced electrons or positrons is described.

Table of Contents

	Page
Title	1
Abstract	2
Table of Contents	3
Introduction	
Charm and SU(4)	6
The Discovery of the ψ	7
A Charm Hunt	8
References	10
Chapter 1 - The Big European Bubble Chamber	
1.1 Introduction	17
1.2 General Description and History	18
1.3 Detailed Description and Measurement of Constants	18
1.4 Problems Affecting Picture Quality	21
1.5 The Beam	23
References	24
Chapter 2 - Data Processing : Scanning and Measuring	
2.1 Introduction	32
2.2 Scanning	32
2.3 V^0 and $V^{\pm}$ Definitions	33
2.4 Scanning Efficiency and Rough Digitising	34
2.5 HPD Measurements : Changes to Hardware and Software for BEBC film measurement	36
2.6 Throughput Efficiency	38
2.7 Remeasures	38
2.8 Improved Measurement System	40
2.9 Rescue Geometry	41

2.10 Measurement Techniques in Other Laboratories 43

References 44

Chapter 3 - Geometrical Reconstruction and Kinematical Fitting Procedure

3.1 Introduction 51

3.2 The HYDRA system 51

3.3 Geometry : Summary of the Problems 52

3.4 Track Match 53

3.5 Treatment of Multiple Scattering 55

3.6 Improvements to the Basic Geometry Programme 56

3.7 Kinematic Fitting 58

3.8 Beam Parameters 60

References 62

Chapter 4 - Strange Particle Inclusive Physics

4.1 Introduction 70

4.2 Cross Section Formula 70

4.3 Beam Contamination 70

4.4 Correction Factors 72

4.5 Cuts and Checks on Data for Inclusive Distributions 76

4.6 Total Inclusive Cross Sections 77

4.7 Inclusive Variables 79

4.8 Differential Cross Sections - Longitudinal Variables 83

4.9 Differential Cross Sections - Transverse Variables 85

4.10 Differential Cross Sections as Functions of M_x^2 , t 87

4.11 Triple Regge Limit 90

References 93

Chapter 5 - A Search for Narrow Resonances

5.1 Introduction 125

5.2 Search for Narrow Resonances in 12 GeV/c $\bar{p}p$ Interactions 126

5.3 Production of $K^{*}(890)$ and $Y^{*}(1385)$ 127

5.4 Event Selection and Weighting Procedure for 6 prong V^{o} events 128

5.5 Study of the Peak Found in $K^{o}\pi^{\pm}\pi^{+}\pi^{-}$ Mass Distributions 131

5.6 A Search for Supporting Evidence 135

References 137

Chapter 6 - A Search for Known Charmed Particles

6.1 Introduction 165

6.2 Evidence for the Existence of Charm 165

6.3 Upper Limits for the Production of Charmed Particles 167

6.4 Search for Direct Electron Production 170

6.5 Comparison of Inclusive K^{o} Production in $e^{+}e^{-}$ and $\bar{p}p$ Annihilations 174

References 177

Acknowledgements 188

INTRODUCTION

This thesis describes the author's work in connection with an antiproton - proton experiment at 12 GeV/c using the Big European Bubble Chamber (BEBC) in collaboration with physicists from Bruxelles, CERN, Imperial College, Mons, and Orsay. This introductory chapter discusses the theoretical need for charmed quarks and the discoveries of November 1974 indicating the existence of charmed particles which gave the main motivation for this experiment.

Charm and SU(4)

The quantum number "charm" was originally introduced [1] to account for the absence of strangeness-changing neutral currents.

Consider the reactions : $K^+ \longrightarrow \pi^+ e^+ e^-$ $\Delta Q = 0,\ \Delta S = -1$ (1)

and $K^+ \longrightarrow \pi^0 e^+ \nu_e$ $\Delta Q = -1,\ \Delta S = -1$ (2)

The branching ratios for these two reactions are :

(1) 3×10^{-7} and (2) 5×10^{-2}

Similarly, $K_L^0 \longrightarrow \mu^+ \mu^-$ $\Delta Q = 0,\ \Delta S = \pm 1$ (3)

has a branching ratio of 1×10^{-8}, whereas

$K^+ \longrightarrow \mu^+ \nu_\mu$ $\Delta Q = -1,\ \Delta S = -1$ (4)

has a branching ratio of 6×10^{-1}. So both $\Delta Q = 0, \Delta S = \pm 1$ reactions ((1) and (3)) are heavily suppressed.

The familiar SU(3) picture of hadrons was extended [1,2] by adding a fourth, charmed quark (Figure 1a and Table I) to give SU(4). The Weinberg - Salam model [3,4] gives a form of the hadronic charged current from which a natural selection rule emerges for the decay of charmed particles, namely

$\Delta Q = \Delta C = \Delta S$, $\Delta I = 0$ (amplitude $\sim \cos\theta_c$, θ_c is the Cabibbo angle)

or, $\Delta Q = \Delta C$, $\Delta S = 0$, $\Delta I = \frac{1}{2}$ (amplitude $\sim \sin\theta_c$)

The model also provides lepton - quark symmetry since it uses four leptons $\begin{pmatrix}\nu_\mu\\ \mu^-\end{pmatrix}$, $\begin{pmatrix}\nu_e\\ e^-\end{pmatrix}$ and four quarks $\begin{pmatrix}u\\ d'\end{pmatrix}$ and $\begin{pmatrix}c\\ s'\end{pmatrix}$.

The fourth quark opens up a whole new spectroscopy of elementary particles ; the octets and singlets of "old" mesons are replaced by 15-plets and singlets (Figure 1b) and the $\frac{1}{2}^+$ baryon octet, for example, becomes a 20-plet (Figure 1c). Lists of the quark contents and quantum numbers of some of the predicted particles are shown in Tables II and III.

The masses of these charmed particles were estimated [5] to lie in the range 1.4 to 5 GeV/c^2 for mesons, and 2.4 to 19 GeV/c^2 for the lowest baryon states. The dominant decay modes ($\sim\cos\theta_c$) were expected to be non - leptonic, with a strange particle in the final state. The total branching ratio for charmed particles to hadrons was calculated as $\simeq 10^{13}$ sec^{-1}, and for a decay such as $D^0 \rightarrow K^- \pi^+$, with $M_D \simeq 2$ GeV/c^2, $\Gamma(D^0 \rightarrow K^- \pi^+) \simeq 5 \times 10^{12}$ sec^{-1}.

The Discovery of the ψ

In November 1974, a resonance was discovered at a mass of 3.1 GeV/c^2 with a very small width, in e^+e^- collisions at Spear [6] . At the same time a MIT - BNL collaboration found a narrow resonance in p - Be interactions at 3.1 GeV/c^2 [7] decaying to e^+e^-. Both of these resonances have been identified as coming from the decay of a meson (called the ψ by [6] and the J by [7]) consisting of a pair of $c\bar{c}$ quarks (the ϕ_c of Table II). A second resonance was discovered shortly afterwards at a mass of 3.7 GeV/c^2 [6] , the ψ', which has been identified as a $c\bar{c}$ meson (ϕ_c') - the first radial excitation of the ψ.

These discoveries fixed the mass scale of the charmed particles,

so that, for example, the D meson should have a mass around 2 GeV/c^2 [5 - addendum]. The ψ also gave high energy physicists the incentive to look for this new spectroscopy of particles.

A Charm Hunt

It was suggested [5] that a good place to look for charmed particles would be in $\bar{p}p$ annihilations, where they could be produced either singly in reactions like :

$$\bar{p}p \rightarrow \phi_c + n\,\pi's \quad , \quad \phi_c' + n\,\pi's$$

$$\bar{p}p \rightarrow \eta_c + n\,\pi's \quad , \quad \eta_c' + n\,\pi's$$

or in pairs : $\bar{p}p \rightarrow D^0\bar{D}^0 \quad , \quad D^+D^- \quad , \quad D\bar{D} + n\,\pi's \qquad (n \geq 1)$

$\bar{p}p$ annihilations offer the highest centre of mass energy in "central" (i.e. non - peripheral) collisions, compared with π^-p, K^-p etc. at the same energy, and represent a large source of high p_T events. (This is the most promising region to look for the production of high mass objects as detailed in section 5.2).

If charm behaves as strangeness does [5] , it is predicted that

$$\frac{\sigma(\text{charmed})}{\sigma(K)} \approx \frac{\sigma(K)}{\sigma(\pi)} \quad .$$

Figure 2 shows $\sigma_{\text{annihilation}} \simeq (\sigma_{\bar{p}p} - \sigma_{pp})$ and $\sigma_{K^0_{\text{seen}}}$ for $\bar{p}p$ interactions. It can be seen that a large fraction of the annihilation cross section goes into K^0_sKX, so that if the above relation is true, antiproton reactions should be good candidates for producing charm.

Many narrow enhancements have already been observed in $\bar{p}N$ interactions at lower energies. These include a sharp enhancement at 3.1 GeV/c^2 in $\bar{p}n$ data at 5.5 GeV/c [10] and at 2.37 and 2.61 GeV/c^2 (Figure 3) in $\bar{p}p$ data at 5.7 GeV/c [11] . This evidence also indicated that $\bar{p}p$ interactions might be a fruitful place to look for narrow peaks.

It was therefore proposed [12] to look for the production of charmed particles in 12 GeV/c ($E^{*} = 4.93$ GeV) $\bar{p}p$ interactions in BEBC.

There were several advantages to using BEBC, which include the following :-

a) The mass resolution can be estimated from ε ($\sim 250\mu$), the uncertainty in reconstructing points on a track in the bubble chamber, and the magnetic field (3.5 Tesla). Events of the type $\bar{p}p \rightarrow D^{o}\ \bar{D}^{o}$ ($D^{o} \rightarrow K^{-}\pi^{+}$, $\bar{D}^{o} \rightarrow$ all) were generated, and the errors on effective and missing masses were calculated assuming $M_D \sim 2.15$ GeV/c^2, $\Gamma_D = 0$, and isotropic angular distributions for both production and decay of the D's, for both the 2m HBC and BEBC. At 12 GeV/c, ΔM_D for BEBC was $\pm$ 9 MeV/c^2 compared to $\pm$ 24 MeV/c^2 for the 2m chamber (H = 1.75 Tesla, $\varepsilon = 70\mu$).

b) Particle identification in BEBC promised to be good, with its large size giving a high probability for δ- rays on secondary tracks, a good measure of dE/dx over a long track length, trapping of low energy particles ($\lesssim$ 2 GeV/c), and a high probability of secondary interactions. This advantage would be useful for anomalous events - e.g. non-conservation of strangeness, and anomalous V^{o} decays.

c) The large size of the chamber gives good strange particle detection efficiency, and relatively good γ- ray detection efficiency ($\sim$ 15 %).

At the time when this experiment was proposed (February 1975) there was very little data available on inclusive strange particle production in $\bar{p}p$ interactions [13] , especially above 10 GeV/c. This experiment was therefore proposed to fill in some of the gaps in conventional $\bar{p}$ physics as well as to look for the production of new particles.

References

1. B. J. Bjorken, S. L. Glashow Physics Letters 11,(1964),255
2. S. L. Glashow Phys. Rev. D2,(1970),1285
3. S. Weinberg Phys. Rev. Lett. 19,(1967),1264 ;
   Phys. Rev. Lett. 27,(1971),1688
4. A. Salam, J. C. Ward Physics Letters 13,(1964),168
5. M. K. Gaillard, J. Rosner, B. Lee
   Rev. Mod. Phys. 47,(1975),277
6. J. Augustin et al. Phys. Rev. Lett. 33,(1974),1406
   G. S. Abrams et al. Phys. Rev. Lett. 33,(1974),1453
7. J. Aubert et al. Phys. Rev. Lett. 33,(1974),1404
8. H. Atherton Nucl. Phys. B16,(1970),416
9. F. T. Dao et al. Physics Letters 51B,(1974),505
10. H. Braun et al. Report to 1971 Amsterdam Conference
    CBH 71-3 Strasbourg
11. H. Atherton et al. CERN/D.PhII/Phys 71-18
12. CERN-Imperial College CERN/TCC 75-8 (February 1975)
13. H. Muirhead J. de Phys. Suppl. 34,(1974),365

TABLE I

Quark	Quantum Number				
	I	I_3	Q	S	C
u	$^1/_2$	$^1/_2$	$^2/_3$	0	0
d	$^1/_2$	$-^1/_2$	$-^1/_3$	0	0
s	0	0	$-^1/_3$	-1	0
c	0	0	$^2/_3$	0	1

$$Q = I_3 + \frac{B + S + C}{2}$$

TABLE II

Charmed 0^- Mesons

C	Label	Quark content	Isospin	Strangeness
1	D^+	$c\bar{d}$	$^1/_2$, $I_3=^1/_2$	0
1	D^0	$c\bar{u}$	$^1/_2$, $I_3=-^1/_2$	0
1	F^+	$c\bar{s}$	0	+1
0	η	$\sim\frac{1}{\sqrt{6}}(u\bar{u}+d\bar{d}-2s\bar{s})$	0	0
0	η'	$\sim\frac{1}{2}(u\bar{u}+d\bar{d}+s\bar{s})$	0	0
0	η'_c	$\frac{1}{\sqrt{12}}(u\bar{u}+d\bar{d}+s\bar{s}-3c\bar{c})$	0	0
-1	$\bar{D}^0$	$\bar{c}u$	$^1/_2$, $I_3=^1/_2$	0
-1	D^-	$\bar{c}d$	$^1/_2$, $I_3=-^1/_2$	0
-1	F^-	$\bar{c}s$	0	-1

Charmed 1^- Mesons

C	Label	Quark content	Isospin	Strangeness
0	ω	$\sim\frac{1}{\sqrt{2}}(u\bar{u}-d\bar{d})$	0	0
0	ϕ	$\sim s\bar{s}$	0	0
0	ϕ_c	$\sim c\bar{c}$	0	0
+1	D^{*+}, D^{*0}, F^{*+}	—— as D^+, D^0, F^+ ——		
-1	$\bar{D}^{*0}$, D^{*-}, F^{*-}	—— as $\bar{D}^0$, D^-, F^- ——		

TABLE III

Charmed $\frac{1}{2}^+$ Baryons

C	Label	Quark content	I	I_3	Strangeness
1	C_1^{++}	cuu	1	+1	0
1	C_1^{+}	$c(ud)_{sym}$	1	0	0
1	C_1^{o}	cdd	1	-1	0
1	C_o^{+}	$c(ud)_{anti}$	0	0	0
1	S^{+}	$c(su)_{sym}$	$\frac{1}{2}$	$+\frac{1}{2}$	-1
1	S^{o}	$c(sd)_{sym}$	$\frac{1}{2}$	$-\frac{1}{2}$	-1
1	A^{+}	$c(su)_{anti}$	$\frac{1}{2}$	$+\frac{1}{2}$	-1
1	A^{o}	$c(sd)_{anti}$	$\frac{1}{2}$	$-\frac{1}{2}$	-1
1	T^{o}	css	0	0	-2
2	X_u^{++}	ccu	$\frac{1}{2}$	$+\frac{1}{2}$	0
2	X_d^{+}	ccd	$\frac{1}{2}$	$-\frac{1}{2}$	0
2	X_s^{+}	ccs	0	0	-1

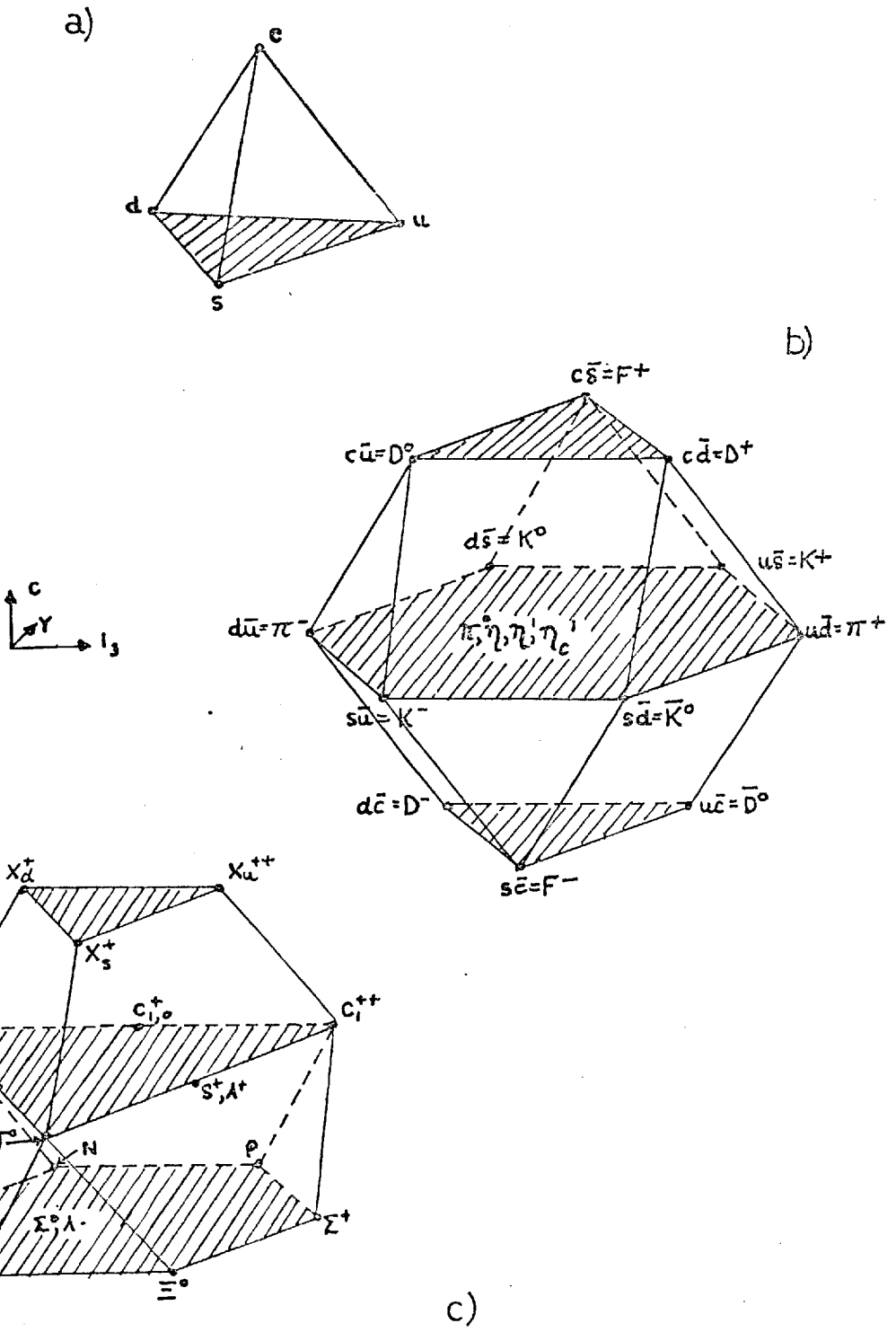


Figure 1 : Weight diagrams for SU(4).

a) The 4 quarks of SU(4) - the SU(3) triplet u ("up") d ("down"), and s ("strange"), with C=0, and singlet c ("charmed"), with C=1.

b) 15 - plet + singlet of pseudoscalar mesons

c) 20 - plet of $J^P = \frac{1}{2}^+$ baryons

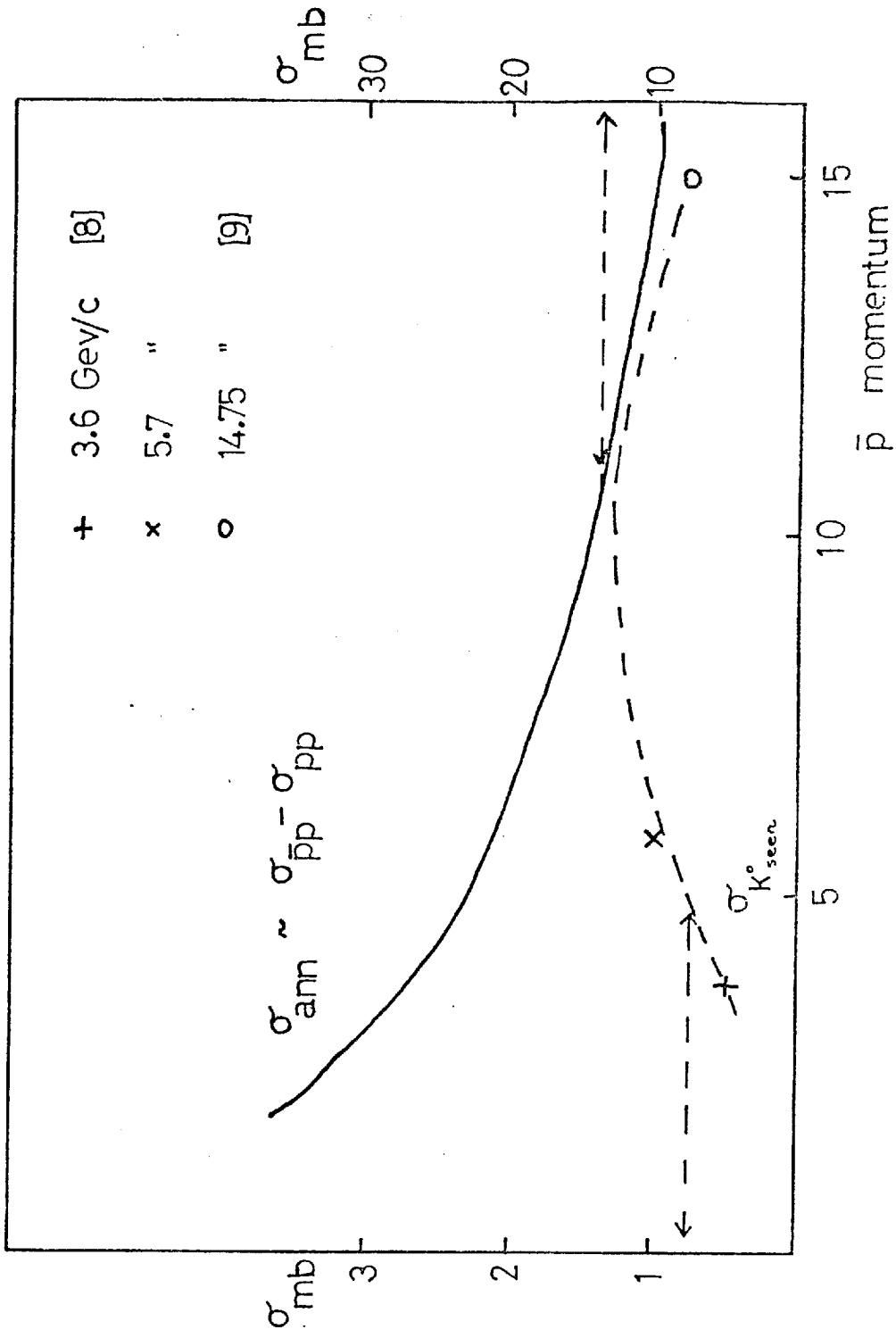


Figure 2 : The Annihilation cross section, derived from the difference between the $\bar{p}p$ and pp total cross sections, and the inclusive K^{o}_{seen} cross section. (Note separate scales.)

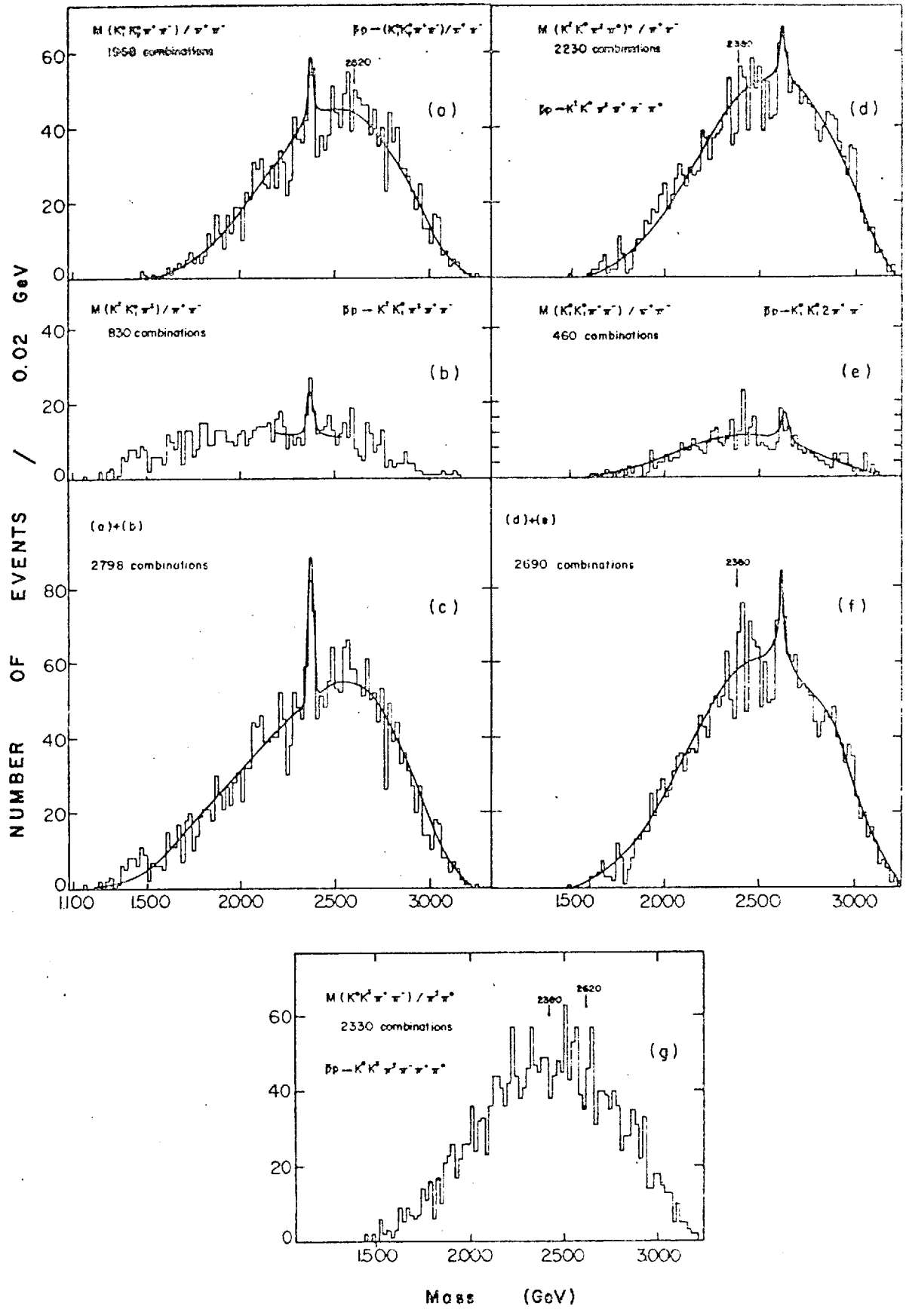


Figure 3 : Effective mass plots of non-strange neutral combinations from a $\bar{p}p$ experiment at 5.7 GeV/c [11] .

The Big European Bubble Chamber

1.1 Introduction

The obvious development of high energy physics in the 1960s was towards higher energies. This in turn meant higher multiplicity events with several neutral particles produced; these are complicated to study with counters. With a large volume of liquid however, the detection of the decays of neutral particles and γ-conversions from π^0 and Σ^0 decays is improved, producing a more detailed picture of the interaction that has occurred. The study of energetic neutrino beams also requires a large mass of liquid, since the cross sections involved are so small.

This need for large bubble chambers has been satisfied in Europe by the construction of the Big European Bubble Chamber (BEBC) at CERN. [1]

There are four main design differences between this new breed of large cryogenic bubble chambers and conventional bubble chambers, like the CERN 2 metre HBC.

1) Small spherical windows, called "fisheyes", one for each lens, are used instead of large flat glass windows.

2) The large volume of liquid is photographed through wide-angle lenses, close to the hydrogen. The field angle of the lenses used in BEBC is 108°.

3) An inexpensive and efficient way to illuminate the large volume is by covering the inside of the chamber with Scotchlite to give so-called "bright field illumination". The Scotchlite reflects incident light from annular flash tubes surrounding each camera lens straight back to the camera. When this reflected light meets a bubble the light is scattered and lost. Thus

the particle tracks appear on the film negative as bright images on a dark background.

4) Superconducting magnets are used, as they require less power and can produce larger field strengths than conventional electromagnets.

1.2 General Description and History

It was decided in 1967 to build a large bubble for use with the CERN Proton Synchrotron. The first tests were carried out in BEBC in 1972. The apparatus consists of a 3.7 metre diameter cylindrical vacuum chamber holding 35,000 litres of liquid. This is enclosed by a second vacuum chamber containing the cryostats which hold the two superconducting coils. An iron magnetic shielding wall weighing approximately 2000 tons surrounds the whole assembly. Figure 1 shows the actual chamber vessel being lowered into its vacuum chamber during construction in 1971. Figure 2 shows a cross-section of the apparatus, showing the positions of the piston, cameras, fisheyes, and superconducting magnet.

1.3 Detailed Description and Measurement of Constants

Magnetic Field

The magnetic field is produced by two superconducting coils, each immersed in a cryostat containing liquid helium. Direct mapping of the magnetic field inside the $22m^3$ useful volume has never been done. Instead, measurements have been made on the boundary surface, using 181 Hall probes, to an accuracy $\Delta B/B \sim 0.001$. The field inside the useful volume is then reconstructed by doing a least-squares fit of the field values from the Hall probes to a Legendre Polynomial series, giving a set of coefficients from which the field at any point inside the volume can be calculated. The values

found for B_z and B_ϕ, the vertical and radial components, are typically of order 35 Kilogauss and 50 gauss respectively.

The Hall probe system was built so that variations of the field during an experiment could be observed and corrected for. For example, when the superconducting magnet is charged and discharged, the varying radial field seen by the conductor of the magnet induces eddy currents which tend to oppose the change of field. This field is persistent as it is associated with a superconductor. It has been measured and gives a value of 200 gauss at the centre of BEBC after a complete charge or discharge of the magnet. It decays slowly, disappearing completely when the coils are no longer in the superconducting state. It was also predicted that another source of small eddy currents would be from the fast movement of the metal piston in the inhomogeneous field outside the useful volume.

Chamber Vessel and Coordinate System

The chamber vessel is made of stainless steel the thickness of which varies from 50 to 100 mm. for the walls and 5 mm. for the windows.

The chamber coordinate system, conventionally employed for event description, has its origin at the centre; the x-y plane is the beam plane and the z axis points up towards the cameras. Reference fiducial crosses are printed on to the Scotchlite and are identified by a 2, 3 or 4 digit number according to the plane they lie in and their angular position in that plane (Figure 3). The positions of the fiducials were determined at room temperature by triangulation. Their positions at the 25K working temperature were then calculated from the known thermal contraction properties of the chamber by applying the appropriate scale factor to these measurements.

Optics

There are five optical units; four of them have wide-angle lenses with annular flash tubes and see a useful volume of 22 m^3. The fifth can house either another camera or a periscope. The optical axis of each is inclined to the chamber z axis by 13°. Each unit has three hemispherical windows at different temperatures between 26K and 300K. Figure 4 shows the layout of the views used in this experiment.

All lenses were calibrated in the laboratory by photographing a 1m. square precision grid plate at different distances from the lens. These photographs were then measured on ERASME, a semi-automatic CRT measuring machine used at CERN. (This machine will be described briefly in Chapter 2.) The results of the measurements for each lens were combined to simulate a three-dimensional point matrix. The coordinate system used in these measurements was defined by the four "camera-based fiducials", which are incorporated into the optical system and printed on each photo. (They are the four crosses in dark circles at the extreme corners of the frame in Figure 3). An optical model describing the properties of the lenses was chosen and the distortion coefficients and pupil shift parameters (the pupil moves along the optical axis for large viewing angles) were determined by fitting the measured grid points to their known spatial positions. The 16 parameters from these fits are included in the title block for the geometry programme so that the transformation from the distorted, real film plane to the undistorted, ideal film plane can be made.

The geometrical constants of the chamber (i.e. the position of the pupil, direction of the optical axis, and the fisheye parameters

to allow for small non-concentricities of the fisheye windows) were determined in a similar way by fitting the known positions of the 90 fixed fiducials on the walls of BEBC to their corresponding measured positions on the film. The constants for each camera were fitted separately in this procedure.

1.4 Problems Affecting Picture Quality

Thermal Turbulence

The tracks are photographed through several metres of liquid. Hydrogen has a large thermal expansion coefficient, a small viscosity, and a small thermal conductivity so that heat is mainly transported by convection, which causes turbulence. The consequences are that bubbles are physically displaced and light rays suffer multiple scattering through the turbulent hydrogen.

Illumination and Distortion

Dark field illumination (where the track image on film is produced by light scattered from the track bubbles, no light being reflected from the background material) is used in conventional chambers like the CERN 2 metre HBC. The tracks are viewed through a plane glass window by three cameras. To produce a window large enough for BEBC, in a similar style, would have been technically unfeasible because of thermal cooling problems. So bright field illumination, as described in the introduction to this chapter, must be used in BEBC. The large volume is illuminated by small light sources surrounding each lens, and the lenses collect light reflected from the Scotchlite covered surfaces of the chamber rather than from the bubbles themselves.

Dark field illumination requires bubbles of 100 to 300μ in

diameter. However, with bright-field illumination bubbles of this size would be invisible since the contrast drops sharply when the size of the geometrical image of the bubble approaches the size of the diffraction spot produced by the lens. Thus, bubbles of diameter 500 to 700μ are required. At the 26K working temperature of BEBC, bubbles grow to 200 to 300μ in 1 ms. and therefore grow to the correct size for bright-field illumination with a 4 ms. flash delay. (The diameter of a bubble is proportional to the square root of the bubble growth time.) Thus the track distortion due to eddy motion is worse, and there is less ionisation information available per unit track length.

Scotchlite and Variable Contrast

Scotchlite was fixed to all visible surfaces inside BEBC. Much has been learned from the problems encountered in this experiment, and not least from the track visibility problem. Even from the pictures taken in the 1m. model of BEBC, it was obvious that there would be problems with changing density difference across the film giving a variable contrast between the tracks and the background. Two reasons for this are the loss of reflecting power of Scotchlite with increasing angle of incidence, and the attenuation of light inside a wide-angle lens, especially around the edges.

Other problems for the measurement of the film concerned the ring of parasitic bubbles above the piston ring, across which the tracks must be followed by automatic measuring machines. (see Figure 5) Two plastic pistons made for BEBC broke during tests before this experiment was run, so a metal piston was hastily made. The soldering on the top of the piston caused a fissure to appear during the run, which allowed gaseous hydrogen to leak into the chamber and

produce a further large patch of parasitic bubbles which rotated slowly with the piston rotation.

Teflon seals were used between the moving piston and the chamber walls. If they were too tight, teflon dust was released and scattered over the piston head and lower parts of the chamber, reducing the contrast in these regions still further. If they were too loose hydrogen gas leaked into the chamber, giving the characteristic boiling ring. These problems, as they affected the scanning and measuring processes, will be discussed in chapter 2.

The following improvements have been made to the arrangement of the Scotchlite for future experiments :-

a) The parasitic bubbles and teflon dust-covered piston head have been covered by a floating disc.

b) Scotchlite covered screens have been built and erected at an angle to the vertical chamber walls, so that the angle of incidence of light on the Scotchlite is more favourable.

These changes have greatly improved the quality of pictures obtained in later BEBC experiments, as can be seen from Figure 6 .

1.5 The Beam

An RF-separated beam of antiprotons from an external target of the CERN Proton Synchrotron was used for this experiment. The general layout of the elements of the U7 beam line, which separated and transported the antiprotons towards the West Area and into BEBC is shown in Figure 7 .

References

1. G. Harigel — BEBC Users Handbook — CERN Feb 1977
2. U5 Beam — CERN Yellow Report 74-1
3. P. Lazeyras — Private communication

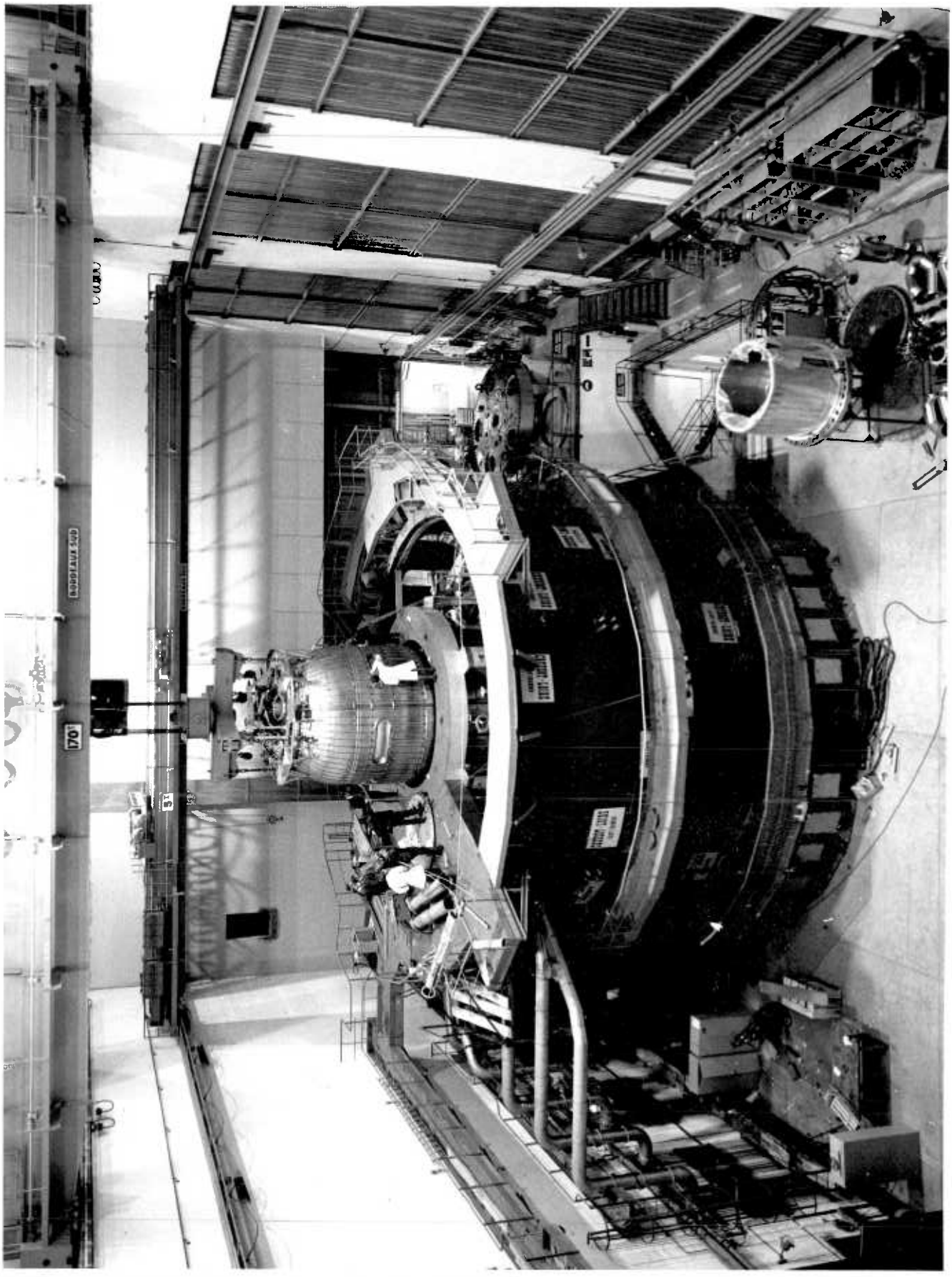


Figure 1.1 : The stainless steel tank of BEBC being lowered into the vacuum chambers and superconducting coils during construction in 1971.

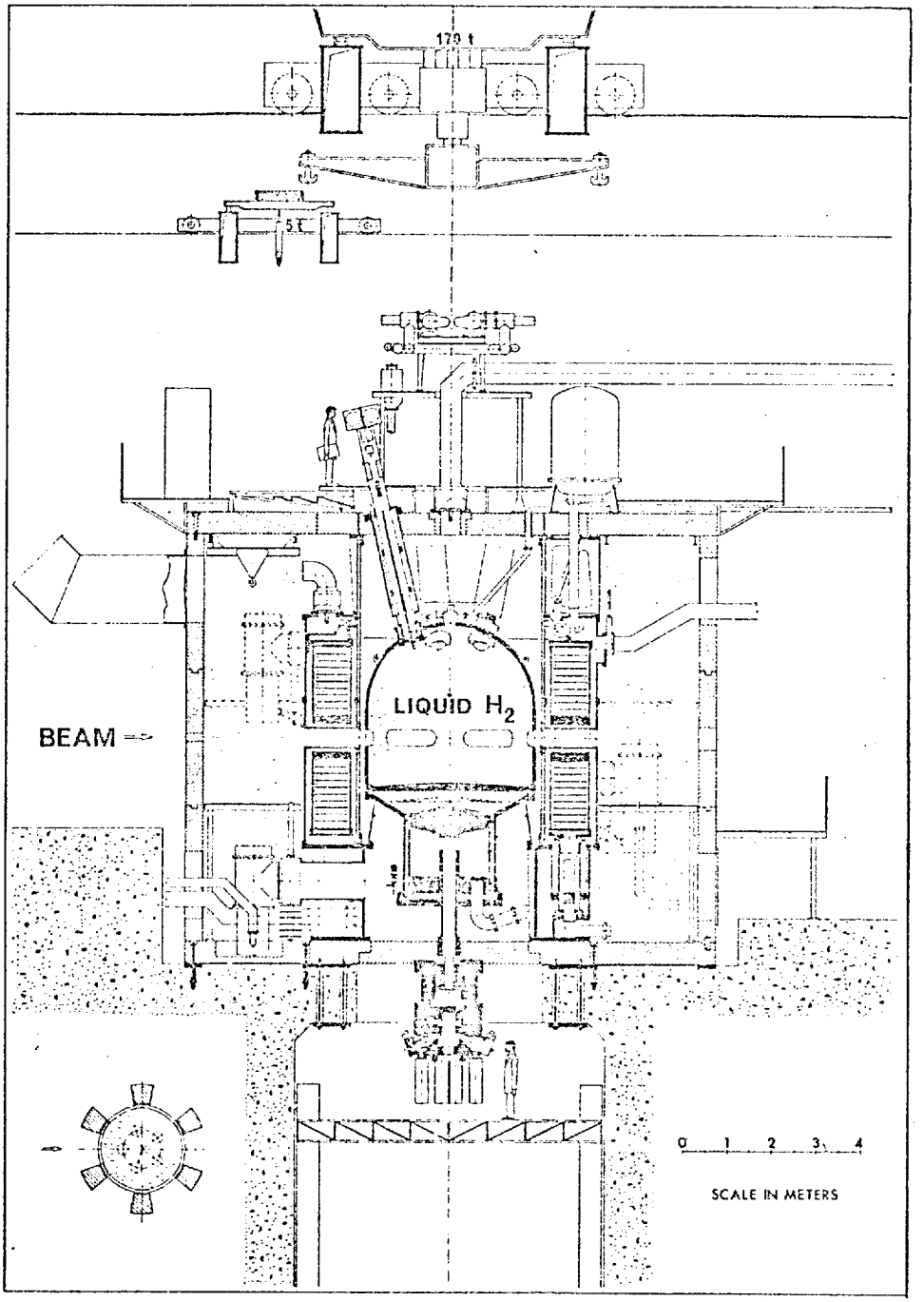


Figure 1.2 : Vertical cross-section of BEBC, showing the dome-shaped chamber, magnets, shielding, cameras, expansion piston etc.

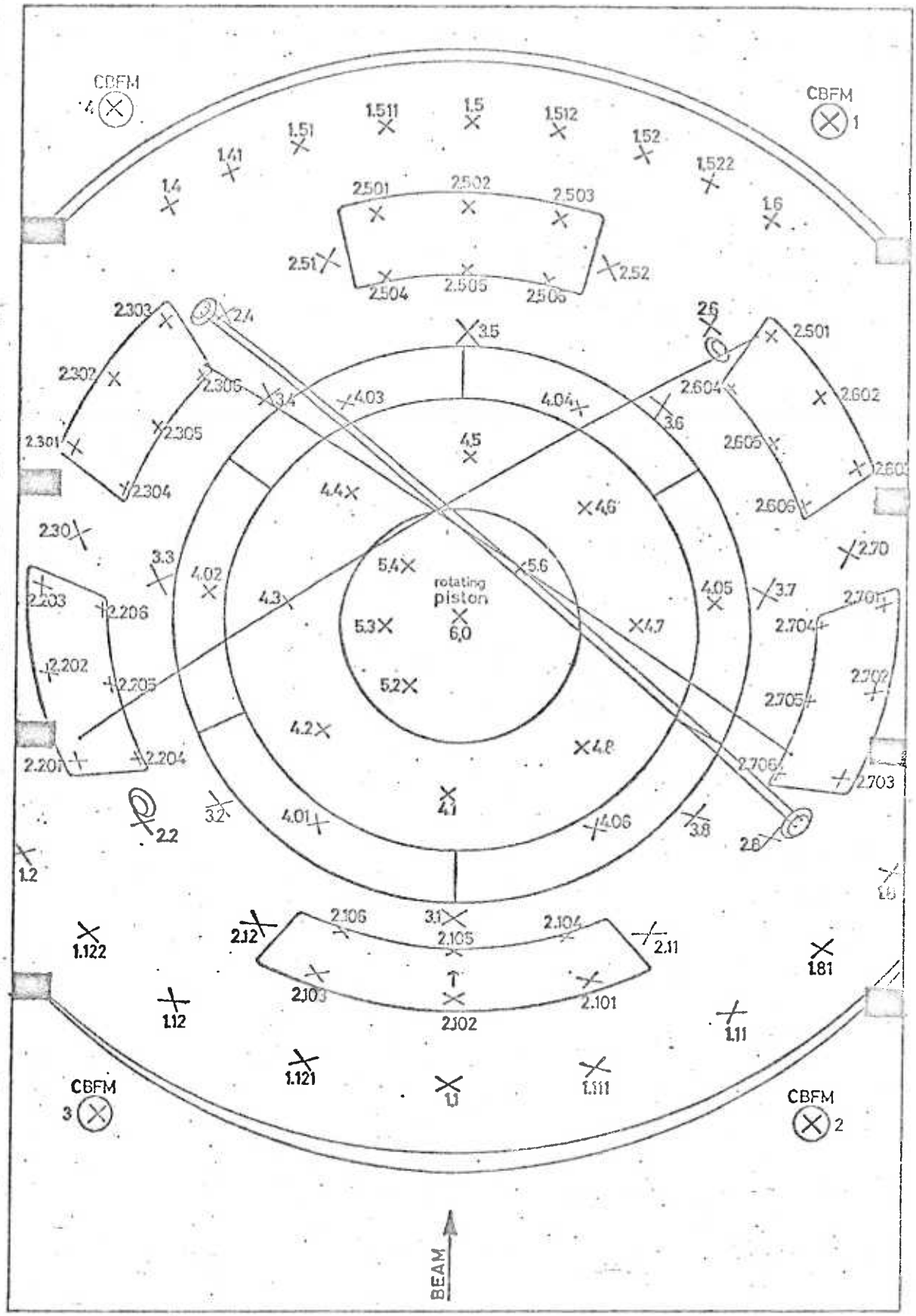


Figure 1.3 : Layout of reference fiducials in BEBC. There are 90 chamber-based fiducials printed on to the Scotchlite, and 4 camera-based fiducials (1,2,3,4 in circles).

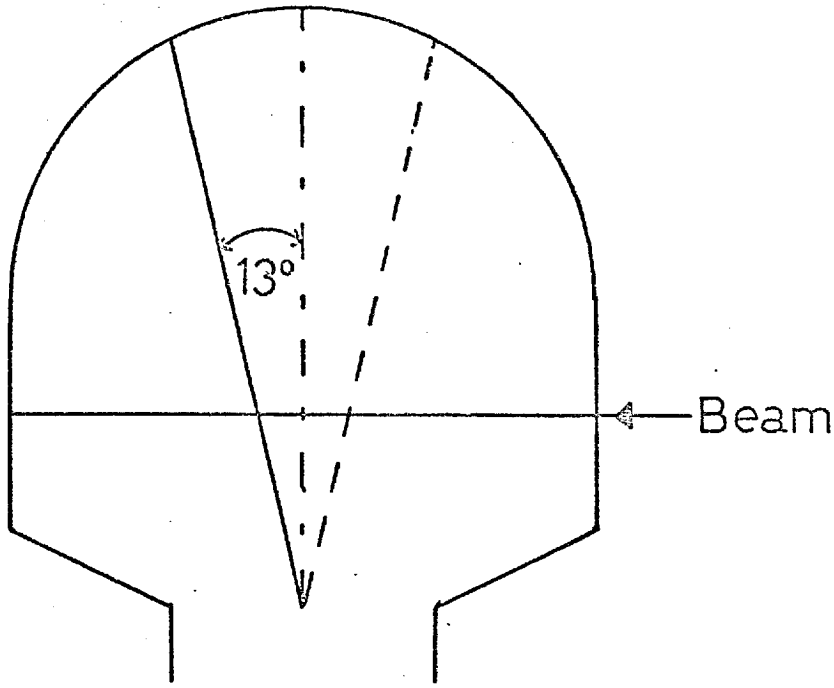


Figure 1.4 a) Vertical cross-section of BEBC showing inclination of the camera optical axis to the vertical, and the position of the beam plane.

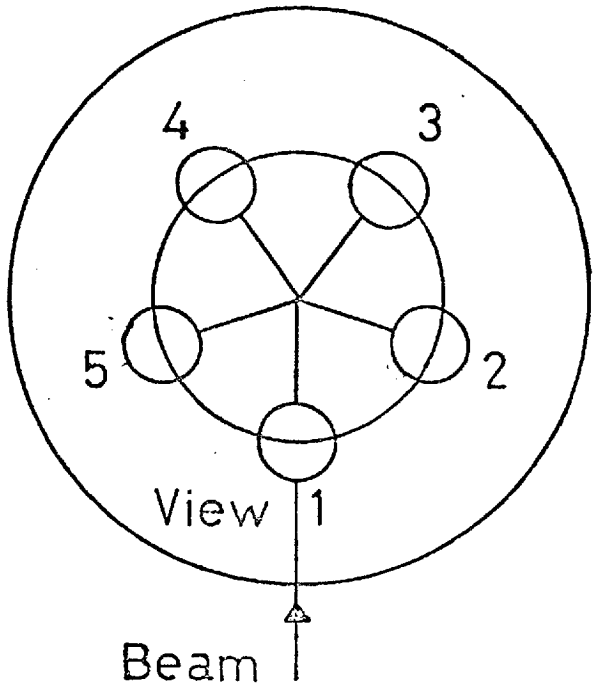


Figure 1.4 b) Plan view of BEBC, showing the camera positions relative to the incoming beam direction.

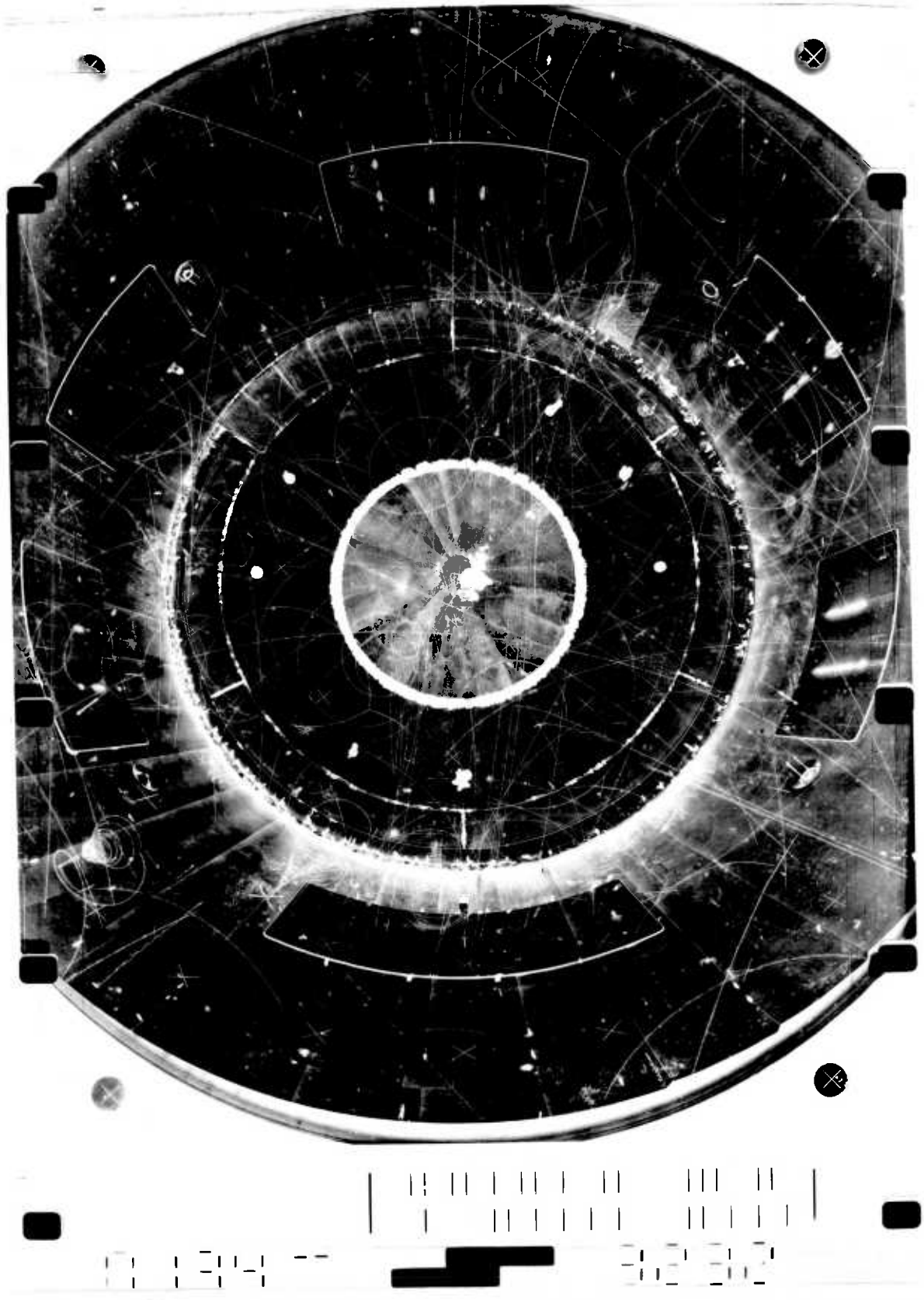


Figure 1.5 : A frame from the 12 GeV/c $\bar{p}$ experiment. This picture comes from one of the early rolls, before the teflon dust became a serious problem. The contrast and general picture quality was at its best at this stage.

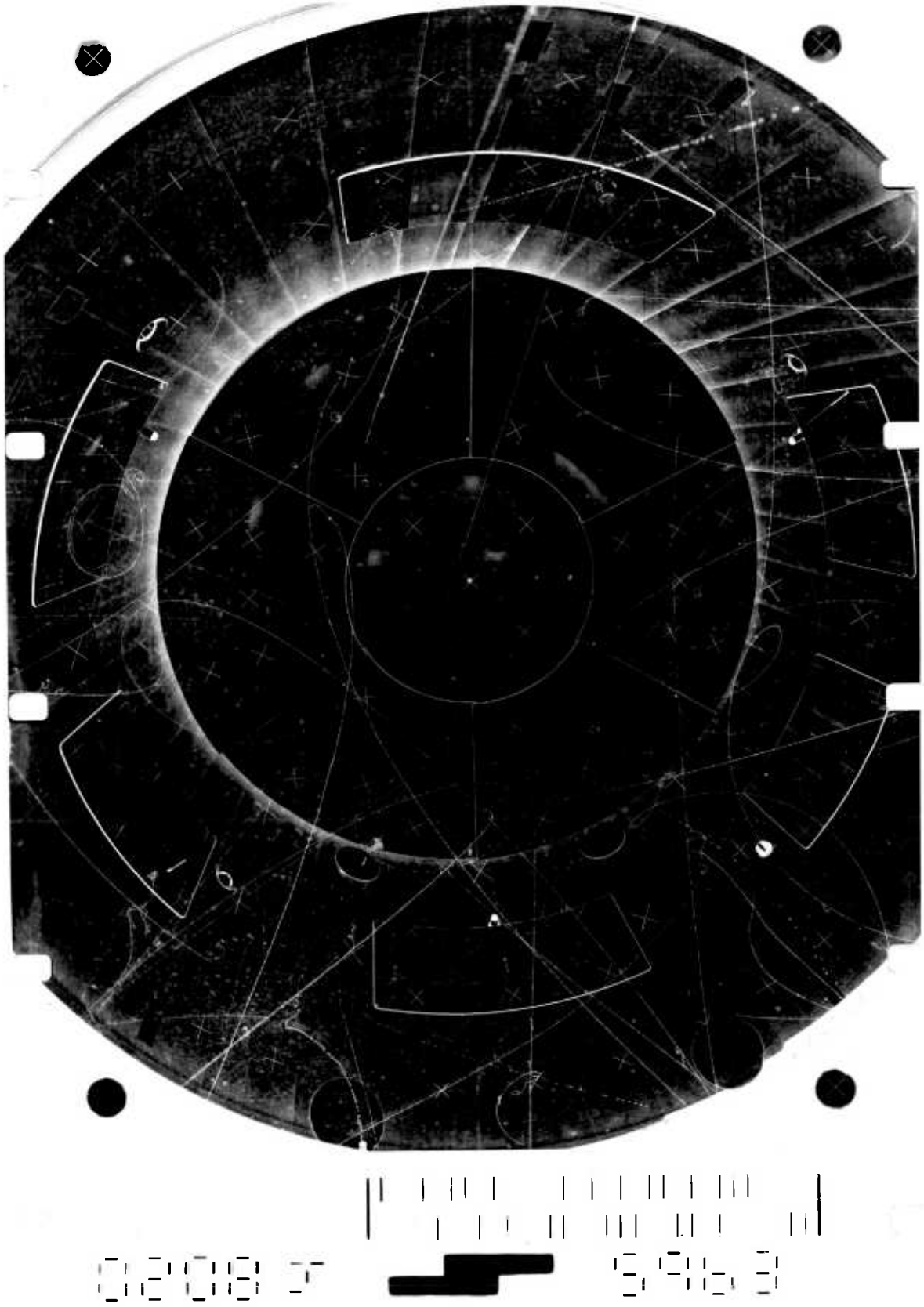


Figure 1.6 : A frame from a recent narrow-band ν experiment in BEBC filled with a Ne - H_2 mixture. There are fewer fiducial crosses than before, and many of them are printed on to the moveable Scotchlite screens. There are no problems with teflon dust and parasitic bubbles, and the contrast is much more uniform across the picture.

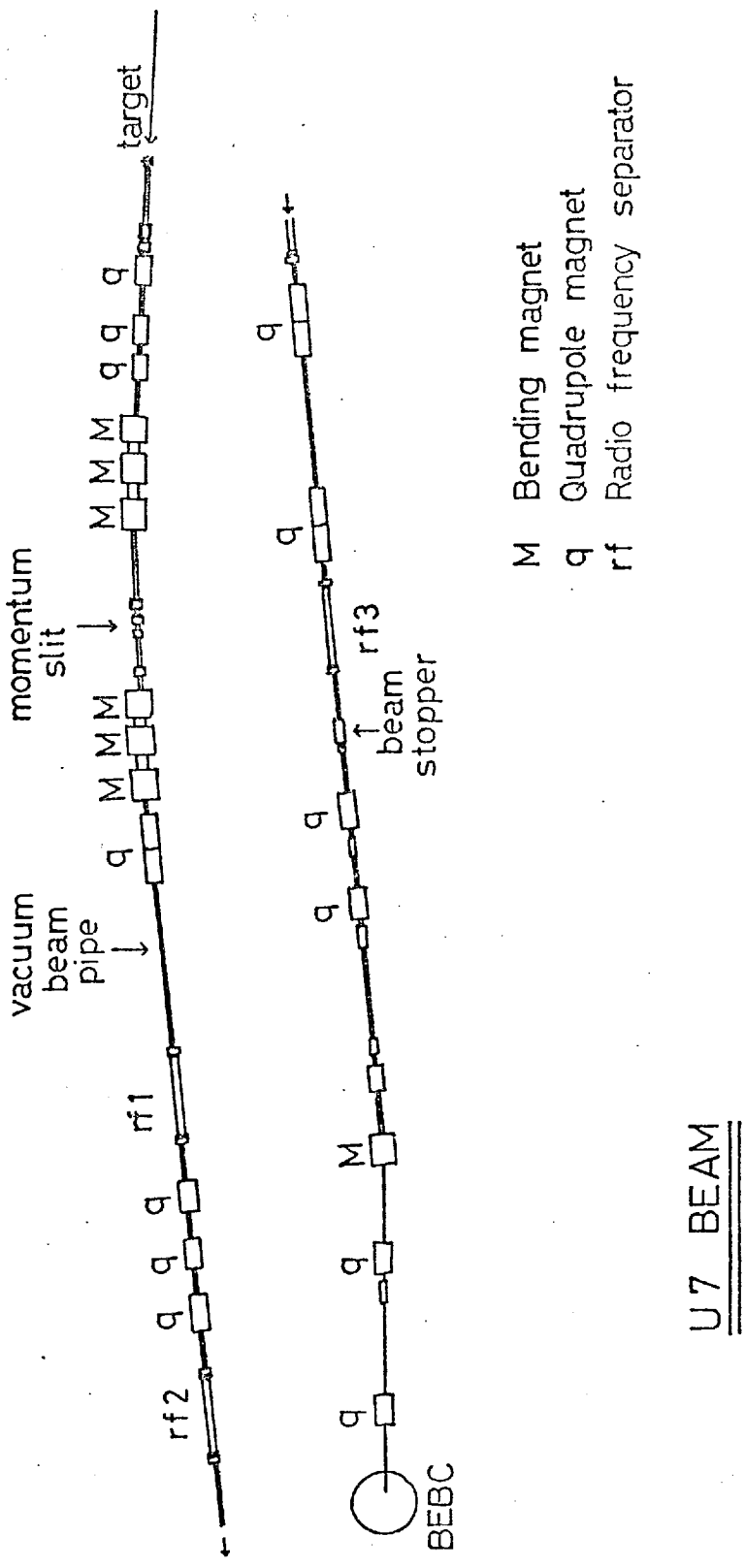


Figure 1.7 : Elements of the U7 beam line. The proton beam from the CERN PS hits a target (top right), and after separation and focussing, the antiprotons reach BEBC (bottom left).

DATA PROCESSING : SCANNING AND MEASURING

2.1 Introduction

The prime objective of this experiment was to look for charmed particles by observing their decays to strange particles. The signature of strange particle decays searched for was the V^0 and the charged $V^{\pm}$, coming from the primary vertex.

This chapter describes the method of scanning and pre-digitizing for the automatic measuring machine at Imperial College (an HPD), the scanning and throughput efficiencies, and the problems encountered in the measurement of film from BEBC.

2.2 Scanning

All events with primary vertex occurring within the fiducial volume, defined as the regions A, B, and C as seen on View 1 (see Figure 1), and with at least one strange particle associated with them, were recorded by the scanners. This fiducial volume was chosen so that the minimum track length of all tracks from the primary vertex would be 50 cm. (for the fastest tracks), thus allowing a reasonable measurement of track curvature and direction, and giving a good probability for V^0s to decay within the chamber. V^0s were accepted anywhere in the chamber if their tracks were long enough to be measured.

The number of beam tracks entering the fiducial volume was recorded every tenth frame for cross section calculations and a "Zuon book" was kept. A zuon was defined as any event that the scanner could not explain. For example, an event with an odd number of tracks from the primary vertex, an even prong neutral star, a two-prong secondary interaction with two negative tracks, or a track with two successive kinks ($V^{\pm}$) might have been recorded. All events

in the Zuon book were checked by a physicist. No even prong neutral stars were found; these might have indicated the decay of a long-lived heavy neutral particle. Odd prong events with a positive track missing could be explained as events with a slow proton (momentum less than 100 MeV/c) which does not leave a visible track due to its short range in liquid hydrogen at low momenta. The momentum distribution for tracks flagged as stopping protons did in fact show a depletion of events at low momenta. Those events with a negative track missing could be explained by reactions of the type

$$\pi^- p \longrightarrow \pi^0 n$$

where the π^-, produced at the primary vertex of the $\bar{p}p$ interaction interacts very near to the vertex, before producing a visible track.

2.3 V^0 and $V^\pm$ Definitions

The large volume of BEBC means that there is a significant probability that γ's, produced mainly from the decay $\pi^0 \longrightarrow \gamma\gamma$, will convert to e^+e^- pairs inside the chamber. The γ detection efficiency has been calculated, and is about 20%. It was therefore necessary to define a V^0, for scanning purposes, by one or more of the following criteria :-

a) Non-zero opening angle.

b) One or both arms with a secondary interaction or $\pi\mu e$ decay.

c) One or both arms with bubble density greater than minimum, taking into account the possibly large dip angle.

An ambiguous V^0 was one which did not fulfil any of these definitions but was not an electron-positron pair.

Similarly, a length cut was imposed for charged V's so that events chosen as ones including a charged strange particle were not heavily

contaminated with π decays. Thus, a $V^{\pm}$ was defined as a kink occurring less than 8 cm. from the primary vertex on a Bessy scan table (x15 magnification from film).

2.4 Scanning Efficiency and Rough Digitising

9000 frames were scanned twice and the differences between the two scans resolved by a check scan. The number of events found on each scan (N_i ,i=1,2) and the number of events found common to both scans (N_{12}) were calculated. The efficiency for a single scan, λ_i, is equal to the number of events found in that scan, N_i, divided by the "true" number of events, N_T,

$$\lambda_i = N_i / N_T$$

An estimate of this true number of events is N_1N_2/N_{12}. The mean single scan efficiency for different topologies was calculated and the results are shown in Table 1. No estimate was made of biases in the scanning due to the loss of events with high topology where the V^0 decayed so close to the vertex that it was not identified. (For example, a 601 (6 prong with one V^0) which was classified as a simple 8-prong would have been rejected.)

Since the chronological development of the system used at Imperial College to measure the BEBC film is somewhat complicated, a brief summary of this aspect will be given before the system itself is described in detail.

The Imperial College group was the first (with this experiment) to attempt full-scale automatic measurement of BEBC film. This meant that many new hardware and software problems had to be overcome. The chain of programs used initially was the same as that used for the measurement of conventional bubble chamber film.

(see figure 2). A good description of the measurement of film from conventional bubble chambers, using the Imperial College HPD, can be found in ref. 1 . The film was scanned and rough-digitised on separate passes. This pre-digitisation stage, required by the HPD, serves to list the frames of interest and define rough "roads" where the tracks of the required event can be found so that it becomes unnecessary to digitise the whole frame. The success rate for complete events along this chain was only 50% so a second pass through the HPD was made with new rough digitisings. Only a further 10% were recovered by this process, so after several months, the philosophy behind the old programmes was changed to take account of all the lessons learned from this new bubble chamber, and a new chain of programmes was written. The original (1st measurement) roads were used (i.e. no more rough digitising took place) and all the film was processed through the HPD and geometry programmes again.

All of the programmes up to the geometry input stage (programme SMOG) were written to accommodate measurements from 3 views only. Also, except for the two Bessy scan tables, all scanning and pre-measurement tables were 3-channel machines only. It was therefore practical to measure only three of the four views. The three originally chosen, for reasons of symmetry and large stereo angles (see figure 4 , chapter 1), were views 1,3 and 4. After several rolls had been measured, it was apparent that measurements from view 1 were worse than from the other two views, as the residuals on this view were consistently larger. So views 2,3 and 4 were used for measurements of the rest of the film. However, with the advent of a new set of geometry titles from CERN, the differences between the views became less noticeable.

Two fiducials were measured on each view, together with all vertices and up to four points per track, instead of the usual two points used for previous experiments. The high magnetic field, orientation of the camera axes and fisheye optics of BEBC caused many tracks to have high curvature and to appear non-circular on film, so it was decided to measure such tracks in several segments to simplify track following through large angles. The vertex and first two points were used to define the "road" for the first segment and each subsequent point was used to define another segment. For the remainder of the measurement procedure these segments were treated as separate tracks. For each segment, the programme MIST decided whether it should be measured on the normal or abnormal scan of the HPD, according to the angle each segment made with the edge of the film.

2.5 HPD Measurements - changes to hardware and software for BEBC film measurement

The demagnification from bubble chamber to film is large for BEBC; greater than x50 from the beam plane, and there is a rapid variation of this demagnification with position in the chamber. The laser of HPD1 at Imperial College has a spot size of between 5 and 10μ (It has not been measured, but a similar system has been studied at the Rutherford Laboratory.) This is of the same order as the bubble size on film. The scan line separation was decreased from 60μ for 2m HBC film to between 30 and 35μ to allow for this greater demagnification.

It has already been noted (chapter 1.4) that bright-field illumination gives white tracks on a dark background, so it was necessary to reverse the logic in the photomultiplier circuits to enable BEBC

pictures to be digitised. However, the picture number is black on white, requiring the same logic as the 2mHBC film. Thus two circuits were built which were switched between the picture number scan and the start of the normal HPD scan.

The contrast between tracks and background is often very poor and varies from low contrast over the piston where dust was present to good contrast nearer the edge of the film. To cope with this problem, the photomultiplier tubes were fitted with automatic gain control (AGC) circuits. The digitisings were averaged over 100 to 200μ of the scan to give a background level, which was then compared with the signal from the track. When this signal to background ratio fell below a certain limit, the gain of the photomultiplier was increased to allow for the lack of contrast, and vice versa when the contrast improved.

Another problem concerned the images of the chamber-based fiducials. Conventional bubble chambers with flat glass windows have fiducials whose arms are at right angles to one another and at 45^{o} to the edge of the film. This makes their identification from the digitisings in the known region of the fiducials relatively easy. The fiducials in BEBC, stuck on to the curved chamber walls and viewed through fisheye optics, are not so easily identified. Thus, the HPD measurement programme HAZE had to be provided not only with the predicted coordinates of the 20 fiducials to be measured, but also with the tangents of the angles between their arms and the edge of the film. These angles were measured at Imperial College using a conventional digitising table. Also, many of the fiducial arms were curved, requiring that a parabola be fitted to them instead of a straight line.

The final two links in the processing chain before geometry are the RESCUE programme, which allows a scanner to recover some tracks which the HPD has failed to find or to follow correctly, and the SMOG programme, which produces the final geometry input. The HAZE programme outputs the entire contents (digitisings) of a road on to a magnetic tape when it has failed to find a track, or when the track has an error code associated with it (e.g. gaps along the track; less than five points; track leaves the road, etc.). These digitisings are displayed on a CRT display by the off-line programme RESCUE[2].A light-pen can then be used by the scanner to redefine a new narrow road for the track. The filtering process is then repeated and new master points are calculated for the track. After the measurements have passed through HAZE and RESCUE, the SMOG programme recombines the data from the three views, links the track segments together, and prepares the data for output on a magnetic tape which can be used as direct input to the geometry programme.

2.6 Throughput Efficiency

The throughput efficiency was defined as the ratio of the number of events with a successful V^0 kinematic fit, but not necessarily with all primary vertex tracks present, to the total number of scanned events. The geometry and kinematics programmes will be described in more detail in chapter 3. The throughput efficiency was found to be about 50% only, so a programme of remeasurements was initiated.

2.7 Remeasures

A programme was written to examine the output from the kinematics programme, where the parameters describing the charged primary vertex tracks come from the mass dependent fits in geometry and those descrit-

ing the V^o come from the kinematic fit to that vertex. The output from the remeasures programme, REAM, was in the form of computer printout, giving details of which events were to be rough-digitised completely again (prior to a second pass through the HPD), and those which required only one or two tracks to be re-rough-digitised, and magnetic tape output of track parameters for partial events. All events appearing on the kinematics tape were compared with the master list (a list stored on disk, containing the roll-frame-event number, topology, measurer's number and machine number of all events, created from the ONEDIT output). Events which did not appear on the kinematics tape were automatically sent for full remeasurement as "HAZE failures". If the topology measured, given on the master list, agreed with the number of tracks with good mass fits from geometry, the V^o fits were checked and failures were output requiring the remeasurement of all V^o tracks and the beam track. A track was also failed if it had been badly measured (i.e. the helix fit residual was greater than 12μ). If the number of failed primary vertex tracks was greater than five, or greater than 40% of the expected number, the event was sent for full remeasurement. If not, the good tracks were output to tape and a graphics picture was produced offline, on a Tektronix graphics display unit, showing the projection of the geometrical helix fits on the different views. A hard copy of this was used by the scanners to indicate which track or tracks were to be remeasured. The picture was compared with the film and tracks not appearing in the picture were remeasured. Again, the V^os were checked for kinematic failure and their remeasurement requested when necessary. All these remeasurements, partial and complete, were processed as complete events and a special version of geometry was used to merge the two sets of measurements from passes 1 and 2, eliminating duplicate tracks. This

method was reasonably successful and certainly speeded up the remeasurement process. However, the overall throughput after two measurements was still only about 60%.

A detailed study was made of about 60 events from three different rolls. They were processed normally, but after each programme the results were studied in detail to detect track segments which had failed. It was hoped that this method would indicate one or two main causes of the poor pass rate. The results from part of this study are summarised in Table II.

The main lesson learned from the above investigations was that there was no one cause, but that tracks could be lost all along the chain and an overall improvement could be obtained only if all the programmes were improved. It was therefore decided to remeasure all events, concentrating on the lower topologies and using all four views. By this stage, the 6-, 8-, and 10-prong topologies had been remeasured on a conventional measuring machine with a throughput efficiency of 86%.

2.8 Improved Measurement System

The chain of programmes used for the final measurement of the film for this experiment is shown in figure 4 .

A new version of MIST was written, which calculated the roads for the fourth view and reduced the number of segments into which each track had been divided.

The first of these improvements was achieved by performing a helix fit in space to the measured road points. This helix was then projected on to the fourth, unmeasured view. An approximate track match procedure was attempted, but if this failed, all possible roads

were kept and used in HAZE to search for the tracks on the fourth view; wrong combinations of measured roads would hopefully lead to a nonsense fourth view road. As a bonus, the lengths of all roads were increased by 10%.

Some changes were made to the HPD hardware which improved the measurements. The most important of these was the removal of a diverging lens which had been introduced to produce the even illumination required for estimation of ionisation on 2mHBC film. The light intensity incident on the film in the HPD was increased by a factor of 20, but the "evenness" of illumination was decreased by a factor of 2 or 3. This loss was unimportant since the AGC could compensate where necessary.

The other major improvement to the measurement system was the introduction of geometry into the RESCUE programme.

2.9 Rescue Geometry

The programme REGEOM takes the HPD measurements and performs standard geometrical reconstruction before any light-penning is attempted. If there are no measurements of a particular track on one view, the helix fit found from the other views is projected on to the digitisings, which have been stored, for the missing view, and this is then used as a road.

The following criteria are used to decide which tracks must be light-penned :-

1) A gap between master points (measurements) greater than 20 cm. in space.
2) Length of track on one view very different from length on other views. If the road is short on this view, the track is not sent

to be rescued.

3) Residual greater than 20μ.

4) A gap at the beginning of the track.

5) Track not used in any multiple chosen by track match. This is the largest source of tracks to be rescued.

6) No points on the track.

Approximately 30% of all tracks are sent to be light-penned. The event is rerun through geometry and the same process repeated, except that once a track has been light-penned, it is not failed a second time. The maximum number of passes through geometry is three. One event is processed every two minutes on average, but it is possible to have two REGEOM programmes running alongside one another, each sending tracks to be light-penned, so that while one event is being processed through geometry, the other is being rescued.

The treatment of short tracks has also been altered. The measurements from tracks which are shorter than 600μ (on film) are automatically treated as two point tracks. That is, any measurements are discarded and the track is flagged as a connecting track in the geometry data structure. The end point (vertex) measurements are obviously kept. Tracks between 600 and 1800μ in length with less than two measurements are treated as above, but those with more points are treated normally.

The events are then processed through an offline version of the GEOMETRY programme which will be described in the next chapter.

2.10 Measurement Techniques in Other Laboratories

The 250,000 photographs were divided into three sections ; half of the total film was measured at CERN and one quarter each in Bruxelles and Imperial College.

The film at CERN was measured using ERASME (Electron Ray Scanning and Measuring Equipment), controlled by a PDP10 computer. After the film had been scanned and pre-measured off-line (all vertices and at least one point per track), this CRT device automatically measures 23 fiducials, all vertices and tracks on 4 views. An operator checks and rescues vertices and tracks when necessary. When all measurements have been accepted, the complete event is passed to HYDRA geometry for track matching and space reconstruction. Diagnostics may be displayed to the operator, such as wrong topology, track missing on one view, or residuals too large. The operator must then choose whether to accept the event or remeasure some part of it. Only about three events an hour can be measured, but the throughput efficiency is about 95% for all tracks (81% for a 4-prong event).

Bruxelles measured most of their film on a POLLY machine, which is also a CRT device. An operator measures three fiducials, all vertices, and two points per track on two views only. The first point on each track is used to guide POLLY and the second marks either a decay or interaction vertex or the point where the track leaves the chamber. 16 fiducials are automatically measured by POLLY. The event is measured and track reconstruction proceeds using TVGP. Bad measurements, unmatched tracks etc. are returned to the operator for remeasurement, which may include measurement of the third view. 60% of all tracks are reconstructed on two views and the remaining 40% on three views. The events are passed through HYDRA geometry off-line. The overall throughput efficiency for events is 78%.

References

1. B.K. Penney IC/HEP/T/20 May 1971

2. B.K. Penney IC HENP Physics Note August 1971

TABLE I

Scanning efficiencies for the different topologies.

No. of prongs	Efficiency (%)
0	77.1 ± 12.3
2	75.2 ± 6.5
4	75.4 ± 6.8
6	72.7 ± 11.5
8, 10	78.5 ± 24.1

TABLE II

10% complete evts. - all tracks through Geometry with 3 views

20% complete evts. - all tracks through Geometry with 2 or 3 views

35% events had one track segment which failed

25% events had more than one track segment which failed

5% events failed before MIST programme

5% events failed at HPD (HAZE) stage (no digitisings etc.)

50% of all track segments are sent to the RESCUE programme, and of these :-

44% fail because a) the track leaves the road (i.e. bad roadmaking)
or b) not enough digitisings
or c) circle fit to master points failed

36% fail because a) there are less than 5 master points
b) the master points do not extend over the whole length of the road

20% fail for other, more technical reasons in HAZE

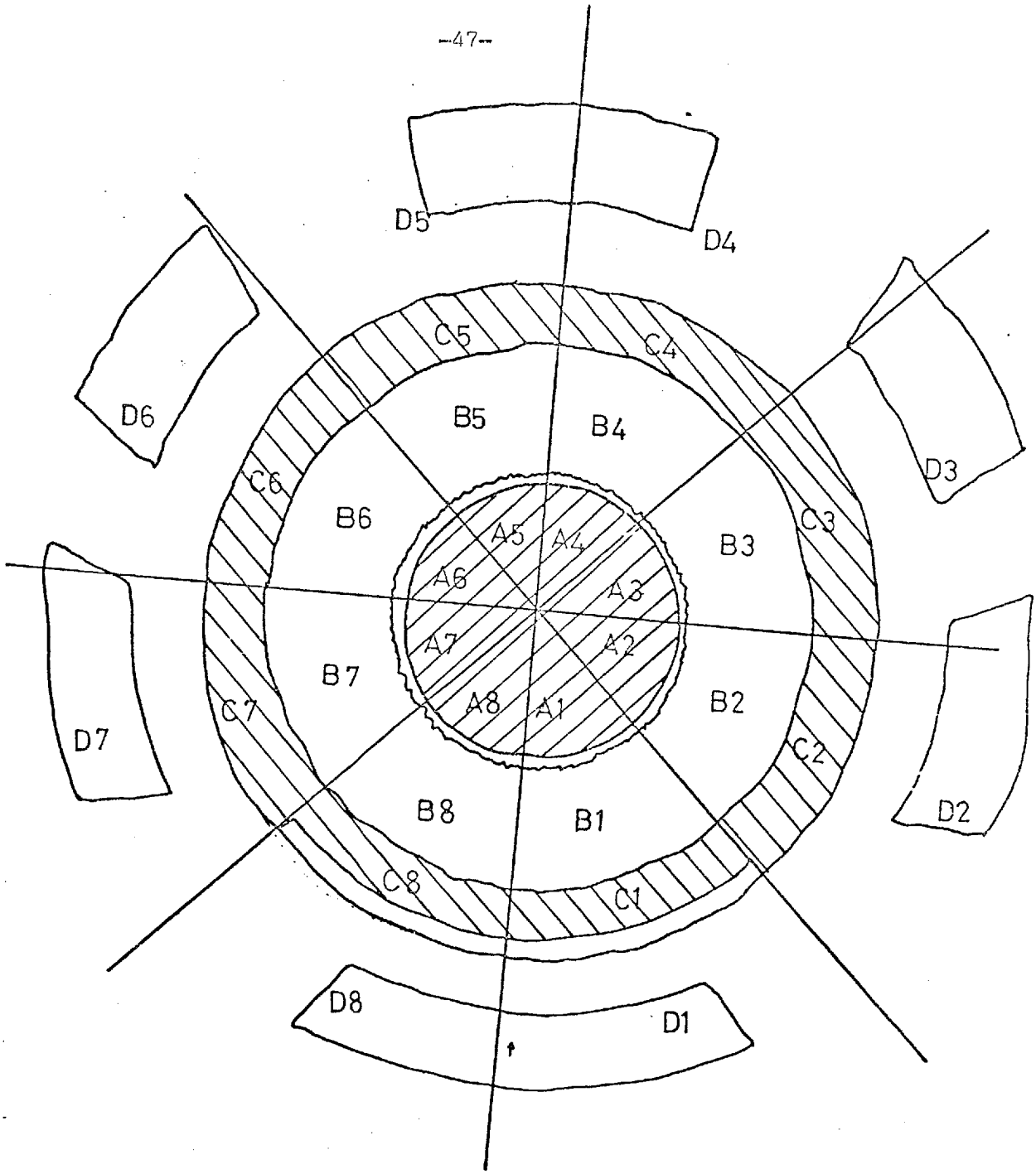


Figure 2.1 : BEBC was divided into 32 regions for scanning and measuring purposes. The 8 radial lines were defined by the positions of fiducials in sections B (see Figure 1.3) and the concentric circles separating sections A, B, C, and D were the edges of the scotchlite on the piston and chamber walls.

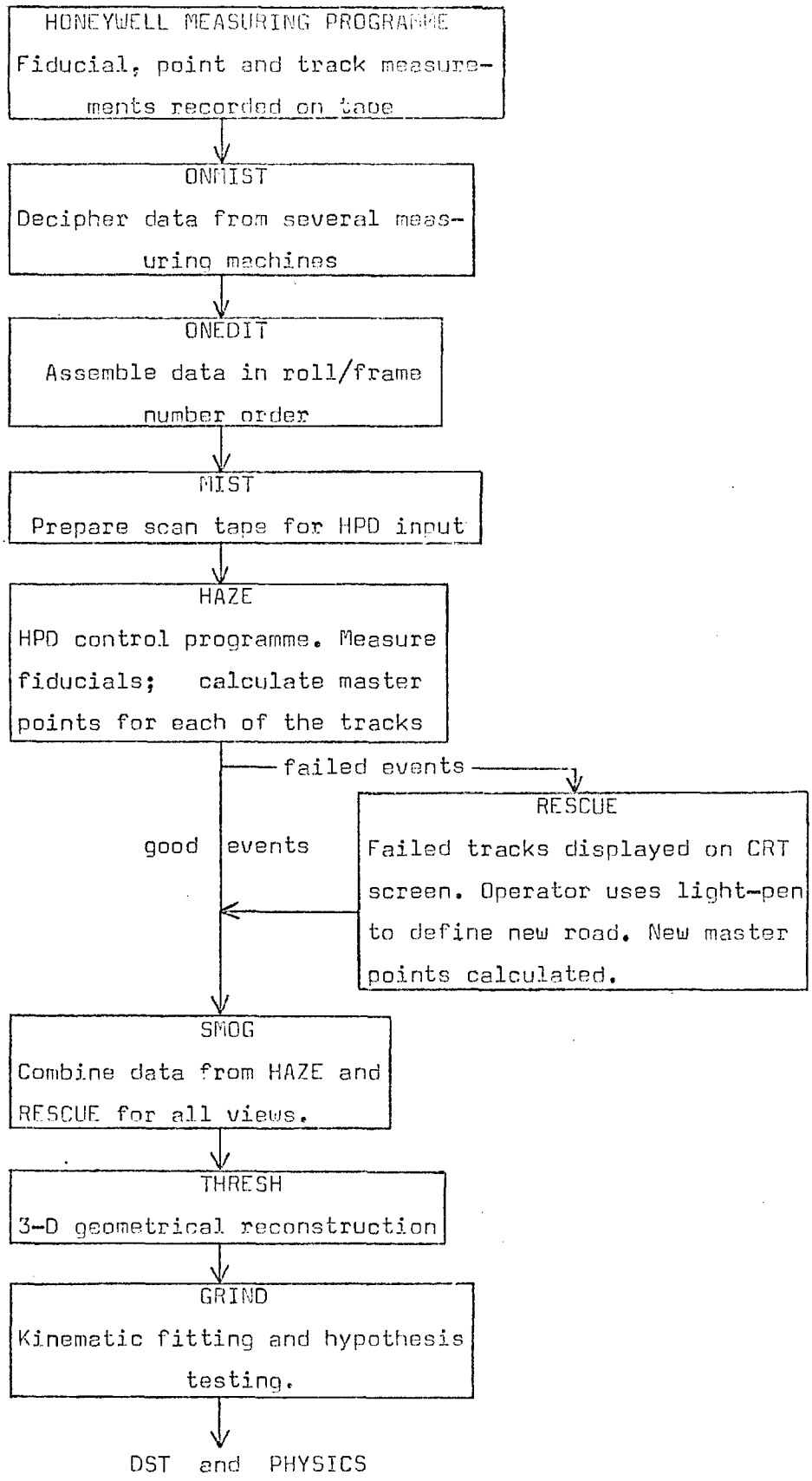


Figure 2.2 : Chain of programmes used in measurement of film from conventional bubble chambers.

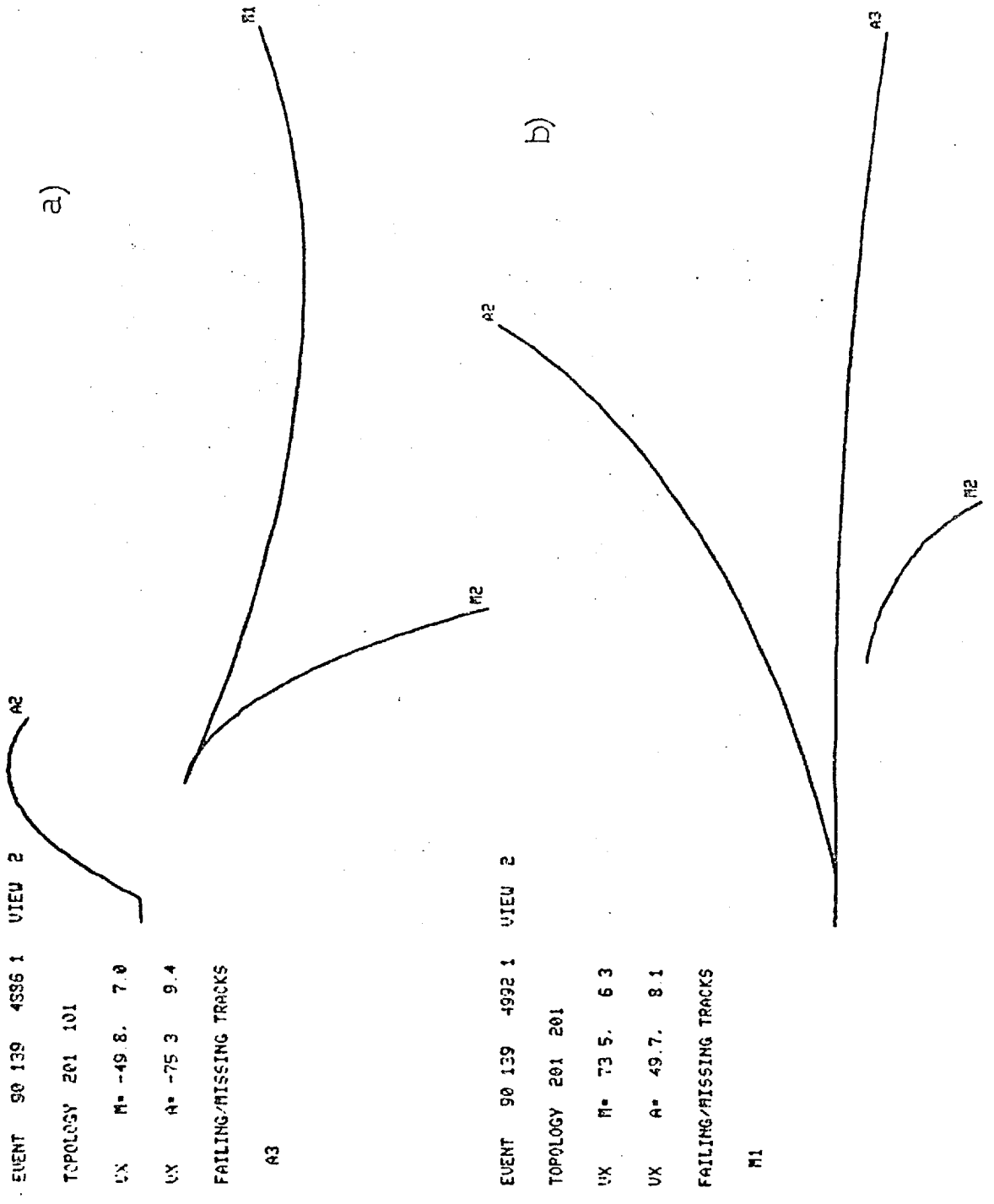


Figure 2.3 : An example of tektronix output from the programme REAM, showing :-

a) an event with one primary track, A3, missing

b) another two-prong event with one of the V^0 tracks, M1, missing.

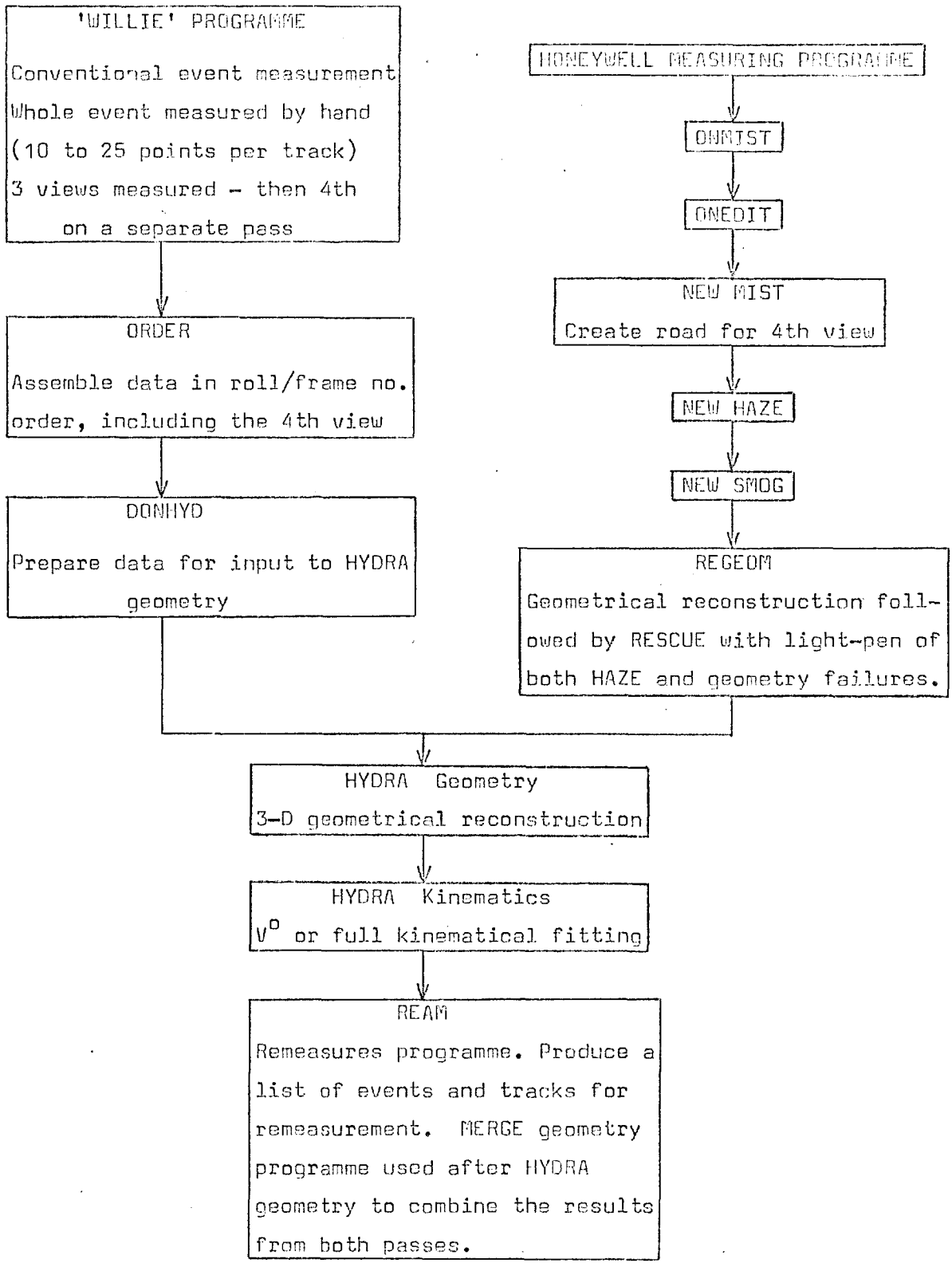


Figure 2.4 : Chain of programmes used for 4-view measurement of BEBC film both by HPD and 'Willie' machines. Full details are given in the text.

GEOMETRICAL RECONSTRUCTION AND KINEMATICAL FITTING PROCEDURE

3.1 Introduction

This chapter deals with the problems involved in the geometrical reconstruction and kinematic fitting of events in BEBC. This was the first physics experiment in which the programmes developed at CERN to cope with the specific problems encountered when using a large bubble chamber, like BEBC, could be tested. However, these programmes had been used with conventional chambers during their development. The new approach to the problem of multiple scattering and the difficulties found with the track matching procedure are discussed in some detail. Attempts to identify particles (π from K and p etc.) are discussed, together with the problem of ambiguous V^0 kinematic fits (K/Λ°, $K/\bar{\Lambda}^\circ$, $\bar{\Lambda}^\circ/\gamma$ etc.).

3.2 The HYDRA System

HYDRA is a set of "systems routines" and applications programmes developed at CERN for use in high energy physics experiments. It attempts to extend the range of the FORTRAN language and facilitate the manipulation of the complex data structures created in the analysis of high energy physics events.

The "shape" of a bubble chamber event can be compared to that of a tree, with a trunk (beam track), main branches (primary tracks), and twigs (secondary interactions, decays, both V^0 and $V^\pm$). The basic HYDRA data structure consists of a set of BANKS (referred to by a 2 to 4-letter identifier such as TF for track fit bank, or IN for an interaction bank etc.), jointed together into a similar tree-like

structure by LINKS, and containing DATA ELEMENTS (coordinates, momenta, angles, errors etc.). An example of a simple data structure is shown in figure 1. Banks can be added to this structure by the creation of another link and can be dropped simply by setting the appropriate link to zero. This tree structure allows the geometrical reconstruction and kinematic fitting to proceed as naturally as possible by linking together all banks relevant to a particular track and further linking these tracks to their appropriate vertices. Further references to the "mechanics" of the HYDRA system will not be made, but an understanding of this basic system of data handling is useful.

3.3 GEOMETRY: Summary of the Problems

The following list of problems and requirements applies to any large bubble chamber geometry programme; the programme used for this experiment was built up from the geometrical applications routines made available with the HYDRA system [1].

a) The spherical boundaries of the fish-eye optical systems and the inclination of the optical axes necessitate the transformations from local camera coordinate systems to a single chamber system.

b) The optical axes are not parallel to the magnetic field causing tracks to appear non-circular, with variable curvature, loops and cusps. This in turn causes problems for the reconstruction of near corresponding points.

c) Track matching is necessary with high energy, high multiplicity events where the relative positions of tracks change from one view to the next.

d) Fiducials and camera positions may move during the expansions: it is assumed that these displacements are the same for each

expansion, otherwise fits to establish the optical constants would have to be repeated for each frame.

e) The inhomogeneous magnetic field requires a three-dimensional description, and thus an analytical expression is found, whose coefficients, given in the titles, allow the field to be calculated at any point in the chamber.

f) Turbulence within the liquid adds to the errors on the reconstructed tracks; no corrections can be made for this.

3.4 Track Match

The purpose of track match is to associate those images, from different views, which correspond to the same track in space. The general philosophy is to leave unassociated as few track images as possible. The basic procedure is as follows :-

1) Pairs of images on two views are constructed, which pass suitable acceptance tests; they are called "doubles".

2) The maximum multiplicity multiples are generated (i.e. quadruples if four views have been measured). A multiple is a consistent set of doubles. For example, the doubles 2200, 2020, 2003, 0220, 0203, 0023 may be combined into the multiple 2223 if they have compatible values for azimuth and dip angles. (Each digit represents a track image on one view.) A double whose space azimuth and dip angles cannot be found, because the angle between the optical axes and the track images concerned is too small, is considered compatible with all other doubles.

3) The space curvature for each element of the multiple is checked for consistency, and successful multiples are stored as "space track candidates".

4) Each candidate is divided into arcs, and a few near corresponding points are computed for each arc.

5) The largest list (greatest number of multiples) of compatible candidates is set up. When one track image appears in more than one multiple, a decision is made using the results of the near corresponding points calculation.

6) All unused doubles, with no element belonging to an accepted multiple, are returned to step 2, where the next lower order multiples are generated and steps 2 to 6 are repeated. This process is repeated until all the doubles are used, either in higher multiples, or on their own.

The main problem with this method of track matching is the generation of spurious space tracks reconstructed as doubles. This can occur for various reasons :-

a) When two beam tracks lie very close to one another on film so that both fall within the road constructed for the HPD, the HAZE programme sometimes chooses the wrong beam track on two views. This allows the GEOMETRY programme to produce two doubles, and thus two beam tracks. This problem was resolved by accepting the beam track which passed closer to the measured primary vertex position.

b) The introduction of a fourth view, by constructing roads for that view at the MIST stage, sometimes leads to two or three measurements being made of the same track. It is then possible for track match to find a triple and a double, or two or three doubles for that same track (in the case of events with more tracks from a vertex than expected from the measured topology). The extra tracks were eliminated by preferentially rejecting doubles which

included this fourth view, using the extra constraint of charge conservation at the vertex as a check.

c) Bad measurements also lead to the generation of spurious doubles, and these were treated in the same way as those in section b).

Approximately 10% of events suffered from the problems listed above, and most of them could be recovered by the methods described.

3.5 Treatment of Multiple Scattering

The deviations due to multiple scattering for tracks of momentum less than about 500 MeV/c are typically an order of magnitude larger than the measurement errors. Geometrical reconstruction programmes like THRESH [2] do not take this multiple scattering into account explicitly in the least squares fitting of tracks, to estimate their initial direction and momentum. Details of the "parametrization method" for the treatment of multiple scattering can be found in Ref. 3 , and a summary of this method as it is used in the large bubble chamber geometry programme developed for use with HYDRA is given here.

The principle of the method is to follow the scattered track more closely by introducing extra parameters into the description of the trajectory. The trajectory is divided into several segments and for each segment, two scattering parameters (angles) are fitted, together with the five standard parameters of the fit ($1/p, \lambda, \varphi$, x (or y), and z; where x,y,z are the coordinates of a point on the track; λ, φ, are the dip and azimuthal angles which specify the direction of motion of the particle at that point, and p is the momentum.). At each measurement point, partial derivatives of the film distances, d_i , (the perpendicular distance in the film plane from a given measured point to the projected trajectory) are calculated with

respect to all the parameters. As with the standard method, the expression $\sum_{i=1}^{n} d_i^2$, where n is the number of measurements, is minimised to find the new track parameters for the segment. The segment length, l, is chosen such that

$$\frac{\kappa^2 l^3}{24} = \sigma_c^2$$

where σ_c is the measurement error in space (about 500μ for HPD measurements)

κ is a scattering constant which is related to the r.m.s. scattering angle.

The actual number of "break points" (each segment has one break point) is set as the highest number required for the highest mass fit possible. Thus, if the proton mass fit is excluded because the measured track length is greater than the range of a proton for that momentum, the number of break points is obtained from the kaon mass fit. For a low energy track, the number of break points is typically between 3 and 5, but for tracks of momentum greater than 1.5 GeV/c, where measurement errors dominate, there may be no extra parameters required for the fit.

3.6 Improvements to the Basic Geometry Programme

A new technique was adopted in CERN, and later at Imperial College, for tracks that had been "badly" measured, as indicated by a high ($>20\mu$) helix fit residual on film. It was thought that the large size of BEBC, coupled with the demagnification of the bubble images on to film giving fine track images, caused the scanners to miss some small angle scatters or decays when they measured the tracks. This would account for some of the "bad" measurements. A version of GEOMETRY was therefore developed, unfortunately called RESCUE GEOMETRY (and not to be confused with REGEOM in section 2.9)

which attempted to isolate the scatter or kink by reducing the length of the track in several stages and refitting the trajectory after each cut. If this failed to improve the residual, bad measurements on one view were assumed to be the cause and each view was dropped in turn and the fits again recalculated. If after all these attempts the fit was no better, the original measurements and views were restored. The effects of RESCUE GEOMETRY on the residuals for HPD and Willie (a conventional film plane digitiser) measurements can be seen in figures 2 and 3. The long "tail" of the residual distribution disappears after RESCUE GEOMETRY has been used. The track length distribution is altered only slightly; the mean length is reduced from 64 cm. to 62 cm. The use of RESCUE GEOMETRY increases the CPU time marginally for those events that are in need of this treatment. About three events per minute are processed using the PDP10 computer when all topologies are included.

An on-line version of this programme was developed at Imperial College so that the measurements and helix fits for all four views could be displayed on a Tektronix graphics display unit. Interaction with the GEOMETRY programme allowed an operator to drop individual points or complete views and then return to the geometry programme for refitting. This programme was too slow to be used for production work, but it did demonstrate some of the problems which occurred when tracks were measured in several segments (cf. section 2.5). Missing segments on one or more views sometimes led to systemmatic pulls on the fitted helices; the problem was most serious with two view tracks. This showed the advantage of measuring on all four views with as few segments as possible (cf. section 2.9).

The accuracy of measurement obtained in BEBC is a factor of two worse than that predicted at the time the experiment was proposed.

It was calculated that with a magnetic field of 35 Kgauss and the long track length available in BEBC, the uncertainty in reconstructing points on a track would be 250 - 300μ in space; a value of 500μ was used for the HPD and ERASME, and 650μ for the Willie measurements.

3.7 Kinematic Fitting

The kinematic fitting programme used has the logic of GRIND [4] but has been rewritten into the HYDRA structure for use with Hydra geometry programmes. The hypotheses corresponding to K^0, Λ^0, $\bar{\Lambda}^0$, and γ were tested for all measured V^0s, but no primary vertex fit was attempted for the majority of the data used in the inclusive analysis. A data summary tape (DST) was prepared, which contained all the allowable mass fits from geometry, for primary tracks, and the V^0 kinematic fit (or fits, when a kinematic ambiguity existed).

The masses and widths of unique V^0s, assigned to one of the hypotheses K^0, Λ^0, $\bar{\Lambda}^0$, calculated from their measured decay tracks are shown in Figure 4. A Gaussian curve was fitted to each of the three distributions and the mean and standard deviation (σ) found for each plot is also shown in Figure 4. Ambiguities, amounting to 17% of the total number of fitted V^0s, between K^0/Λ^0, $K^0/\bar{\Lambda}^0$, Λ^0/γ hypotheses etc. were resolved after a study of the distribution of the angle between one of the decay tracks and the V^0 flight path, in the rest frame of the V^0. The decay angular distributions for uniquely fitted V^0s were depleted in certain regions (see Figure 5). A simple decision was made using the χ^2 probabilities for the two ambiguous fits; the resulting angular distributions are shown in Figure 6. Although this method leads to some contamination of the sample by misidentified V^0s, all the V^0s are used, giving maximum

possible statistics. One alternative approach to this problem of ambiguities is to weight all ambiguous fits by the inverse of the χ^2 for the fit, normalised by the sum of these numbers for all the fits for that V^0 i.e.

$$\text{Weight for } i^{th} \text{ fit} = \frac{1/\chi^2_i}{\sum_{j=1}^{n} 1/\chi^2_j}$$

, where n = the number of mass fits for this V^0.

Three other methods, using only the unique V^0 fits, were tried. The first of these methods was to weight events in depleted regions of the decay angular distribution so that the resultant distribution was flat. This method was satisfactory for K^0 and Λ^0, but could not be used for $\bar{\Lambda}^0$ since there were sections of the $\bar{\Lambda}^0$ decay angular distributions where there were no events. A second method again used the decay angular distribution of unique V^0 fits. Depleted regions were cut out completely, and the overall normalisation was correspondingly adjusted. This worked for K^0 and $\bar{\Lambda}^0$, but the decay distribution for Λ^0s did not have well defined regions of event loss; so this method was also rejected as it could not be applied to all types of kinematic fit. The last of the three methods was as follows. For each bin of each distribution plotted (e.g. invariant cross-section as a function of $x_{Feynman}$ - see Chapter 4), the distribution of the decay angle was also plotted. The events were then weighted in order to make this distribution flat, and the original distribution was replotted using the new weights. This method was of course very time-consuming. Since the actual physics did not appear to change significantly on changing from one of these methods to another, the simplest method - that of choosing kinematic fits by the χ^2 probability - was used.

The preliminary work which was done to look for narrow spikes in effective mass plots, used the geometry quantities found for each primary vertex track on the DST. The χ^2 probability for each mass fit was found to be a fairly good guide as to the true nature of the particle for tracks of momentum less than about 1 GeV/c. Figure 7 shows the χ^2 for different mass fits plotted against one another, for various momentum intervals. For the purposes of plotting effective masses of $K^o n\pi$, $\Lambda^o n\pi$, etc. (where n is an integer ≥ 1), a 'π' was defined as any track for which the χ^2 for the pion mass fit was less than 1.5 times the χ^2 for the best mass fit (lowest χ^2 fit). For tracks of greater than 1 GeV/c momentum, the values of χ^2 for different mass fits were essentially equal, so all fast tracks were taken as possible pions and were therefore plotted. A more complicated weighting procedure was used for the six-prong + V^o events, when a full multivertex kinematic fit was attempted; this will be discussed in detail in Chapter 5 , on the "I" particle.

3.8 Beam Parameters

In order to transform variables into the antiproton-proton centre of mass system, the beam parameters (momentum and angles φ and λ) at the primary interaction vertex must be known. The errors in these parameters are often large, especially if the track length available for measurement is short. For much of the 'bump hunting' the missing mass recoiling against different systems of particles was required, and in order not to smear out any narrow effects that may have been present, it was necessary to have a good estimate of the total centre of mass energy available in the initial state.

Many beam tracks were measured very carefully, using the ERASME system at CERN, and a set of titles was produced which gave the values

of momentum, dip, and azimuthal angles as a function of the beam entry position y',z' on the beam entry window. Thus, for any interaction point in the chamber, the standard beam parameters could be found by swimming the track from the interaction point back to the beam entry window and computing a weighted average of the measured and standard values. If the two sets of parameters were incompatible, the beam and event were rejected. Since it was known (see section 4.3) that the properties of the beam (e.g. contamination from π and μ) changed during the run, the beam parameters were computed for several different rolls. In fact the beam momentum at the centre of the beam entry window ($y' = z' = 0$) was found to vary between 11.9 and 12.02 GeV/c. This could therefore be taken into account at the analysis stage by performing the averaging process described above.

The contamination of the beam by light particles is discussed in section 4.3 .

References

1. HYDRA Users Manual — CERN, May 1974
2. THRESH — CERN Programme Library
3. P. Laurikainen et al. — Nucl. Instr. & Methods 98,(1972),349
4. GRIND — CERN Programme Library

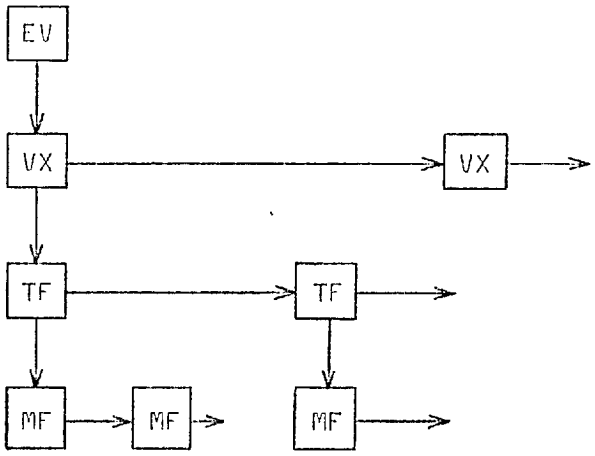


Figure 3.1 : A Simple HYDRA Data Structure

EV : Event bank containing data elements such as roll/frame number and links to the VX bank

VX : Vertex bank containing data elements such as x, y, and z coordinate of the vertex, with errors and links to TF banks and to other VX banks

TF : Track fit bank containing data elements such as the fitted track length, and track labels, and links to MF banks and to other TF banks

MF : Mass fit bank, containing as data elements the results of a mass-dependent fit to the measurements and links to other MF banks associated with this track.

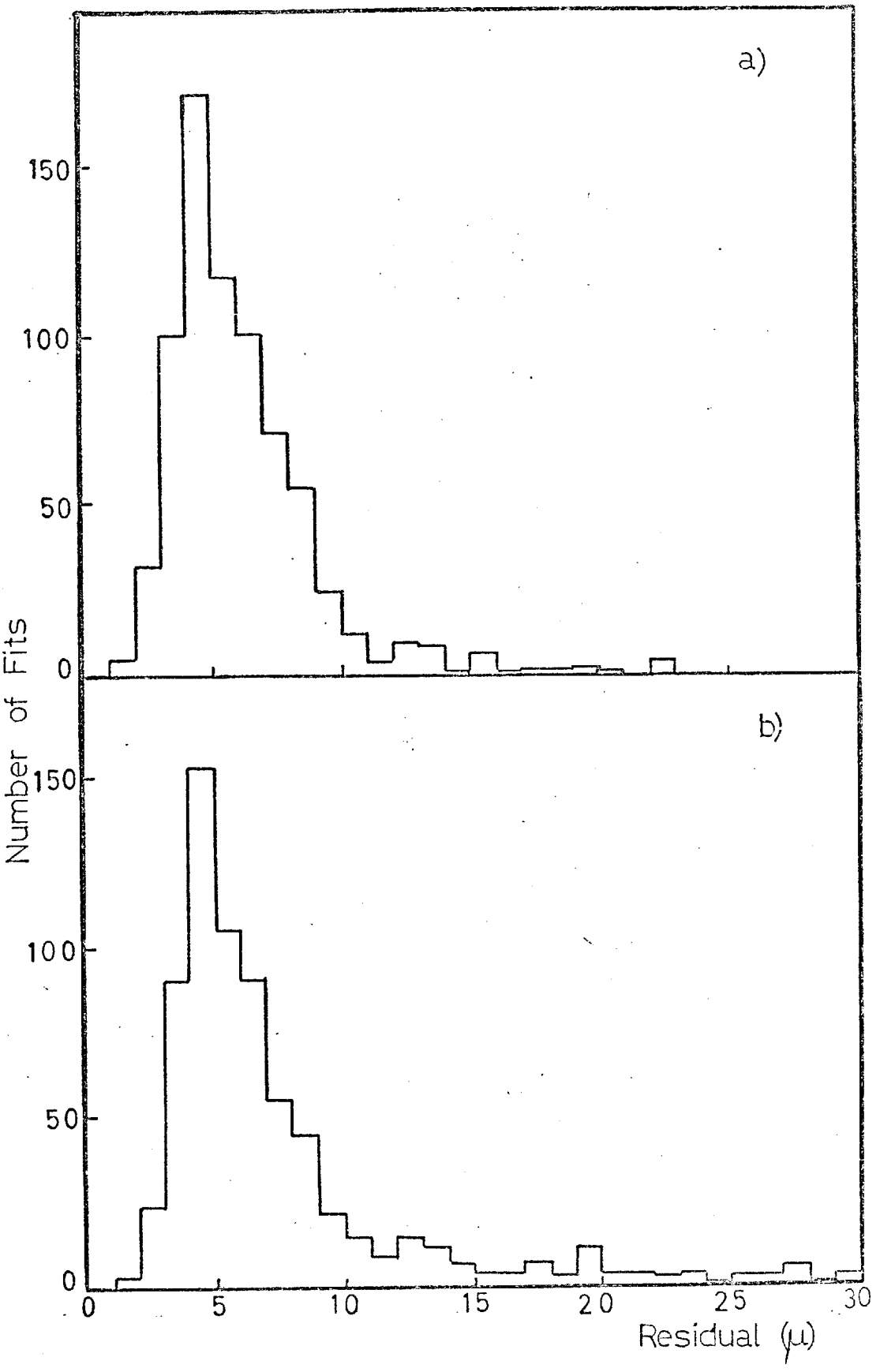


Figure 3.2 : Best mass fit residuals for tracks measured on the HPD.

a) with RESCUE geometry

b) without RESCUE geometry

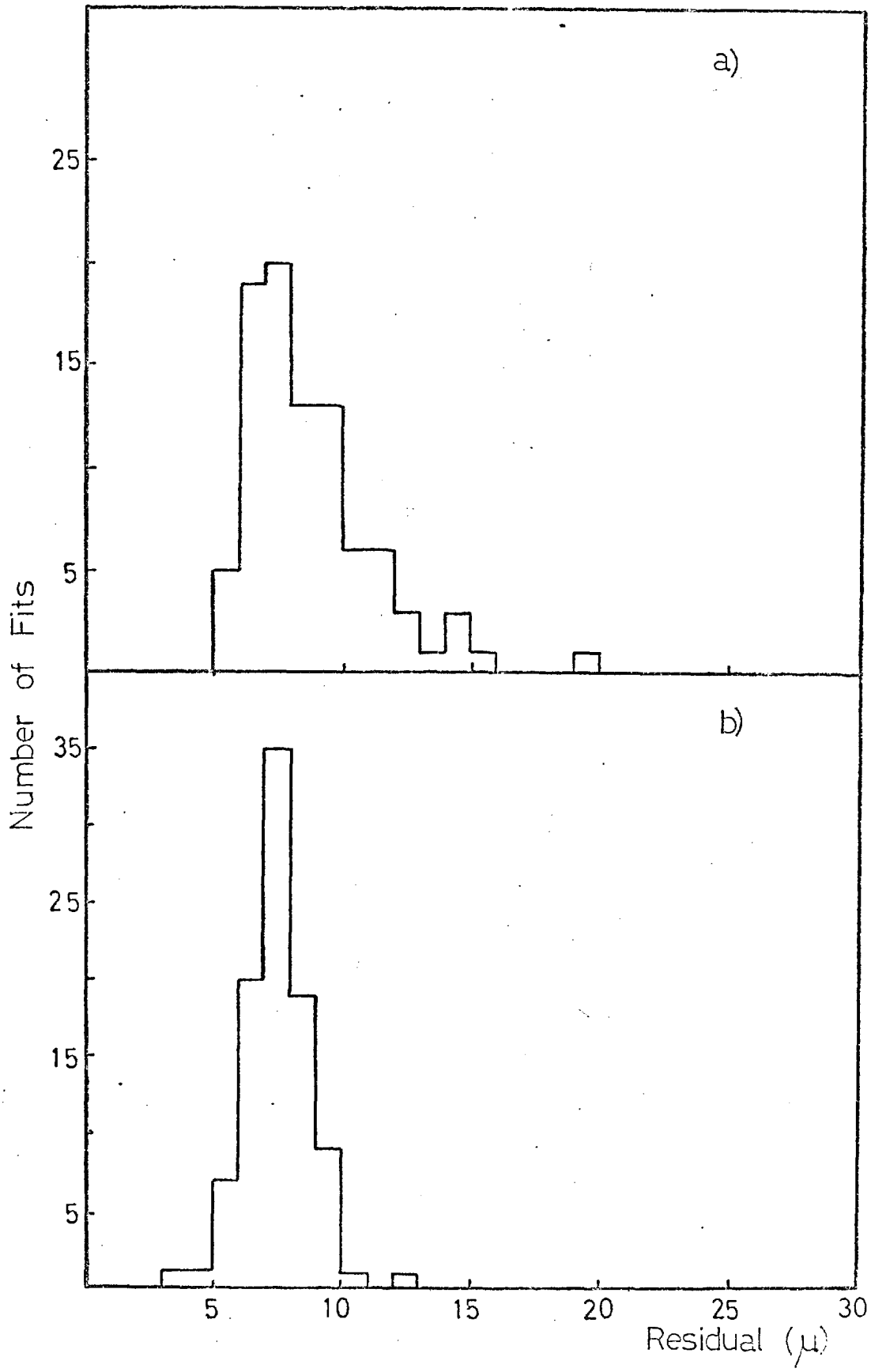


Figure 3.3 : The effect of RESCUE geometry on best mass fit residuals of tracks measured using Willie.

a) Ordinary geometry

b) RESCUE geometry

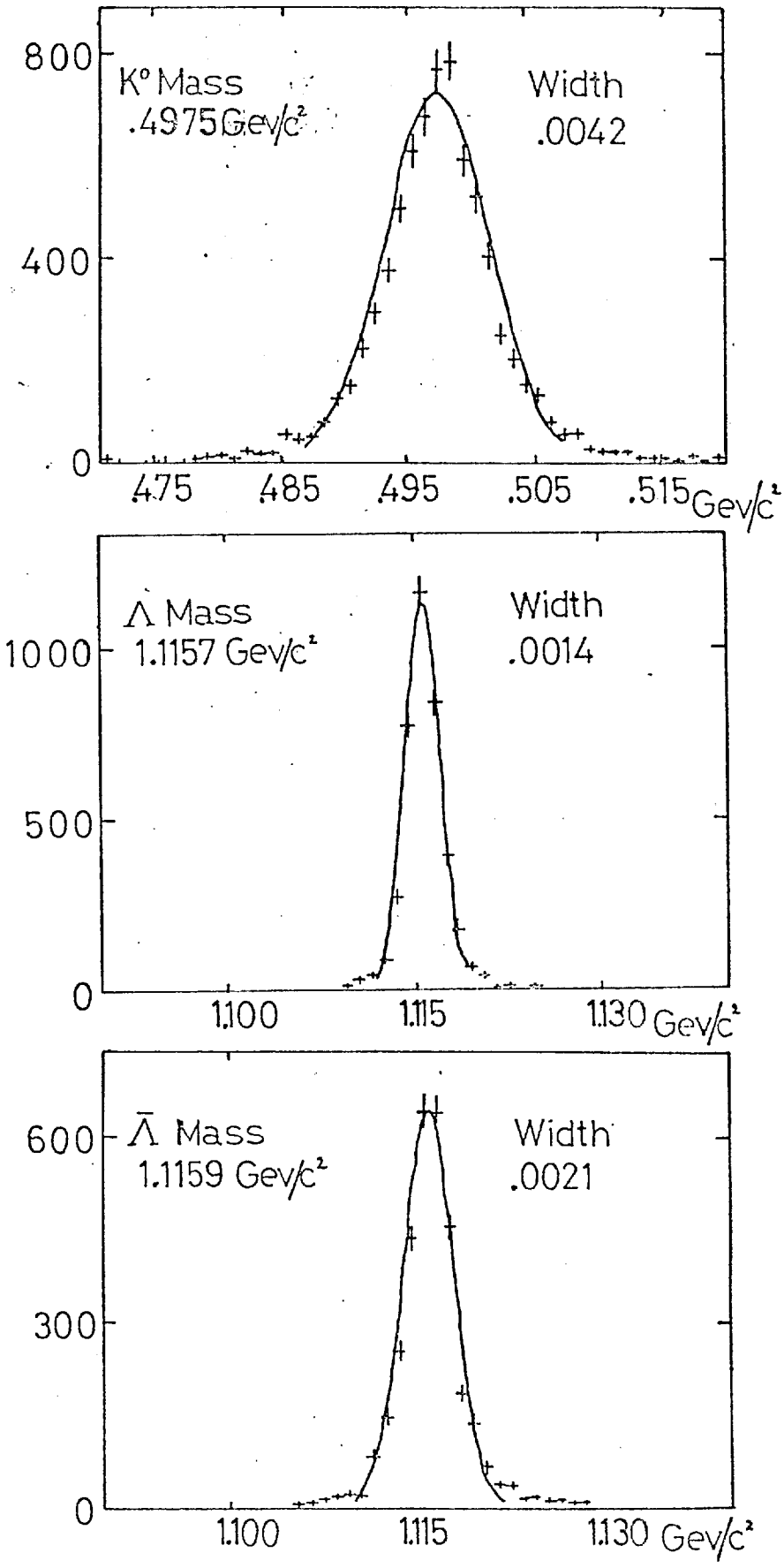


Figure 3.4 : Effective mass for V^0s, calculated from the measured track parameters of each of the decay particles. The curves are gaussian fits to the data points over the limited ranges shown. The fitted mean and width are indicated on the figure.

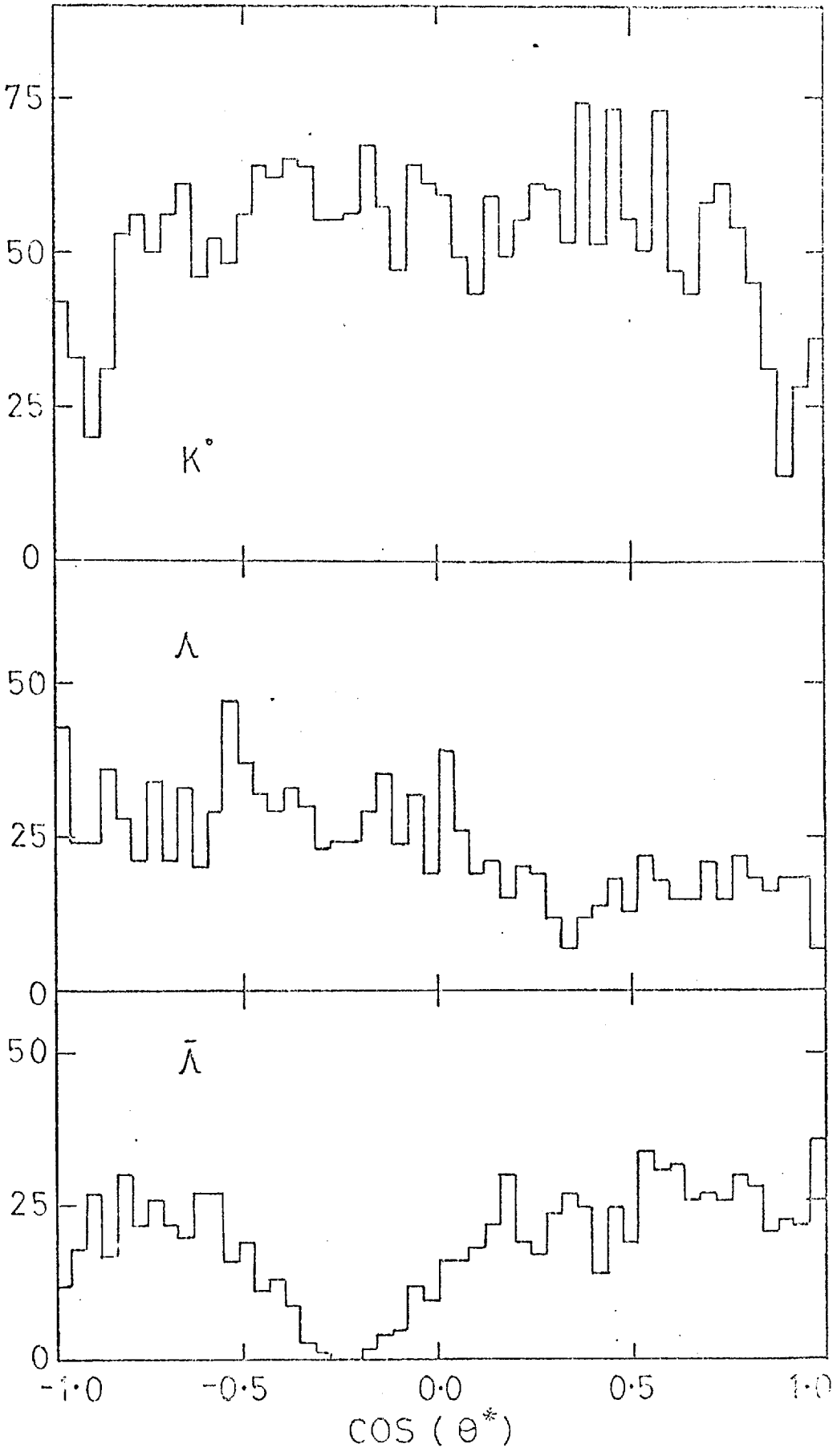


Figure 3.5 : Decay angular distribution for uniquely fitted V^0s.

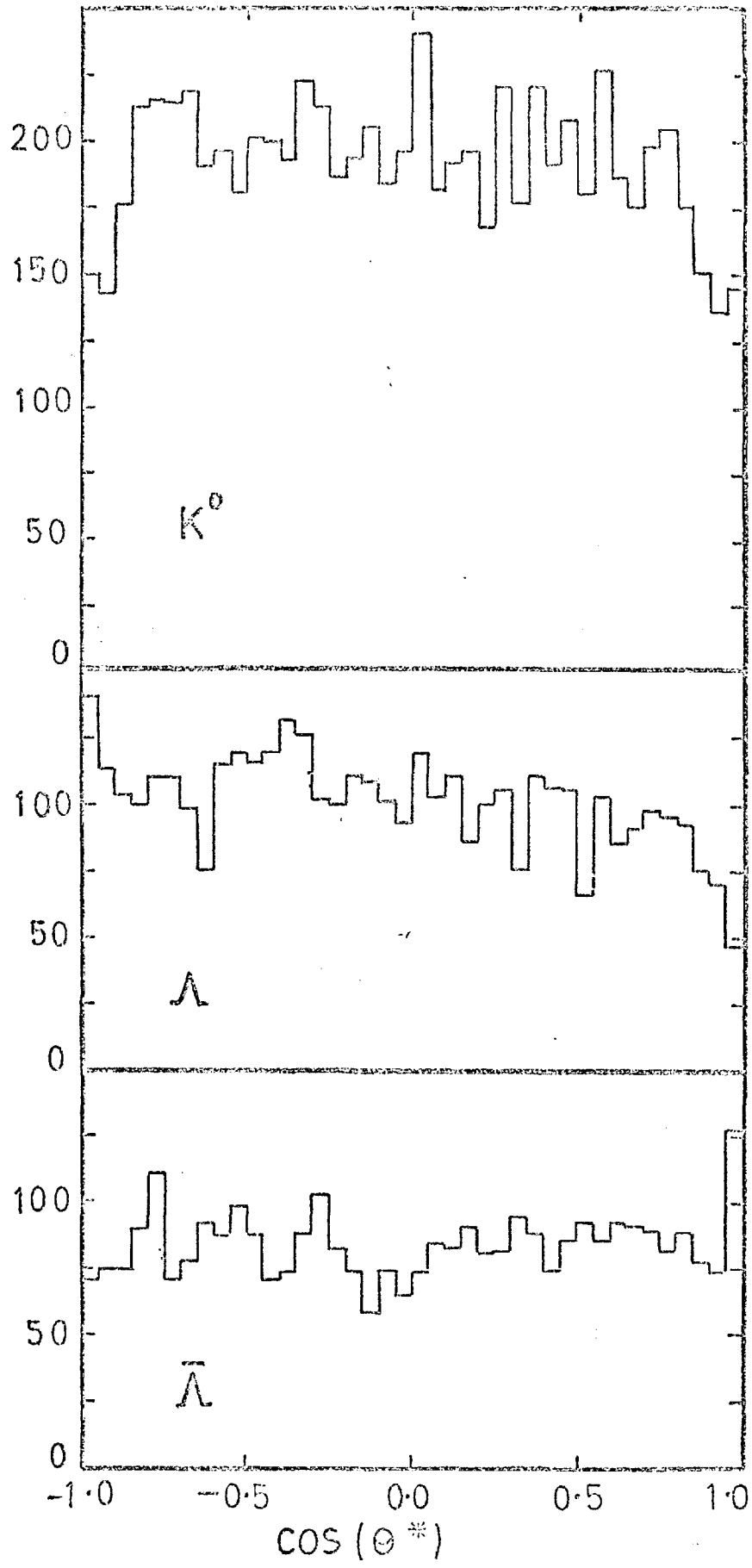


Figure 3.6 : Decay angular distribution for all V^0s after a χ^2 selection has been made.

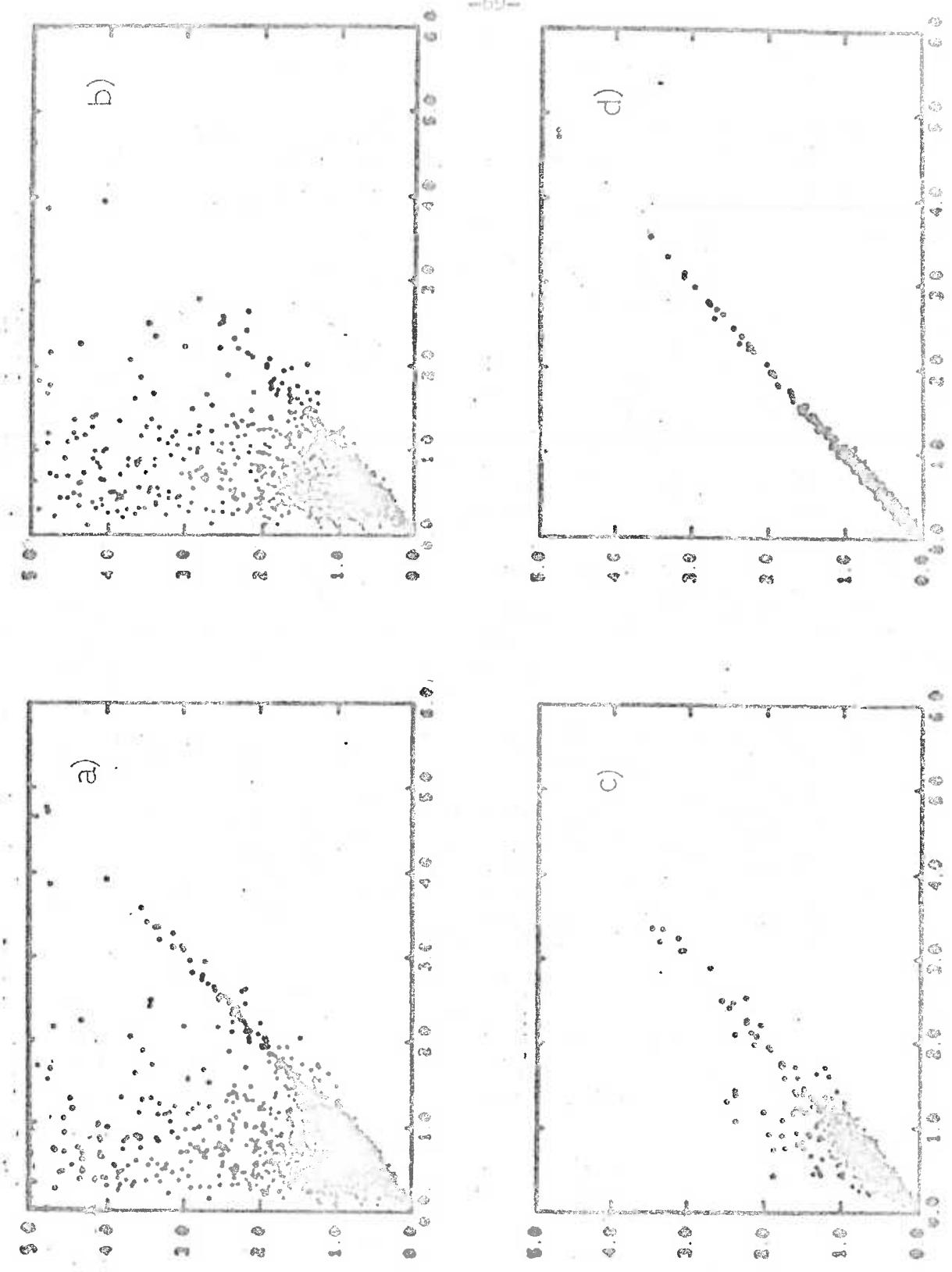


Figure 3.7 : Scatter plots of χ^2 for K mass fit versus χ^2 for π mass fit, for charged tracks.

a) all tracks

b) momentum, $p < 0.5$ GeV/c

c) $0.5 \leq p < 1.0$ GeV/c

d) $p \geq 1.0$ GeV/c

STRANGE PARTICLE INCLUSIVE PHYSICS

4.1 Introduction

Inclusive cross-sections for the production of strange particles (K^o_{short}, Λ^o, $\bar{\Lambda}^o$) in 12 GeV/c antiproton-proton interactions are calculated in this chapter. There is a detailed description of the correction factors used in this calculation. A brief account of the variables used in inclusive analyses is followed by presentation of the distributions of differential cross-sections as functions of x, p_T^2 , y (rapidity), M_x^2 (recoil mass to the V^o), and t (the four-momentum transfer squared). The chapter concludes with a Triple Regge analysis of the reactions $\bar{p}p \rightarrow \Lambda^o + X$ (in the target fragmentation region) and $\bar{p}p \rightarrow \bar{\Lambda}^o + X$ (in the beam fragmentation region).

4.2 Cross-Section Formula

The formula used to calculate the inclusive V^o cross-sections is :

$$\sigma = \frac{N_I \; A}{N_A \; \rho \; L \; N_o}$$

where N_o = Number of incident particles

N_A = Avogadro's constant = 6.022×10^{23} mole^{-1}

A = Atomic Number = 1, for hydrogen

ρ = Target density = 0.0624 gm/cm^3 for liquid H_2 at 26 K

L = Fiducial length

N_I = Number of interactions within the fiducial volume

4.3 Beam Contamination

The beam contamination by π^- and μ^- was estimated by two different methods. The first of these used the frames (about 200 in

every 6000) where the r.f. separators had been turned off so that no antiprotons entered the bubble chamber. A beam count was made on these frames using a template based on beam tracks from normal (r.f. on) frames; all interactions on 'good' beam tracks were recorded. It was noticed that it was possible to divide the film into three distinct sections, according to the number of beam tracks found per frame (see Figure 1). The boundaries between these sections corresponded to a re-tuning of the antiproton beam. Table I gives the contamination by light particles calculated for the three sections. 5% of these beams interacted and so, correcting for the beam attenuation as described later in this chapter for the antiprotons, it was estimated that (21.7 $\pm$ 2.6) % of the total light particle contamination was due to pions. Using the sample of film at Imperial College, the total light particle contamination was found to be approximately 10%.

The second method utilised the fact that the maximum radius of a δ-ray that can be produced by a 12 GeV/c antiproton is 16 cm. in space in a 35 Kgauss field. This corresponds to a diameter of 8 cm. on a Bessy scan table. Several rolls of film were scanned twice for δ-rays on beam tracks where the δ-ray diameter was greater than 5 cm. on the table. The δ-ray scanning efficiency after two scans was found to be 80%. The diameters were measured on view one and corrected for magnification differences according to their position in the chamber. The radii in space of the δ-rays are plotted in figure 2a together with the expected δ-ray distribution for antiprotons after a correction for scanning efficiency has been made. (Figure 2b shows the distribution of δ-ray radii for the r.f.-off frames together with the expected distribution for light particles.) A total of

38 δ-rays were found with a radius greater than 16 cm. in space, corresponding to a total light particle contamination of (6±1) %. It should be noted, however that the rolls used in this scan came from the central section of figure 1, where the contamination was smallest. Thus the results from the r.f. off method were used in the calculation of inclusive cross sections for V^0 production.

4.4 Correction Factors

Several factors were used to correct the number of K^0, Λ^0, and $\bar{\Lambda}^0$ observed for losses due to scanning and throughput efficiencies, decays outside the chamber or too close to the primary vertex to be identified, interactions of V^0 before decay etc.. Each of these factors will be described briefly below.

Beam Attenuation

It is necessary to correct the number of beam tracks entering BEBC, calculated from the results of a beam count on every tenth frame throughout the film, to allow for interactions within the chamber which reduce the effective $\bar{p}$ track length used in the cross section calculation. This effective track length is just the corrected number of $\bar{p}$ ($N_{\bar{p}}$) multiplied by the fiducial length (L) ; from the distribution of primary vertex coordinates, the value used for L was 240 cm.

Thus, using the cross section formula given in section 4.2, the beam attenuation factor, F_A , is given by :-

$$F_A = \frac{A}{N_A \rho \sigma L} \cdot \frac{N_I}{N_{\bar{p}}}$$

$$= \frac{A}{N_A \rho \sigma L} \left[1 - \exp(-N_A \rho \sigma L/A)\right]$$

where σ = the $\bar{p}p$ total cross section at 12 GeV/c (1)

= 51.7 mb.

Thus the value found for F_A was $F_A = 0.798$

Scanning Efficiency

This was discussed in section 2.4, and the results are given in Table I (chapter 2).

Throughput Efficiency

The data were divided into two sections by topology since the 6,8, and 10 prong events were measured on Willie (a conventional measuring machine) because of their poor HPD throughput. Throughput, as defined in section 2.6, is the ratio of the number of fitted V^0 appearing on the DST to the number originally found by the scanners. An estimate was made of the percentage of unfitted V^0s that were really γs. Energy loss from electrons and positrons by Bremmstrahlung was not taken into account separately in the geometry programme, so a larger proportion of γs failed in kinematics than did V^0s. All γs were subtracted from the total number of V^0s before the throughput efficiency was calculated. The efficiencies used in the calculation of the inclusive cross sections are as follows :-

0, 2, 4 prongs : (59 ± 10) %

6, 8, 10 prongs: (86 ± 14) %

Decay Weights

This factor includes both a correction for V^0 decaying too close to the primary vertex to be found by the scanners and a correction for V^0 which decay after leaving the bubble chamber.

Each event was given a weight, W, calculated from the following expression :

$$W = \left[\exp(-ml_{min}^{proj}/pc\tau_o\cos\lambda) - \exp(-ml_{pot}/pc\tau_o)\right]^{-1}$$

where m = the mass of the V^o (K^o, Λ^o, or $\bar{\Lambda}^o$)

p = the momentum of the V^o in the lab. frame

$c\tau_o$ = the mean decay length of the V^o

l_{min}^{proj} = the minimum decay length of the V^o, projected on to the xy plane

λ = the dip angle of the V^o

l_{pot} = the potential decay length of the V^o. i.e. the distance from the primary vertex to the edge of the fiducial volume, measured along the line of flight of the V^o. For this calculation, BEBC was defined as a cylinder of radius 170 cm. and depth 100 cm.

Figure 3 shows the mean decay weight plotted against the value chosen for the minimum projected length, l_{min}^{proj}, for K^o, Λ^o, and $\bar{\Lambda}^o$. The projected length was used rather than the actual length since it is more directly related to the source of the scanning losses. From Figure 3 it can be seen that the mean weight becomes constant at about 3.5 cm., so this value was used as the minimum projected length for all V^os.

The values used for the mean decay weight for K^o, Λ^o, and $\bar{\Lambda}^o$ in the cross section calculation were :

1.165 for K^o , 1.194 for Λ^o, and 1.132 for $\bar{\Lambda}^o$.

Ambiguities

The problem of kinematic ambiguity was mentioned in section 3.7. A decision, based on the χ^2 of the fits, was made for each ambiguous V^o.

Although this necessarily contaminates the sample of K^0 etc., by including misidentified Λ^0, $\bar{\Lambda}^0$, and γ, for the purposes of cross section calculation such cross-feed effects contributed only a small systematic effect, which has been taken into account in the calculation of the cross section errors.

V^0 Interactions

A factor was included to account for those V^0s which interacted as they passed through the bubble chamber and therefore did not appear as an associated V^0. The cross sections for $\Lambda^0 p$ and $\bar{\Lambda}^0 p$ interactions at different momenta [2] are more or less constant over the range of momenta found for Λ^0 and $\bar{\Lambda}^0$ in this experiment. The mean momenta (from distributions of Λ^0 and $\bar{\Lambda}^0$ lab. momentum) and cross sections were used to calculate corrections to the numbers of Λ^0 and $\bar{\Lambda}^0$ of 2% and 7% respectively. The cross section for $K^0_{short} p$ interactions is smaller, and corrections were estimated to amount to less than 1%.

V^0 from π^- Interactions

The numbers of K^0 and Λ^0 produced by the calculated π^- contamination (section 4.3) were subtracted from the observed number of K^0 and Λ^0, after the above corrections had been applied. The cross sections for $\pi^- p \rightarrow K^0 + X$ and $\pi^- p \rightarrow \Lambda^0 + X$ were obtained from reference 3.

All the above factors, together with a correction for unseen decay modes of the V^0, were used to calculate the 'true' number of V^0, N_T.

$$N_T = \left(N_V \cdot \frac{F_F}{F_S F_C F_I} - N_\pi \right) \cdot F_U$$

where N_V = The observed number of V^os

F_F = Mean decay weight

F_S = Scanning efficiency

F_C = Throughput efficiency

F_I = V^o interaction correction

F_U = Correction for unseen decay modes

N_π = Number of V^o produced by π^-

Also, the number of antiprotons, $N_{\bar{p}}$, was calculated using the relation :

$$N_{\bar{p}} = N_o \cdot \frac{F_A F_T}{F_B}$$

where N_o = The number of beam tracks entering BEBC

F_A = Beam attenuation factor

F_T = Track counting efficiency (99%)

F_B = Light particle contamination

4.5 Cuts and Checks on Data for Inclusive Distributions

A discussion of kinematic ambiguities and the decisions made event by event can be found in section 3.7 .

The χ^2 probability was calculated for each V^o fit from the χ^2 and number of degrees of freedom for that fit. Only 3C fits were used, when this information was available on the DST. The number of degrees of freedom was not known for events measured by the Bruxelles group, and so the probability in this case was calculated assuming all fits were 3C. A plot of the kinematic fit probability for a sample of 0C and 1C fits was made, assuming they were 3C. A peak was observed at high probability. The probability distributions for all known 3C fits plus Bruxelles events are shown in figure 4. There is a small peak at high probability, which presumably

comes from the 0C and 1C Bruxelles fits (less than 1/6 th of the total number of events) and a larger peak at low probability (figure 4d, e, and f). A cut was therefore made to exclude fits with a probability less than 1%. To check that this cut is unbiased, the decay length and laboratory momentum distributions for rejected (low probability) events and accepted events were compared. No differences were observed.

The decay length distributions for V^0s were studied. There appears to be a loss of V^0s at lengths less than about 3 cm., which is consistent with the length chosen from the mean decay weight distributions (section 4.4). All V^0 decaying closer to the primary vertex than 3.5 cm., projected on to the xy plane, were rejected and a weight , W, was applied as in section 4.4 to each event which decayed within the secondary interaction fiducial volume, to account for decays outside the chamber or less than 3.5 cm. from the primary vertex. The x coordinate of the primary vertex was required to lie within the range -150 cm. to +90 cm.

4.6 Total Inclusive Cross Sections

The inclusive cross sections for the production of K^0_s , Λ^0, and $\bar{\Lambda}^0$, after the above corrections have been made, are as follows :

$$\bar{p}p \longrightarrow K^0_s + X \qquad 2.14 \pm 0.19 \text{ mb.}$$

$$\bar{p}p \longrightarrow \Lambda^0 + X \qquad 1.24 \pm 0.11 \text{ mb.}$$

$$\bar{p}p \longrightarrow \bar{\Lambda}^0 + X \qquad 1.14 \pm 0.11 \text{ mb.}$$

The Λ^0 and $\bar{\Lambda}^0$ cross sections are equal within experimental errors, as required by C-invariance. The variation of each of these three cross sections as a function of the incident antiproton momentum is

shown in figure 5. [4-8] . All these cross sections are seen to be rising between 10 and 100 GeV/c and the values obtained from this experiment are consistent with the general trend. (The points reported at 14.75 GeV/c [6] seem open to question.)

The inclusive neutral strange particle cross sections for $pp \longrightarrow V^0 + X$, and $K^{\pm}p \longrightarrow V^0 + X$ are shown in figure 6 as a function of incident beam momentum. All the cross sections rise with increasing incident momentum, except that for Λ^0 production in K^-p interactions. At 12 GeV/c, $\sigma(\bar{p}p \longrightarrow K^0 + X) \sim 3.7\,\sigma(pp \longrightarrow K^0 + X)$, which implies that annihilation still makes a dominant contribution to K^0_s production as a result of processes of the type $\bar{p}p \longrightarrow K\bar{K}$ + mesons. If it is assumed [9] that

(i) $\sigma(K^0_{short}) = \sigma(K^0_{Long})$, so that $\sigma(K^0 + \bar{K}^0) = 2\,\sigma(K^0_s)$

(ii) $\sigma(K^0\bar{K}^0) = \sigma(K^0K^-) = \sigma(\bar{K}^0K^+) = \sigma(K^-K^+)$,

so that $\sigma(K\bar{K}) = 2\,\sigma(K^0_s)$

then the results obtained at lower energies suggest that $K\bar{K}$ production in $\bar{p}p$ annihilations rises from $\sim$5% in interactions at rest to $\sim$20% in interactions at 12 GeV/c. The energy dependence of the Λ^0 production cross section is similar for both $\bar{p}$ and p beams.

The energy dependence of the K^0_s cross section for pp and $\bar{p}p$ interactions cannot be compared at low energy due to the dominance of annihilation processes in $\bar{p}p$ interactions. However, at higher energies, the annihilation cross section is less significant and the energy dependence does tend to be similar.

The topological inclusive cross sections for $\bar{p}p$ interactions at 12 GeV/c are given in Table II. The fraction of the total inclusive cross sections associated with each charged multiplicity for

$\bar{\Lambda}^0$, Λ^0, and K_s^0 are shown in figure 7, and compared with those for pp interactions at 12.4 GeV/c [8] . The average charged multiplicity of $\bar{p}p$ interactions with an associated K^0 is higher than that for those with an associated Λ^0 or $\bar{\Lambda}^0$. There is no effect of a similar magnitude in pp interactions.

4.7 Inclusive Variables

Consider the reaction

$$A + B \longrightarrow C_1 + C_2 + \cdots + C_n + C_{n+1} + \cdots + C_{n_c}$$

where A is the projectile particle, B is the target particle, and the n_c particles , C_i , are the outgoing particles. Particles C_1 to C_n are observed, and C_{n+1} to C_{n_c} are neutral or undetected. The cross section for channel c can be expressed as

$$\sigma_c = \frac{1}{p_{in} s^{\frac{1}{2}}} \int |M_c|^2 \delta\left(\sum_1^{n_c} \underline{p}_j - \underline{p}\right) \delta\left(\sum_1^{n_c} E_j - E\right) \prod_1^{n_c} \frac{d^3 \underline{p}_j}{E_i} \qquad \text{..(equn 1)}$$

where M_c is the Lorentz invariant transition matrix element

$\underline{p}_i$, E_i are the momentum and energy of the i^{th} outgoing particle

$\underline{p}$, E are the momentum and energy of the total incoming system

The total cross section, σ_T , is just the sum of these channel cross sections, namely :

$$\sigma_T = \sum_c \sigma_c$$

The Lorentz invariant n-particle distribution in momentum space can be expressed as the sum of the n-particle exclusive part and the n-particle inclusive distribution, depending on s and 3n momentum variables :

$$f_n(s, \underline{p}_1, \ldots, \underline{p}_n) = \left(\prod_1^n E_i\right) \frac{d^{3n}\sigma_n}{\prod_1^n d^3 \underline{p}_i} \qquad \text{.. (equn 2)}$$

It has been known for some time [10] that there are striking differences between the behaviour of the transverse momentum of a particle (p_T: the component normal to the incoming direction) and its longitudinal momentum ($p_{\parallel}$: the component in the same direction as the incoming particle). The longitudinal momentum can take any value which is allowed by the available phase space, whereas the transverse momentum has an average value between 0.3 and 0.4 GeV/c, regardless of the nature of the particle or the total centre of mass energy ($\sqrt{s}$). A separation of the three-dimensional momentum vector into an essentially scalar longitudinal variable and a two-dimensional transverse momentum vector, is the basis of the longitudinal phase-space analysis suggested by Van Hove [11] . The invariant single-particle distribution of equation 2 can then be written in the form

$$f_1(s,p_{\parallel},p_T) = E_1 \frac{d^3\sigma}{dp_{\parallel}d^2p_T} \qquad \text{.. (equn 3)}$$

with E_1 = the energy of the single particle

If the incoming particles are unpolarized, as is the case in this experiment, the differential cross section can be integrated over one of the transverse variables to give a function of three variables only. The remaining transverse variable is usually chosen as $|p_T|$ or p_T^2 . Integration over both transverse variables is also possible without losing too much information since the differences and similarities between various particles are more striking when studied in the longitudinal variable, as outlined in the previous paragraph.

The distributions can be studied in various different frames of reference. The three most commonly used are the target rest frame (laboratory system), the beam rest frame, and the centre of mass frame. This last frame of reference has the advantage of symmetry, especially

in this experiment, with the totally neutral antiproton-proton initial state, and it will be used for much of the inclusive analysis which is to follow.

Feynman introduced [12] a variable, x , which is the reduced centre of mass longitudinal momentum and which has the advantage of making the kinematic range covered energy - independent. It is defined as :

$$x = \frac{p^*_{\parallel}}{p^*_{\parallel\,max}}$$

where $p^*_{\parallel}$ is the centre of mass longitudinal momentum and $p^*_{\parallel\,max}$ is the maximum value of the centre of mass longitudinal momentum. For this inclusive analysis, $p^*_{\parallel\,max}$ is defined by the reaction $\bar{p}p \longrightarrow V^o\bar{V}^o$, and is given by

$$p^*_{\parallel\,max} = \tfrac{1}{2}\sqrt{s - 4m^2_{V^o}}$$

In the high energy limit, x can be approximated by $x = 2p^*_{\parallel}/\sqrt{s}$. The search for possible Feynman scaling [12] is best done in the centre of mass system using x instead of $p^*_{\parallel}$.

There are still some disadvantages in using the variables already described. First of all, each event must be weighted by a factor $\prod_1^n E_i$ (which reduces to just E_1 for single particle distributions); but even after this weighting, there is still a sharp maximum at x = 0 (see figure 8, which shows the x distribution for K^o in this experiment). Also, the distribution changes shape in transforming from one frame to another. A new variable, y , was introduced to describe the particle i uniquely and to have the following properties :

(1) A Jacobian $\prod_1^n E_i$ to cancel the factor in equation 2.

(2) The expansion of the region near x = 0 relative to the large |x| region.

(3) Invariance under longitudinal Lorentz transformations, except for a scale factor.

This new variable, the longitudinal rapidity, was defined such that

$$\sinh y = \eta_{\parallel} = \frac{p_{\parallel}}{m'} \quad , \quad \text{where} \quad m' = \sqrt{m^2 + p_T^2}$$

Using the relation $\cosh y = (1 + \sinh^2 y)^{\frac{1}{2}}$ gives

$$\cosh y = \gamma_{\parallel} = \frac{E}{m'} \quad .$$

The derivative $\frac{dp_{\parallel}}{dy} = m' \frac{d(\sinh y)}{dy} = m' \cosh y = E$, as required.

Since $\tanh y = \frac{p_{\parallel}}{E} = \beta_{\parallel}$, we have

$$y = \tfrac{1}{2} \log_e \left(\frac{1 + \beta_{\parallel}}{1 - \beta_{\parallel}} \right) = \tfrac{1}{2} \log_e \left(\frac{E + p_{\parallel}}{E - p_{\parallel}} \right)$$

In transforming from one frame to another, the rapidity changes by a constant

$$\text{e.g.} \quad y' = y - \tfrac{1}{2} \log_e \left(\frac{1 + \beta'_{\parallel}}{1 - \beta'_{\parallel}} \right)$$

One disadvantage is that the kinematic range increases with increasing values of s.

$$\text{For } p^*_{\parallel} : \quad p^*_{\parallel A} - p^*_{\parallel B} = 2p^*_{in} = \sqrt{s}$$

$$\text{For } y : \quad y_A - y_B = \log_e \left(\frac{s}{m_A + m_B} \right)$$

Therefore, it is useful to define [13] a 'reduced longitudinal rapidity' ξ , such that

$$\xi = \frac{y - y_B}{y_A - y_B} \quad .$$

ξ is the same in any two frames connected by a longitudinal Lorentz transformation. However, very little published data has so far been presented in terms of this variable, so that comparison of rapidity

distributions at different energies is difficult.

4.8 Differential Cross Sections - Longitudinal Variables

If Feynman scaling is true, then it is expected that equation 3 will become independent of s over the whole phase space region. Integration of equation 3 with respect to the two transverse variables and transformation from $p_{||}$ to x gives the invariant single particle distribution function ,

$$f_1(x) = \frac{1}{\pi . p_{||}^{*max}} \int E^* \frac{d^2\sigma}{dx . dp_T^2} . dp_T^2$$

$$= \frac{E^*}{\pi . p_{||}^{*max}} \frac{d\sigma}{dx}$$

This distribution is shown in figure 8 for K^o produced in the reaction $\bar{p}p \longrightarrow K^o + X$, where X is any number of charged and/or neutral particles. There should be a forward-backward symmetry about $x = 0$, since an equal number of K^o and $\bar{K}^o$ are produced. There is a depletion of events for $x < 0$, which is thought to be due to a scanning loss of backwards produced V^os which cannot be corrected for by the decay weight factor. (This distribution is in fact unweighted.) Therefore, only K^o emitted in the forward hemisphere have been used for most of the analysis to follow. The K^o are seen to be produced predominantly in the central region near $x = 0$. The equivalent distribution for pp interactions at 12 GeV/c [7] is also shown in figure 8, where the K^o are also seen to be produced predominantly in the central region. The difference between the two distributions, those for $\bar{p}$ and p beams, is shown as an inset in figure 8 as a function of x. If the excess of K^o observed in antiproton interactions is due to annihilation, then it can be seen that the annihilation-produced K^o are to be found at larger values of $|x|$ than the non-annihilation K^o.

Figure 9 shows the invariant single-particle distribution for K^0 as a function of x for different p_T^2 ranges. The shape does not change significantly from one p_T^2 range to the next, implying that there is little correlation between the transverse and longitudinal variables at this energy. However, the shoulder seen at $x \sim 0.7$ disappears for the highest p_T^2 interval.

The single-particle distribution, F(x), for K^0 for various incident beam momenta is shown in figure 10. There is little energy dependence between 12 and 100 GeV/c. (In figure 10 the 14.75 GeV/c data has been renormalised since the published cross section of that experiment appears to be inconsistent with the x-distribution and with other cross sections at neighbouring energies. Even after this renormalisation, the slope of the x-distribution is somewhat different from those at 12, 32, and 100 GeV/c.)

The x-distributions for Λ^0 and $\bar{\Lambda}^0$ are shown in figures 11 and 12, and for separate p_T^2 regions in figure 13. They are expected to be mirror images of each other about x = 0, and indeed the Λ^0 and $\bar{\Lambda}^0$ are seen to behave as fragments of the target proton and the projectile antiproton respectively. Also, the differential cross section appears to be the same for both Λ^0 and $\bar{\Lambda}^0$ for the same value of $|x|$, bearing in mind the small measured difference in their production cross sections. The data are again compared with 12 and 12.4 GeV/c proton-induced reactions in figure 11, and the difference $F(x)_{\bar{p}p} - F(x)_{pp}$ obtained by folding the $\bar{p}p \longrightarrow \Lambda^0 + X$ distribution is also shown in figure 13. This indicates that the production of Λ^0s in antiproton interactions is of a fragmentation type , but that this is much less so in proton interactions. The data are also compared with data from experiments using different incident particles in figure 14.

The differential cross section for the inclusive production of K^0

has been plotted in Figure 15 as a function of the rapidity, y, with both lab. and centre of mass scales. The rapidity shows no structure in the central region, which might have been hidden in the plot of invariant cross section versus x (Figure 8). Figure 16 shows the corresponding distributions for Λ and $\bar{\Lambda}$.

4.9 Differential Cross Sections - Transverse Variables

The p_T^2 dependence of the inclusive K_s^o differential cross section, $d\sigma/dp_T^2$, is shown in Figure 17 for forward hemisphere K_s^o. A fit of the form $d\sigma/dp_T^2 = Ae^{-bp_T^2}$ was made, but the results were poor (χ^2/No. of degrees of freedom = 60.5/25 ; corresponding to a confidence level of only 0.03%) indicating some significant departure from a pure exponential form. A fit using the sum of two exponentials (4 parameters), $d\sigma/dp_T^2 = Ae^{-bp_T^2} + Ce^{-dp_T^2}$, gave a better result (χ^2/no. of degrees of freedom = 11.29/25). The values of the fitted parameters b and d are shown in the figure. The four parameter fit shown was made in the range $0 < p_T^2 < 0.95$.

It was mentioned in section 4.7 that there is little change in the transverse momentum distribution as the total centre of mass energy changes. Comparing the K^o distribution of Figure 17 with those found in 32 GeV/c and 100 GeV/c [15,17] $\bar{p}p$ interactions confirms this, and the slope b found from fitting an exponential to the data at 32 GeV/c is 4.2 ± 0.8 $(GeV/c)^{-2}$. There is little variation of the slope of the p_T^2 distribution for different incident particles, only in the overall normalisation.

The corresponding distributions for Λ and $\bar{\Lambda}$ are shown in Figure 19. Here, both distributions can be fitted with a simple exponential, with a confidence level greater than 10% over the whole range of p_T^2. The fitted parameters are $b(\Lambda) = 4.30 \pm .09$ and $b(\bar{\Lambda}) = 4.18 \pm .09$.

This is unlike the result found at 5.7 GeV/c [14] where the fit indicated a significant deviation from pure exponential form. Also shown are the results from the 12 GeV/c pp $\rightarrow \Lambda X$ data [7].

It is also interesting to study the variation of the transverse momentum with a longitudinal variable. This has already been discussed in one case, with the separation of the data for different p_T^2 ranges in the single particle distributions in x and y (section 4.8). The average transverse momentum $\langle p_T \rangle$ can also be studied as a function of x or ξ, for example. There is some evidence for an effect often observed in the first of these distributions known as the "seagull effect", a decrease of $\langle p_T \rangle$ at small $|x|$, in the distribution for the K^o, figure 19a). This effect was not observed in the same reaction at 14.75 GeV/c [6] . The average transverse momentum over the whole x range is $\langle p_T \rangle^{K^o} = 0.449 \pm .004$ GeV/c. The $\langle p_T \rangle$ distributions for Λ and $\bar{\Lambda}$ are shown in Figure 19b),c) and do not show the seagull effect. The average transverse momenta for Λ and $\bar{\Lambda}$ are :

$\langle p_T \rangle^{\Lambda} = 0.487 \pm .004$ GeV/c and $\langle p_T \rangle^{\bar{\Lambda}} = 0.482 \pm .005$ GeV/c.

The $\langle p_T \rangle$ shows no variation with s, the total centre of mass energy squared, for proton induced reactions, up to 400 GeV/c [18]. For anti-proton interactions, the $\langle p_T \rangle$ for Λ , $\bar{\Lambda}$ is marginally higher at 100 GeV/c ($0.52 \pm .04$ and $0.54 \pm .06$ GeV/c [17]) but the same within errors as lower energy data. An increase in $\langle p_T \rangle$ is observed in $K^+p \rightarrow K^oX$ interactions [18] (from 0.37 GeV/c at 5 GeV/c to 0.41 GeV/c at 16 GeV/c).

The mean transverse momentum of the V^o is plotted as a function of the associated charged multiplicity in figure 20 for K^o, Λ, and $\bar{\Lambda}$. There is a slight fall off at higher multiplicities and the maximum occurs for all three types of V^o at a value of $n \simeq 2$.

4.10 Differential Cross Sections as Functions of M_X^2, t

It has already been noted (section 4.7) that an inclusive distribution is just a sum of exclusive distributions. An analogy can be drawn between the quasi two body and single particle inclusive approaches.

Consider the reaction $a + b \rightarrow c + X$, and define the four invariants :

$$s = (p_a + p_b)^2$$

$$t_{ac} = (p_a - p_c)^2$$

$$t_{bc} = (p_b - p_c)^2$$

$$M_X^2 = s_{ab\bar{c}} = (p_a + p_b - p_c)^2$$

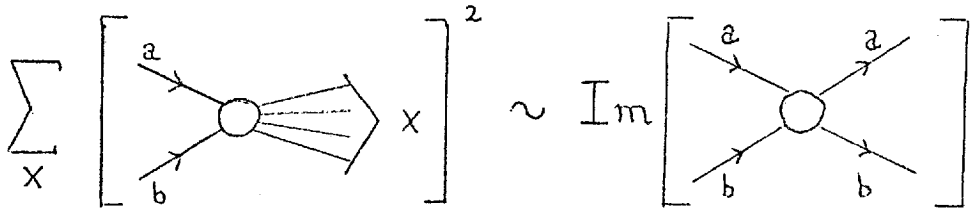
There exists one relationship between them, leaving only three independent variables, namely

$$s + t_{ac} + t_{bc} = m_a^2 + m_b^2 + m_c^2 + M_X^2$$

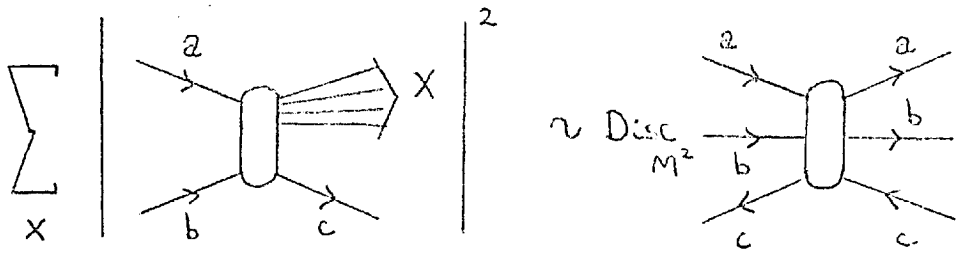
so one can use two body kinematics on the reaction $a + b \rightarrow c + X$ .. (4)

For example, the two-body optical theorem relates the total cross section, σ_T , to the forward elastic scattering amplitude, T_{el} , such that

$$\sigma_T \propto \frac{1}{s} \text{Im } T_{el} \Big|_{t=0}$$



Mueller introduced [19] a generalised optical theorem, which relates the cross section for reaction (4) to the imaginary part of the forward elastic scattering amplitude for the process $ab\bar{c} \rightarrow ab\bar{c}$.



The Triple Regge Limit, as suggested by Caneschi [20] , de Tar [21], etc., which is a special case of the fragmentation limit above, applies when the conditions of $|t|$ fixed and small, s/M^2 large and M^2 large are satisfied.

The allowed Regge exchanges in the reaction

$$\bar{p}p \rightarrow \Lambda^0 + X \qquad \ldots (5)$$

are K, K^*, and K^{**}, in contrast with Λ^0 produced in the reaction $K^-p \rightarrow \Lambda^0 + X$ where, besides the strange-meson trajectories, baryon exchange is also allowed. Following Ganguli [14] , who has done a Triple Regge analysis of reaction (5) at $p_{incident} = 5.7$ GeV/c, a similar analysis was performed using the data from this experiment for both reaction (5) in the target fragmentation region and for the reaction

$$\bar{p}p \rightarrow \bar{\Lambda}^0 + X \qquad \ldots (6)$$

in the beam fragmentation region. Ganguli was unable to distinguish between the K^* - K^{**} and the K trajectories.

In section 4.8, differential cross sections were studied as functions of x and p_T^2 , so that any "approach to scaling" behaviour would become apparent. In this section, the cross sections will first be studied as functions of M_X^2 (or M_X^2/s), the mass of the system recoiling against the V^0, and t, the momentum transfer from the target (beam) to the Λ^0 ($\bar{\Lambda}^0$).

The differential cross sections $d\sigma/dM_X^2$ for K^0, Λ^0, and $\bar{\Lambda}^0$ are shown in Figure 21 for all topologies. No fine structure can be seen

in these plots or in the plots for individual topologies.

The mean charged multiplicity is shown in Figure 22 as a function of the missing mass squared, M_X^2. There is an approximately linear dependence on $\log(M_X^2/M_o^2)$ (with $M_o^2 \sim 1$ GeV^2) which has been observed in several single particle inclusive reactions. This dependence appears to be almost independent of the momentum and the nature of the incoming particle [23] . Since the quantum numbers of the X system in reactions (5) and (6) are charge conjugate to (same as) those of the K^-p system, the baryon data are compared with the average total multiplicity as a function of s, the centre of mass energy squared, determined in K^-p interactions [22]. The agreement is quite satisfactory.

The parameters characterizing the charged multiplicity distributions (average number of charged particles $\langle n \rangle$ and dispersion $D = [\langle n^2 \rangle - \langle n \rangle^2]^{\frac{1}{2}}$) associated with K^o, Λ^o, and $\bar{\Lambda}^o$ production are given in Table III.

The invariant distribution function can be written in terms of the variables t and M^2 as

$$f(s,t,M^2) = \frac{-2p^*_{proj.}}{\pi\sqrt{s}} \cdot \frac{d^2\sigma}{dt.d(M^2/s)}$$

where $p^*_{proj.}$ is the momentum of the projectile in the overall centre of mass system. Figure 23 shows the scatter plot of M^2/s versus t for Λ^o and $\bar{\Lambda}^o$. There is a flattening of the t distribution with increasing missing mass, which is in agreement with the expectation that high masses are produced mainly through large momentum transfers. The inclusive differential cross section is shown in Figures 24 and 25 for Λ^o and $\bar{\Lambda}^o$ respectively as a function of t, namely the x-projection of figure 23. An exponential of the form Ae^{bt} was fitted to the data (figures 25a) and 26a)) up to $t = 10$ (GeV/c)^2. Data for reaction (5)

at an incident antiproton momentum of 5.7 GeV/c [14] and for the reaction $pp \longrightarrow \Lambda^0 X$ at 12.4 GeV/c [8] had been well fitted by a more complicated expression [24] :

$$\frac{d\sigma}{dt} = A.e^{bt} \quad , \text{ for } |t| < |t_{br}|$$

$$= A.e^{bt_{br}}.e^{c(t-t_{br})} \quad \text{for } |t| > |t_{br}|$$

where t_{br} is the value of t at a break point, i.e. where the slope of the exponential changes sharply.

The parameters A, b, c, and t_{br} were allowed to vary in the fit. There appeared to be a break point in both sets of data around 1 $(GeV/c)^2$. The data from this experiment were fitted using the above expression over the full range of t, and the fitted values of the four parameters are shown in Table IV . A break point was found near $|t_{br}| = 5\ (GeV/c)^2$. Since the data above $|t| = 5\ (GeV/c)^2$ is limited, the data below this value of |t| were rebinned in narrower bins, but no effect similar to that found at either 5.7 GeV/c or 12.4 GeV/c was observed (Figures 24 b) and 25 b)).

4.11 Triple Regge Limit

The Triple Regge Limit, as described in section 4.10, leads to the formula :

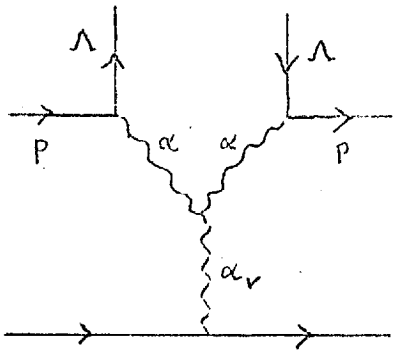
$$\frac{d^2\sigma}{dt.d(M^2/s)} = \beta_o(t)\left(\frac{M^2}{s}\right)^{\alpha_v(0) - 2\alpha(t)}.s^{\alpha_v(0) - 1}$$

for the double differential cross section, where

$\beta_o(t)$ = Residue functions (independent of beam particle a)

$\alpha_v(0)$ = Leading trajectory coupling to $a\bar{a}$ at zero momentum transfer

$\alpha(t)$ = Leading Regge trajectory in the $b\bar{c}$ (or t-) channel



Allowed exchanges α_v, are the Pomeron and/or mesons (ρ, A_2, ω^o, f^o). Ganguli [26] fitted the inclusive Λ^o production cross section from both proton and antiproton reactions by assuming that the Pomeron and an odd signature meson trajectory (e.g. ω^o) only were required. The allowed Regge exchanges $\alpha(t)$ are the strange meson trajectories, K, K^*, and K^{**}. The invariant cross section for the fragmentation of proton into Λ^o, or antiproton into $\bar{\Lambda}^o$, can be re-written assuming unity for the Pomeron intercept and 0.4 for the ω^o trajectory as :-

$$\frac{d^2\sigma}{dt.d(M^2/s)} = \beta_o(t)\left[(M^2/s)^{1-2\alpha(t)} + s^{-0.6}(M^2/s)^{0.4-2\alpha(t)}\right]$$

The effective trajectory, $\alpha(t)$, is assumed to have the form :-

$$\alpha(t) = \alpha(0) + \alpha' t$$

The data were fitted to the expression

$$\frac{d\sigma}{d(M^2/s)} = \int_{t_u}^{t_L} A.(M^2/s)^{1-\alpha(t)}.dt$$

for the five different t regions : $-t < 0.4$; $0.4 < -t < 0.8$; $0.8 < -t < 1.2$; $1.2 < -t < 1.8$; $1.8 < -t < 3.2$, taking into account the edge effects at the upper limit in M^2/s of the phase space. For each M^2/s bin, the maximum and minimum allowed values of t were calculated using the formula :-

$$-t^{min}_{max} = \left[\sqrt{\left(\frac{s + m_\Lambda^2 - M^2}{2\sqrt{s}}\right)^2 - m_\Lambda^2} \mp \sqrt{\left(\frac{s}{4} - m_p^2\right)}\right]^2 - \left[\frac{m_\Lambda^2 - M^2}{2\sqrt{s}}\right]^2 \qquad [25]$$

If the t bin limits are t_i and t_{i+1} , for $t_{max} < t_{i+1}$, $t_u = t_{max}$ and for $t_{min} > t_i$, $t_L = t_{min}$. When the value of $t_{max} < t_i$ or $t_{min} > t_{i+1}$, the integral was set to zero. The double differential cross section was integrated over these limits and the resultant expression was fitted using a minimum χ^2 method. The results of these fits, all at a confidence level of greater than 1%, are shown in Figures 26 and 27 for Λ^0 and $\bar{\Lambda}^0$ respectively.

The values of α from the fits are plotted as a function of t in Figure 28. A straight line was fitted to each set of data to give the effective trajectories

$$\alpha^{\Lambda}_{eff} = (0.116 \pm .013) + (0.986 \pm .048)\ t$$

$$\alpha^{\bar{\Lambda}}_{eff} = (0.062 \pm .014) + (0.963 \pm .037)\ t$$

The results found at 5.7 GeV/c for reaction (5) were

$$\alpha^{\Lambda}_{eff} = (0.02 \pm .04) + (1.01 \pm .04)\ t$$

which are in good agreement with the results from this experiment. Ganguli [26] finds

$$\alpha^{\Lambda}_{eff} = -(0.2 \pm 0.1) + (0.8 \pm 0.1)\ t$$

for $p_{lab} > 10$ GeV/c, fitting the inclusive cross sections for $pp \rightarrow \Lambda^0 X$ and $\bar{p}p \rightarrow \Lambda^0 X$. No distinction could be made between the K and K^* trajectories at 5.7 GeV/c, but the data from this experiment appear to favour the K^* trajectory at low t (less than -1.0 $(GeV/c)^2$).

References

1. W. Galbraith et al. Phys. Rev. 138,(1965)
2. F. Eisele et al. Physics Letters 60B,(1975),297
3. J. Ballam et al. Phys. Rev. D4,(1971),1946
4. C. Walck et al. 9.1 GeV/c $\bar{p}p$ Proc. of Int. Symp. on $\bar{p}p$ Ints. Loma-koli, Finland, 1975

   R. Carlsson et al. 9.1 GeV/c $\bar{p}p$ Nucl. Phys. B99,(1975),451
5. P.D. Gall 12 GeV/c $\bar{p}p$ DESY F1-76/02, (1976)
6. F.T. Dao et al. 14.75 GeV/c $\bar{p}p$ Physics Letters 51B,(1974),505
7. V. Blobel et al. 12 GeV/c pp Nucl. Phys. B69,(1974),454
8. K. Jaeger et al. 12.4 GeV/c pp Phys. Rev. D11,(1975),1756
9. H. Muirhead and P.S. Gregory Proc. IIIrd European Symposium on $\bar{N}N$ Interactions, Stockholm, 1976
10. For example, W. Kittel Proc. 1972 CERN School of Physics, Grado CERN 72-17
11. L. Van Hove Physics Letters 28B,(1969),429 ; Nucl. Phys. B9,(1969),331
12. R. Feynman Phys. Rev. Letts. 23,(1969),1415
13. L. Van Hove Phys. Rev. 1c,(1971),347
14. S. Ganguli et al. 5.7 GeV/c $\bar{p}p$ Nucl. Phys. B53,(1973),458
15. R. Barloutaud 32 GeV/c $\bar{p}p$, $K^{\pm}p$ Talk at XVIII International Conf. on High Energy Physics, Tbilisi, 1976 DPhPE 76-17

   M.A. Jabiol et al. 32 GeV/c $\bar{p}p$ France-USSR and CERN-USSR collaborations preprint (1977)
16. A. Fridman 50 GeV/c $\bar{p}p$ Talk at VIIIth Symposium on multiparticle dynamics, Kaysersberg, 1977
17. D. Ward et al. 100 GeV/c $\bar{p}p$, pp Physics Letters 62B,(1976),237
18. W. Dunwoodie et al. 5, 8.2, 16 GeV/c $K^{+}p$ CERN/DPhII/Phys 74-40
19. A.H. Mueller Phys. Rev. D2,(1970),2963
20. L. Caneschi Phys. Rev. Letts. 22,(1969)

21. C.E. De Tar et al. Phys. Rev. Letts. 26,(1971),675

22. For example, E. de Wolf et al. Nucl. Phys. B87,(1975),325

E. Albini et al. Nuovo Cimento 32A,(1976),101

23. T. Whitmore Phys. Rev. 27,(1976),187

24. H. Atherton CERN/DPhII/Phys 73-12 ; Nucl. Phys. B69,(1974)

B. French CERN/EP/Phys 76-59

25. N. Schmitz CERN 65-24, Vol 1

26. S. Ganguli CERN/EP/Phys 76-36

TABLE I

Roll number range	light particle contamination (tracks/frame)
$\leqslant$ 141	1.36 ± 0.03
142 - 160	0.69 ± 0.03
$\geqslant$ 161	1.01 ± 0.03

TABLE II

Topological cross sections for K^0_s, Λ^0, and $\bar{\Lambda}^0$ production in $\bar{p}p$ interactions at 12 GeV/c

Topology n	σ_n (K^0_s) mb.	σ_n (Λ^0) mb.	σ_n ($\bar{\Lambda}^0$) mb.
0	0.19 ± .04	0.21 ± .04	0.19 ± .04
2	0.65 ± .08	0.64 ± .06	0.60 ± .08
4	0.84 ± .11	0.34 ± .05	0.31 ± .06
6	0.41 ± .05	0.04 ± .02	0.03 ± .01
8	0.06 ± .02	0.013 ± .006	0.011 ± .006

TABLE III

	K^0_s	Λ^0	$\bar{\Lambda}^0$
$\langle n \rangle$	3.53 ± .03	2.40 ± .03	2.38 ± .03
D	1.93 ± .18	1.59 ± .15	1.54 ± .17

TABLE IV

Fig.	b	c	t_{br} (Gev/c^2)
24a	.705	.417	4.731
24b	.703	-	-
25a	.629	.261	5.800
25b	.589	-	-

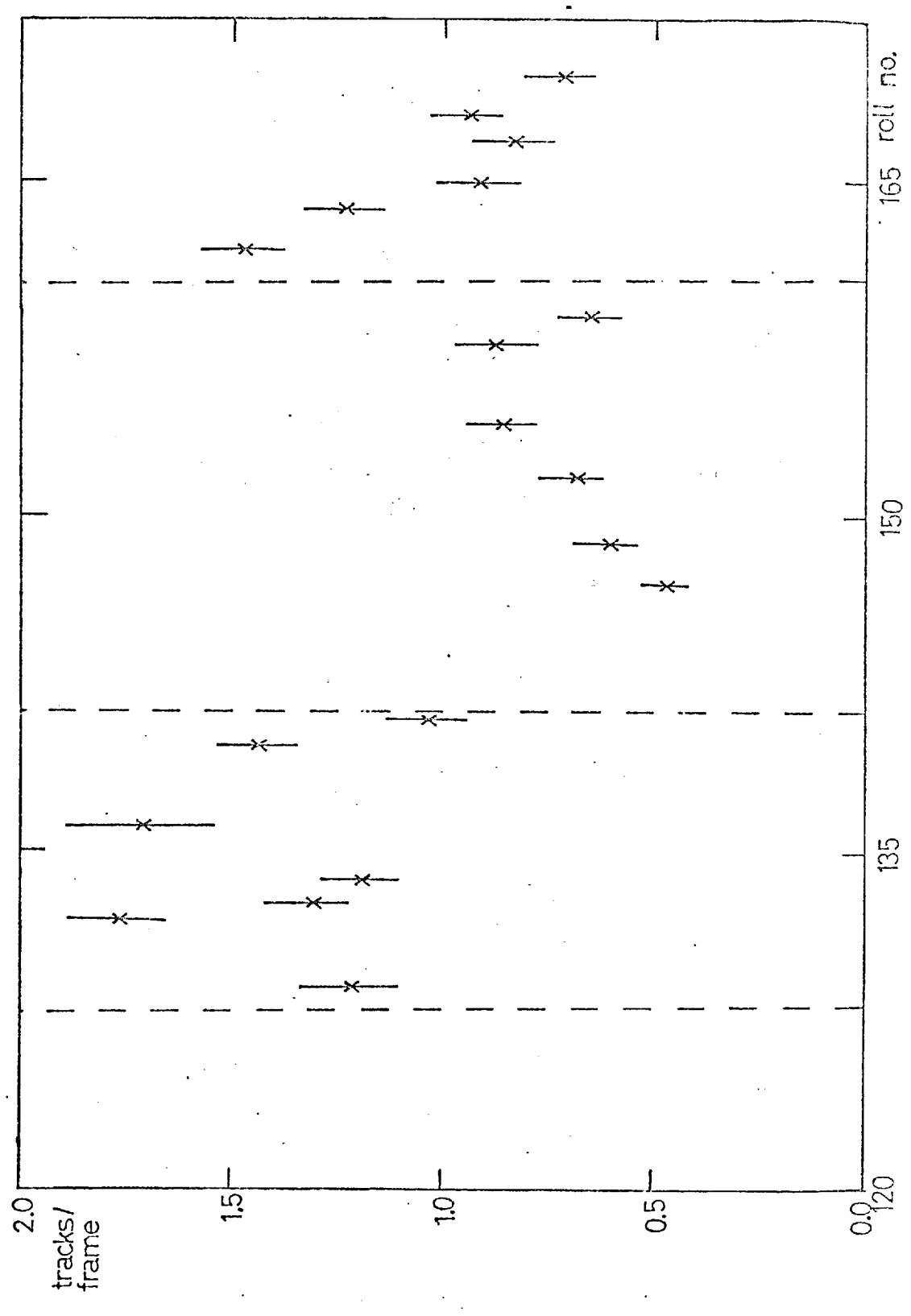


Figure 4.1 : The number of beam tracks per frame, for r.f.-off frames, as a function of roll number.

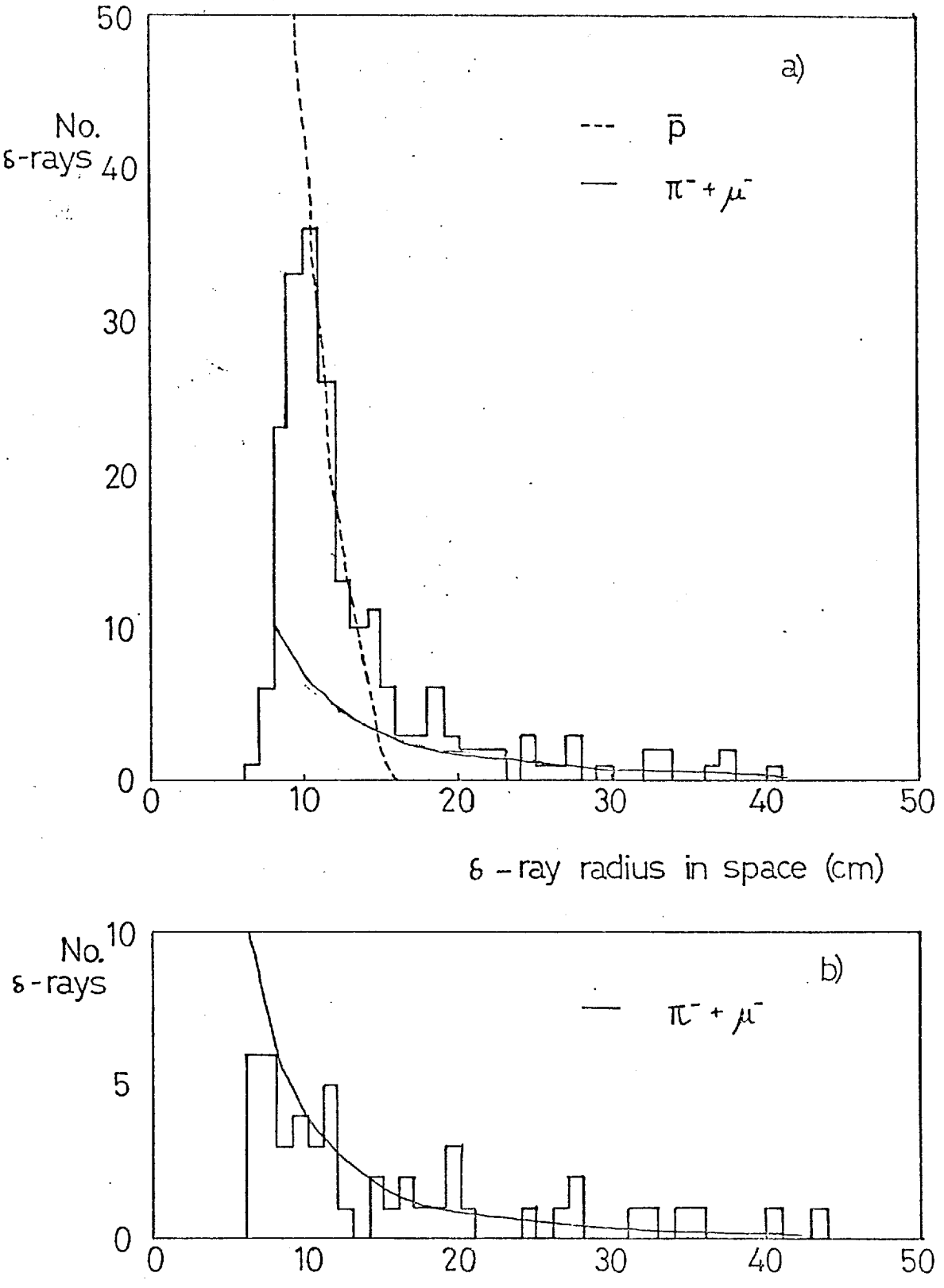


Figure 4.2 : a) Distribution of δ-ray radii in space, with predicted curves for $\bar{p}$ and light particles, normalised to the total number of $\bar{p}$ and licht particles respectively.

b) The same as for a), but with the r.f. separators turned off. No $\bar{p}$ are expected in these frames.

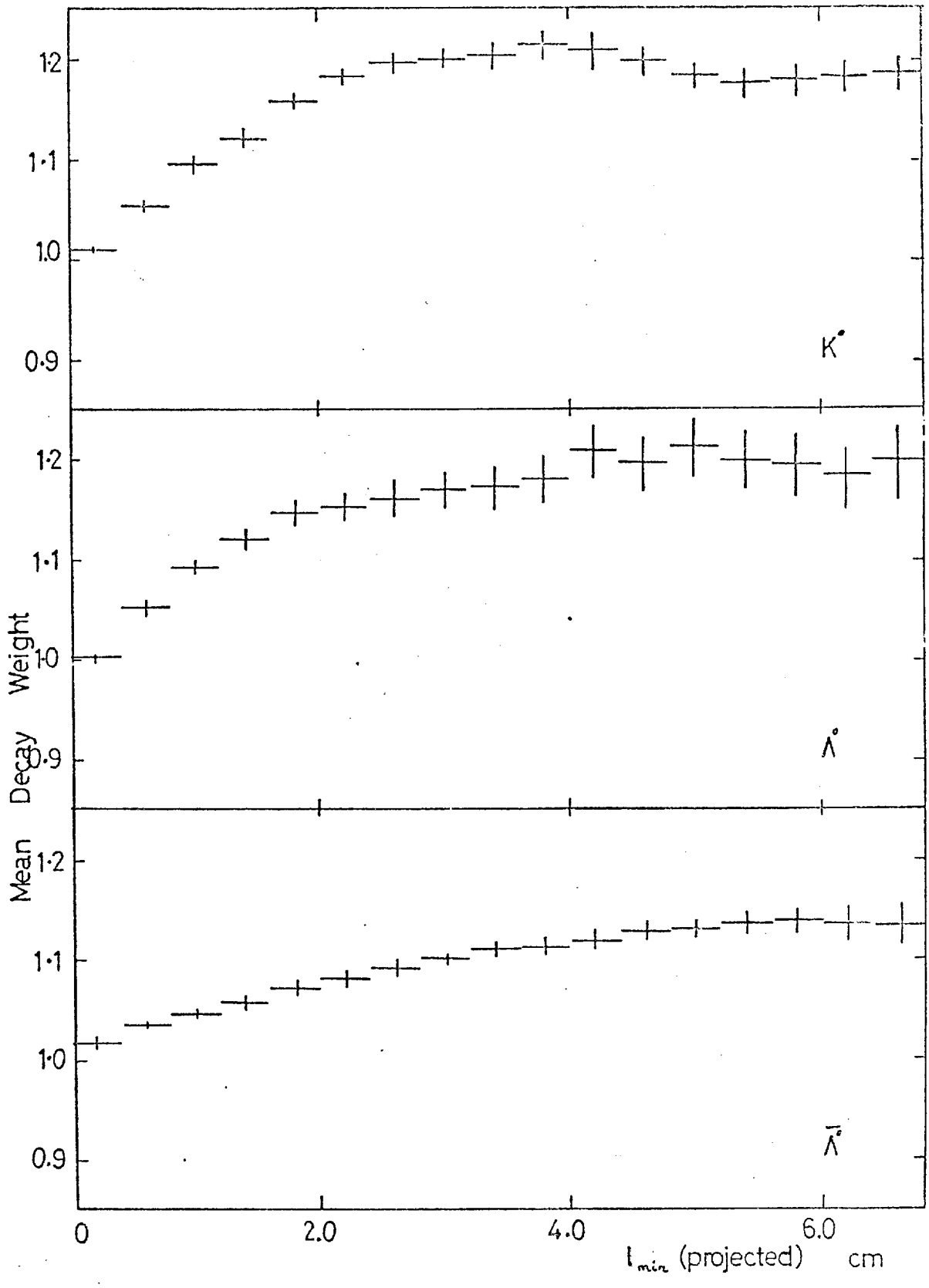


Figure 4.3 : Mean decay weight for V^0 calculated for different minimum projected decay lengths (see text).

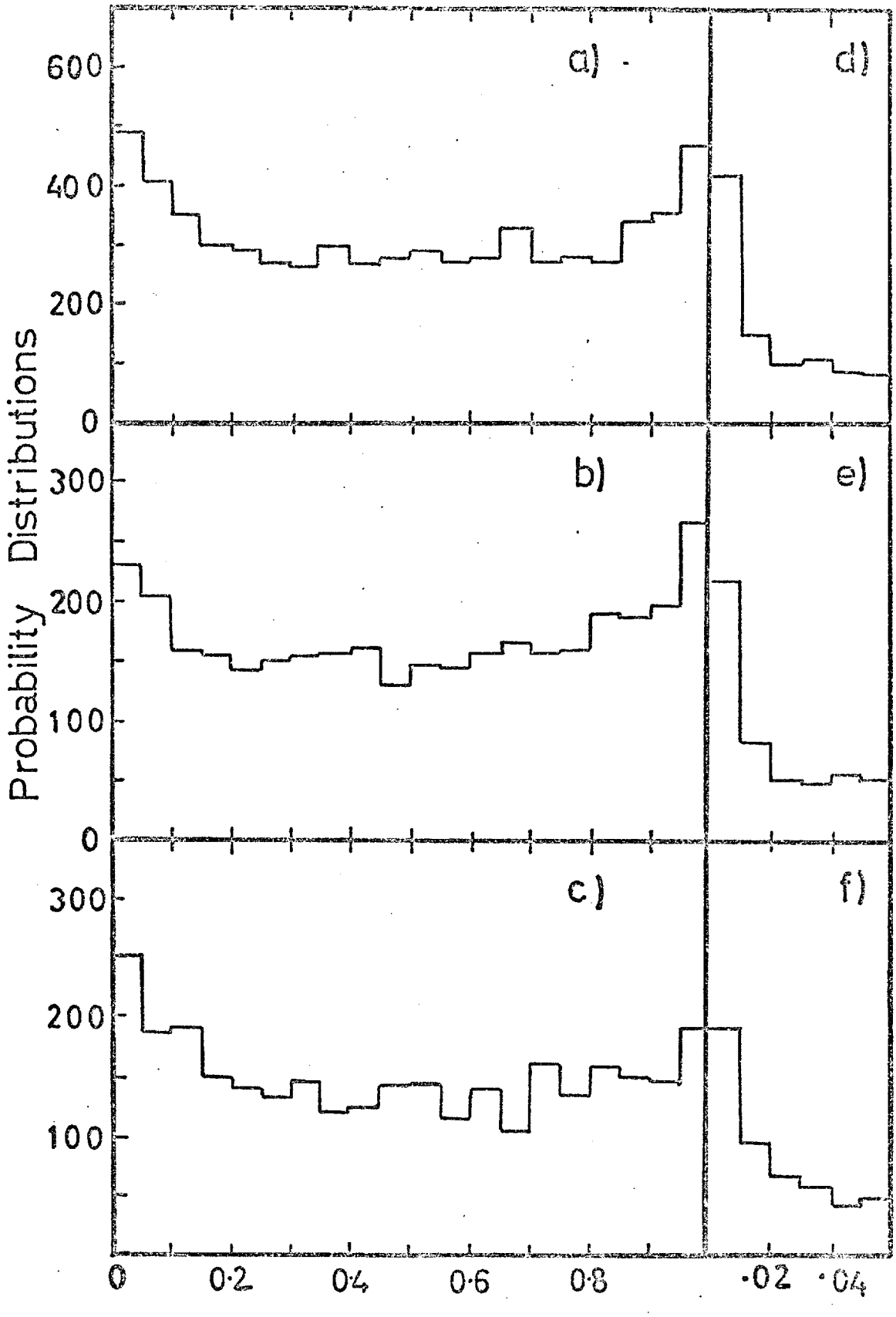


Figure 4.4 : χ^2 probabilities for V^0 kinematic fits. a) K^0, b) Λ^0 c) $\bar{\Lambda}^0$, d) K^0 low probability, e) Λ^0 low probability, f) $\bar{\Lambda}^0$ low probability. A cut was made, rejecting fits with probability < 1% (d-f). a-c are the distributions after this cut has been made.

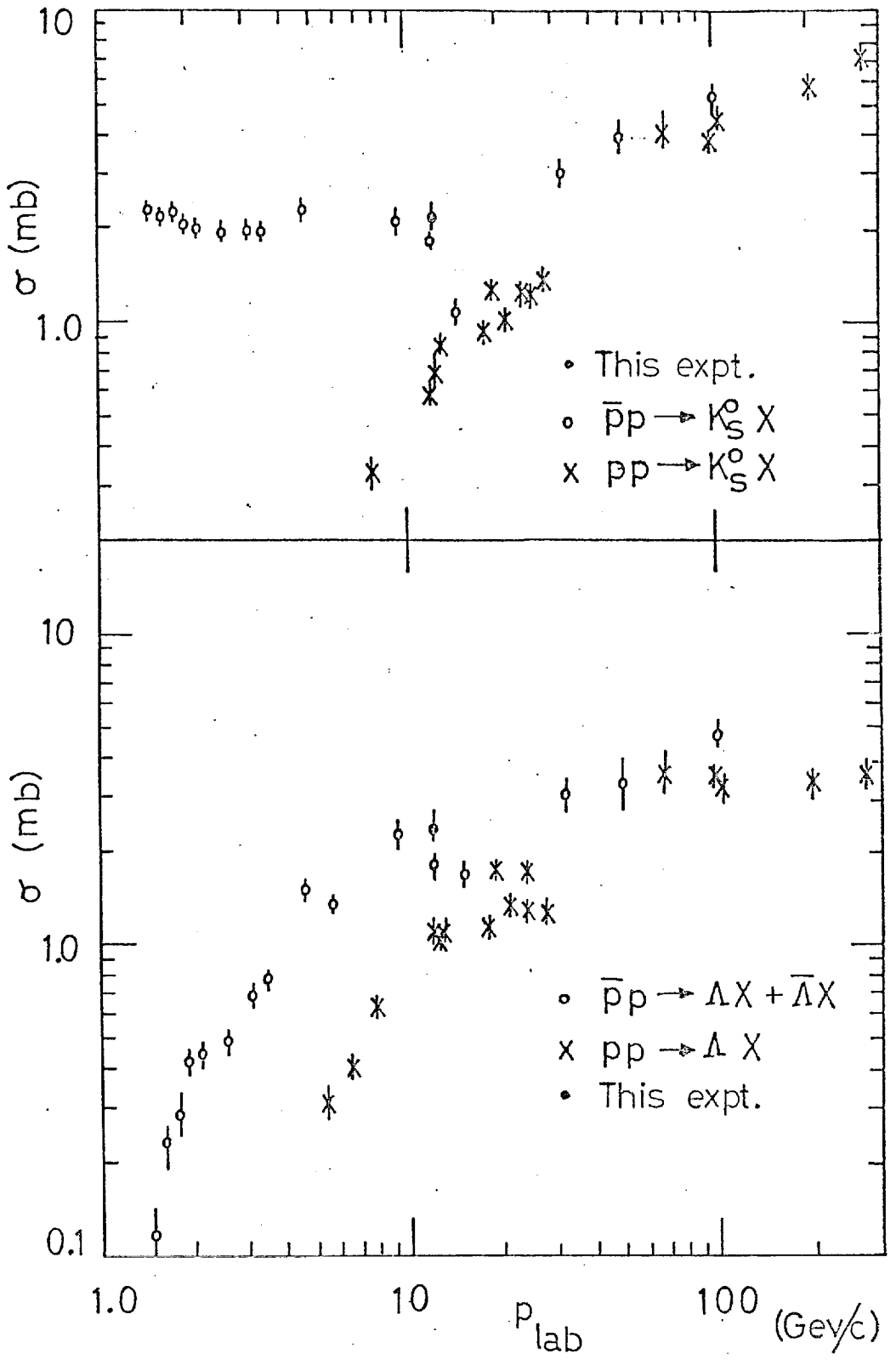


Figure 4.5 : Inclusive cross sections for the reactions $\bar{p}p \rightarrow K^o_s X$ and $\bar{p}p \rightarrow \Lambda^o X + \bar{\Lambda}^o X$ as a function of incident beam momentum. The cross sections for $pp \rightarrow K^o_s X$ and $pp \rightarrow \Lambda^o X$ are also shown, for comparison.

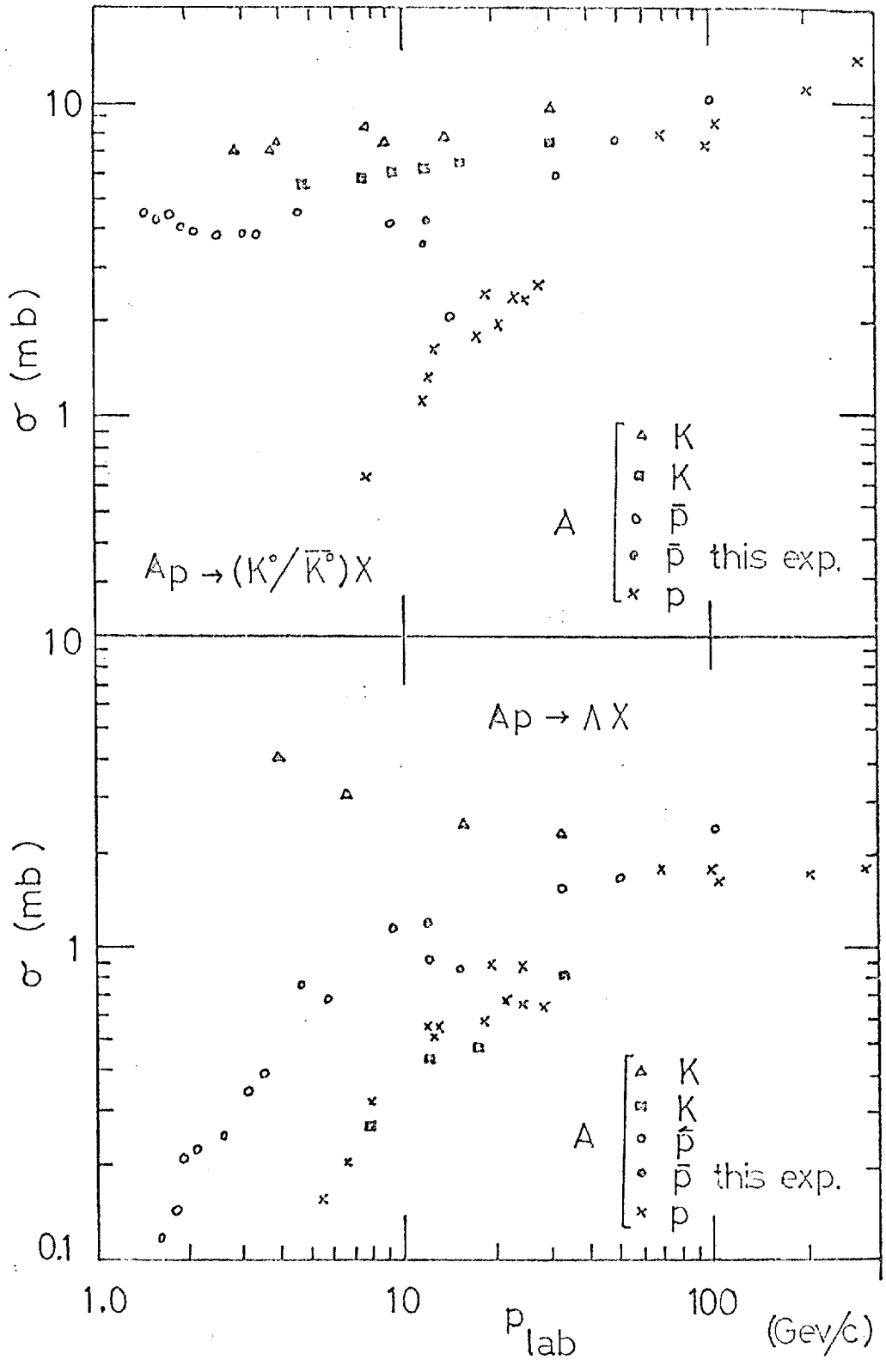


Figure 4.6 : Total Inclusive Cross Sections for $K^0/\bar{K}^0$ and Λ^0 production as a function of laboratory momentum, for various incident particles.
(Error bars are omitted for clarity.)

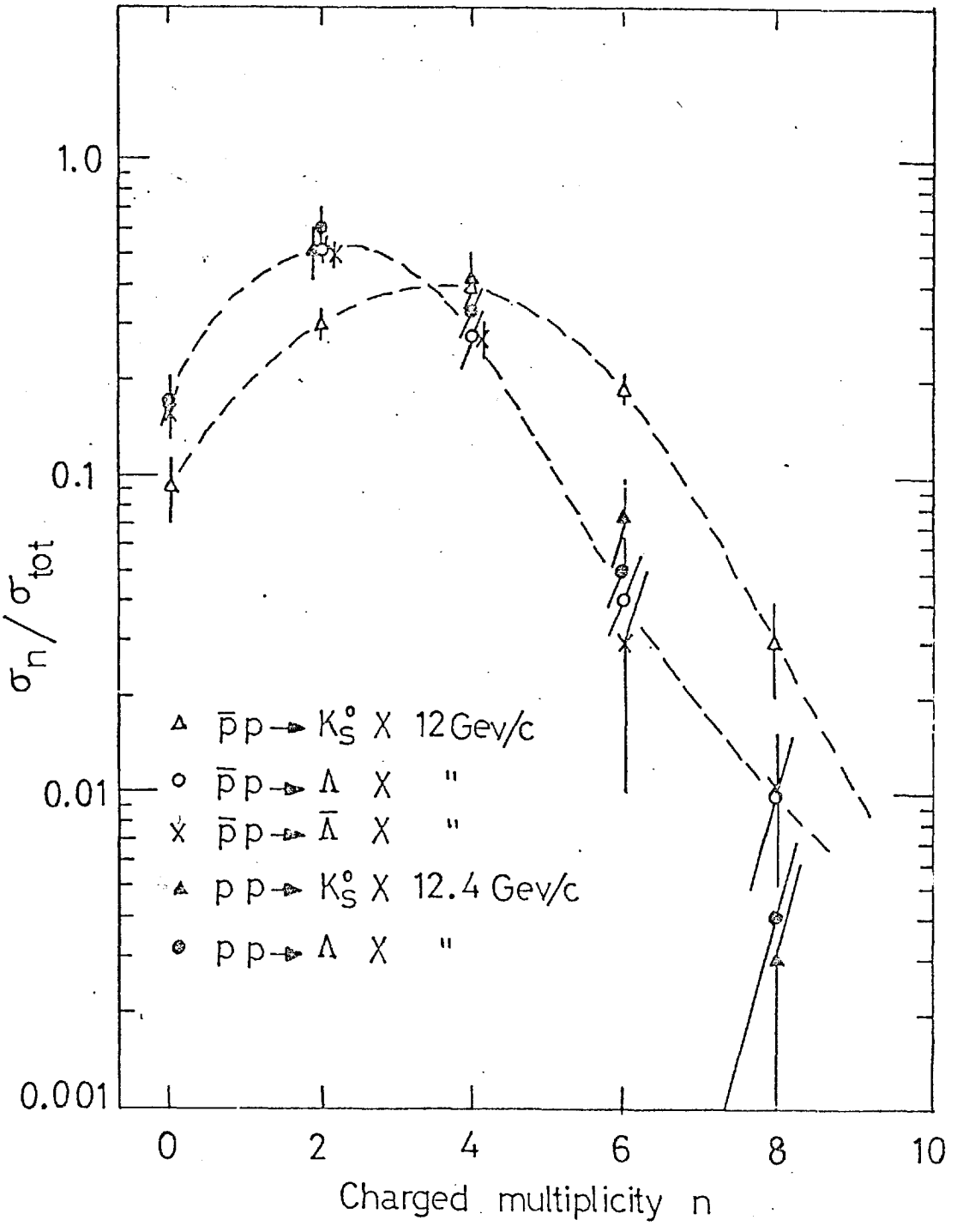


Figure 4.7 : Fraction of the inclusive cross section associated with each charged multiplicity n, for the reactions shown. The curves are hand-drawn to guide the eye.

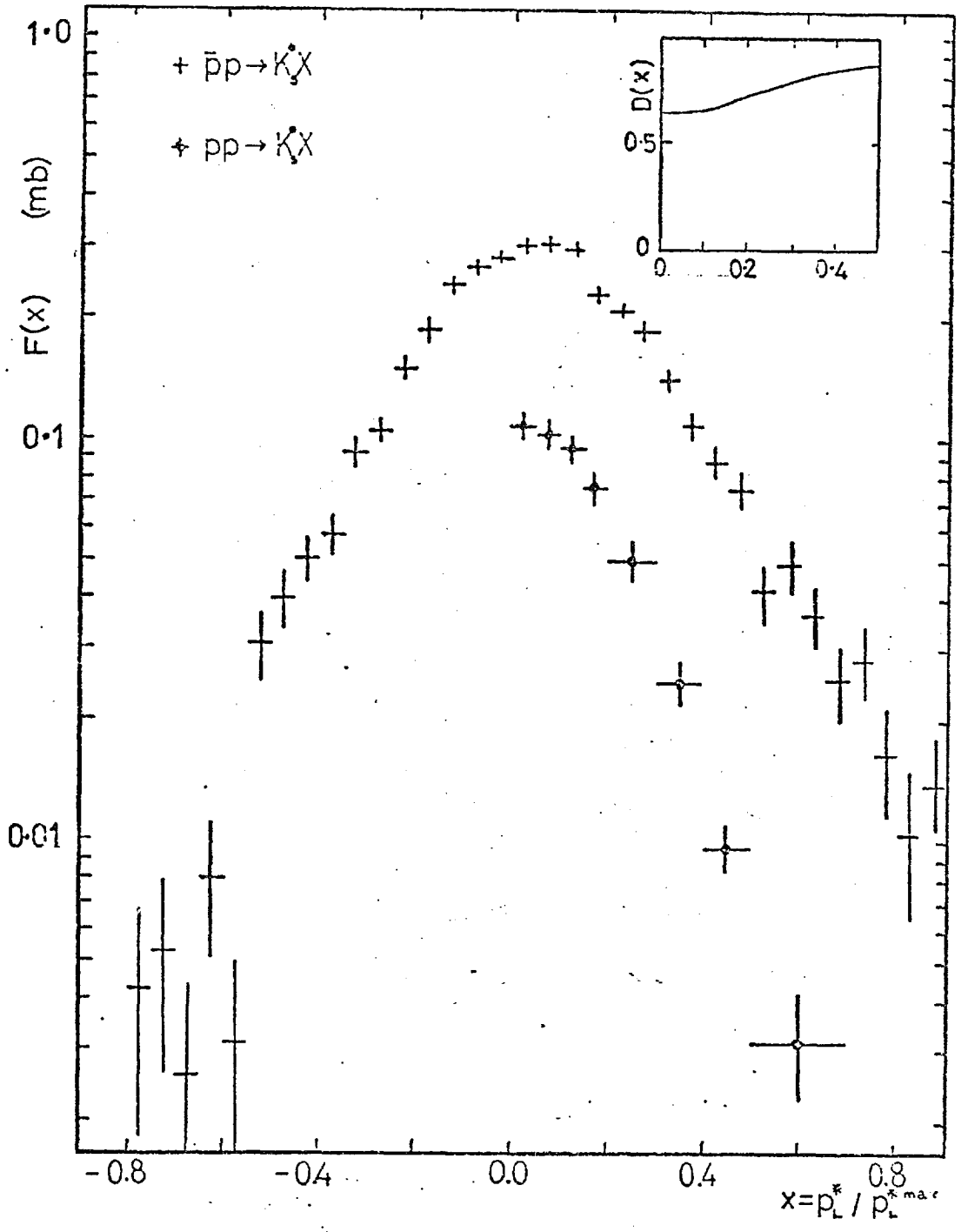


Figure 4.8 : The invariant cross section

$$F(x) = \frac{1}{\pi p^*_{L_{max}}} \int_{E^*} \frac{d^2\sigma}{dx.dp_T^2} \cdot dp_T^2$$

as a function of x for $\bar{p}p \rightarrow K^0_s X$ and $pp \rightarrow K^0_s X$, at 12 GeV/c.

The insert shows $D(x) = (F(x)_{\bar{p}p} - F(x)_{pp})/F(x)_{\bar{p}p}$.

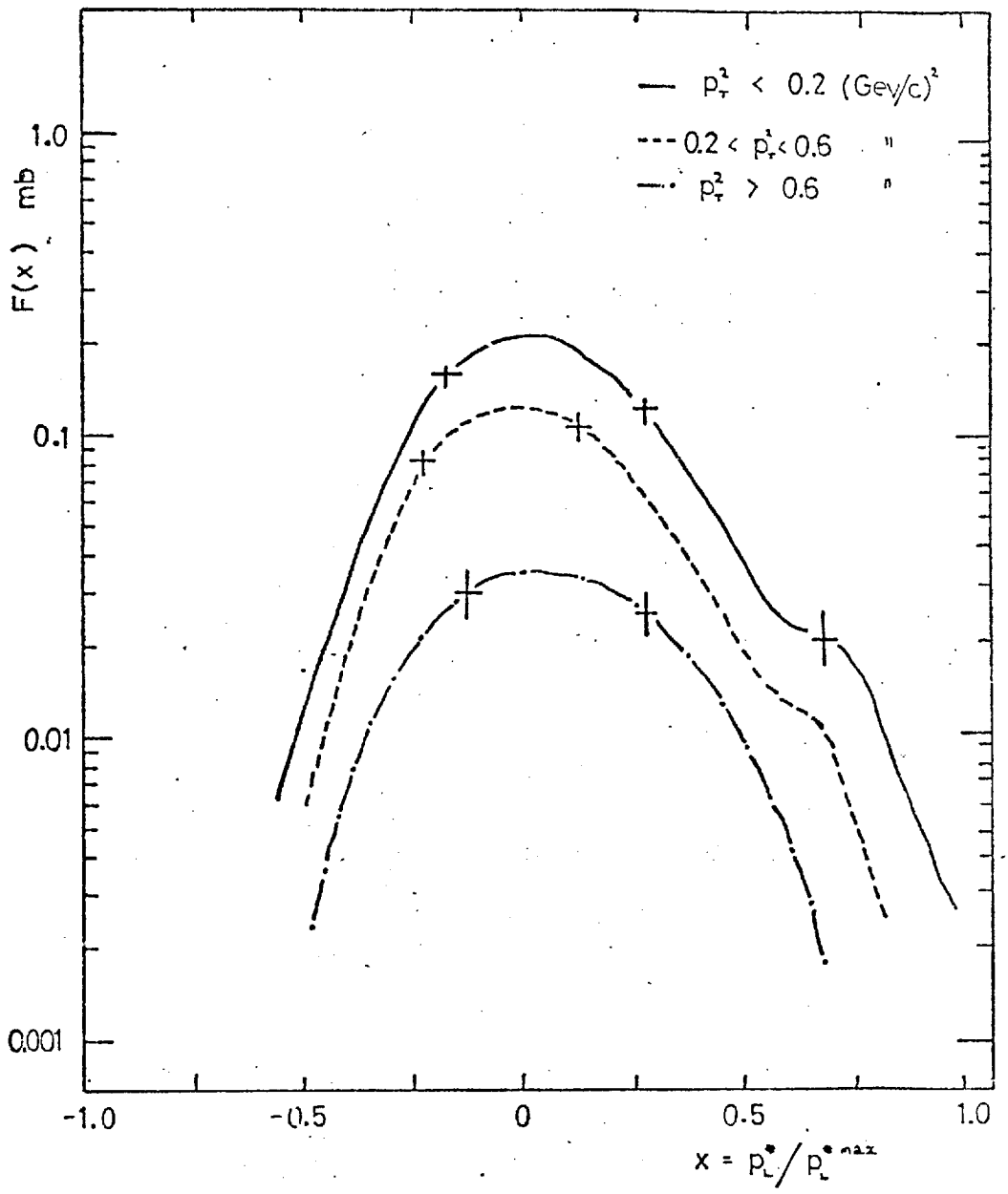


Figure 4.9 : The invariant cross section

$$F(x) = \frac{1}{\pi p^*_{L_{max}}} \int E^* \frac{d^2\sigma}{dx.dp_T^2} \cdot dp_T^2$$

as a function of x for different p_T^2 ranges, for the reaction $\bar{p}p \rightarrow K^0_S X$.

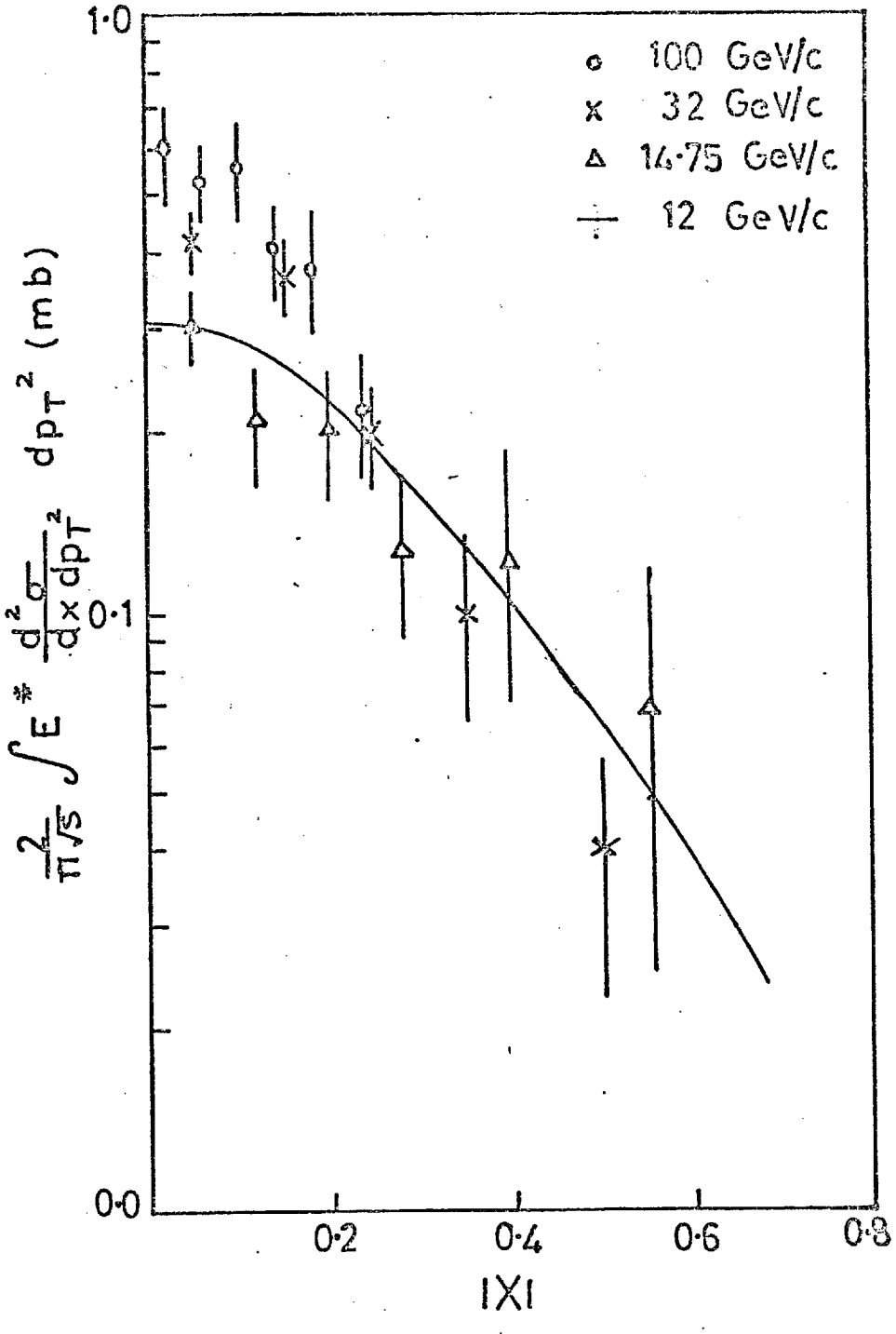


Figure 4.10 : Invariant cross section F(x) as a function of x for $\bar{p}p \rightarrow K^0X$ at different incident beam momenta.

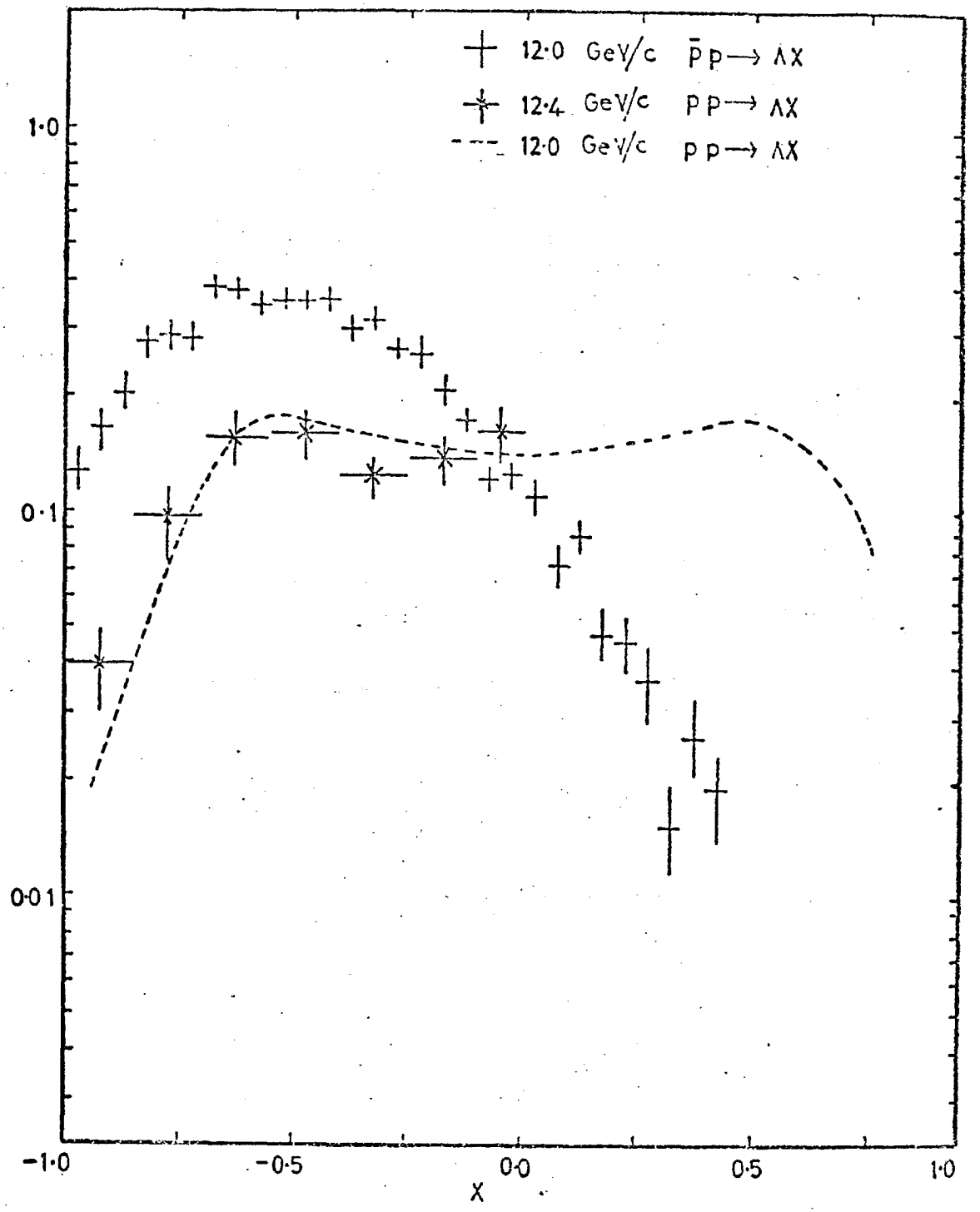


Figure 4.11 : The invariant cross section

$$F(x) = \frac{1}{\pi p^*_{L_{max}}} \int E^* \frac{d^2\sigma}{dx.dp_T^2} \cdot dp_T^2$$

as a function of x for $\bar{p}p \rightarrow \Lambda^0 X$ and $pp \rightarrow \Lambda^0 X$ near 12 GeV/c.

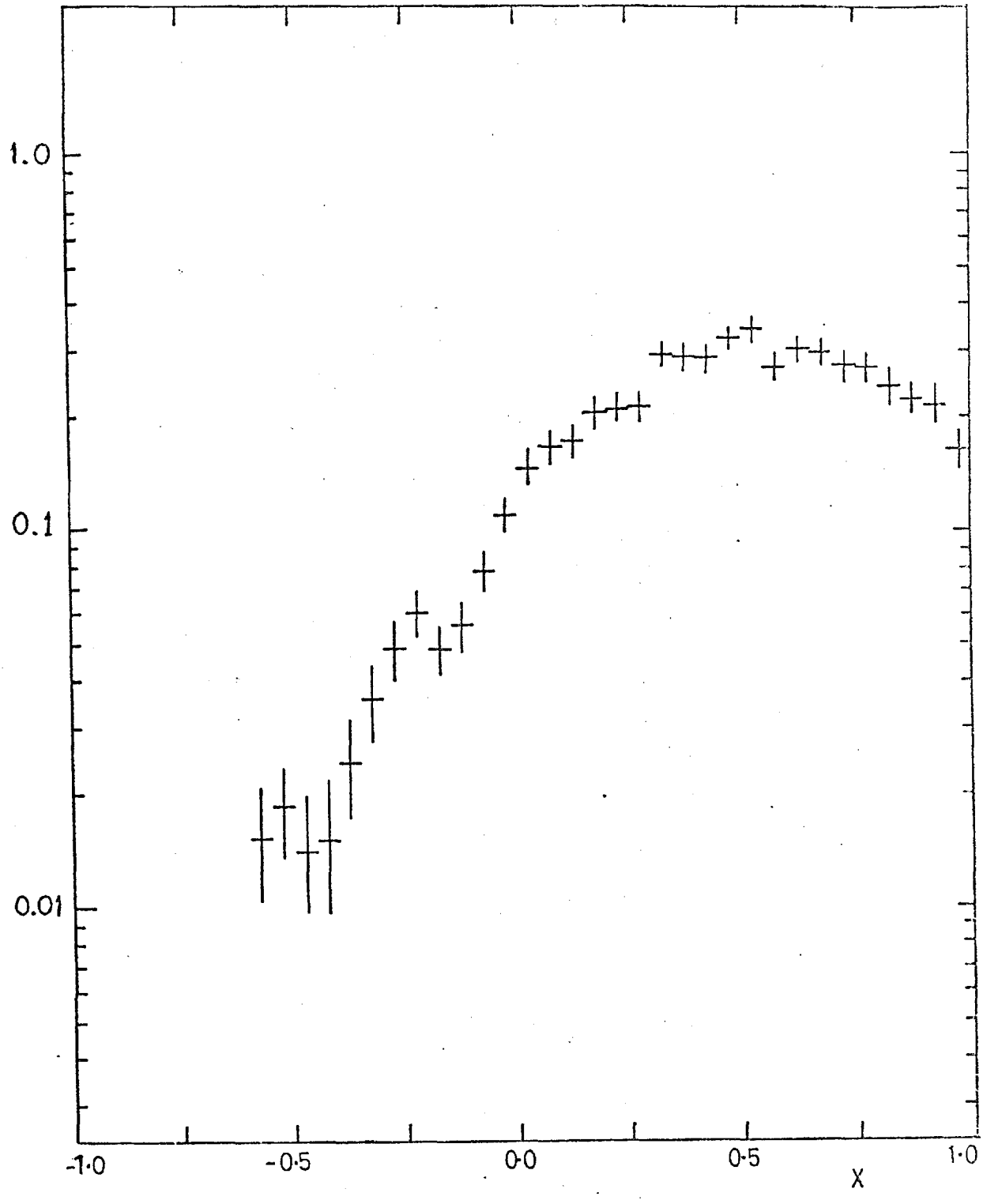


Figure 4.12 : Invariant cross section $F(x) = \frac{1}{\pi p^{*}_{L_{max}}} \int E^{*} \frac{d^2\sigma}{dx.dp_T^2} dp_T^2$

as a function of x, for $\bar{p}p \rightarrow \bar{\Lambda}^{o}X$.

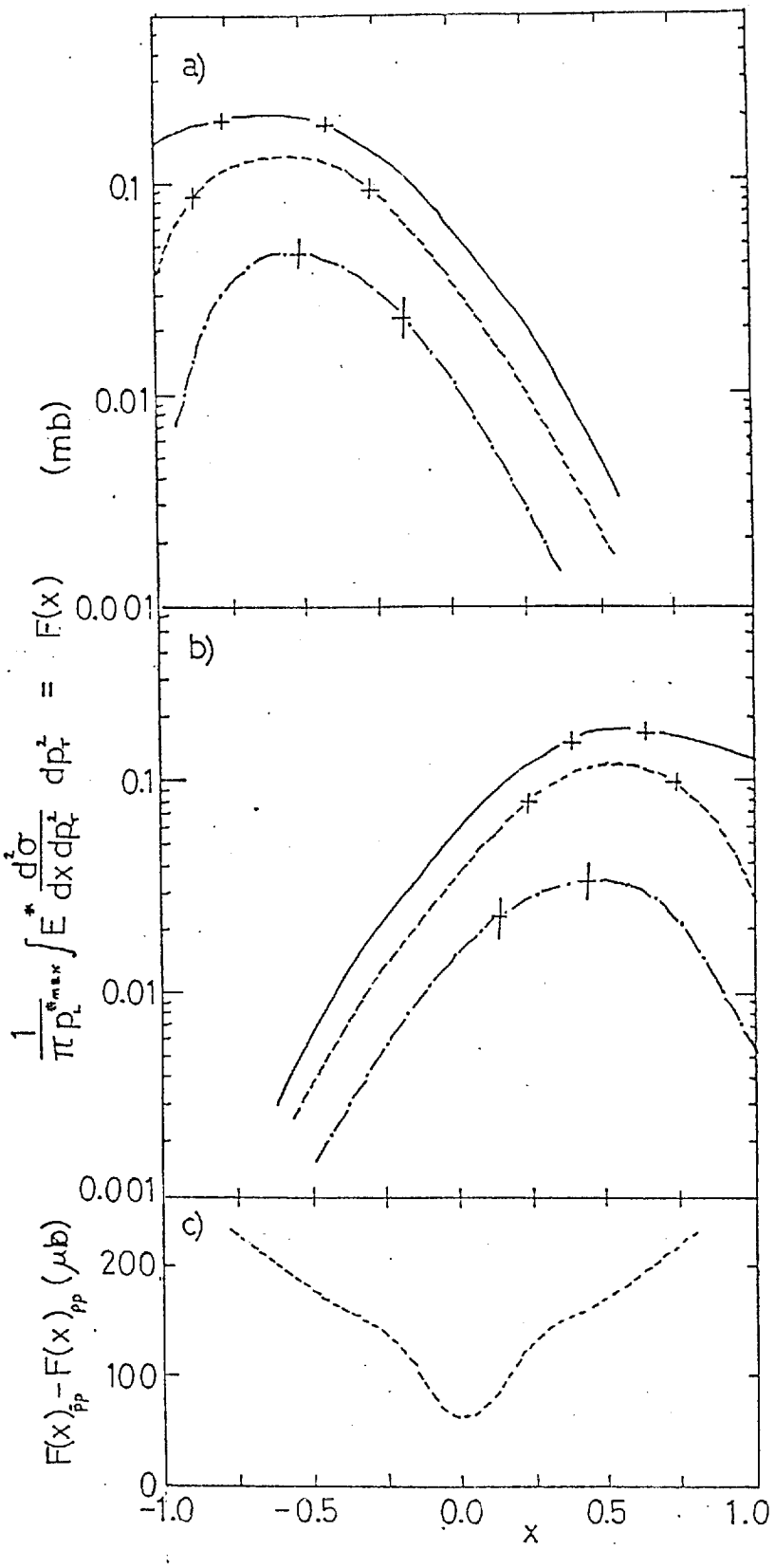


Figure 4.13 : Invariant cross section F(x) as a function of x, for a) $\bar{p}p \rightarrow \Lambda^0 X$, and b) $\bar{p}p \rightarrow \bar{\Lambda}^0 X$, for different p_T^2 intervals :

———— : $p_T^2 < 0.2$ (GeV/c)^2, ------- : $0.2 < p_T^2 < 0.6$

–·–·–·–·– : $p_T^2 > 0.6$ (GeV/c)^2

c) The difference $F(x)_{\bar{p}p} - F(x)_{pp}$. The high energy approximation for x ($p^*_{L_{max}} = \sqrt{s}/2$) was used for both the $\bar{p}$ and p data.

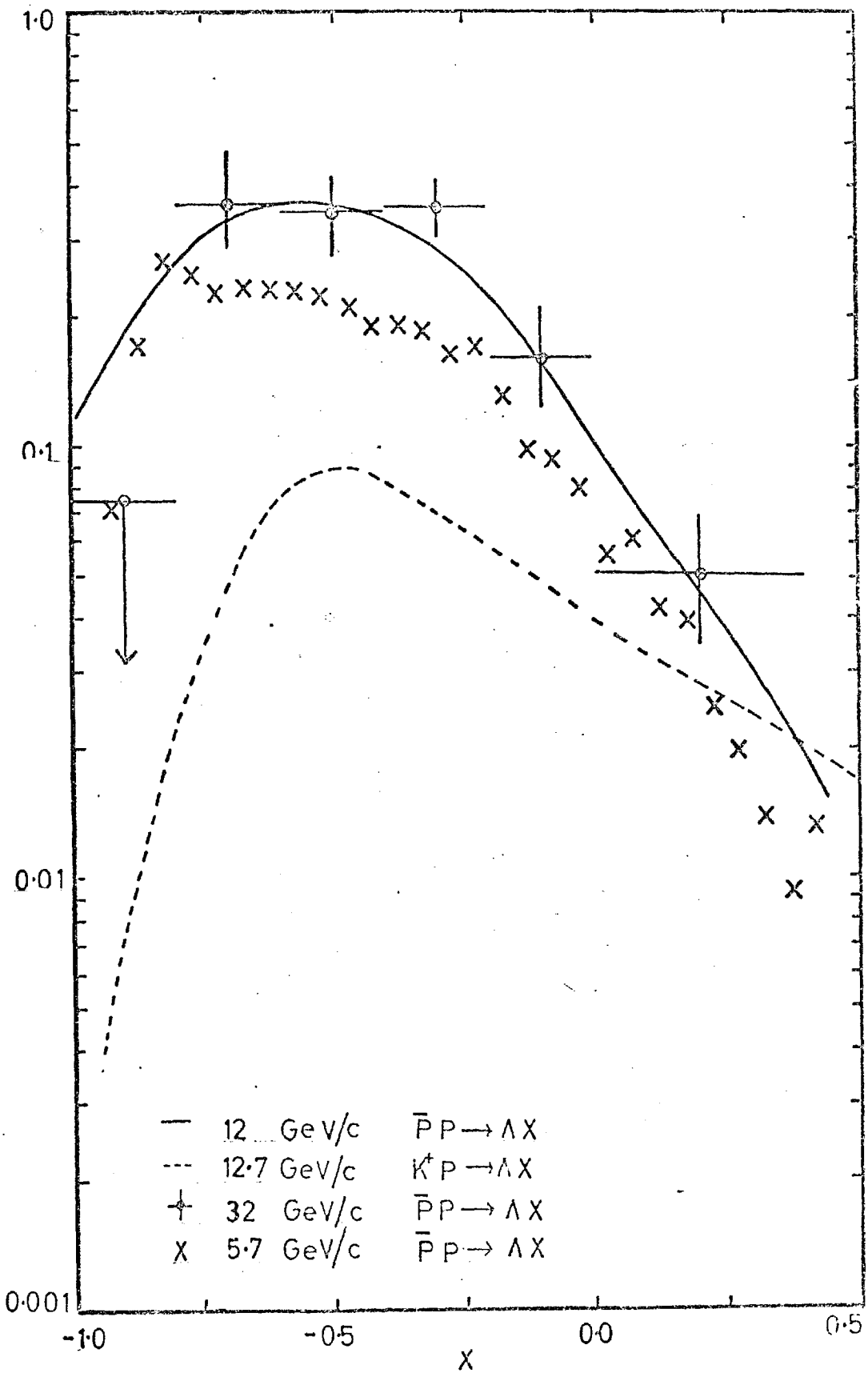


Figure 4.14 : Invariant cross section F(x) for $\bar{p}p \rightarrow \Lambda^0 X$ and $K^+p \rightarrow \Lambda^0 X$ at various momenta.

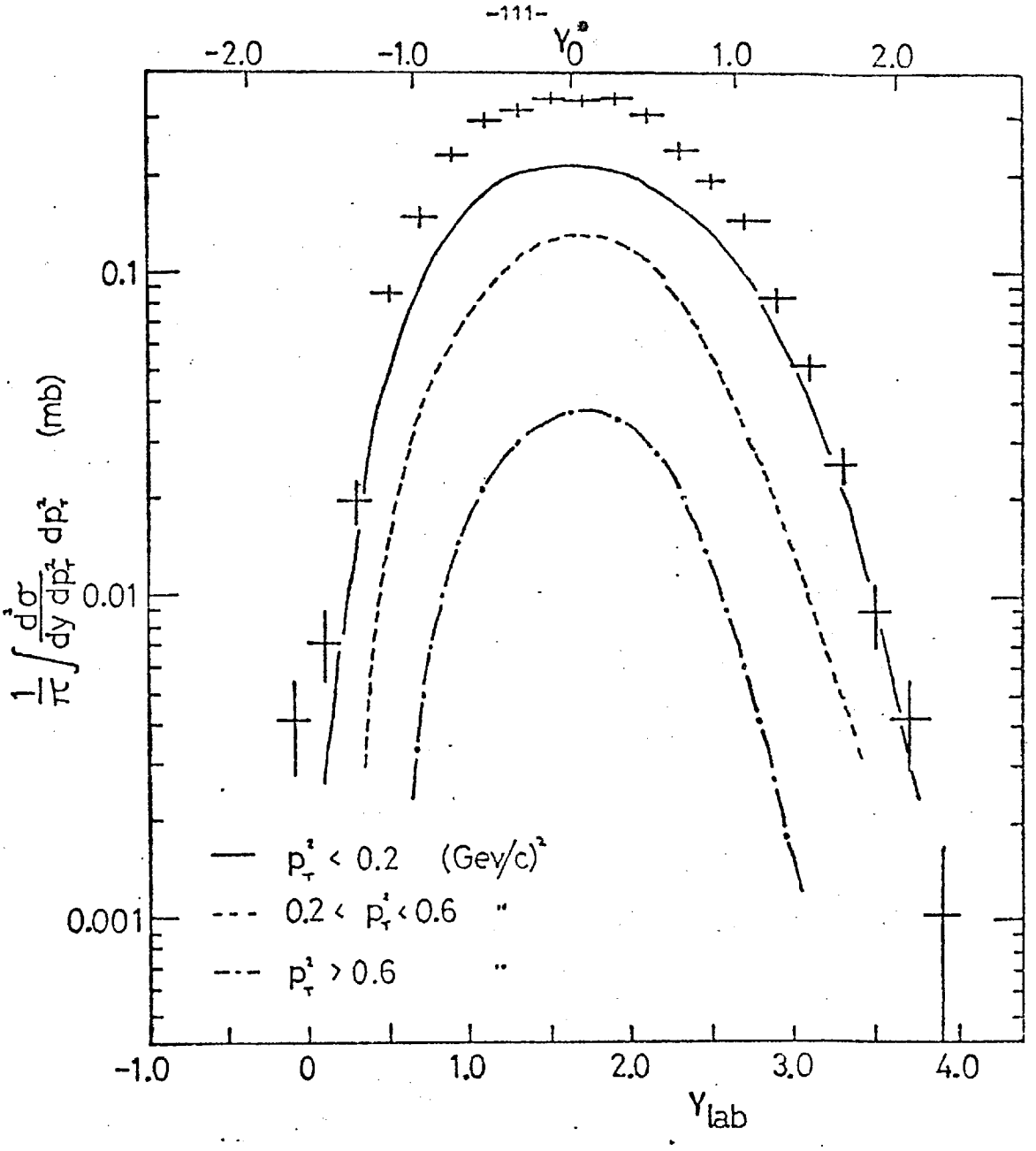


Figure 4.15 : Differential cross section $\frac{1}{\pi}\cdot\frac{d\sigma}{dy}$ as a function of the rapidity, y, for the reaction $\bar{p}p \rightarrow K_s^o X$. The curves represent the cross section in different p_T^2 regions. The lower and upper scales refer to the laboratory and centre of mass rapidity respectively.

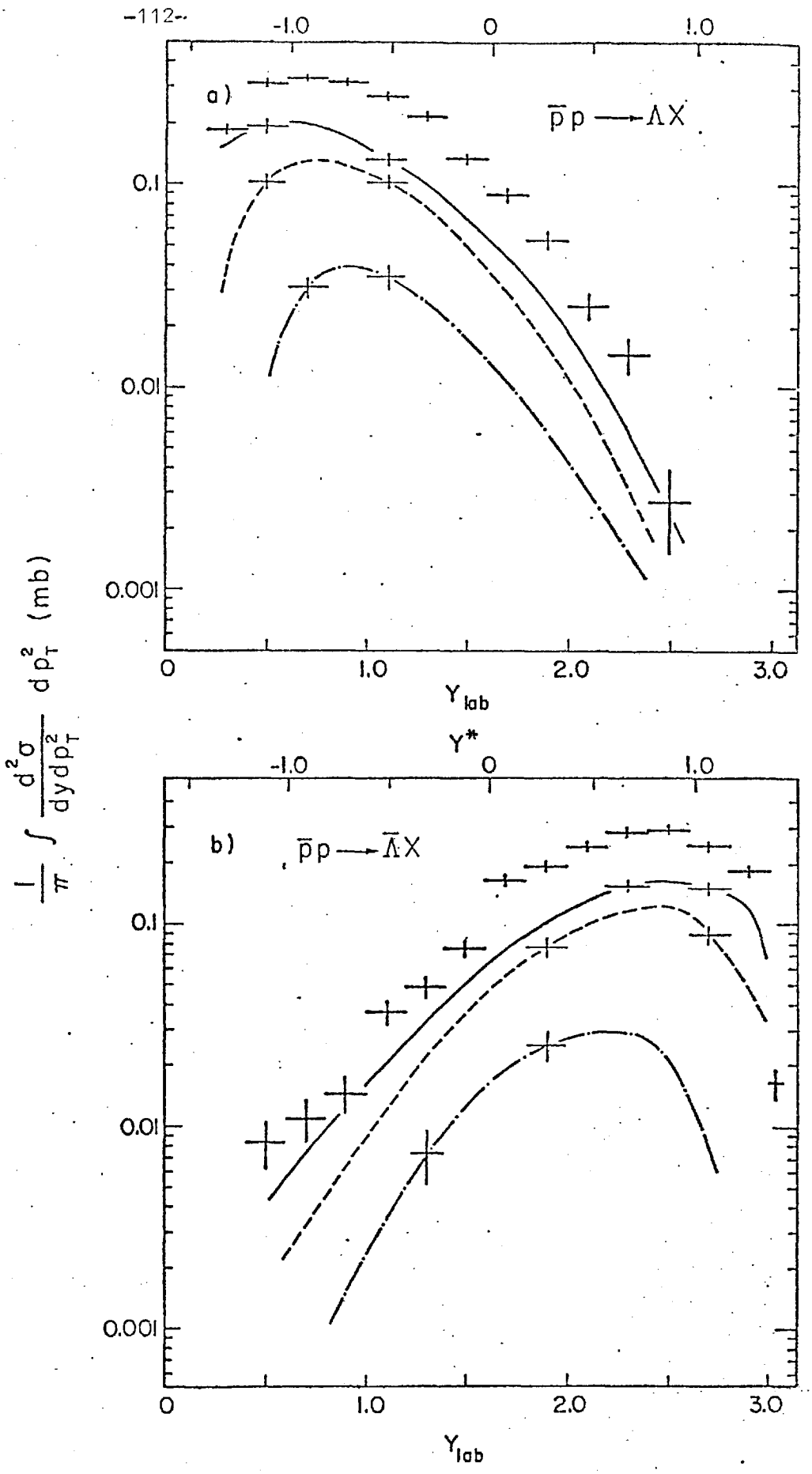


Figure 4.16 : Differential cross section $\frac{1}{\pi} \cdot \frac{d\sigma}{dy}$ as a function of y for:- a) $\bar{p}p \rightarrow \Lambda^0 X$, and b) $\bar{p}p \rightarrow \bar{\Lambda}^0 X$. The curves represent the cross section in the same p_T^2 regions as in Figure 15.

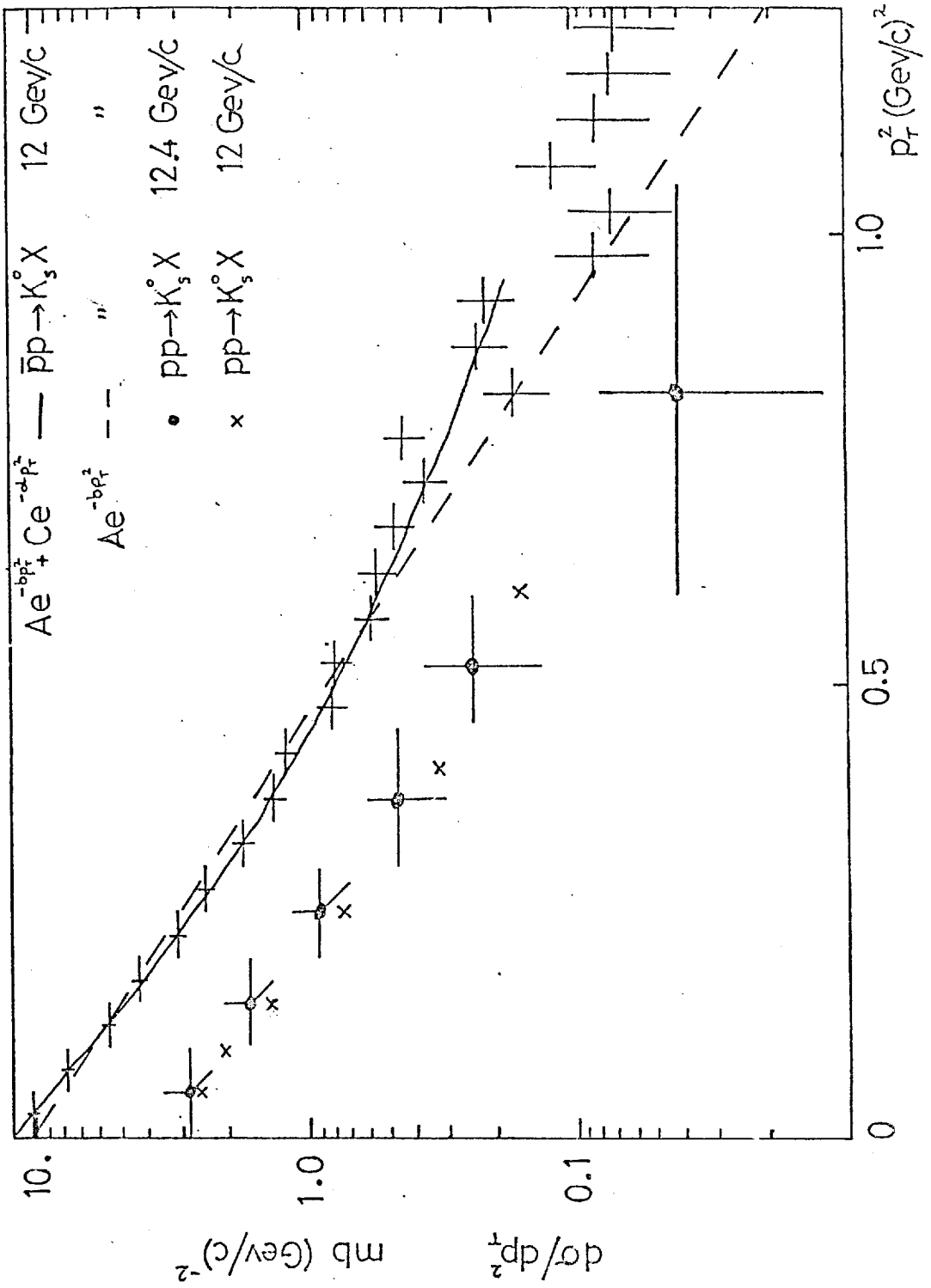


Figure 4.17 : Cross section as a function of p_T^2 for $\bar{p}p \to K_s^o X$. The dashed curve represents the result of the 2 parameter fit with $b = 5.05 \pm .11$ $(GeV/c)^{-2}$. The continuous curve represents the result of the 4 parameter fit described in the text, with $b = 7.32 \pm .25$ $(GeV/c)^{-2}$, and $d = 2.58 \pm .18$ $(GeV/c)^{-2}$. The other data points are for the 12 GeV/c pp data.

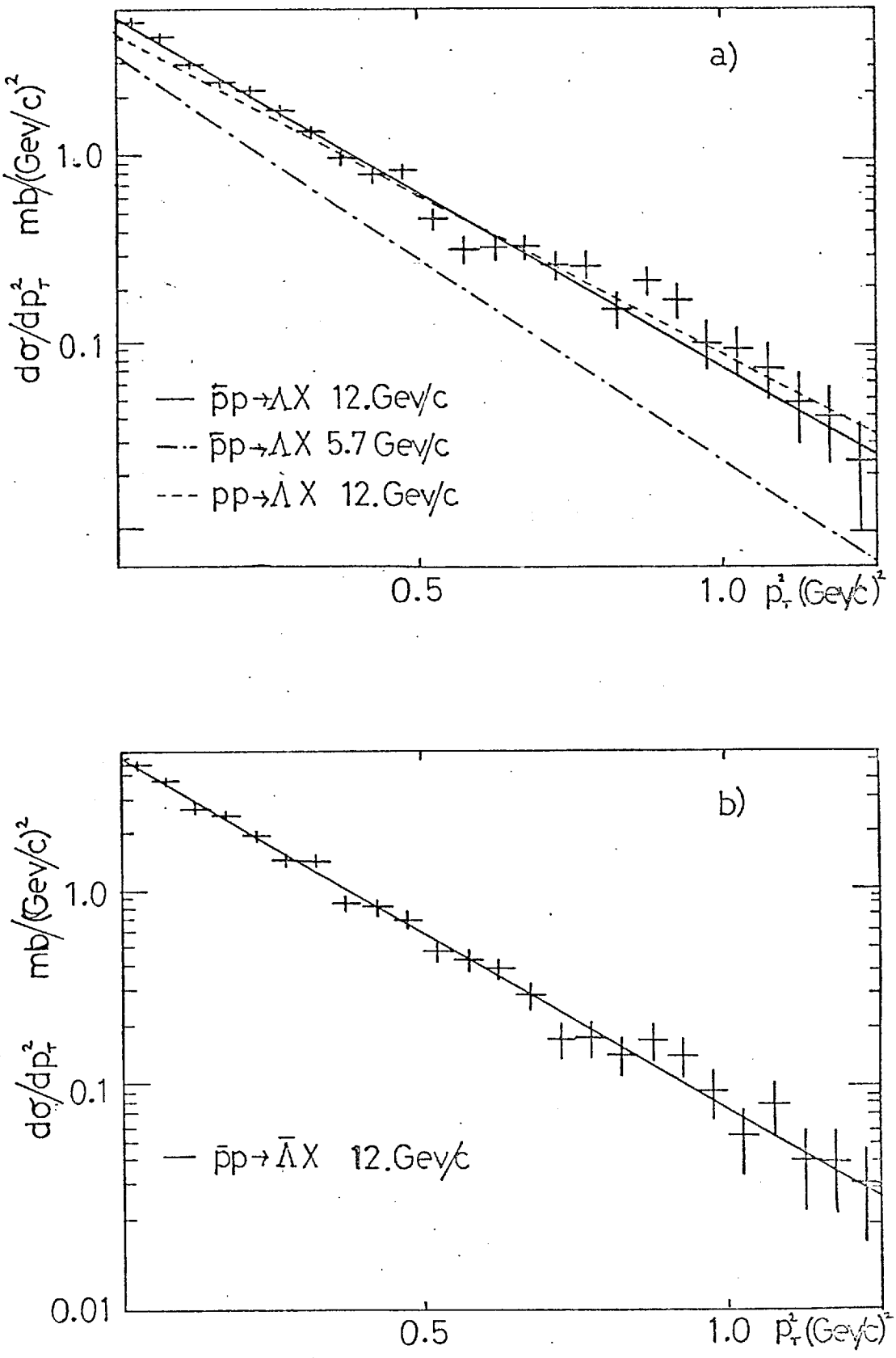


Figure 4.18 : Cross section as a function of p_T^2 for a) $\bar{p}p \rightarrow \Lambda^0 X$ and b) $\bar{p}p \rightarrow \bar{\Lambda}^0 X$. The solid curves represent the results of the fit described in the text. Also shown are the equivalent distributions for $pp \rightarrow \Lambda^0 X$ at 12 GeV/c [7] and $\bar{p}p \rightarrow \Lambda^0 X$ at 5.7 GeV/c [14].

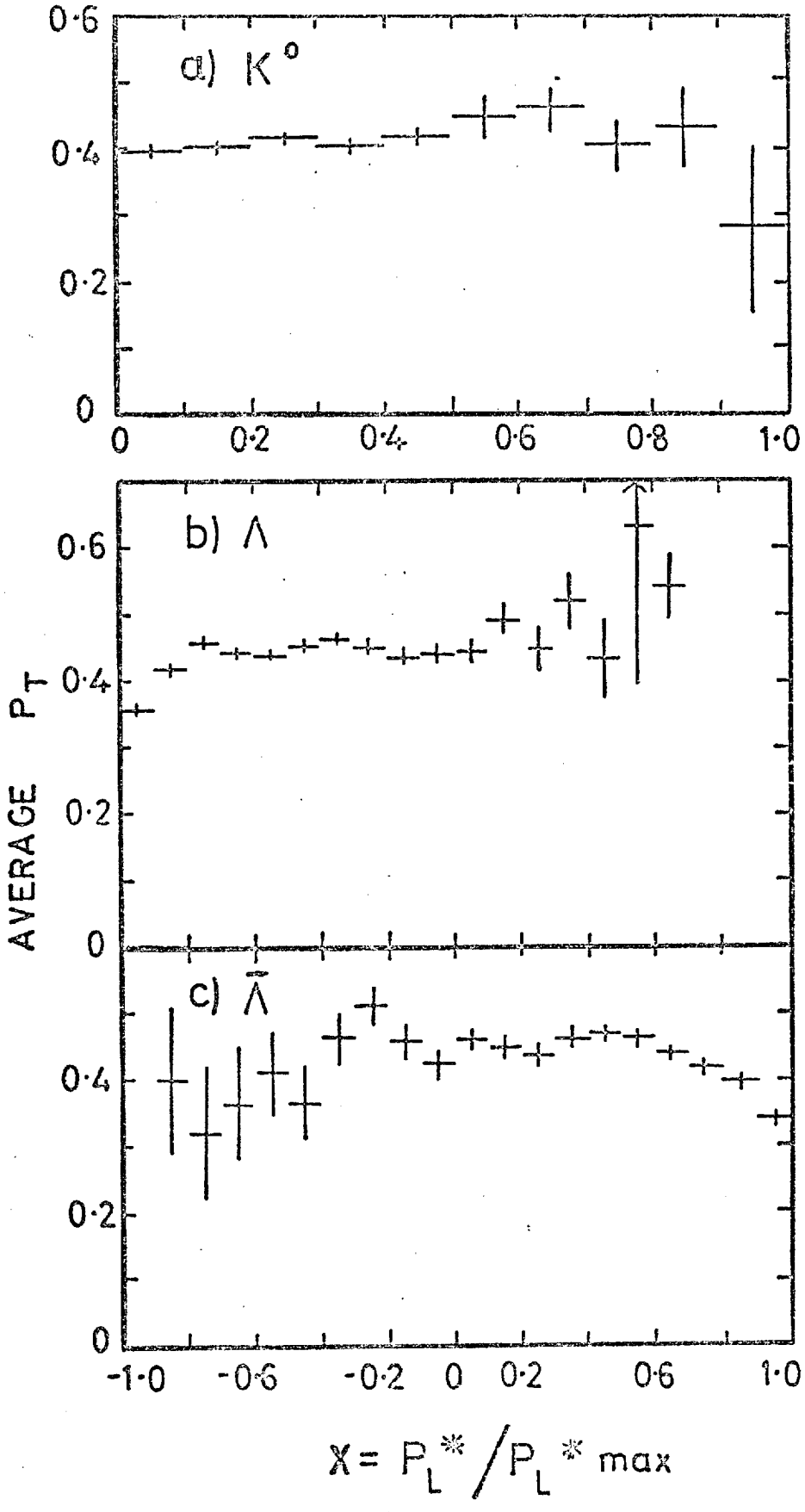


Figure 4.19 : Mean transverse momentum of V^0 as a function of x for : a) $\bar{p}n \rightarrow K_s^0 X$

b) $\bar{p}p \rightarrow \Lambda^0 X$

c) $\bar{p}n \rightarrow \bar{\Lambda}^0 X$.

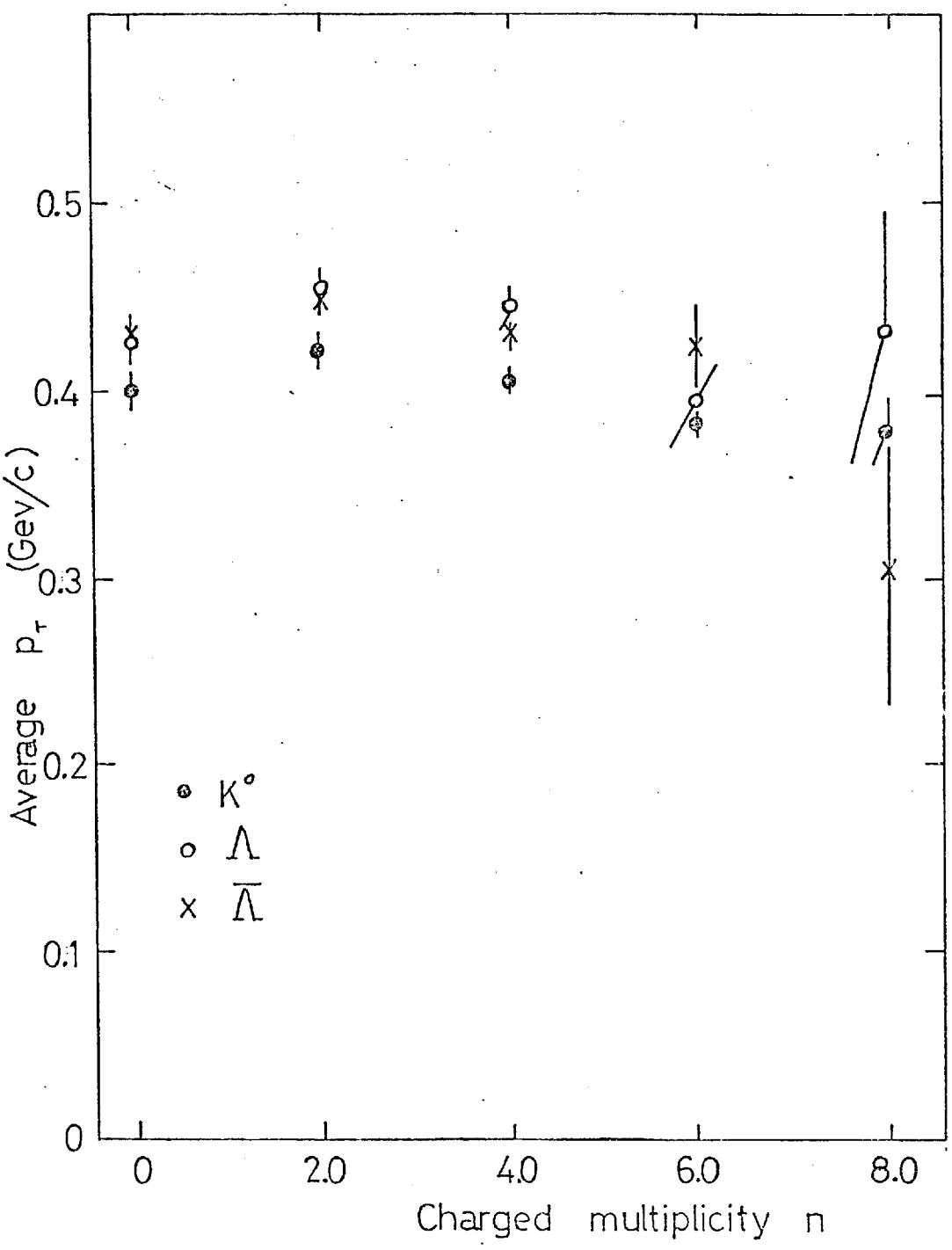


Figure 4.20 : Mean transverse momentum of the V^0 as a function of the associated charged multiplicity.

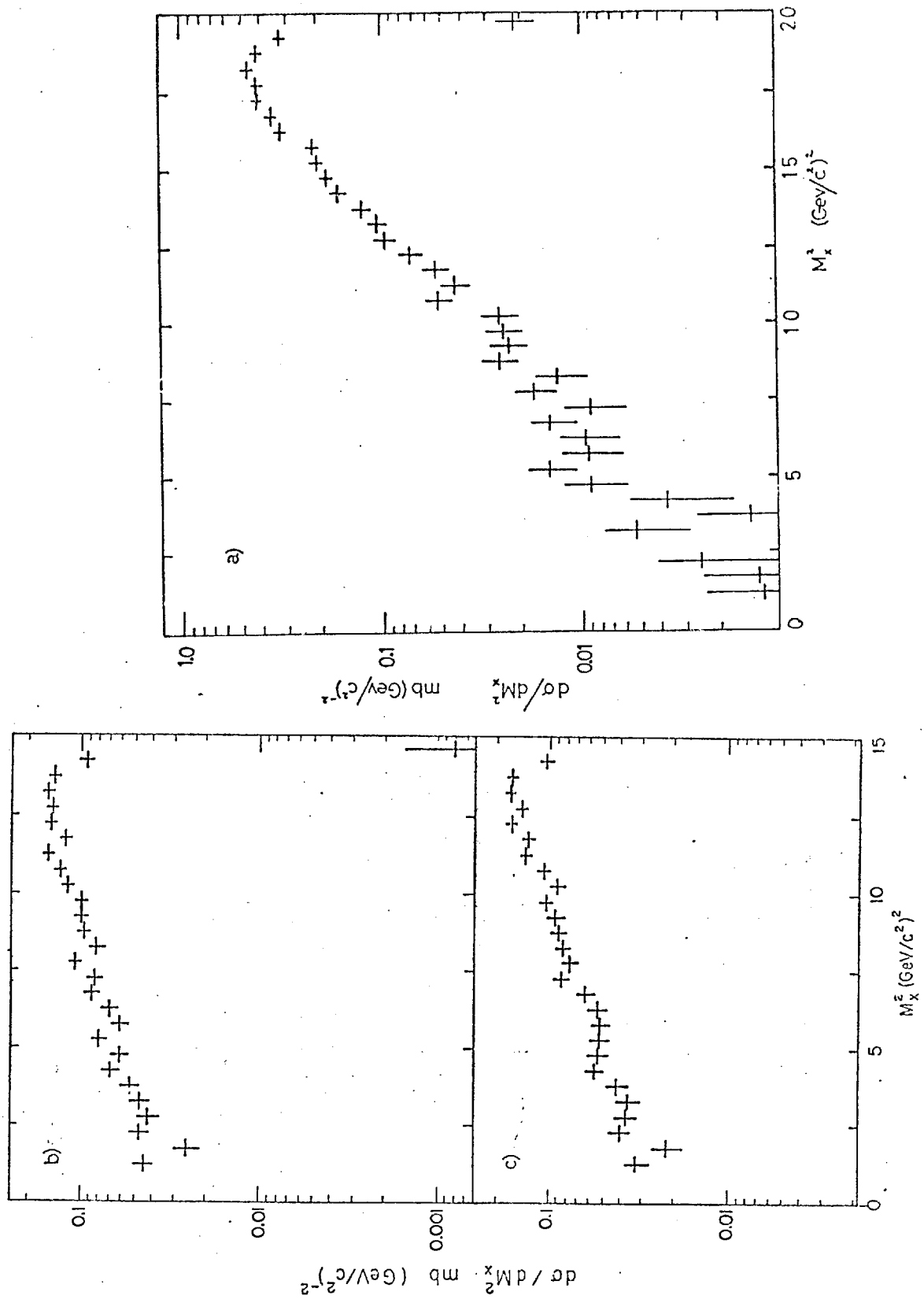


Figure 4.21 : Differential cross section as a function of M_x^2 , where M_x is the mass of the system recoiling against the V^0, for

a) $\bar{p}p \rightarrow K_s^0 X$

b) $\bar{p}n \rightarrow \Lambda^0 X$

c) $\bar{p}p \rightarrow \bar{\Lambda}^0 X$.

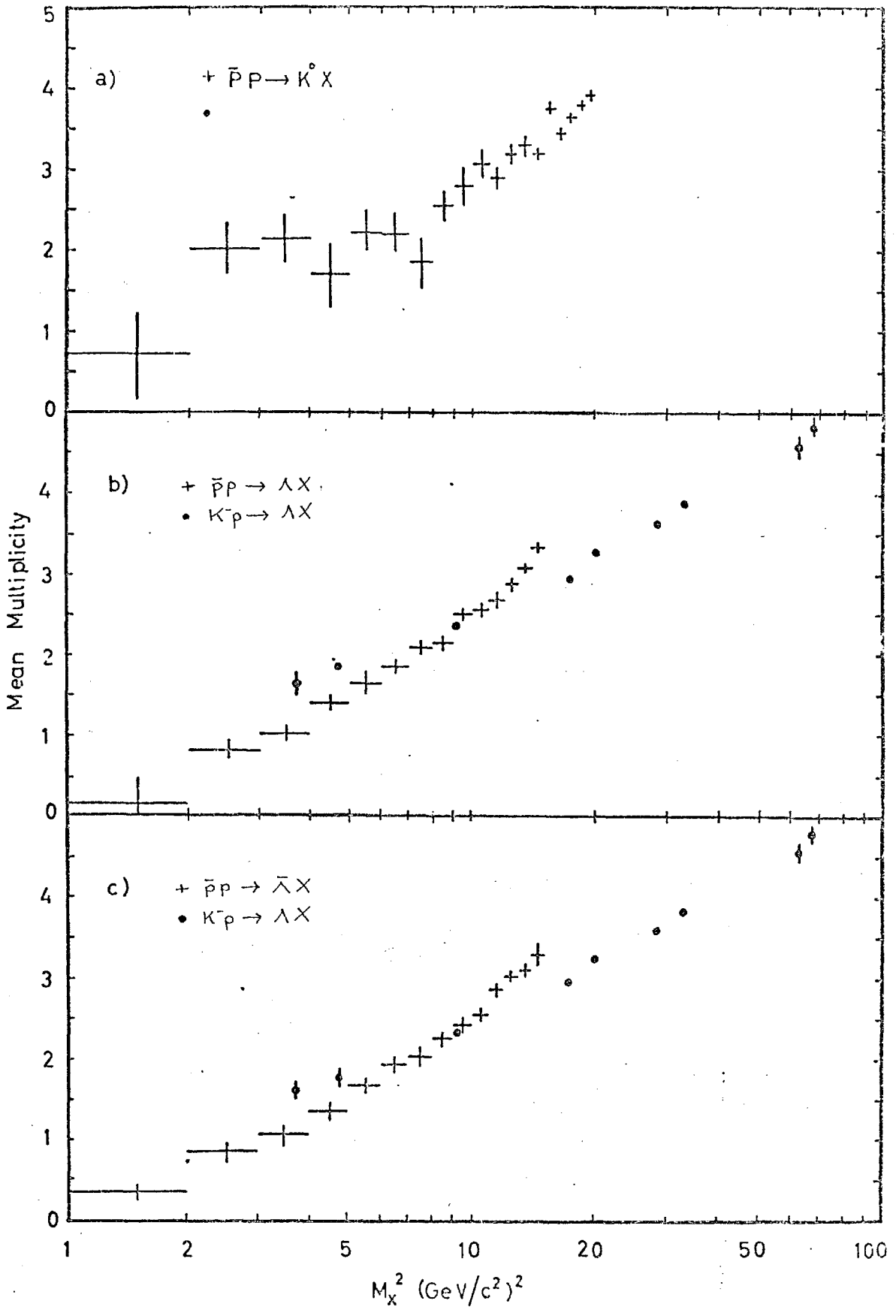


Figure 4.22 : Mean charged multiplicity as a function of M_X^2 , the mass squared recoiling against the V^o for a) $\bar{p}p \rightarrow K^oX$, b) $\bar{p}p \rightarrow \Lambda^oX$, c) $\bar{p}p \rightarrow \bar{\Lambda}^oX$. The mean charged multiplicity for $K^-p \rightarrow \Lambda^oX$ is shown in b) and c) as a function of s, the total centre of mass energy squared [22] .

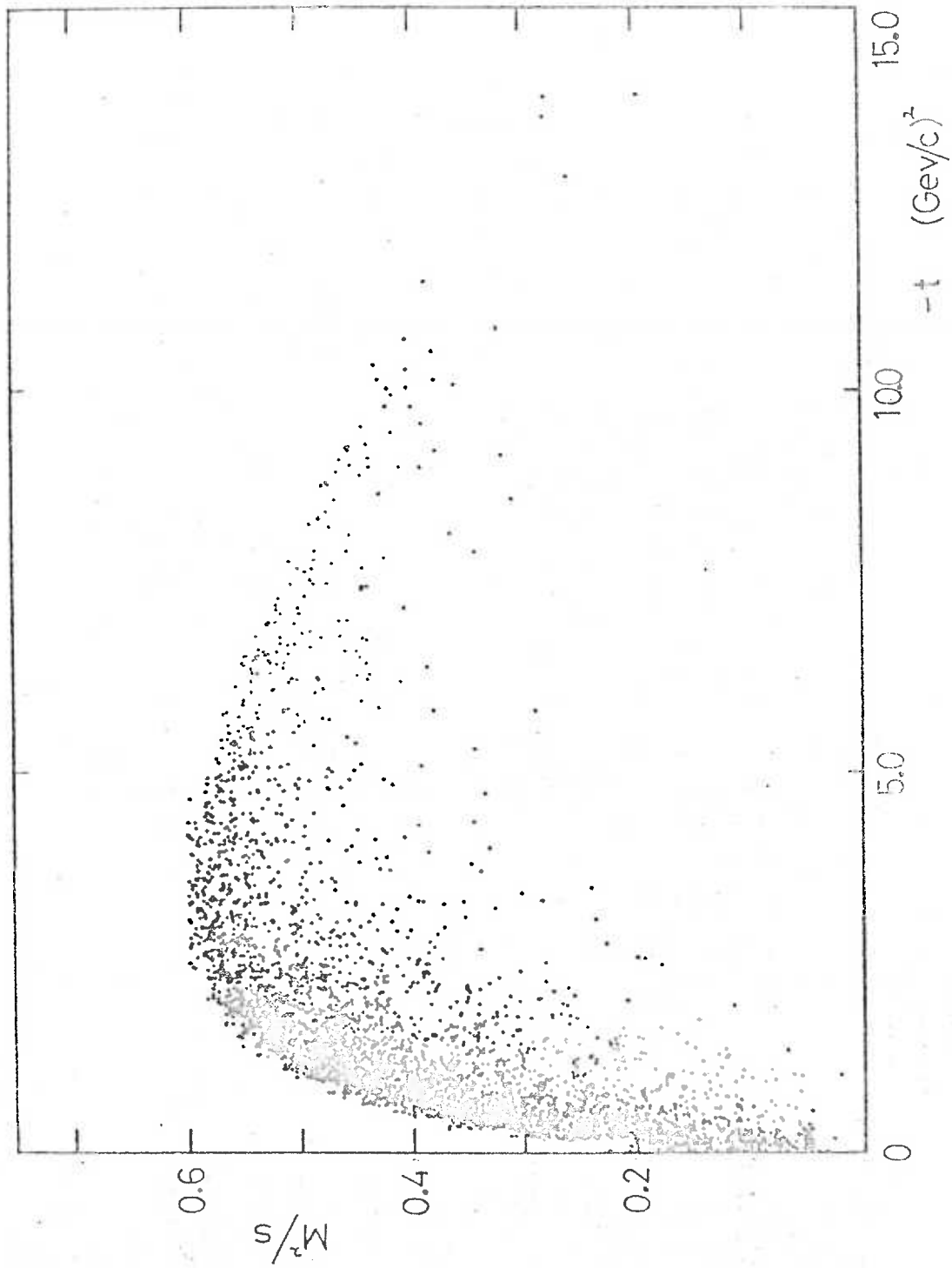


Figure 4.23 : Scatter plot of M^2/s (the recoil mass squared to the V^0 divided by the total centre of mass energy squared) against the four-momentum transfer, -t, for $\bar{p}p \rightarrow \Lambda^0 X$ at 12 GeV/c.

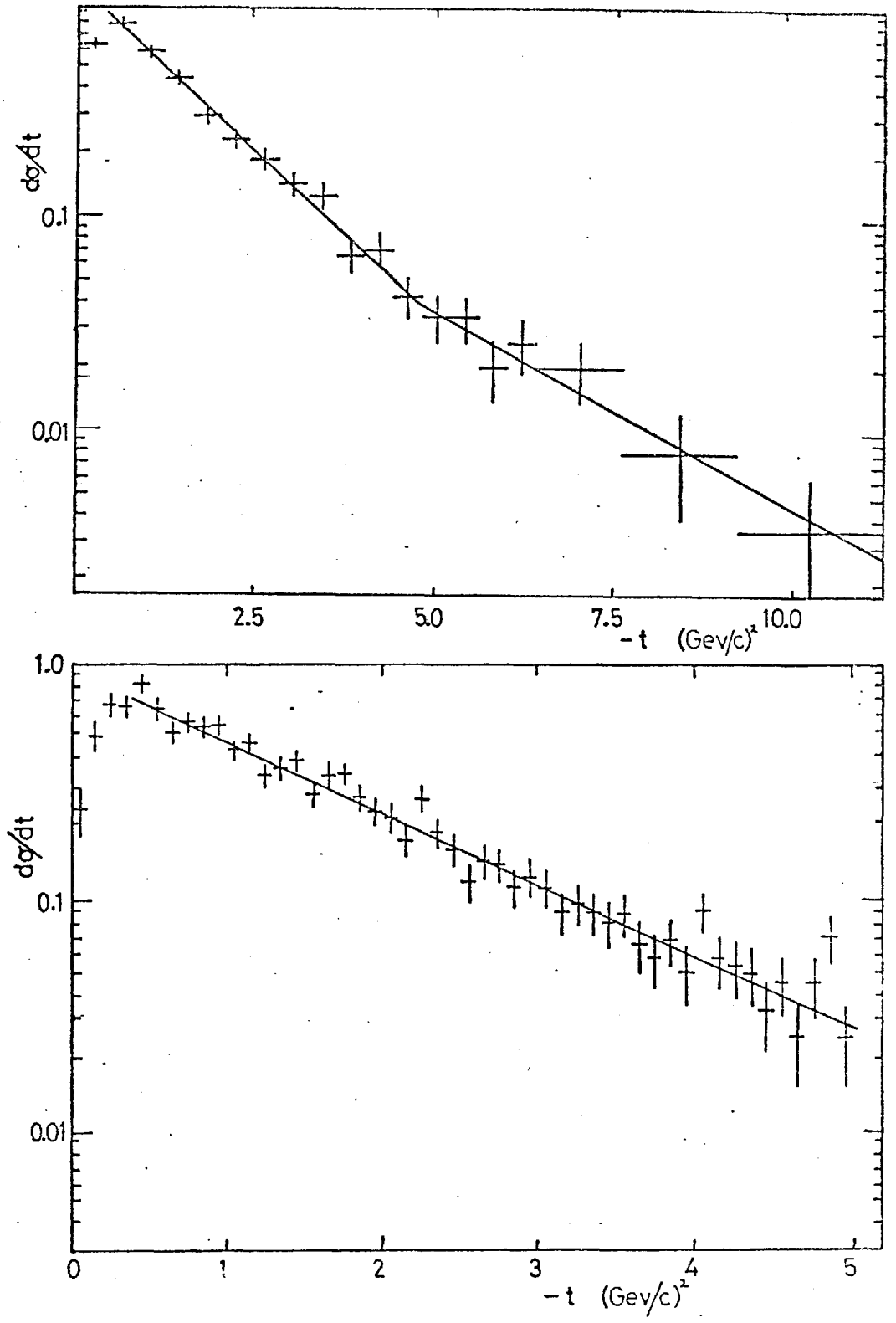


Figure 4.24 : Differential cross section $\frac{d\sigma}{dt}$ as a function of t, for $\bar{p}p \rightarrow \Lambda^{o}X$; The two plots show the effect of different binning in the region below $-t = 5\ (GeV/c)^2$. The fits are described in the text.

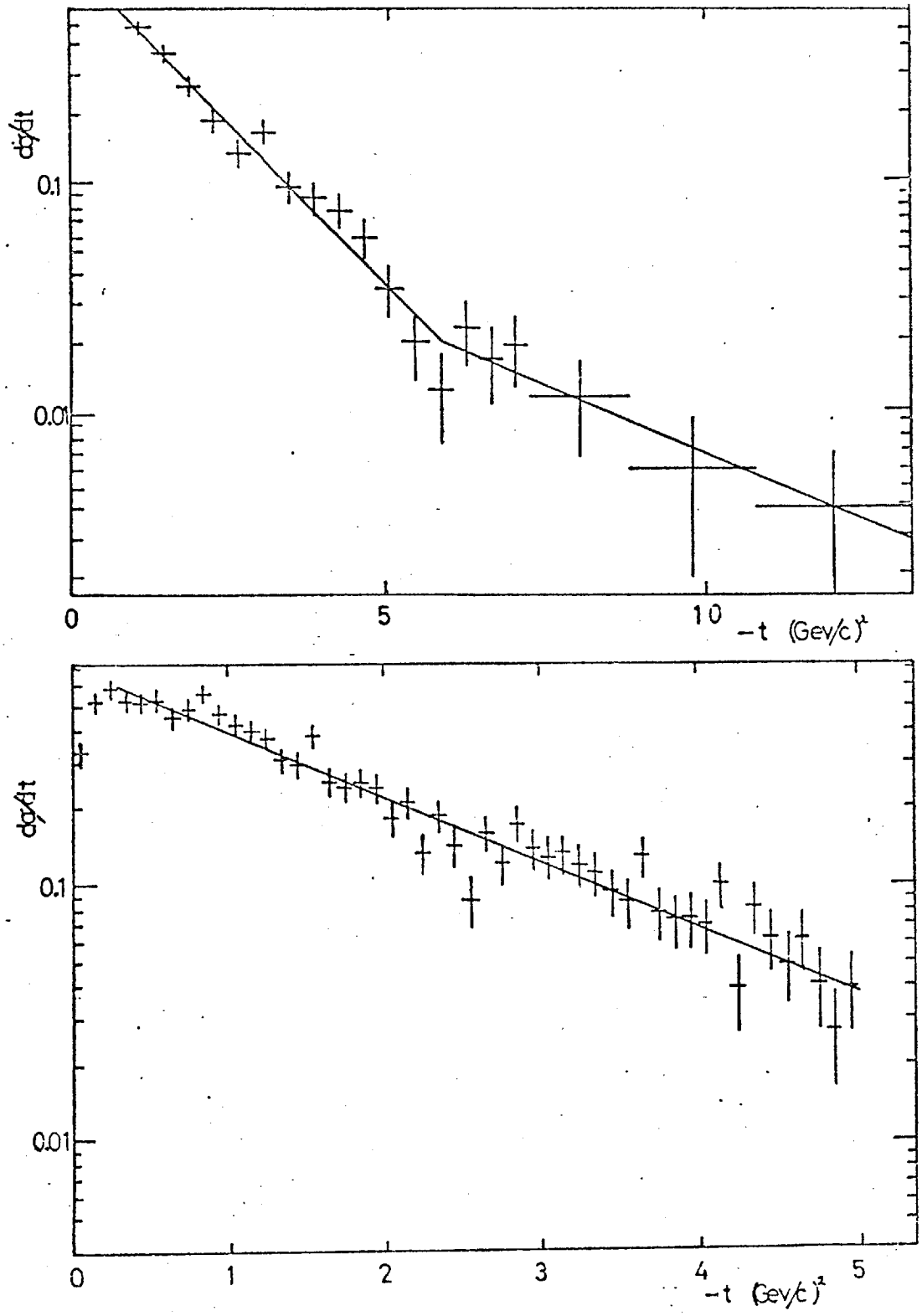


Figure 4.25 : Differential cross section $\frac{d\sigma}{dt}$ as a function of t for $\bar{p}p \rightarrow \bar{\Lambda}^{0}X$. The two plots show the effect of different binning in the region below $-t = 5\ (GeV/c)^2$. The fits are described in the text.

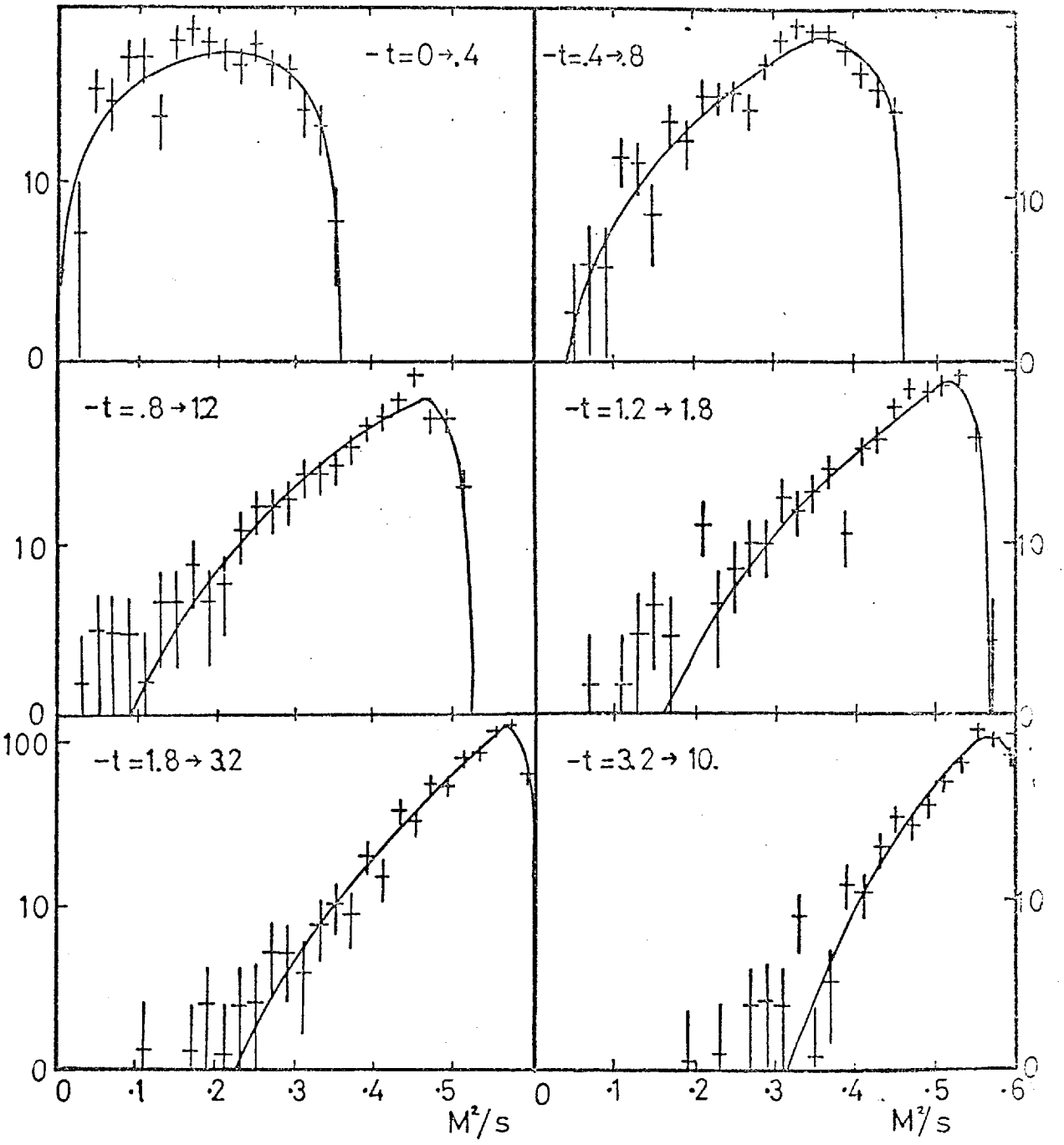


Figure 4.26 : M^2/s distributions for different t bins, for the process $\bar{p}p \rightarrow \Lambda^0 X$. The fits, using a Triple Regge formula, are described in the text.

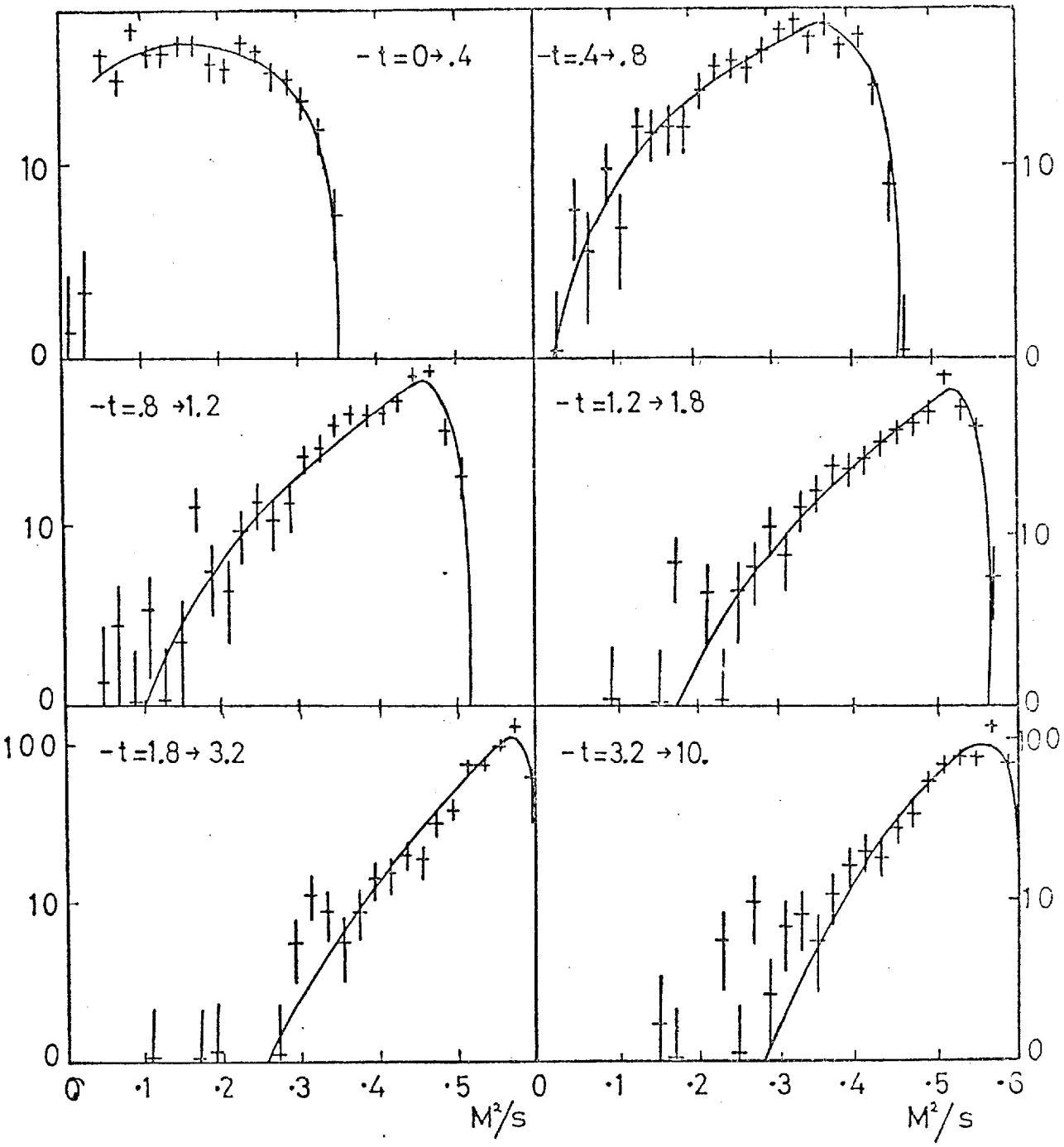


Figure 4.27 : M^2/s distributions for different t bins for the process $\bar{p}p \rightarrow \bar{\Lambda}^0 X$. The fits shown use a Triple Regge formula as described in the text.

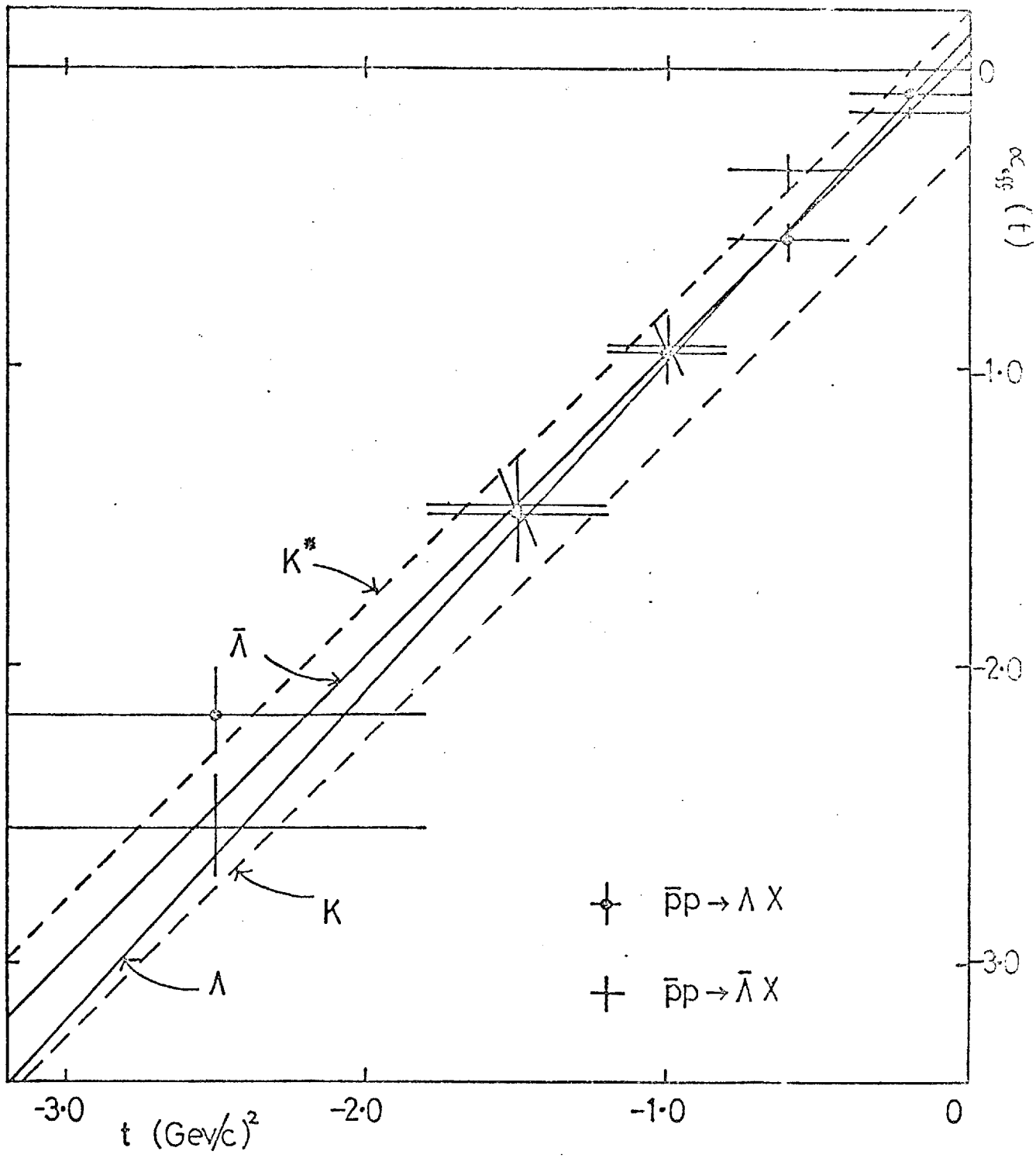


Figure 4.28 : Results of the fits of figures 26 and 27 for $\alpha(t)$, plotted as a function of t. Straight line fits to the Λ^0 and $\bar{\Lambda}^0$ data are shown. The dashed lines show the K and K^* - K^{**} trajectories.

A SEARCH FOR NARROW RESONANCES

5.1 Introduction

This chapter describes the methods used in the search for narrow peaks in effective mass distributions. Both the $K^{*}(890)$ and $Y^{*}(1385)$ resonances were observed and are discussed together with an effect seen in the $(K^{0}3\pi)^{\pm}$ combinations in six - prong events.

This experiment was originally proposed to look for high mass, narrow peaks in effective mass distributions and in this section some of the enhancements found in various experiments are mentioned, concentrating on those combinations which include a strange particle plus one or more pions. French [1] gives a summary of the progress made in meson physics over the years leading up to the discovery of the ψ. Apart from the well established meson resonances (ρ, ω^{0}, $K^{*}(890)$, $K^{*}(1420)$, etc..) many claims have been made for particles for which there is little or no supporting evidence from other experiments.

Several K^{*}- like resonances have been observed in the mass range 1.7 to 2.0 GeV/c^{2} in experiments with $K^{\pm}$ beams. They are summarised in Table I. A number of narrow enhancements have been found in anti-proton experiments (see Table II) ; however, very few of these have stood the test of time. Searches for charmed particles (in $K\pi$, $K\pi\pi$, ... effective mass distributions) or other high mass resonances (e.g. in $\bar{p}p$, $\bar{p}p\pi$, $K\bar{K}$, $K\bar{K}\pi$,...etc.) in 9 GeV/c $\bar{p}p$ annihilations [15] in the mass range 1 to 4 GeV/c^{2} failed to find any peaks greater than 3 standard deviations above background. A similar null result was obtained at 14.75 GeV/c [16] , where $\Lambda^{0}/\bar{\Lambda}^{0}n\pi$ (n=1,2,3) effective mass combinations were also studied.

5.2 Search for Narrow Resonances in 12 GeV/c $\bar{p}p$ Interactions

Effective mass combinations for all combinations of a single neutral strange particle with one or more charged pions were studied in detail, to look for evidence of the production of narrow resonances. Examples of some of these one-dimensional histograms are shown in Figures 1 and 2. Exotic combinations such as $K^0_s \pi^{\pm} \pi^{\pm}$ were also plotted. Charge symmetric pairs were plotted together for combinations including strange baryons, so that the $\Lambda^0 \pi^+$ and $\bar{\Lambda}^0 \pi^-$ histograms for example were added together. Different topologies (0, 2, 4 prong etc.) were plotted, both separately and together.

The recoil (missing) mass corresponding to each effective mass combination was calculated from the average beam parameters (section 3.8) and the momentum and energy of the combination :

$$M^2_{Recoil} = (\sqrt{s} - \Sigma E_i)^2 - (\Sigma p_i)^2 \quad ,$$

where i is the no. of particles in the effective mass combination.

Two-dimensional scatter plots (triangle plots) of the effective mass versus its recoil mass were also studied in a search for pair production of new resonances. Such a process would appear as an excess of entries in one or more bins. Since this kind of effect is difficult to spot on a line-printer scatter plot, and as there were several hundred such plots to be examined, various methods were developed to assist with this task. Graphical output was produced (see for example Figure 3), but even so, an excess of entries in one bin could not be detected easily as several entries on top of one another would appear with the same intensity as a single entry.

A three-dimensional plotting package, originally developed at the Rutherford Laboratory [17] , was adapted for use on the DEC PDP10 at Imperial College. "Lego" type building-block pictures of the two-

dimensional scatter plots, which could be viewed from any position in space (see Figure 4), were used to search for spikes (large signal to background ratio).

A third method which was developed took each selected bin on the scatter plot in turn and performed a polynomial fit to the neighbouring bins (background) and calculated the statistical significance of the "signal" bin. Any spike greater than 3 standard deviations above background could then be singled out for more detailed study.

A special cut was used to try to enhance any signals at high mass (≥ 1.5 GeV/c^2). High mass combinations of two or three particles can occur if one particle is part of the beam fragment and another is part of the target fragment. These particles will be travelling in opposite directions in the overall centre of mass system, and the combined mass will be high. If a true resonance exists, the decay products need not travel in the beam direction and the transverse momentum, p_T , of one of the decay products with respect to the beam direction may be large. Thus, if one selects only those combinations in which one of the component particles has a high p_T with respect to the beam, true resonances may appear above the reduced background. This method has been used successfully [7,18] to enhance high mass resonances like the g^o meson and the $\Delta(1950)$ baryon.

Two well known resonances, the $K^*(890)$ and $Y^*(1385)$ were observed and will be discussed in the next section. The most convincing peak found using the methods described above was at an effective mass of ~ 2.6 GeV/c^2. It was present in both charge combinations of $K^o\pi^+\pi^\pm\pi^-$ in six-prong events, and has been studied in great detail (section 5.5).

5.3 Production of $K^*(890)$ and $Y^*(1385)$

The $K^*(890)$ can be seen in the effective mass distribution of all

$K^0_s\pi^\pm$ combinations (Figure 5). The curve shown in figure 5 is the result of a least squares fit using the following parametrisation [19].

$$\frac{d\sigma}{dM} = a\,(M - (m_{K^0} + m_\pi))^{\alpha}\; e^{-\beta M}\,[1 + b.BW(m_{K^*}, \Gamma_{K^*})]$$

where M = the $K\pi$ invariant mass,

$$BW(m_{K^*}, \Gamma_{K^*}) = \frac{M\Gamma_{K^*}(M)}{(M^2 - m^2_{K^*})^2 + m^2_{K^*}\Gamma^2_{K^*}(M)}$$

and $$\Gamma_{K^*}(M) = \Gamma_{K^*}\left(\frac{q(M)}{q(m_{K^*})}\right)^3 \cdot \frac{m_{K^*}}{M}$$

with $q(M)$ = the momentum of the K^0_s in the $K\pi$ rest frame.

The six parameters to be fitted are a, b, α, β, m_{K^*}, and Γ_{K^*}, and the fit was performed over the range $0.64 < M < 1.2$ GeV/c^2, with the results :

$$m_{K^*} = 886.6 \pm 2.4 \text{ MeV/}c^2$$

$$\Gamma_{K^*} = 43.0 \pm 8.4 \text{ MeV/}c^2,$$

with $\chi^2 = 37$ for 22 degrees of freedom.

The $Y^*(1385)$ was observed in the effective mass distributions of $(\Lambda^0\pi^+ + cc)$ and $(\Lambda^0\pi^- + cc)$, which are shown in Figure 6. The fits shown (solid curves) are similar to those described above for the $K^*(890)$ but over the mass range $1.26 < M < 1.82$ GeV/c^2. The results of the fits for the masses and widths for each of the four combinations are shown in Table III.

5.4 Event Selection and Weighting Procedure

All 6-prong V^0 events were passed through a kinematics programme similar to GRIND [20] , which attempted multivertex fits to the V^0 and primary vertices according to a large number of hypotheses. Fits to hypotheses where all neutral particles are observed were attempted first,

If these failed, one neutral particle was included in the hypothesis and a fit was again tried. Finally, a missing mass fit was tried, where the number and type of missing neutral particles is not known. In general, fits to more than one hypothesis were obtained for each event, usually due to the difficulty of distinguishing between a fast charged K and a π of the same momentum. However, in order to make the maximum use of the information provided by the kinematics programme, which had been able to eliminate many hypotheses, a system of event weighting and selection based on the geometry and kinematics results for each individual track was devised.

Geometrical Mass Fit Probability, P_G^i

Secondary tracks with momentum less than ~1 GeV/c from the decay of V^os were studied, and a method of assigning probabilities to the different mass fits was determined. This method made use of the fact that the energy loss of a charged particle is mass dependent. The study of 6000 tracks from K^o, Λ^o, and $\bar{\Lambda}^o$ decays suggested that the following cuts should be made :-

a) Mass fit rejected if $\chi^2_{fit}/\chi^2_{best\ mass\ fit} > 2$

b) Track rejected if $\chi^2_{best\ mass\ fit} > 3 - 1.7p$, for $p < 1$ GeV/c

> 1.3 , for $p \geq 1$ GeV/c

The "sensitivity to mass dependence" for fits 1 and 2 was defined as :-

$$dM_{12} = \frac{\Delta p_1}{\varepsilon_1} - \frac{\Delta p_2}{\varepsilon_2}$$

where Δp_i = momentum loss of track with mass fit i

ε_i = error on momentum measurement at the primary vertex

The ratio of the χ^2 probabilities, $F_{12} = \chi^2_1/\chi^2_2$, was defined so that $F_{12} \leq 1$. Scatter plots of dM_{12} versus F_{12} were studied and a parametrisation was chosen which is detailed in Figure 7.

The ratio, R_{12}, of the probabilities P_G^1 and P_G^2 of the two mass fits was calculated for the π and K mass fits. If $R_{\pi K} \leq 1$, then $R_{\pi p}$ was also computed ; if not, then R_{Kp} was calculated. The probabilities were then normalised by the relation :

$$P_G^{\pi} + P_G^K + P_G^p = 1$$

The overall geometrical track probability, P_T, for any combination of tracks is than just the product of the probabilities for each mass fit.

$$P_T = \prod_{i=1}^{N} P_G^i \quad , \text{ where N is the number of tracks.}$$

Kinematic Fit Probability, P_K^j

This is given by the χ^2 probability, P_K, derived from the kinematic fit to hypothesis j.

Final Selection

The V^o was required to have a 3 constraint fit, with kinematic fit probability greater than 1%. For each hypothesis i, the overall track probability for tracks at the primary vertex was calculated and only those hypotheses that satisfied the relation $P_T^i > 0.3P_T^{max}$ were selected. Two further cuts were made for multivertex fits (not more than one missing neutral particle), namely

$$P_K^i > 0.1\ \%$$

and $$P_K^i.P_T^i > 0.25(P_K.P_T)^{max}$$

Each hypothesis, j, was then given a weight, W_j, and each time an effective mass combination was plotted it was weighted by this factor. For multineutral (MM) fits,

$$W_j = \frac{P_T^j}{\sum_{j=1}^{m} P_T^j} \quad , \text{ where m = the total number of selected hypotheses.}$$

For multivertex fits (4C and 1C),

$$W_j = \frac{p_T^j . p_K^j}{\sum_{i=1}^{n} p_T^i . p_K^i} \cdot \frac{\sum_{i=1}^{L} p_T^i}{\sum_{i=1}^{n} p_T^i}$$, where L = the total number of multivertex fits.

5.5 Study of the Peak Found in $K^o\pi^{\pm}\pi^+\pi^-$ Mass Distributions

A peak is seen in the effective mass combinations $K^o\pi^{\pm}\pi^+\pi^-$ from the following final states :-

$$\bar{p}p \rightarrow K^o \pi^+ \pi^+ \pi^+ \pi^- \pi^- \pi^- X \qquad (1)$$

$$\text{and} \quad \bar{p}p \rightarrow K^o K^{\pm} \pi^{\mp} \pi^+ \pi^+ \pi^- \pi^- X \qquad (2)$$

where X is zero, one, or more than one unobserved neutral particle. It appears at a mass of 2.60 ± 0.01 GeV/c^2 and the half width at half maximum is 9 MeV/c^2, which is compatible with the estimated experimental resolution (see Introduction), giving the peak a width $\Gamma \leq 18$ MeV/c^2. The effective mass error for the four particle combination, calculated by propagating the track parameter errors from the geometry programme, is shown in Figure 8. Figure 9 shows the unweighted effective mass distributions for $K^o\pi^{\pm}\pi^+\pi^-$ combinations. If all primary vertex tracks are assumed to be pions (reaction (1)), then there are 18 combinations of $K^o 3\pi$ per event. Reaction (2) reduces the average number of combinations to 17.6 . This number is further reduced to 16.8 by using the cuts described in section 5.4 to exclude low probability pions. These cuts have been used to select the combinations for Figure 9.

The product of the production cross section, σ, and the branching ratio, BR, into the observed final state has been estimated for the peak, giving the result $\sigma . BR \simeq 20\,\mu b$. This value was obtained from the six-prong cross section, with corrections for the number of combinations

per event and the neutral decay mode of the K^0_s. The peak appears in both positive and negative charge combinations.

The weighted effective mass distribution for $K^0\pi^{\pm}\pi^+\pi^-$ combinations is shown in Figure 10, where the statistical significance of the peak has increased. It should be noted, however, that the significance of any peak produced in a high multiplicity event when the number of combinations plotted per event is large, is reduced by a factor which depends on the probabilities of one event contributing 0, 1, 2, .. combinations to the signal bin. Calculation of the background underneath such a signal is complicated by the fact that the signal itself can give rise to a combinatorial background in neighbouring bins.

The weighted effective mass distribution for $K^0\pi^{\pm}\pi^+\pi^-$ combinations using the kinematically constrained track parameters, instead of the mass fit parameters from geometry plus the K^0 kinematic fit, is shown in Figure 11 (4C and 1C fits only). The significance of the peak here is considerably reduced. One explanation could be that if a long-lived particle were being produced (the width of the peak is less than the experimental resolution), then it might travel a significant distance in the bubble chamber (a few mm.) before it decays. The multivertex kinematic fit might then distort the track parameters, since all primary vertex tracks are constrained to come from the same point in space, and thus have the effect of broadening the 2.6 GeV/c^2 peak over several effective mass bins. Examination of such events under high magnification on the scanning table failed to find any support for this hypothesis.

Figures 12 to 14 show the weighted effective mass of the system of particles which recoil against a) the $K^0 3\pi$ combination, b) the $K^0 3\pi$ combination plus an extra π, c) the $K^0 3\pi$ combination plus two extra π's. b) and c) were plotted to look for reactions of the type $\bar{p}p \rightarrow I\bar{I}\pi$, and $\bar{p}p \rightarrow I\bar{I}\pi\pi$, where I is the supposed new 'particle'. The two-

dimensional scatter plot of effective mass versus recoil mass is shown in Figure 15. No definite system of particles has been observed to recoil against the I (defined by $2.59 \leq M_{eff}(K^0 3\pi) < 2.62$ GeV/c^2). For this last plot, two control regions are also shown, and these are defined by $2.44 \leq M_{eff}(K^0 3\pi) < 2.48$ GeV/c^2 and $2.74 \leq M_{eff}(K^0 3\pi) < 2.8$ GeV/c^2.

A search was made for evidence of substructure within the I by plotting the effective masses of the $K^0\pi^\pm$, $K^0\pi^\pm\pi^\mp$, $\pi^\pm\pi^\mp$, and $\pi^\pm\pi^+\pi^-$ systems selected from the final state of the I and from the control regions. Figures 16 and 17 show the $K^0\pi^\pm$ and $K^0\pi^\pm\pi^\mp$ mass plots respectively. No difference could be observed between the plots for the I region and the control regions, except perhaps in the case of $K^0\pi^\pm$, where there appear to be two enhancements around 1.5 and 1.7 GeV/c^2. The effective mass distribution for all events (Figure 18) gives weak indications for structure near these values, and there is also a peak in the $K^0\pi^\pm\pi^+\pi^-$ mass spectrum near 1.7 GeV/c^2. A check was made by selecting events with $M_{eff}(K^0\pi^\pm)$ near 1.5 and 1.7 GeV/c^2 and plotting the corresponding $K^0\pi^\pm\pi^+\pi^-$ mass (Figure 19), and the I peak is seen quite clearly.

No neutral state of the I was found in combinations $K^0\pi^+\pi^-\pi^0$ or $K^\pm\pi^\mp\pi^+\pi^-$, but this result is inconclusive since the mass resolution is likely to be reduced for the 1C fits containing a π^0, and there are very few combinations with a well identified $K^\pm$. 371 six-prong V^0 events were check scanned by a physicist to try to identify as many tracks as possible, so that some more kinematic hypotheses could be eliminated. Information such as kinks, indicating the decay of a $K^\pm$ or $\pi^\pm$, associated electron - positron pairs and neutral stars were recorded and scan cards were generated which contained this information for the 190 events so affected. When the analysis programme was run, the scan cards were read and the probability for a hypothesis which conflicted with the

information given on the scan card was reduced by a factor of two. This procedure, however, did little to alter the significance of the I peak with respect to the background.

Figure 20 shows the production angle distribution for all $K^{o}3\pi$ combinations, the I region, and two control regions ; there are no significant differences between the I and its control regions.

Another production characteristic of the I peak which could be linked with the reduced significance of the peak when kinematically fitted track parameters are used is the enhancement of the peak when events with large K^{o} impact parameter are selected. The impact parameter was defined as the distance between the primary vertex and the K^{o} flight path, as calculated from the geometrical track quantities.

A cut of 0.05 cm. in the impact parameter led to the distributions of Figure 21, which show that the I appears to be produced in large impact parameter events. This could again be due to a long-lived particle which travels some distance in the bubble chamber before it decays.

An attempt was made to study the decay of the I by assuming that the appearance of the 1.5 and 1.7 GeV/c^{2} peaks in the $K^{o}\pi^{\pm}$ subsystem indicated a three body decay process of the form :-

$$I \longrightarrow (K^{o}\pi^{\pm})_{\substack{1.5 \\ \text{or } 1.7}} \pi^{+}\pi^{-}$$

Various decay angles were studied, but the statistics were so limited that no conclusions could be drawn.

Searches have been made to try to find any evidence for the I peak in other channels. The information given by the kinematics programme was used with the eight-prong events, but here the combinatorial background is considerably worse, and no peaks were observed.

5.6 A Search for Supporting Evidence

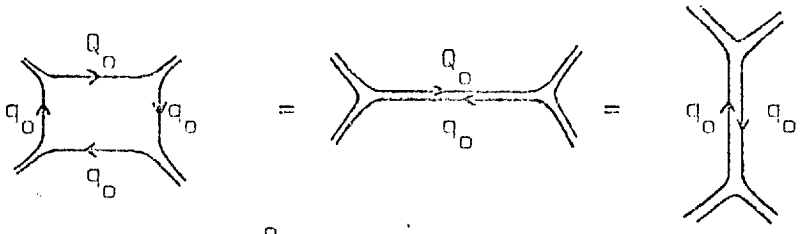
Arguments were presented by Rosner [21] as long ago as 1968 in favour of enhancements with zero baryon number, which would decay mainly to a baryon B, and an antibaryon $\bar{B}$. He suggested that such resonances might be produced in high multiplicity events, and that $\bar{B}B$ enhancements with more unusual quantum numbers may be of interest. For example, resonances with S = -1 and Q = -2 may appear in the $\bar{p}\Lambda^0\pi^-$ spectrum. Experimental evidence for $\bar{B}B$ enhancements in $\bar{p}p$ formation experiments has been available for some time. Three enhancements have been observed in the $\bar{p}p$ total cross section ; the S, T, and U [22 -26] . The S, at a mass of 1.936 GeV/c^2, is narrow (around 6 MeV/c^2) but the T, at a mass of 2.190 GeV/c^2 and the U, at 2.350 GeV/c^2 are much wider (90 ± 20 MeV/c^2 and 160 ± 20 MeV/c^2 respectively). Searches have also been made in production experiments and several non-strange enhancements with narrow widths (of the order of the experimental resolution) have been reported [27 -29] in the mass region 2 to 3 GeV/c^2.

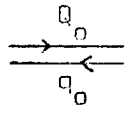
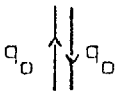
These discoveries prompted the theorists to develop their ideas on multiquark final states and "baryonium" states — states whose coupling to $\bar{B}B$ channels is substantially larger than to channels made up entirely from "normal" mesons like π, K, ρ, K^* etc. [30,31]. In terms of planar dual diagrams, ordinary mesons and baryons may be represented by the boundaries q_i and Q_j , where q_i is an ordinary quark and Q_j is a diquark system which carries baryon number. Thus a π meson may be represented by $\overset{q_o}{\underset{q_o}{\rightleftarrows}}$, a kaon by $\overset{q_3}{\underset{q_o}{\rightleftarrows}}$, and a nucleon by $\overset{Q_o}{\underset{q_o}{\rightleftarrows}}$.

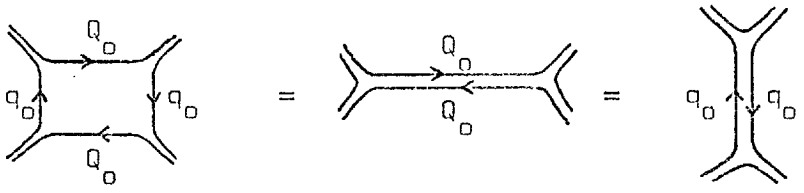
States of baryonium would be represented by diagrams like $\overset{Q_o}{\underset{Q_o}{\rightleftarrows}}$.

The necessity for baryonium states becomes clear when one considers two

body scattering diagrams. πN scattering corresponds to :-



where the resonances  and  may be described as "dual" to one another. For $\bar{B}B$ elastic scattering one has :-



showing the need for baryonium states dual to ordinary mesons.

Chan and Högaasen developed a model for baryonium [32] and predicted masses and decays for a whole new spectroscopy of hadrons.

The six-prong final states in this experiment which include a Λ^0 or $\bar{\Lambda}^0$ were studied to look for evidence of these predicted baryonium states in the channels $\bar{N}\Lambda^0 m\pi$ and $N\bar{\Lambda}^0 m\pi$ $(m=0,1,2)$. There were very few events of this type with a seen $\Lambda^0/\bar{\Lambda}^0$, so 4C and 1C fits with missing $\Lambda^0/\bar{\Lambda}^0$ or $n/\bar{n}$ were included in the analysis. Using the same set of events available at the time of publication [33] of the effect described in section 5.5, and plotting all charged and neutral combinations together ($p\bar{\Lambda}^0 + p\bar{\Lambda}^0\pi + p\bar{\Lambda}^0\pi\pi + cc$, $n\bar{\Lambda}^0 + n\bar{\Lambda}^0\pi + n\bar{\Lambda}^0\pi\pi + cc$), a peak can be seen in the same bin as the I (2.59 to 2.62 GeV/c^2) in Figure 22. However, using the full statistics of the experiment, this intriguing peak disappeared, as shown in Figure 23. The four-prong events were also studied but no significant structure was found.

References

1. B. French Report to Palermo Conf. CERN/DPhII/Phys 75-38
2. A. Firestone et al. Physics letters 38B,(1971),513
3. D. Carmony et al. Phys. Rev. Lett. 27,(1971),1160
4. M. Aguilar-Benitez et al. Phys. Rev. Lett. 30,(1973),672
5. G. W. Brandenberg et al. Paper submitted to International Conf. on High Energy Physics, London, 1974
6. B. Drevillon et al. Ecole Polytechnique - Saclay - RHEL collaboration. Paper submitted to Palermo Conf. 1975
7. M.Deutschmann et al. ABBCCHLVW collaboration preprint, Sept. 1975
8. R. Böck et al. Physics Letters 12,(1964),65
9. T.P. Wangler et al. Physics Letters 9,(1964),71
10. R. Armenteros et al. Physics Letters 9,(1964),207
11. R. Böck et al. Physics Letters 17,(1965),166
12. C.G. Wohl et al. Am. Phys. Soc. Series II 10,(1965),529
13. J. Böhm et al. CERN/DPhII/Phys 75-13
14. B. French et al. CERN/DPhII/Phys 75-22
15. R. Carlssen et al. Nucl. Phys. B99,(1975),451
16. J. Canter et al. Preprint TUFTS 76-1604 (1976)
17. B. Franek , J. Barlow Rutherford Lab. Programme Library and private communication
18. V. Hagopian et al. Phys. Rev. Lett. 36,(1976),296
19. P. Granet et al. Paper submitted to European Conf. on Particle Physics, Budapest, 1977
20. Programme GRIND
21. J.L. Rosner Phys. Rev. Lett. 21,(1968),950
22. A.S. Carroll et al. Phys. Rev. Lett. 32,(1974),247
23. V. Chaloupka et al. Physica Letters 61B,(1976),487
24. W. Brückner et al. Physics Letters 67B,(1977),222

25. R.J. Abrams et al. Phys. Rev. D1,(1970),1917

26. L. Montanet Paper submitted to Vth Conf. on Experimental Meson Spectroscopy, Boston 1977 ; CERN/EP/Phys 77-22

27. H. Braun et al. Physics Letters 60B,(1976),481

28. C. Evangelista et al. CERN/EP/Phys 77-24

29. P. Benkheiri et al. Physics Letters 68B,(1977),483

30. G.F. Chew Proc. of 3rd European Symposium on $\bar{N}N$ interactions Stockholm, 1976

31. C. Rosenzweig Phys. Rev. Lett. 36,(1976),697

32. Chan Hong-Mo, H. Högaasen RL 77-121/A and RL 77-144/A

33. A. Apostolakis et al. Physics Letters 66B,(1977),185

34. J. Canter et al. TUFTS preprint, Sept. 1977

35. G.W. Van Apeldorn et al. Physics Letters 72B,(1978),487

TABLE I

Beam Particle	Momentum GeV/c	Final State	Effective mass combination	Mass MeV/c^2	Width MeV/c^2	Ref.
K^+	12	$K^+\pi^-p$	$K\pi$	1850	300	[2]
K^+	9	$K^+\pi^-p$ $K^0\pi^+\pi^-p$	$K\pi$ $K\pi\pi$	1759±10	60±20	[3]
		Also decays to $K^*\pi$, $K\rho$				
K^- K^+	13 13	$K^-\pi^+n$ $K^+\pi^-\Delta^{++}$	$K\pi$	1800	200	[5]
K^-	7.3	$K^-\pi^+n$	$K\pi$	1760	80	[4]
K^-	14.3	$\bar{K}^0\pi^-p$ $K^-\pi^+n$	$K\pi$	1800		[6]
K^-	10, 16	$K^-\pi^+n$	$K\pi$	1700 - 2000,300		[7]

Production of high mass K^* (1700 - 2000 MeV/c^2) in $K^\pm p$ interactions

TABLE II

Momentum GeV/c	Final State	Effective mass combination	Mass MeV/c^2	Width MeV/c^2	Ref.
3	$K_1^0 K^{\pm}\pi^{+}\pi^{\mp}\pi^{-}\pi^{0}$	$K\pi\pi$	1270±20	60±30	[8] Supporting evidence from [9, 10]
5.7	$\bar{\Lambda}^0 Y^*$	$(KN)^0$, $(KN\pi)^0$	2097	< 38	[11],
		$KN\pi$	1940	35	also [12]
		$(KN\pi)^0$	2300	43	
5.7	$K_1^0 K^0_{\text{unseen}}\pi^{+}\pi^{+}\pi^{-}\pi^{-}$	$K\pi$	1200		[13]
3.6, and 5.7	$K^0K4\pi$, $K^0K5\pi$	$(K4\pi)^{\pm 0}$	2330	All	[14]
		$(K4\pi)^{\pm 0}$	2390	< 20	
		$(K2\pi)^{\pm}$	1460		
		$K^0 3\pi$, $(K^0 2\pi)^0$	1570		
		$K^0K^{\pm}\pi^{\mp}\pi^{\mp}\pi^{0}$	2530		
		$\bar{K}^0K^{\pm}\pi^{-}\pi^{\mp}$	2630		
		$K^0 2\pi$	1270		
		$K^0K^0\pi^{+}\pi^{-}$, $K^0K^{\pm}\pi^{\mp}$	2240	non-strange	
		$(K4\pi)^{\pm 0}$	2950		

TABLE III

Fitted resonance parameters for the $Y^{*\pm}(1385)$ and $\bar{Y}^{*\pm}(1385)$

Resonance	$\bar{Y}^{*-}$	Y^{*+}	$\bar{Y}^{*+}$	Y^{*-}
Mass (GeV/c^2)	1.382 ± .003	1.383 ± .002	1.374 ± .005	1.395 ± .016
Width (GeV/c^2)	0.052 ± .018	0.027 ± .012	0.051 ± .015	0.181 ± .161
χ^2 (22 degrees of freedom)	16.9	18.9	27.0	15.5

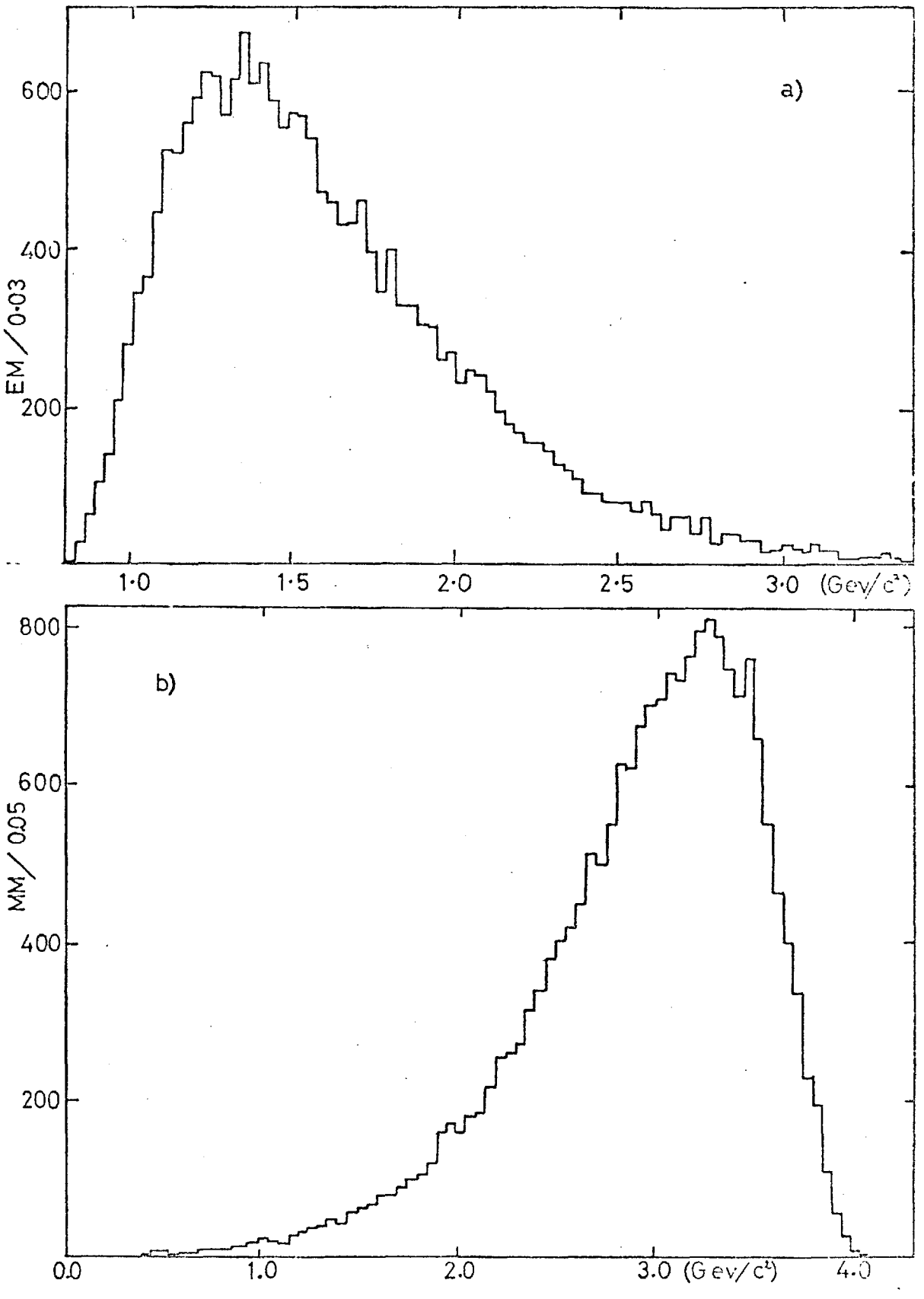


Figure 5.1 : a) Effective mass of $K^0(\bar{K}^0)\pi^+\pi^-$ combinations, in 30 MeV/c^2 bins

b) Recoil mass to $K^0(\bar{K}^0)\pi^+\pi^-$ combinations, in 50 MeV/c^2 bins.

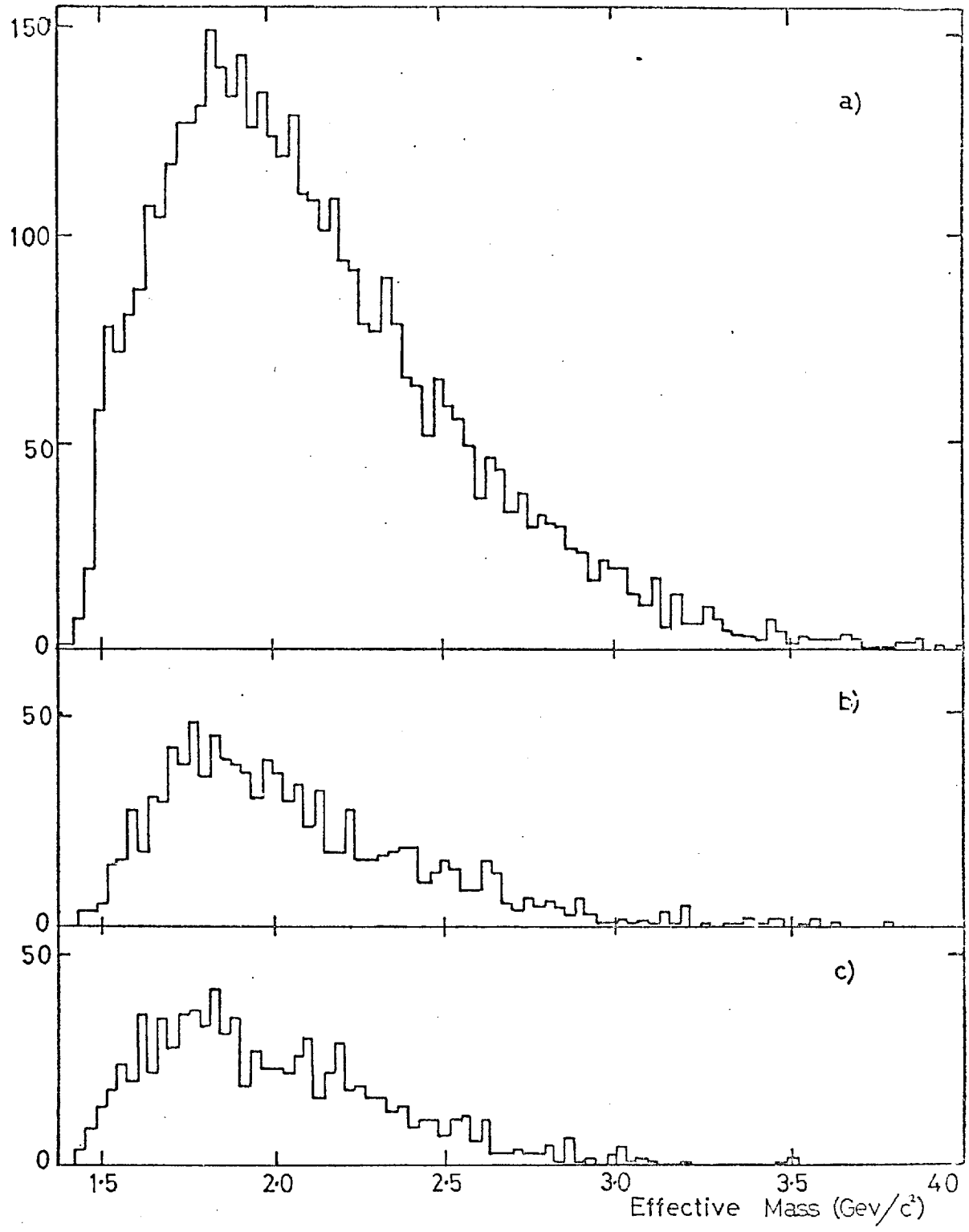


Figure 5.2 : Effective mass distributions, in 30 MeV/c^2 bins, for the combinations

a) $\bar{\Lambda}^0 \pi^+ \pi^-$

b) $\Lambda^0 \pi^+ \pi^+$

c) $\bar{\Lambda}^0 \pi^- \pi^-$

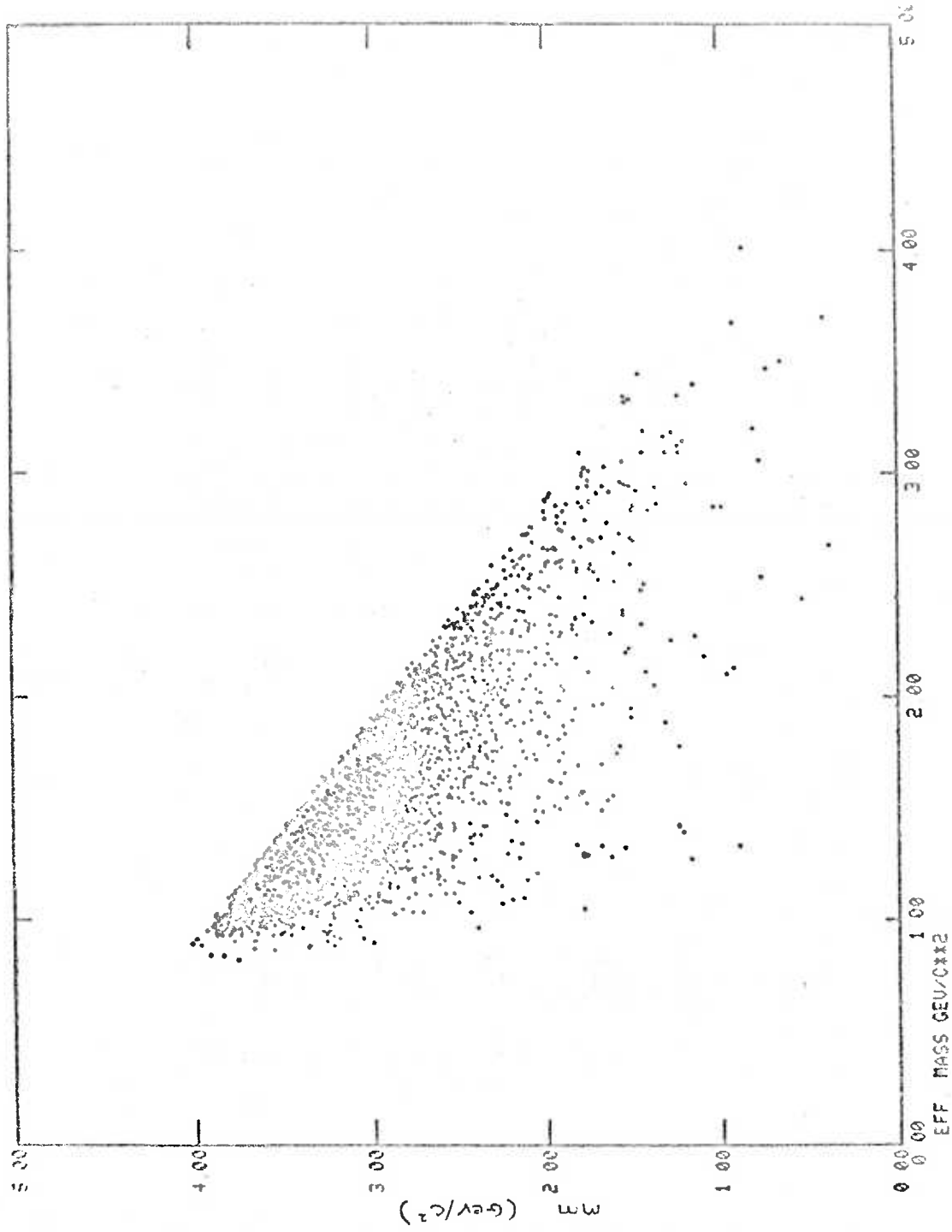


Figure 5.3 : Scatter plot of missing mass versus effective mass of $K^0\pi^+\pi^-$ combinations, for all events excluding zero- and two-prong events.

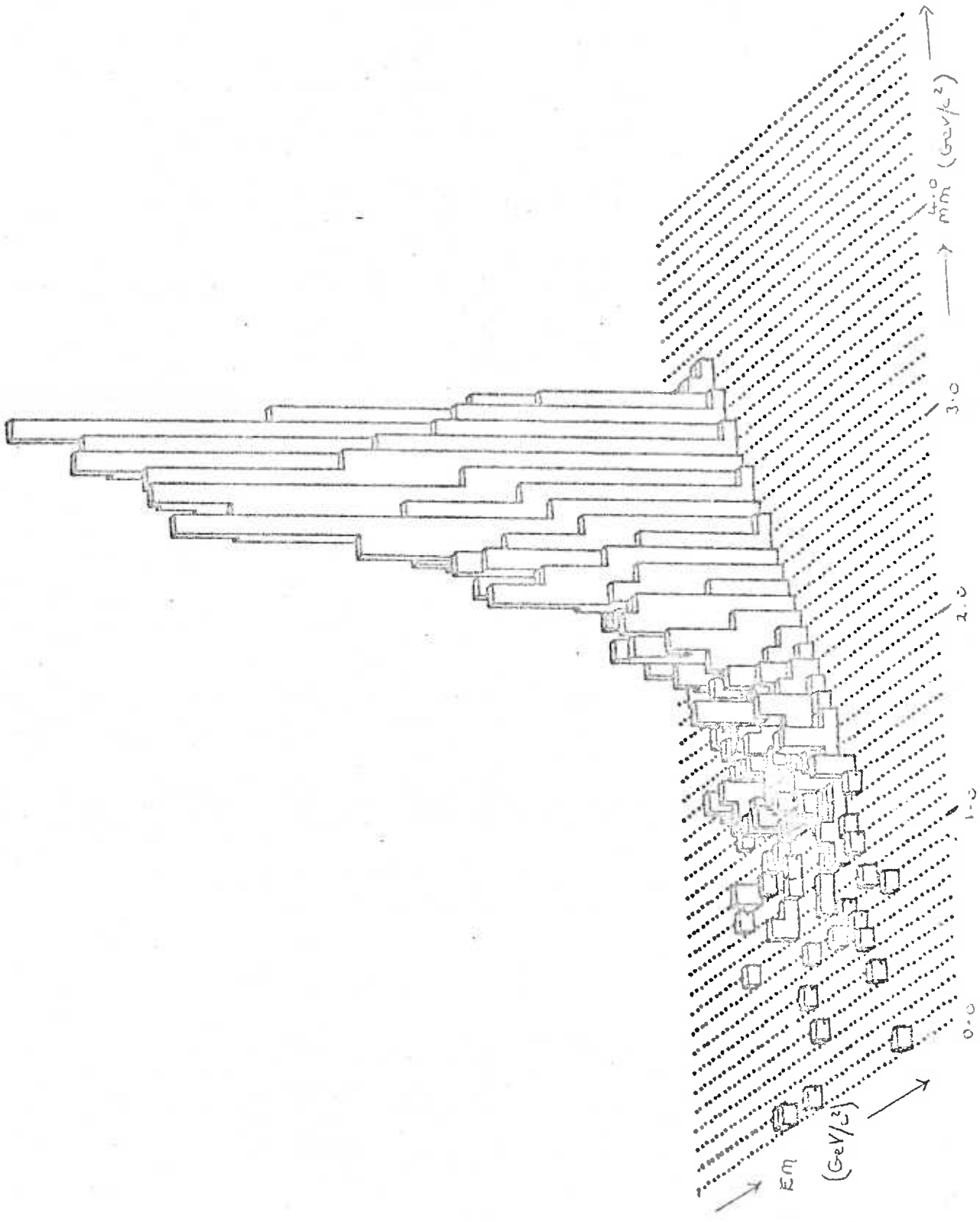


Figure 5.4 : As figure 3, but plotted as a three-dimensional "lego" plot.

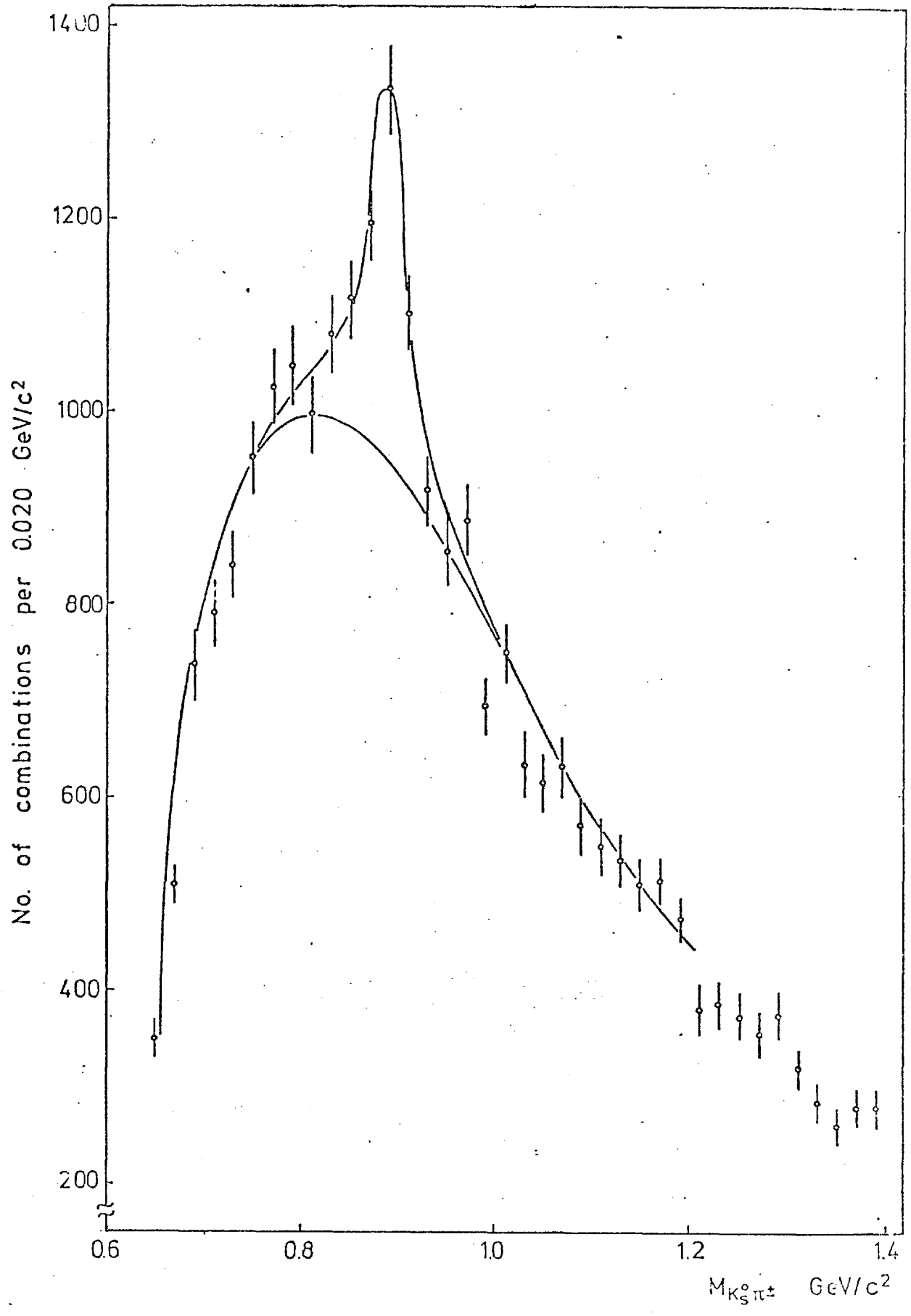


Figure 5.5 : Effective mass of $K^0_S\pi^\pm$ combinations. The curve is the result of the fit explained in section 5.3 .

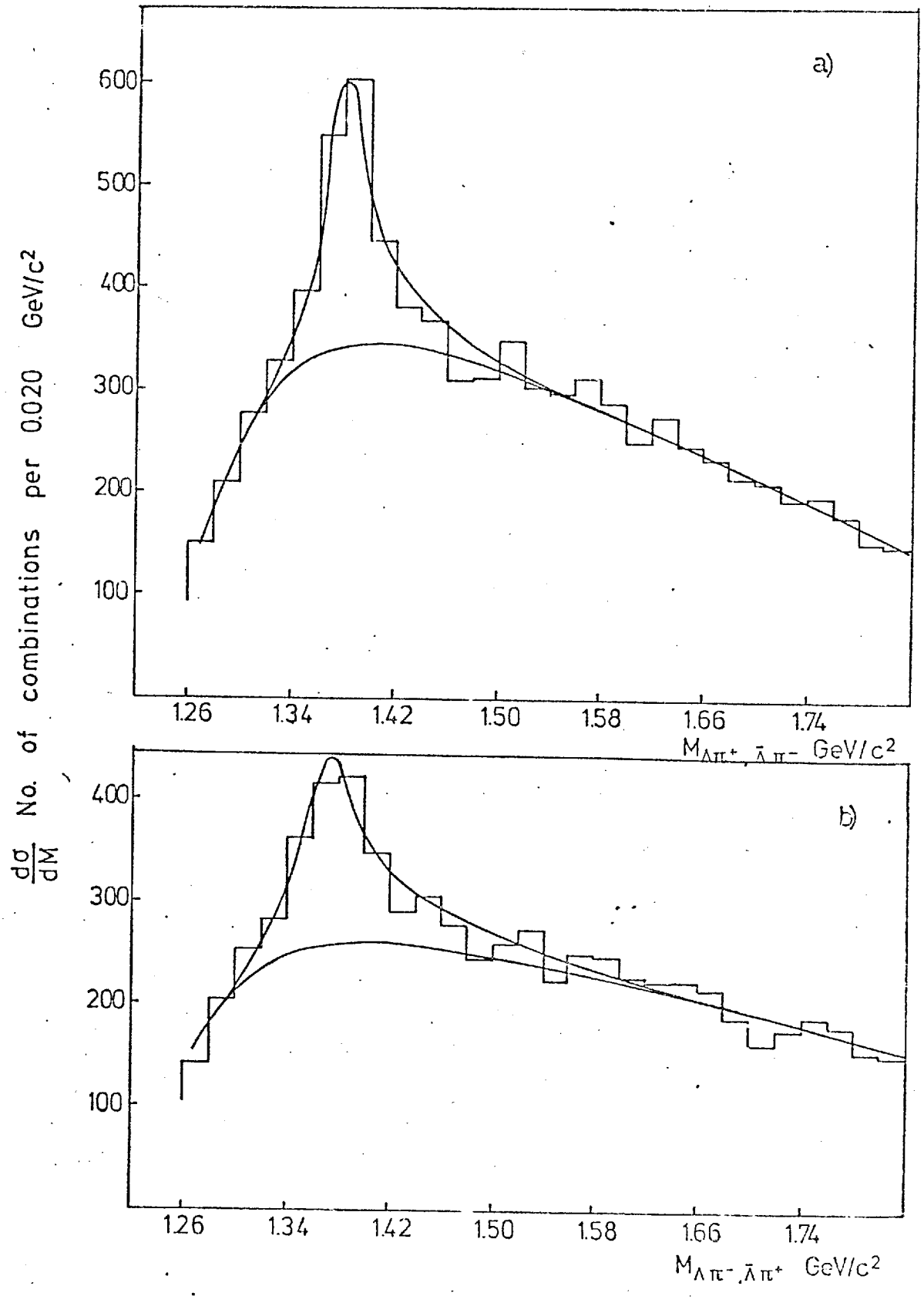
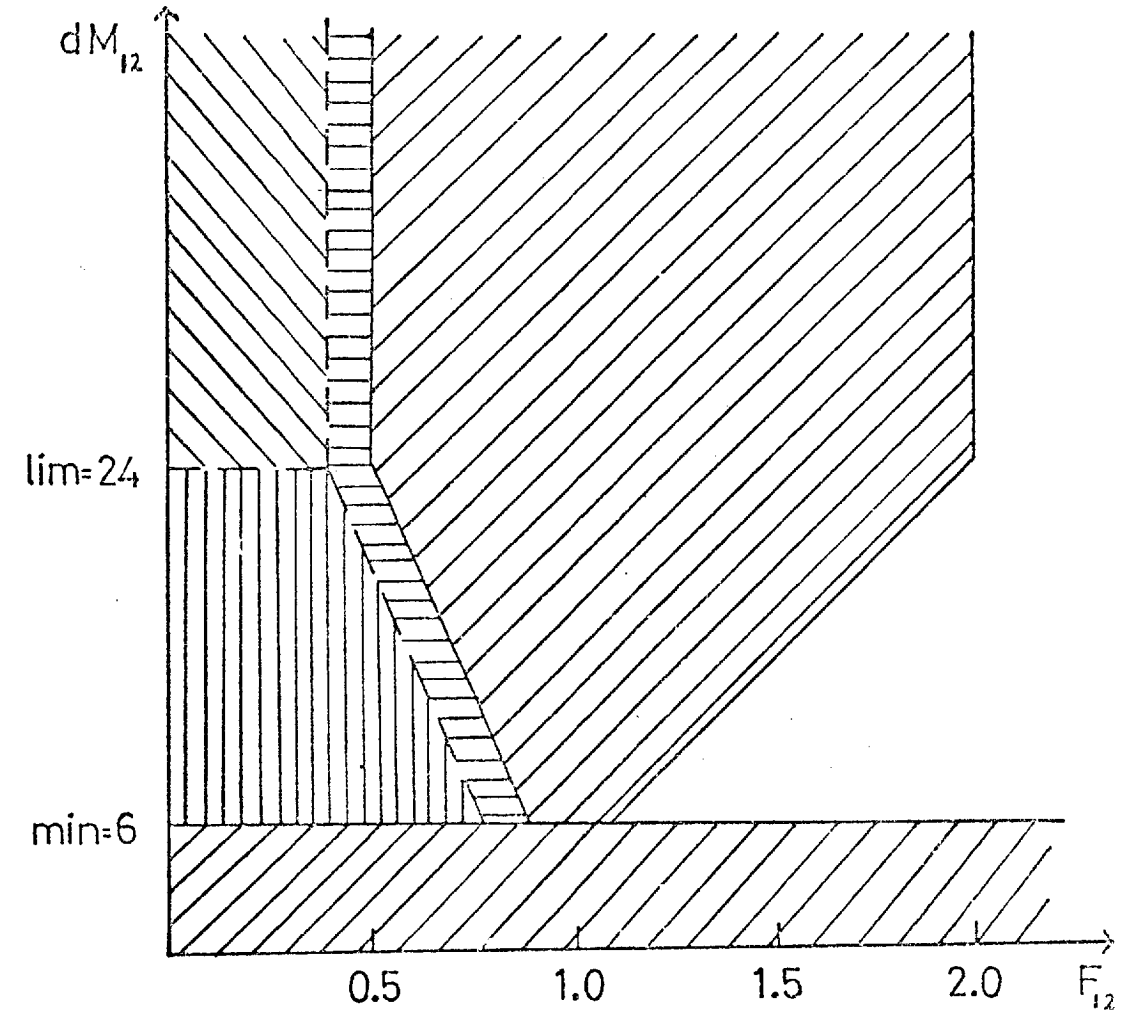


Figure 5.6 : a) Effective mass of $\Lambda^0\pi^+ + \bar{\Lambda}^0\pi^-$

b) Effective mass of $\Lambda^0\pi^- + \bar{\Lambda}^0\pi^+$

The curves are the results of the fits explained in section 5.3 .



$R_{12} = 1$

$R_{12} =$ Linear Decrease

$R_{12} = R_{max} = 999.0$

$R_{12} = \frac{P_1}{1 - P_1}$

$R_{12} = \frac{P_1}{P_2}$; $F_{12} = \frac{\chi_1^2}{\chi_2^2}$

$P_1 = \frac{(P_{max} - 0.5)}{(dM)_{lim} - (dM)_{min}} \left[dM_{12} - (dM_{12})_{lim}\right] + P_{max}$

$P_{max} = 0.999$

Figure 5.7 : Parametrisation for geometrical mass fit probability, P_G^i

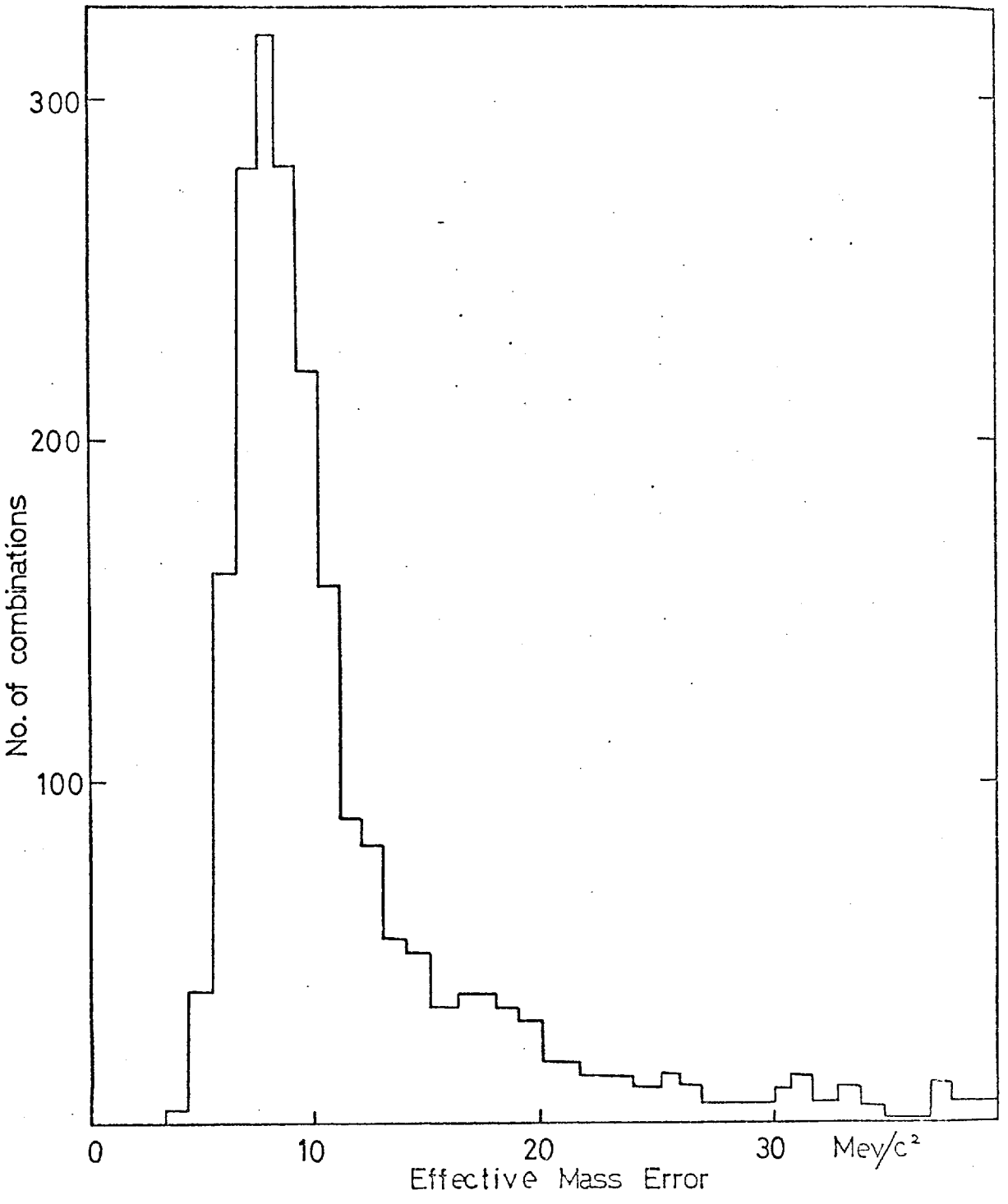


Figure 5.8 : Error on effective mass for the $K^{0}3\pi$ system.

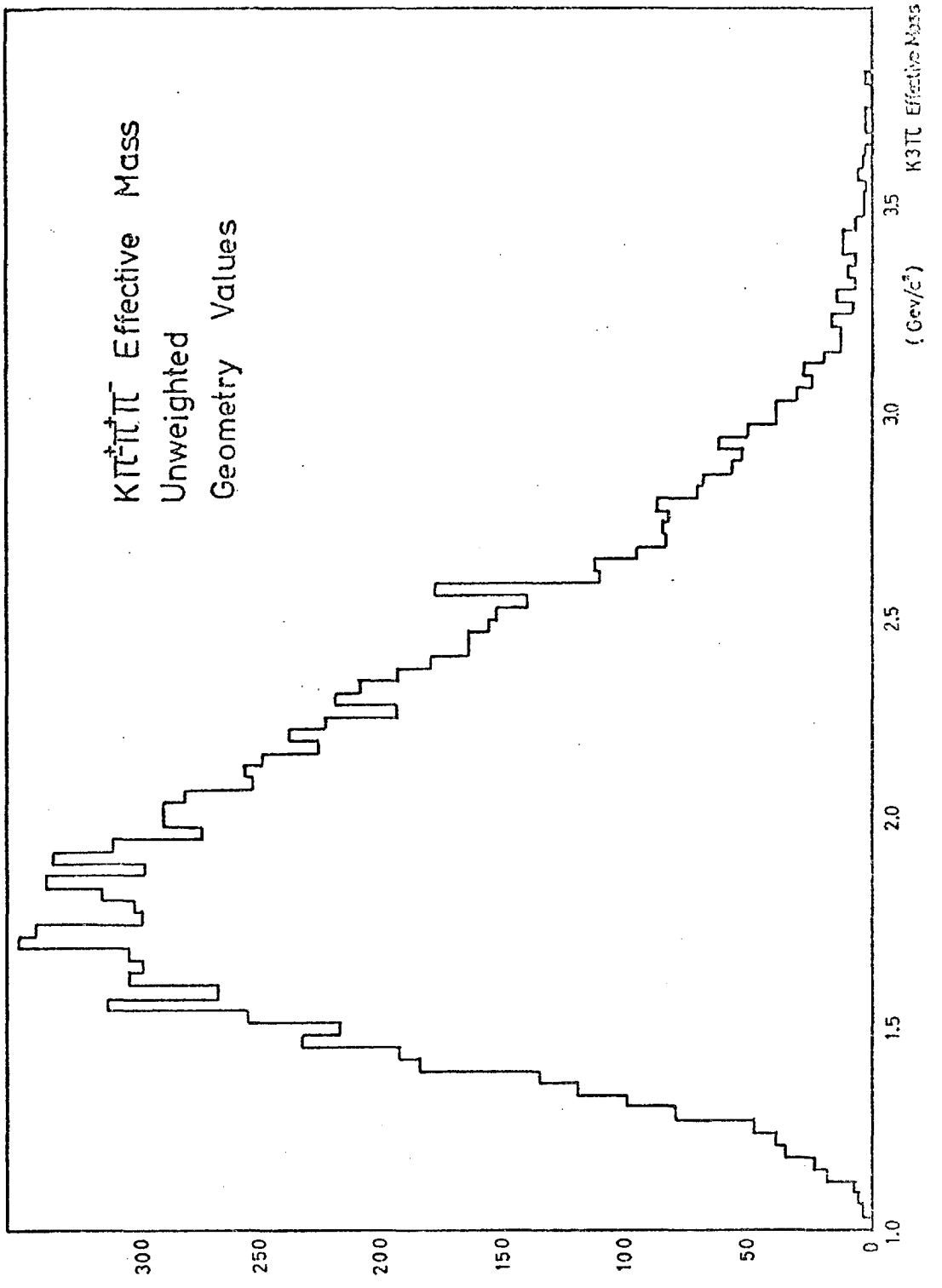


Figure 5.9 : Unweighted $K^0\pi^{\pm}\pi^+\pi^-$ effective mass distribution using the cuts and selection criteria for events as described in the text.

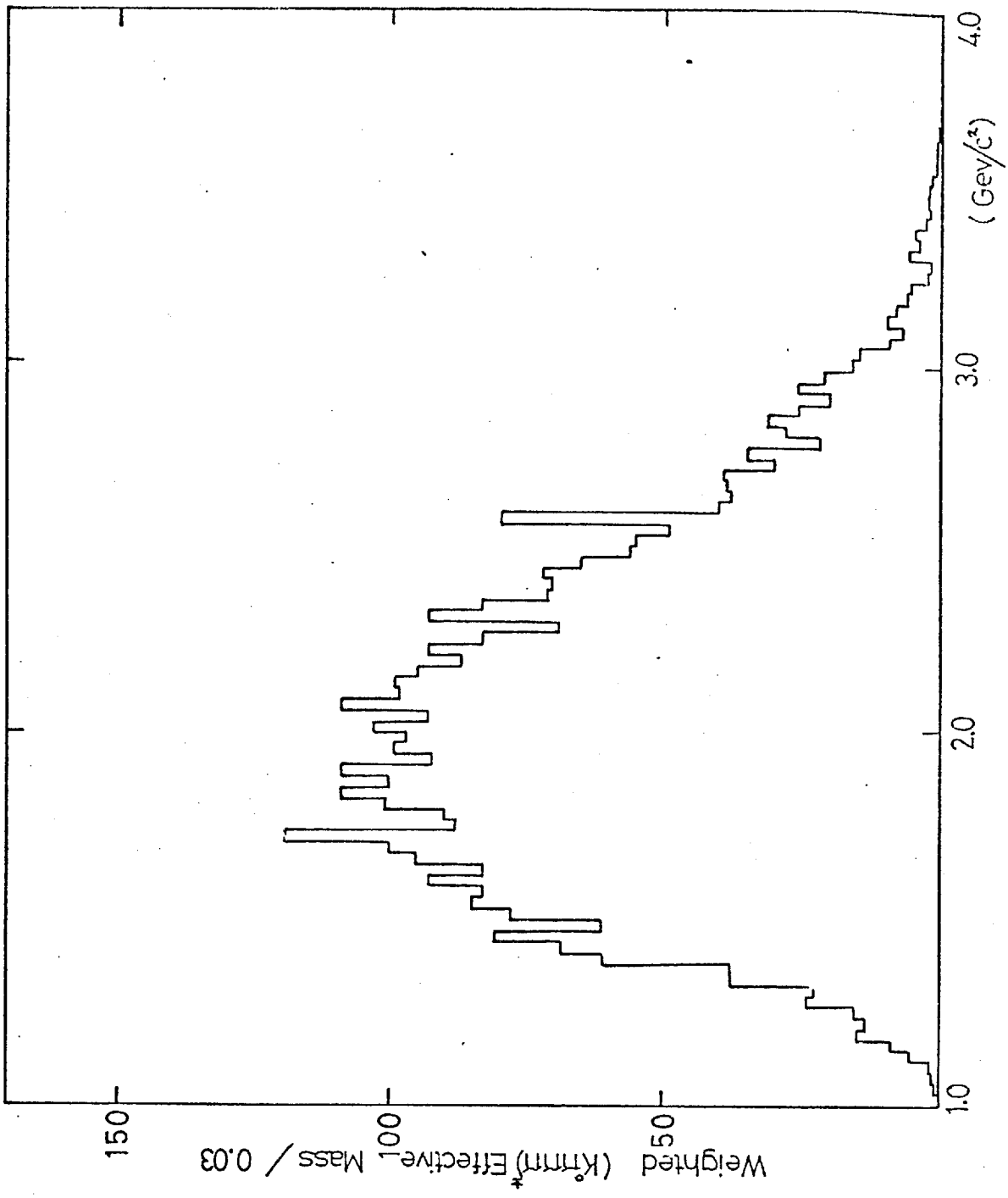


Figure 5.10 : Effective mass distribution for $K^0\pi^\pm\pi^+\pi^-$ combinations, using geometrical track parameters , and weighted according to the rules described in the text.

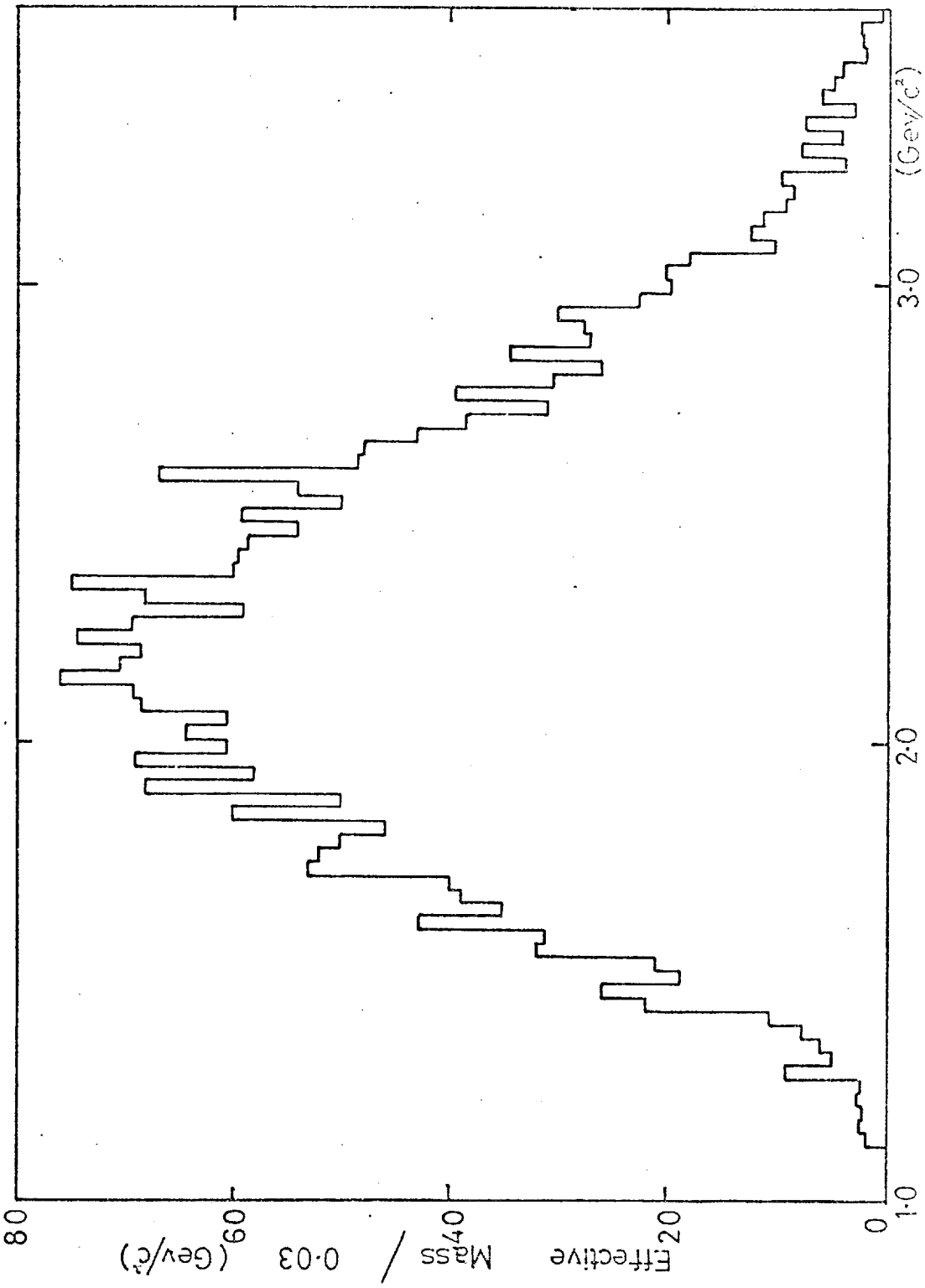


Figure 5.11 : Weighted $K^0\pi^{\pm}\pi^+\pi^-$ effective mass distribution using kinematically constrained track parameters.

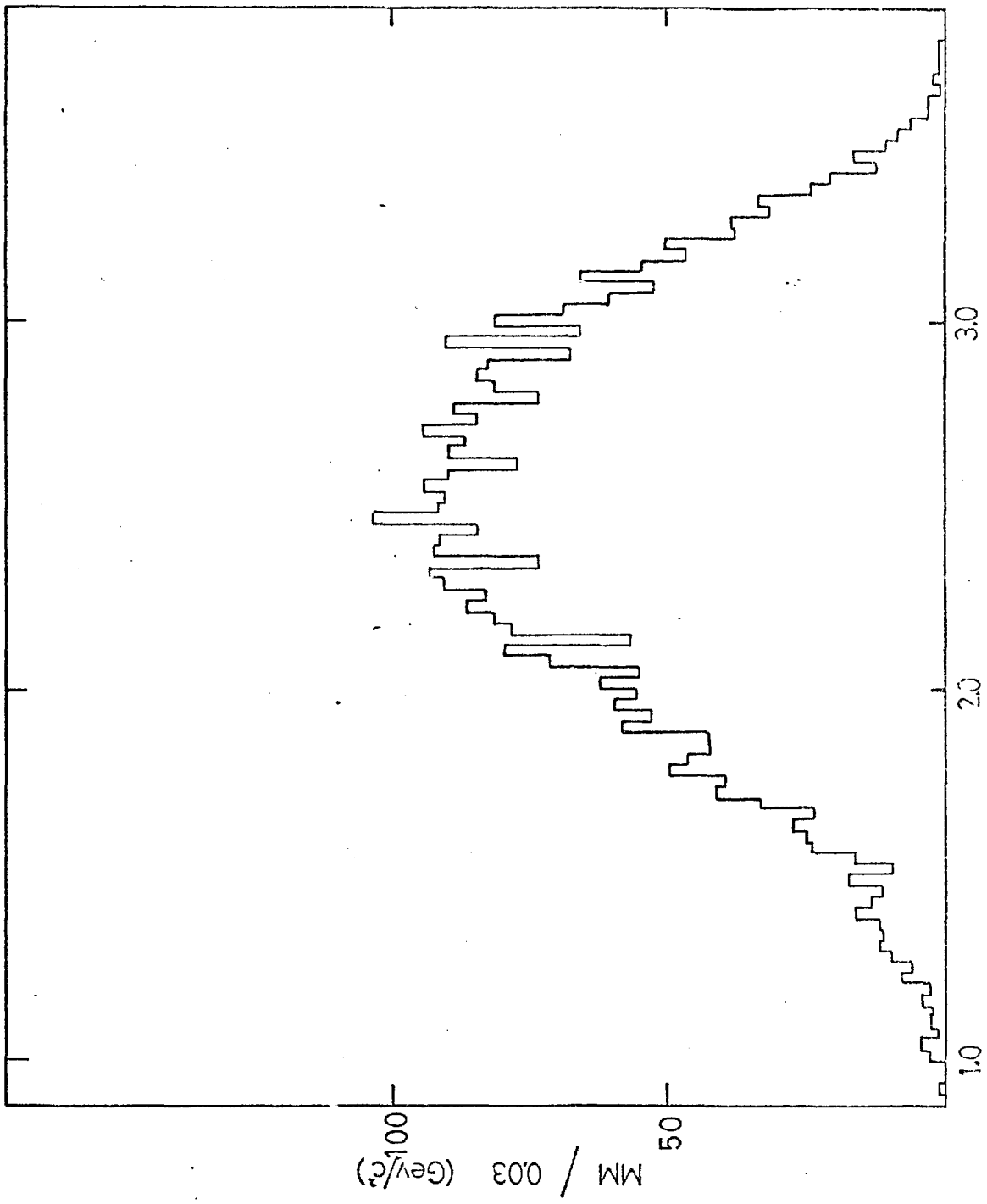


Figure 5.12 : Weighted recoil mass to the $K^0\pi^{\pm}\pi^+\pi^-$ combinations.

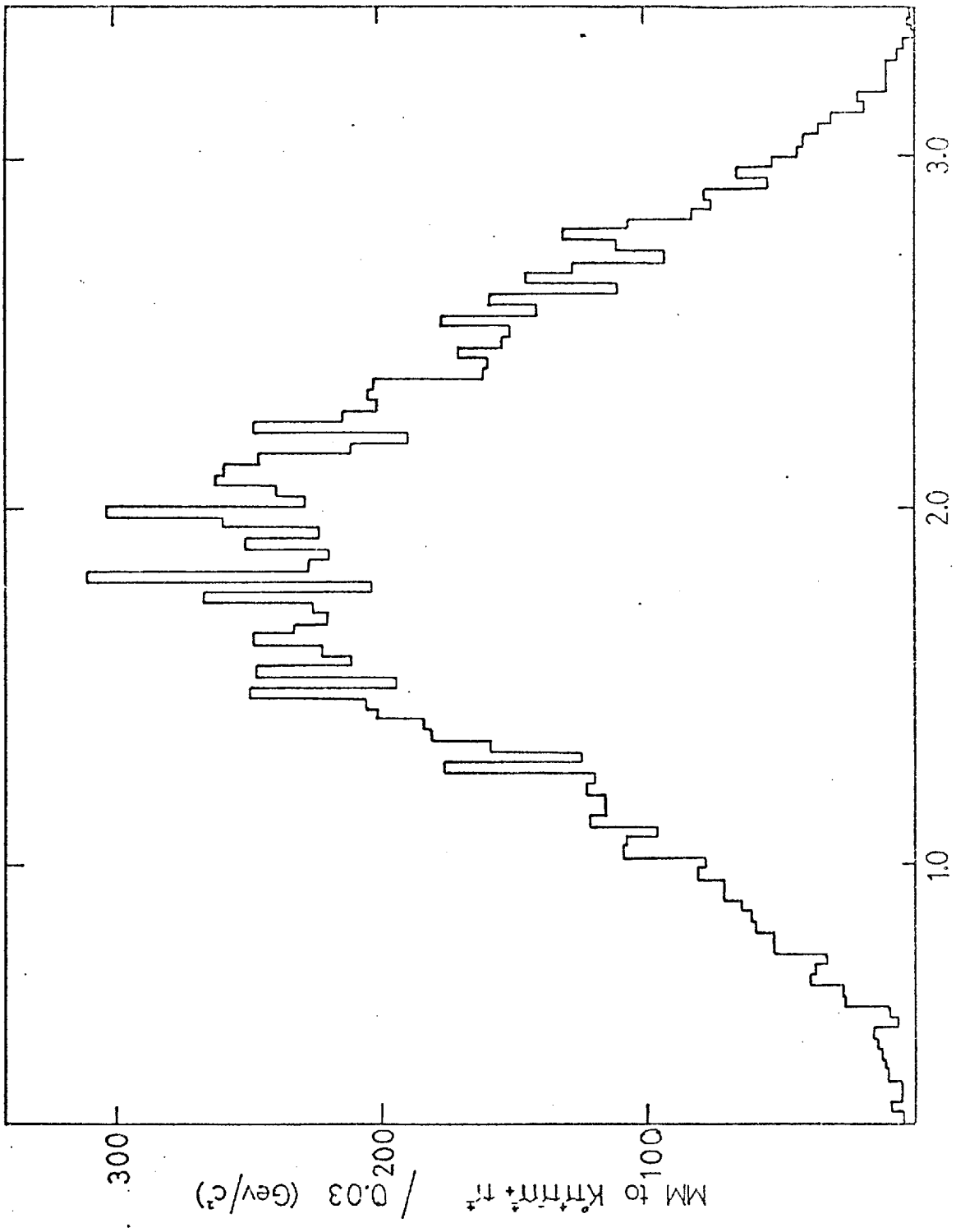


Figure 5.13 : Weighted recoil mass to $K^0\pi^\pm\pi^+\pi^-$ combinations plus an extra pion.

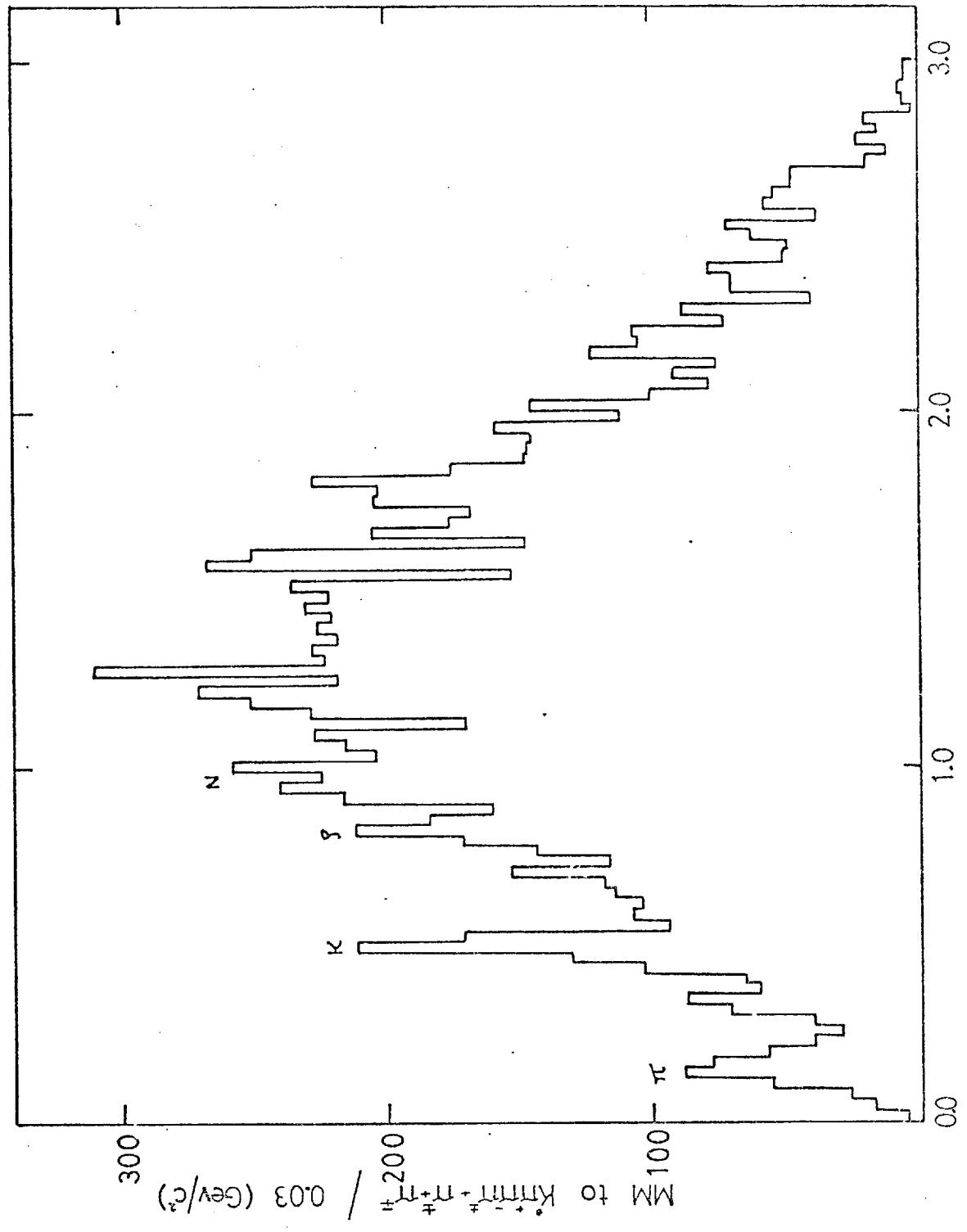


Figure 5.14 : Weighted recoil mass to $K^{\circ}\pi^{\pm}\pi^{+}\pi^{-}$ combinations plus two pions.

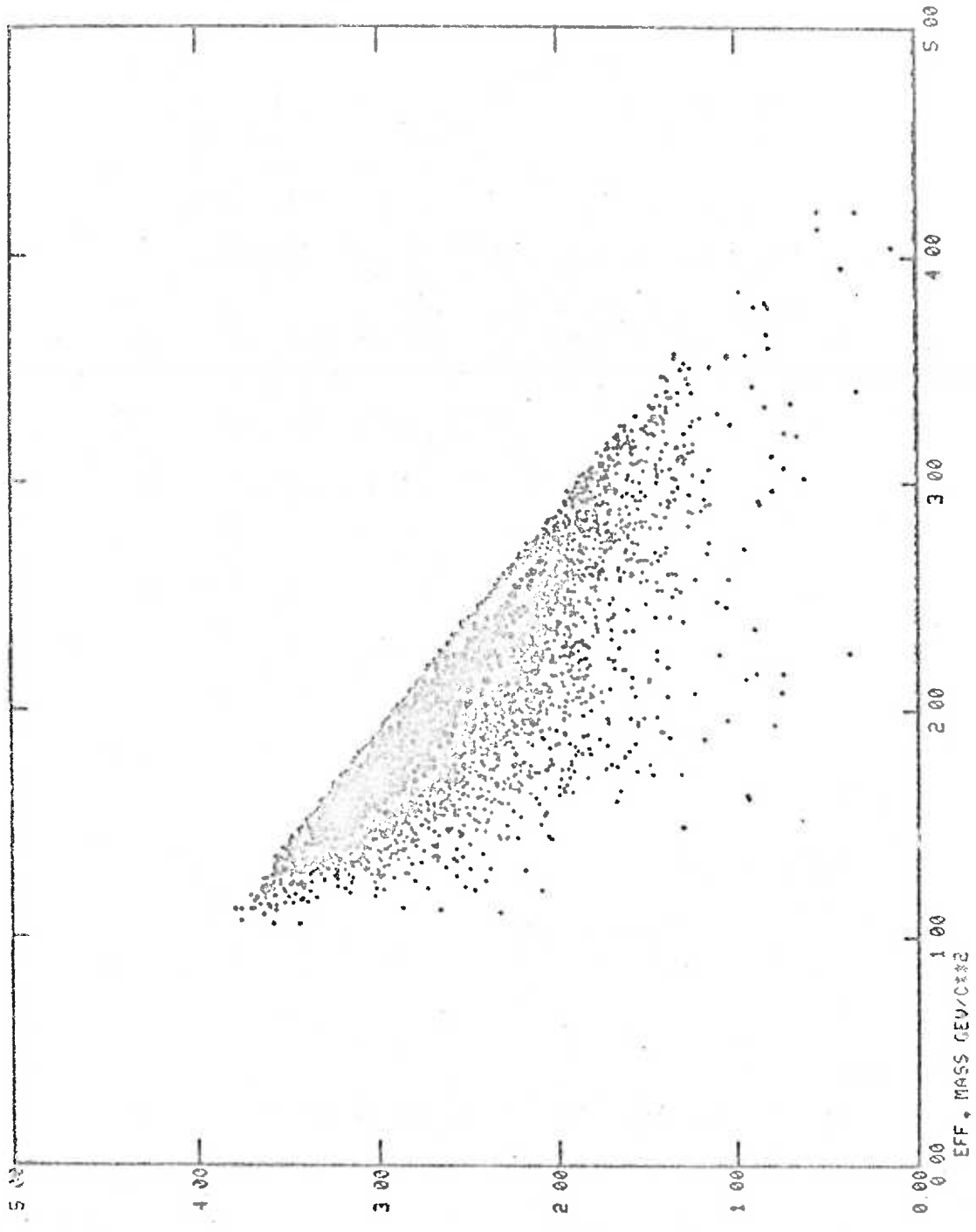


Figure 5.15 : Scatter plot of missing mass versus $K^{o}\pi^{\pm}\pi^{+}\pi^{-}$ effective mass for all six-prong events.

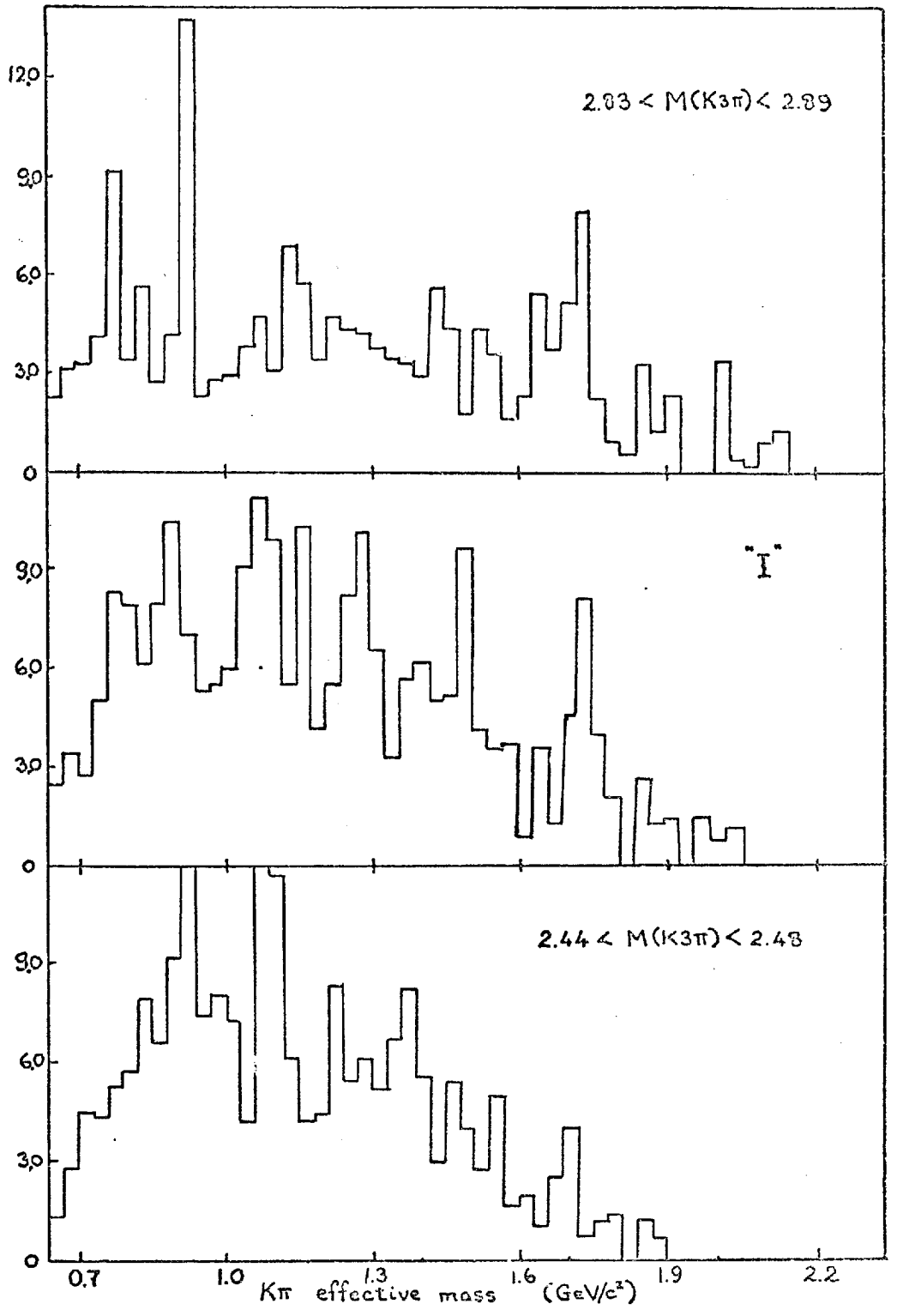


Figure 5.16 : $K^0\pi^\pm$ effective mass for different $K^0\pi^\pm\pi^+\pi^-$ effective mass bins. The "I" was taken as the bin $2.59 < M(K3\pi) < 2.62$ GeV/c^2.

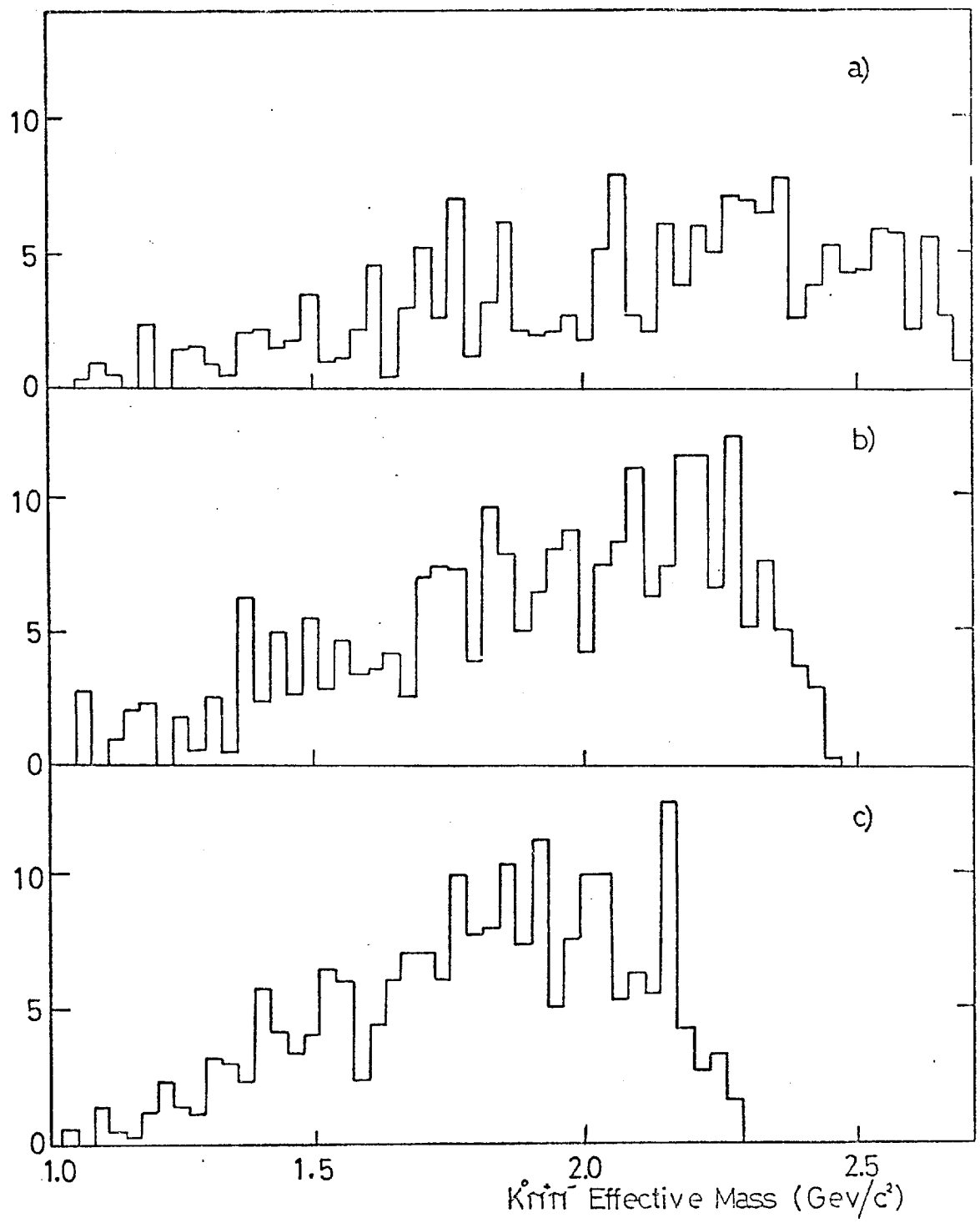


Figure 5.17 : $K^{\circ}\pi^{\pm}\pi^{\mp}$ effective mass distributions for different $K^{\circ}\pi^{\pm}\pi^{+}\pi^{-}$ effective mass bins.

a) $2.83 < M(K3\pi) < 2.89$

b) $2.59 < M(K3\pi) < 2.62$

c) $2.44 < M(K3\pi) < 2.48$

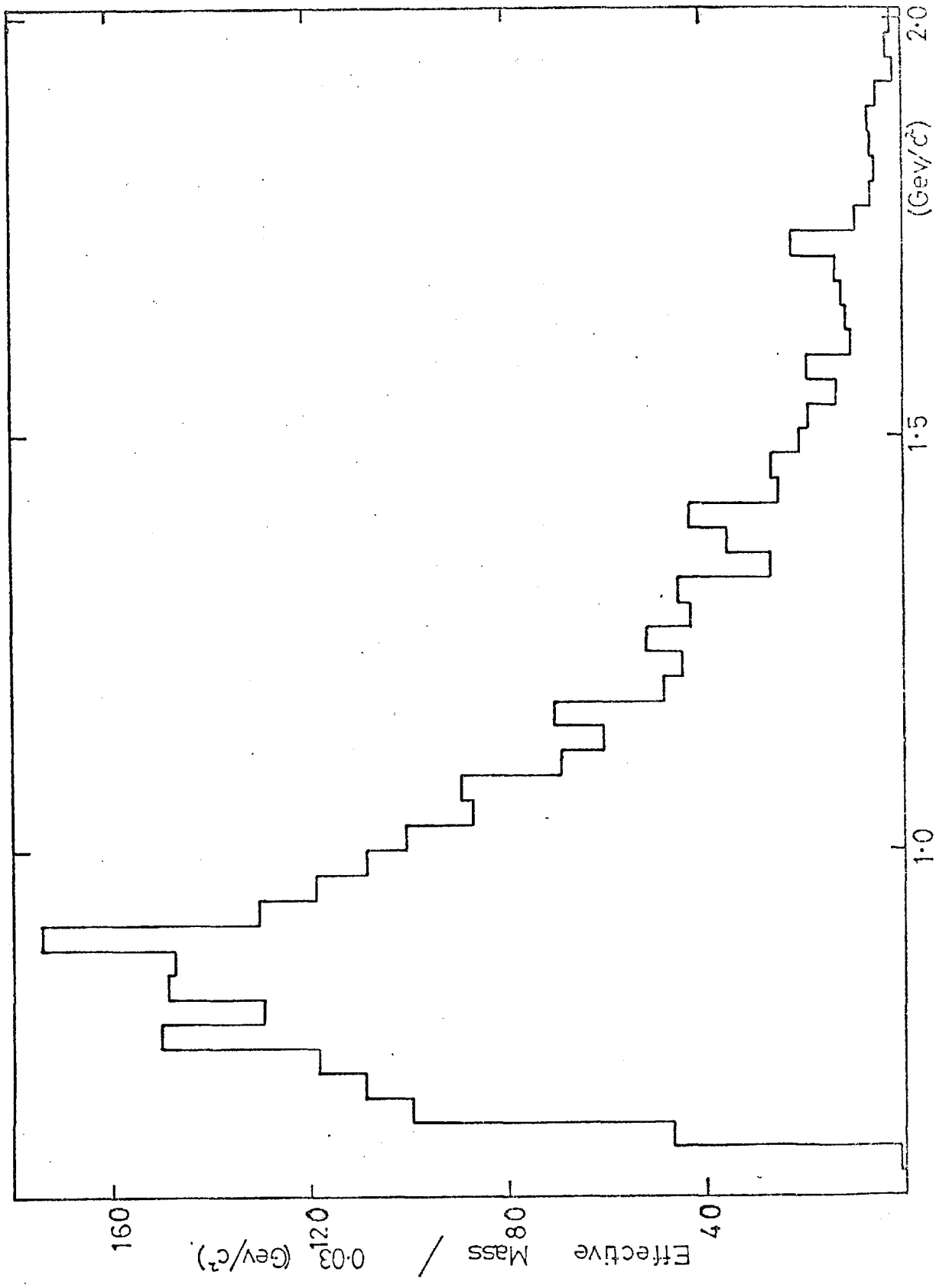


Figure 5.18 : $K\pi$ effective mass distribution for all six-prong events

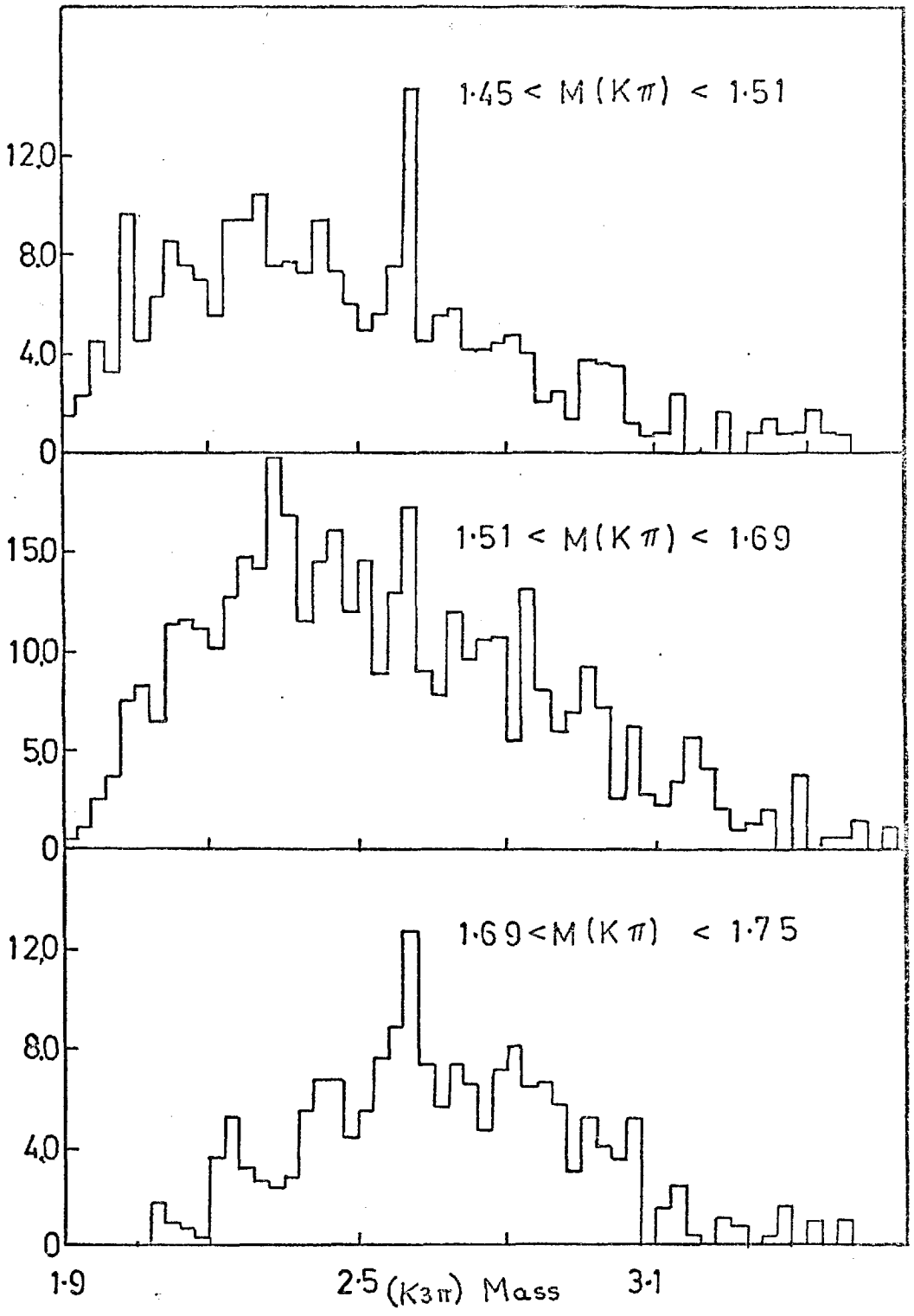


Figure 5.19 : Weighted $K^0\pi^{\pm}\pi^{+}\pi^{-}$ effective mass distribution for different $K^0\pi^{\pm}$ effective mass bins.

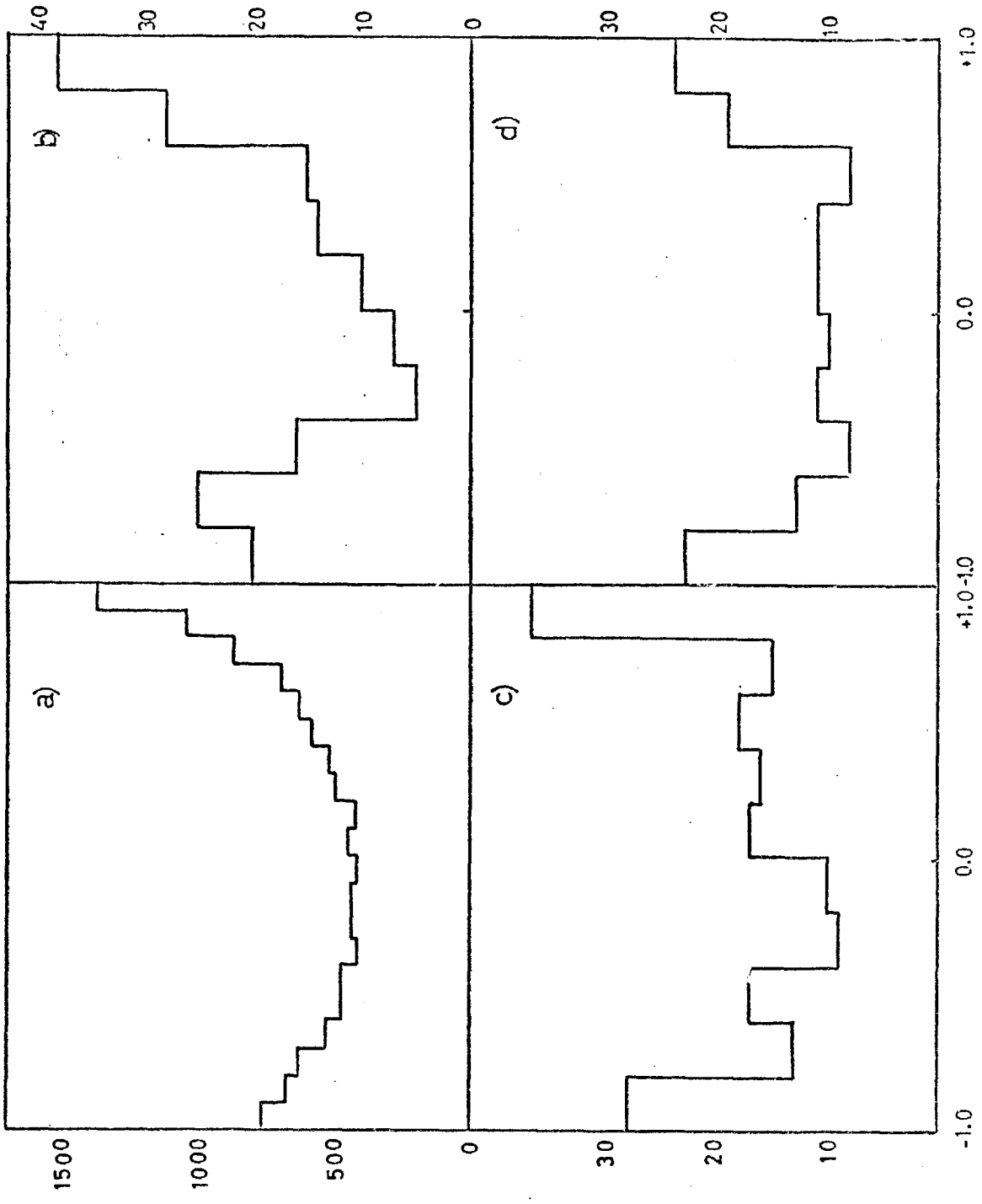


Figure 5.20 : Production angle, $\cos\theta^*$, of $K^0 3\pi$ combinations for :-

a) all combinations

b) $2.59 < M(K3\pi) < 2.62$ GeV/c^2

c) $2.41 < M(K3\pi) < 2.44$ GeV/c^2

d) $2.83 < M(K3\pi) < 2.89$ GeV/c^2

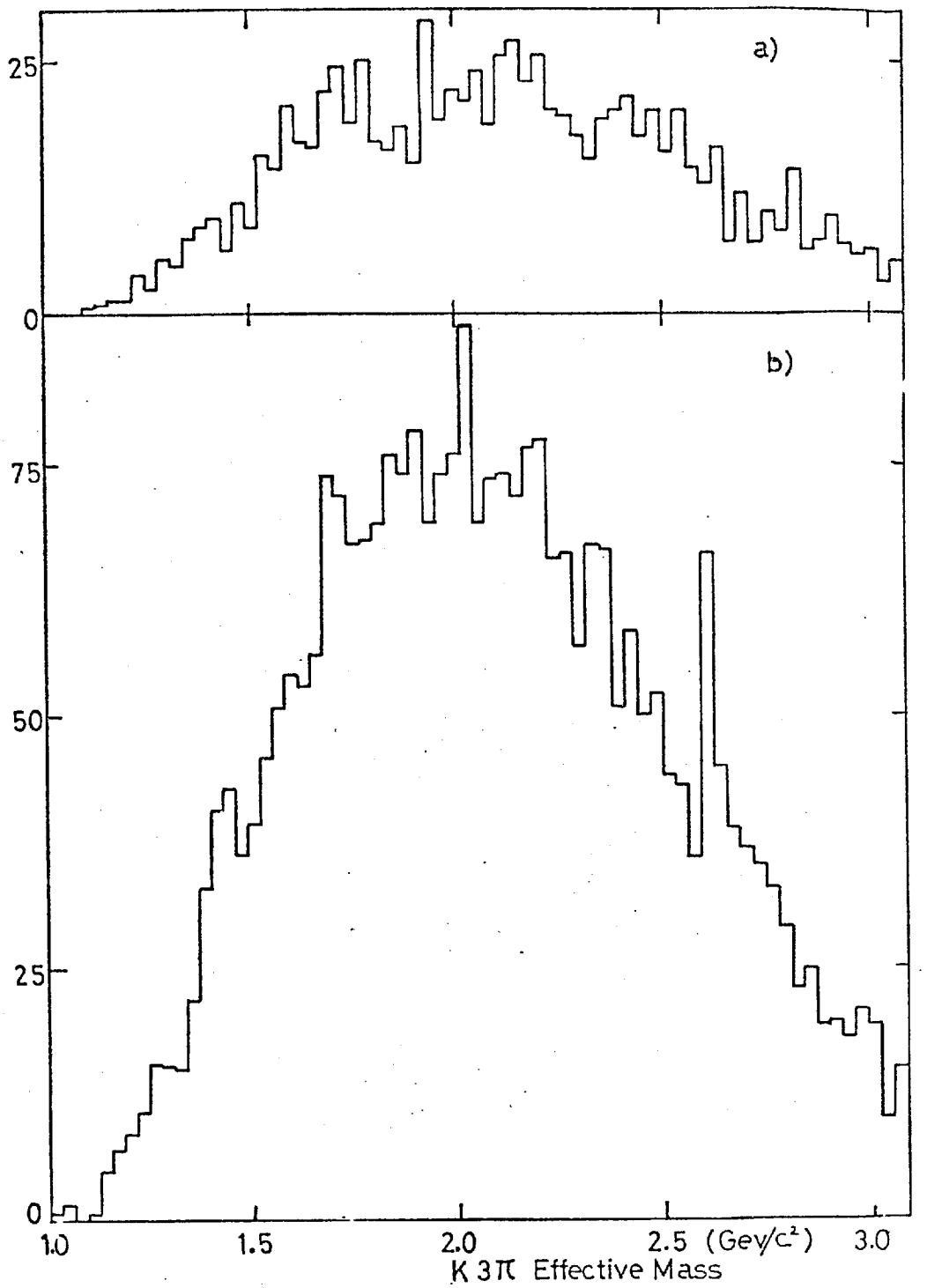


Figure 5.21 : Weighted K3π effective mass distributions for different impact parameters d, plotted in 30 MeV/c^2 bins : a) d < 0.05 cm.

b) d ⩾ 0.05 cm.

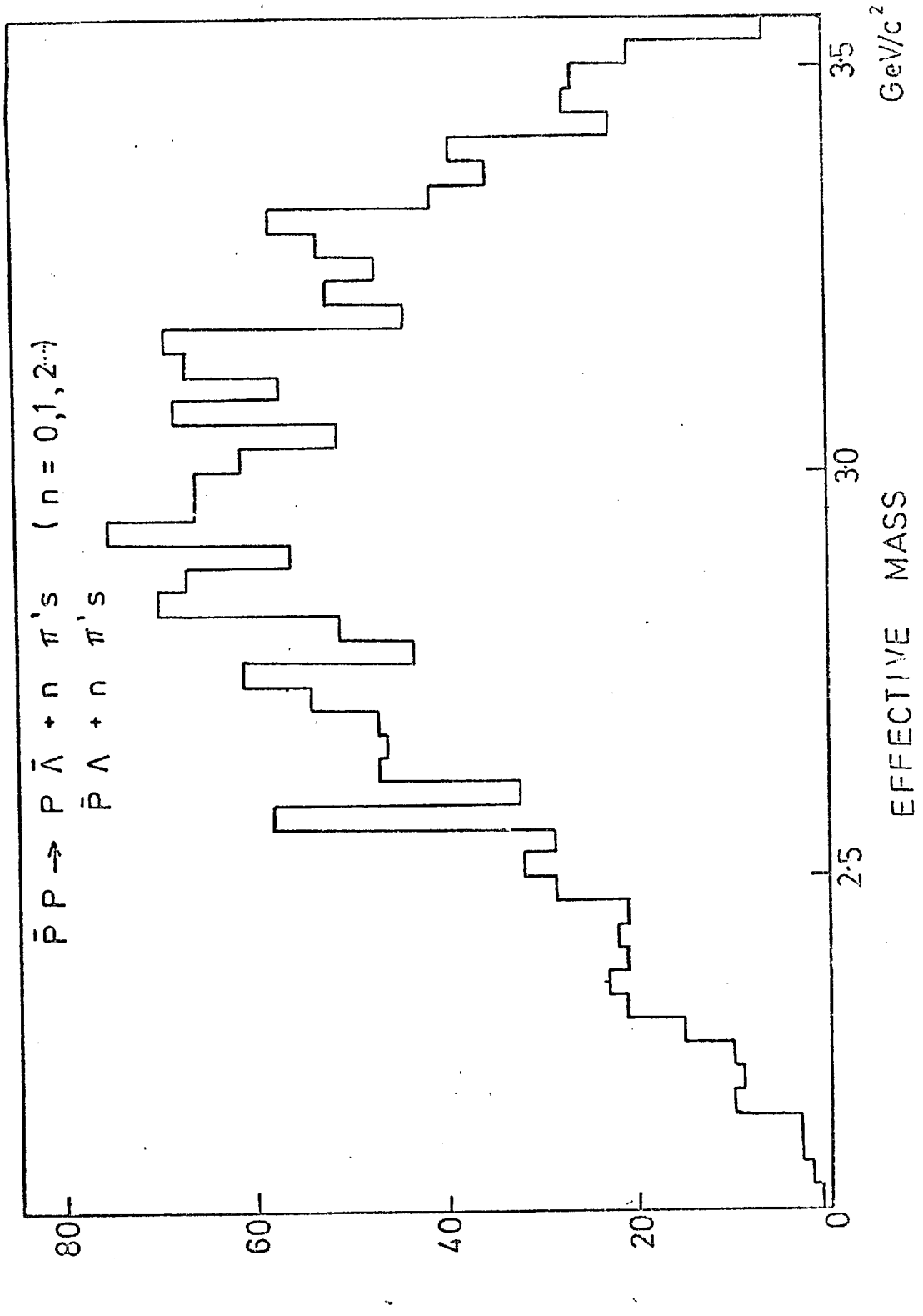


Figure 5.22 : Effective mass distribution for all combinations which include a Λ^0 (or $\bar{\Lambda}^0$) and anti-nucleon (or nucleon) plus 0, 1, or 2 pions.

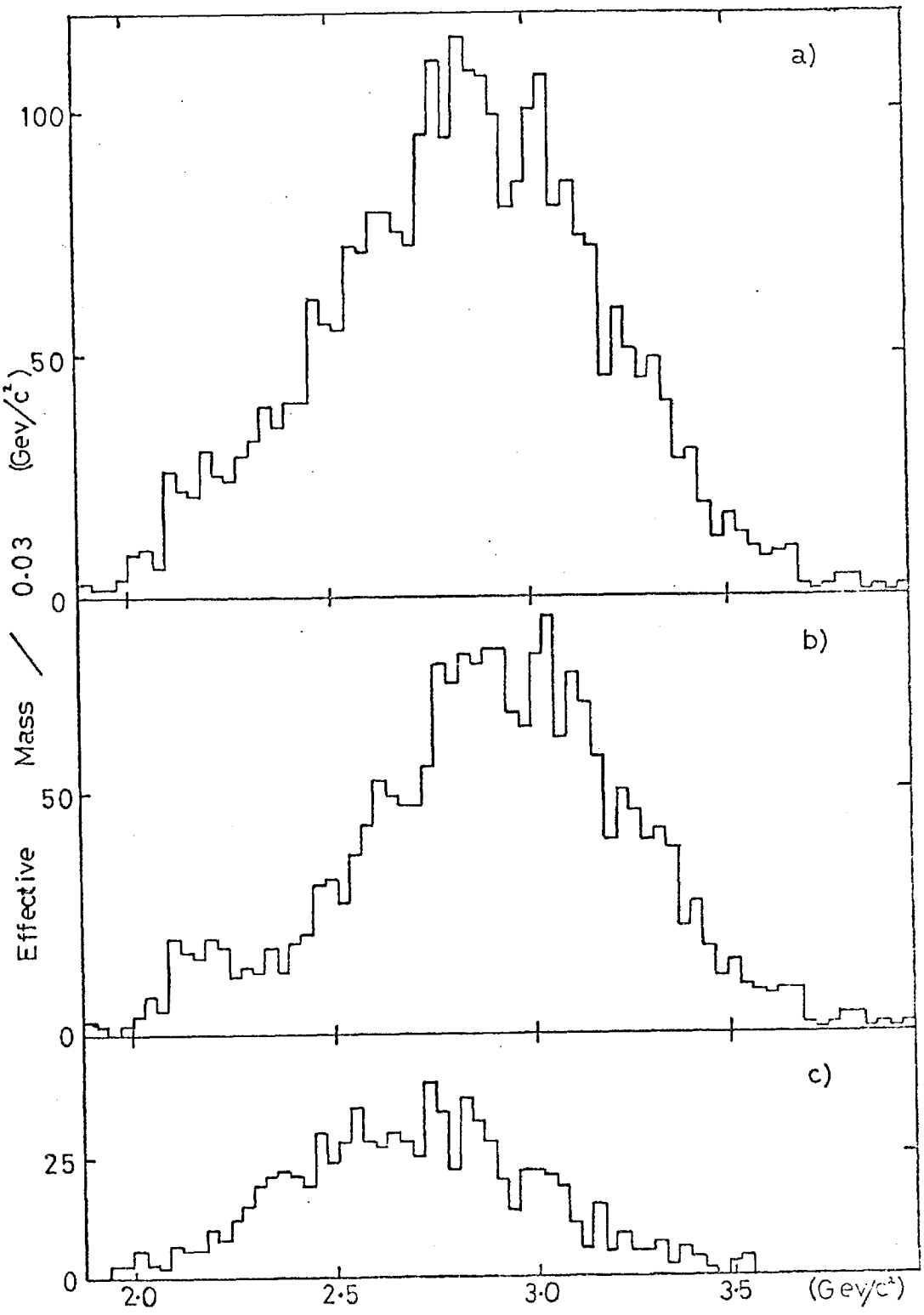


Figure 5.23 : Effective mass distributions for

a) All combinations $\Lambda^0\bar{p}$, $\Lambda^0\bar{p}\pi^+$, $\Lambda^0\bar{p}\pi^+\pi^-$, + c.c.'s
$\Lambda^0\bar{n}$, $\Lambda^0\bar{n}\pi^\pm$, $\Lambda^0\bar{n}\pi^\pm\pi^\mp$, + c.c.'s

b) All charged combinations $\Lambda^0\bar{p}$, $\Lambda^0\bar{p}\pi^+\pi^-$, + c.c.'s
$\Lambda^0\bar{n}\pi^\pm$ + c.c.'s

c) All neutral combinations $\Lambda^0\bar{p}\pi^+$ + c.c.'s
$\Lambda^0\bar{n}$, $\Lambda^0\bar{n}\pi^\pm\pi^\mp$ + c.c.'s

A SEARCH FOR KNOWN CHARMED PARTICLES

6.1 Introduction

This chapter describes some of the results from experiments analysed since the discovery of the ψ in November 1974 (see main introduction to this thesis). No definite identification of a charmed particle has been made in a hadron experiment so an attempt has been made here to derive upper limits for the production cross section times branching ratio ($\sigma \times BR$) for the D meson discovered in e^+e^- annihilations. A search for direct lepton production was also made to look for possible semi-leptonic or leptonic decay modes of the charmed particles. Finally, there is a comparison between K^0 production in e^+e^- and $\bar{p}p$ annihilations in order to detect a possible change in the K^0 yield per annihilation event in $\bar{p}p$ interactions, as has been observed in e^+e^- at a centre of mass energy near 4 GeV, which might also indicate a threshold for charmed pair production.

6.2 Evidence for the Existence of Charm

Most of the evidence for the existence of charmed particles comes from e^+e^- annihilations. Two peaks were found in $K^{\pm}\pi^{\mp}$ and $K^{\pm}\pi^{\mp}\pi^{+}\pi^{-}$ mass distributions at SLAC [1] and identified as coming from the decay of a neutral particle of mass 1.865 GeV/c^2. A peak found in the exotic combination $K^{\pm}\pi^{\mp}\pi^{\mp}$ [2,3] at 1.876 $\pm$ 0.015 GeV/c^2 can be interpreted as a charged charmed meson, composed of $c\bar{d}$ or $\bar{c}d$ quarks, which decays weakly with $\Delta S = \Delta C$ to an uncharmed negative (positive) strangeness state. Parity violation has been observed [4] in the Dalitz plot of the 3 body reaction $D^{\pm} \rightarrow K\pi\pi$ which also indicates a weak decay. Other decay modes have been seen with K^0_S ($\bar{K}^0_S$) plus pions in the final state. Both the charged and neutral states have been identified with the two

predicted isospin doublets of charmed D mesons, namely (D^+D^0) and $(D^-\bar{D}^0)$ (see main introduction to this thesis). Peaks have also been seen at 2.01 GeV/c^2 in the recoil mass spectrum to the charged D's and at 2.01 and 2.15 GeV/c^2 in the recoil system to the neutral D's; the 2.01 GeV/c^2 peak has been interpreted as the excited D^* state. The widths of all the observed D mesons are less than the resolution of the experiments concerned.

Two different states have been found by a DASP collaboration at DESY [5] which may be the F and F^* mesons with measured masses $m_F = 2.03 \pm 0.06$ GeV/c^2 and $m_{F^*} = 2.14 \pm 0.06$ GeV/c^2.

Further evidence for charm comes from ν interactions in the form of one event [6] $\nu p \rightarrow \mu^- \Lambda^0 \pi^+ \pi^+ \pi^+ \pi^-$ which violates the $\Delta S = \Delta Q$ rule and can be explained if a charmed baryon, Λ_c, had been produced which subsequently decayed to either $(\Lambda^0 3\pi)^+$ or $(\Lambda^0 4\pi)^{++}$. A Fermilab photoproduction experiment [7] studying the reaction $\gamma\,\mathrm{Be} \rightarrow \bar{\Lambda}^0$ + pions has produced a narrow peak in the $\bar{\Lambda}^0 \pi^- \pi^- \pi^+$ mass distribution at 2.26 GeV/c^2 and a higher mass ($\sim$ 2.5 GeV/c^2) peak in $(\bar{\Lambda}^0 4\pi)^0$ which is seen to cascade into the first state. No signal was found in the $\Lambda^0 \pi^+ \pi^+ \pi^-$ state however, which is contrary to charm expectations.

Various attempts have been made to look for charmed particles in hadronic interactions. π^- interactions at 19 GeV/c producing $K^+K^-p\pi^-$ and $K^+K^-\pi^+\pi^-\pi^-p$ final states have been studied with the Ω spectrometer at CERN [8] and upper limits for the production $\sigma \times$ BR of between 50 and 2000 nb. have been calculated for reactions like $\pi^-p \rightarrow D^-D^0p$, $\bar{D}^0D^0p\pi^-$ etc. Baltay [9] has studied $\pi^+p \rightarrow V^0 + X$ at 15 GeV/c and quotes upper limits for $\sigma \times$ BR of between 1.5 and 3.7 μb. Inclusive studies have also been made : Aubert [10] has looked for reactions of the type p + Be $\rightarrow$ D + X at 30 GeV/c and has found upper limits of

only a few nb. However, these limits were calculated for masses higher than 2.25 GeV/c^2 and at an energy much higher than that at which the D's were discovered in e^+e^- annihilations. Baltay has also looked inclusively at his data and calculated upper limits for $\sigma \times$ BR for charmed mesons of between 5.7 and 35 μb. and for charmed baryons of between 2.6 and 15 μb.

Cester [11] , using a carbon target and incident antiprotons at $\sqrt{s}$ = 5 GeV found $\sigma \times$ BR upper limits of between 0.6 and 6 μb./nucleon. Searches have also been made in antiproton interactions at 9 GeV/c [12] and 14.75 GeV/c [13] and in the ISR at $\sqrt{s}$ = 53 GeV [14] with no positive results.

A recent proton beam dump experiment performed at the CERN SPS [15] has produced evidence for prompt neutrinos, which, if they come from the production and subsequent decay of charmed particle pairs, would require charm production cross sections in the range 100 to 400 μb.

Indications of the production of charmed particles have also been seen in the increase of the kaon yield per annihilation event found in e^+e^- annihilations; this will be discussed in some detail in section 6.4 . Direct lepton production which may be due to the leptonic or semi-leptonic decay of charmed particles will be discussed in section 6.5 .

6.3 Upper Limits for the Production of Charmed Particles

In this section upper limits for the production cross section times branching ratio of the charmed D mesons found in e^+e^- annihilations [1-3] and of the charmed baryon, Λ_c [7] are calculated. Effective mass distributions for $K^0 n\pi$ (n=1-5) and $\Lambda^0/\bar{\Lambda}^0 n\pi$ (n=1-4) systems have been studied (figure 1) in a search for charmed particles produced in the inclusive reactions :-

$$\bar{p}p \rightarrow D + X$$

$$\bar{p}p \rightarrow D^{*} + X$$

$$\bar{p}p \rightarrow \Lambda_c + X$$

The width of the mass bins used in these distributions was determined by the resolution of the experiment since the charmed particles are very narrow. The error on the effective mass. for the mass regions under consideration, was calculated by propagating the errors of the individual track parameters and was found to be ~ 15 MeV/c^2. An error of ~ 25 MeV/c^2 was calculated for the missing mass. The bin widths were therefore taken as 30 MeV/c^2 for the effective mass and 50 MeV/c^2 for the missing mass distributions. No significant signal is observed in any of the expected mass regions. A quantitative estimate of the upper limits for the production cross sections for charmed particles was obtained using the following method.

Suppose n_o events are found in a bin centred on the D mass, and having a width defined by the experimental resolution, as defined above. The background is estimated using k/2 bins on each side of the D, and a total of N_o events is found in these k control bins. If $\bar{s}$ is the a priori expected number of signal events in the D bin and $\bar{b}$ the expected number of background events per bin, giving $k\bar{b}$ events in the k control bins and $\bar{b} + \bar{s}$ events in the D bin, then the probability, P, of observing n events in bin D and N events in the k control bins is the convolution of two Poisson distributions :-

$$P(n,N \mid \bar{s},\bar{b}) = e^{-(k\bar{b})} \frac{(k\bar{b})^N}{N!} \times e^{-(\bar{b}+\bar{s})} \frac{(\bar{b}+\bar{s})^n}{n!}$$

For a given $\bar{b}$ and $\bar{s}$, the probability, β, of finding a signal larger than that observed is given by :-

$$\beta = \sum_{N=0}^{\infty} \sum_{n=0}^{\infty} e^{-\left[(k+1)\bar{b} + \bar{s}\right]} \frac{(k\bar{b})^N}{N!} \cdot \frac{(\bar{b}+\bar{s})^n}{n!} \qquad (1)$$

subject to the constraint $n - \frac{N}{k} > n_o - \frac{N_o}{k}$.

95% confidence level upper limits are given by a value of $\beta = 1 - .95 = .05$ in equation (1) which has to be solved numerically to find the largest value of $\bar{s}$ compatible with the relation (1). When the number of events in each bin is large (as in the plots of figure 1), the Gaussian approximation has been used where formula (1) becomes a double integral over Gaussians.

The upper limits so derived for the product of the inclusive production cross section times branching ratio for D and D^* mesons and for the Λ_c baryon are given in table I. Using the branching ratios [17] BR $(D^+ \rightarrow \bar{K}^o \pi^+) = 1.5 \pm 0.6$ % and BR $(D^o \rightarrow K^o \pi^+ \pi^-) = 3.5 \pm 1.1$ %, upper limits of $\sigma(D^+) < 320\,\mu$b. and $\sigma(D^o) < 260\,\mu$b. have been determined for the total inclusive D^+ and D^o production cross sections.

The production of pairs of charmed mesons in the reactions :

$$\bar{p}p \rightarrow \bar{D}D$$

$$\bar{p}p \rightarrow \bar{D}^*D \quad (+ \text{charge conjugate})$$

$$\bar{p}p \rightarrow \bar{D}^*D^*$$

has been studied from the scatter plots of the $K^o n\pi$ effective mass versus the mass of the recoiling system (figure 2). The boxes on the figure represent the various $D\bar{D}$ regions; no signal is distinguishable from the background in any of these regions. Table II gives the upper limits for the production cross section times decay branching ratio for the different $D\bar{D}$ combinations, derived at a 95% confidence level assuming Poisson statistics. The branching ratio refers only to the D particle which is supposed to decay into the observed $K^o n\pi$ system, since the missing mass (mass of the recoil system) integrates over all possible decay channels.

The results of table I can be used to compare the production of

charmed particles in e^+e^- and $\bar{p}p$ annihilations. For example, using the production cross section for D^0 decaying via $K^0\pi^+\pi^-/\bar{K}^0\pi^+\pi^-$ [18] :

$$\frac{\sigma.B\ (e^+e^- \rightarrow D^0X\ ;\ D^0 \rightarrow K^0\pi^+\pi^-/\bar{K}^0\pi^+\pi^-)}{(e^+e^- \rightarrow \text{hadrons})} = \frac{1.09 \pm 0.30 \text{ nb.}}{33 \text{ nb.}}$$

$$\sim 3.3\ \%$$

However, using the results from this experiment and the known $\bar{p}p$ annihilation cross section :-

$$\frac{\sigma.B\ (\bar{p}p \rightarrow D^0X\ ;\ D^0 \rightarrow K^0\pi^+\pi^-/\bar{K}^0\pi^+\pi^-)}{(\bar{p}p \rightarrow \text{annihilation})} < \frac{9\ \mu\text{b.}}{12.1 \text{ mb.}}$$

$$< 0.07\ \%$$

So, it appears that the fraction of hadronic interactions producing charmed particles is suppressed by two orders of magnitude over charm production in e^+e^- at the same overall centre of mass energy.

6.4 Search for Direct Electron Production

Another signature, predicted by Gaillard, Rosner and Lee [19], which might indicate the presence of charm, was the semi-leptonic and leptonic decay modes. If the charmed particles decayed preferentially to strange particles then events with for example a K^0_s and e^+ or e^- in the final state would be of interest. A search for direct leptons in this experiment, where only events with strange particles had been recorded, might therefore give interesting results. If any direct leptons found were produced in pairs this would imply that an electromagnetic process was responsible. If however, single leptons were observed, they might indicate the decay of charmed or other new particles with perhaps an associated threshold below which no direct leptons would be observed.

The results obtained by other experiments are far from conclusive. Two neutrino experiments [20,21] had evidence for the production of

anomalous $\mu^- e^+ K^0_s$ events which could not be explained by previously known processes but could be explained by charmed particle production. A Pennsylvania-Stony Brook collaboration [22] has measured the e/π ratio and finds a value 1.10^{-4} using incident π and p at 10, 15, and 24 GeV/c. Their results imply pair production of direct leptons however. Winter [23] quotes a null result in proton-platinum collisions at 19 GeV/c. Muirhead [24] also finds a null result for single $e^{\pm}$ production with 1.6 GeV/c incident antiprotons in a heavy liquid at a level of $e/\pi \sim 5.10^{-5}$ and can explain all their e^+e^- pair production by known processes. Preliminary results from the 14.75 GeV/c $\bar{p}p$ experiment [13] were encouraging. They found 10 $K^0_s e^{\pm}$ events and 3 $\Lambda^0 e^{\pm}$ events in their small sample of 889 events with associated V^0s.

The 72000 pictures at Imperial College were scanned for interactions which included at least one strange particle in the final state (see section 2.1). This produced a list of 8784 events, excluding 0-prongs, of which 7467 events were rescanned to look for single electrons or positrons at the primary vertex and Dalitz pairs. The scanners were asked to record events with at least one track which either spiralled rapidly down to zero momentum, or spiralled and did not interact, and/or exhibited Bremstrahlung characteristics. Using these criteria, a list of 382 e^+ or e^- candidates and 50 Dalitz pairs was produced. Tighter definitions than those used may have excluded some $e^{\pm}$ candidates; for example a positron which did not spiral to zero momentum but annihilated with an electron. All candidates were checked by a physicist and 23 e^+ or e^- candidates survived together with 37 Dalitz pairs. 57% of the film was check scanned for a second time and the efficiencies for finding a single electron or positron or for finding a Dalitz pair were calculated to be 42 $\pm$ 22 % and 42 $\pm$ 17 % respectively. The large errors are due purely to the small numbers of events in each sample. No assumptions

concerning the (reasonably good) visibility of Dalitz pairs compared to single $e^{\pm}$ were made and it is thought that the equality of these scanning efficiencies is coincidental. Having found a possible e^{+} or e^{-} candidate, all other primary tracks were studied carefully in order to find a dalitz pair partner if one existed.

19 $e^{\pm}$ candidates were measured as complete events on Willie, paying special attention to the $e^{\pm}$ candidate. The effective mass of the candidate with, in turn, each of the tracks of opposite charge which did not either interact or decay was calculated (figure 3). The measured events were again scanned using the mass fits from geometry and all candidates which had a Dalitz pair partner (i.e. acceptable e mass fit and $m^2(e^+e^-) < 0.0182$ GeV^2) were rejected. Only three events remained after this scan.

The first event was probably a π^-, since after 1m track length there appeared to be an interaction of the type $\pi^- p \rightarrow \pi^0$ + neutrals, with the π^0 decaying via $\pi^0 \rightarrow \gamma e^+ e^-$. This secondary interaction was only visible on one view but was fairly convincing. The other two candidates were low energy (momentum less than 100 MeV/c) positive tracks which were consistent with a π^+ decaying at rest, at the production vertex.

The total number of Dalitz pairs, including those identified after geometrical fitting, corrected for scanning losses, is 138 $\pm$ 68. Several sources of background for the production of both single e^+ or e^- and e^+e^- pairs have been considered.

a) e^+ from the decay of π^+ at rest at the primary interaction point

b) e^- which are δ-rays

c) Compton electrons and asymmetric γ-rays

d) Secondary reactions like $\pi^- p \rightarrow \pi^0 X$ close to the primary vertex
$$\pi^0 \rightarrow \gamma e^+ e^-$$

e) Semi-leptonic decays of strange particles e.g.

i) $K^{\pm} \rightarrow \pi^{0} e^{\pm} \nu$

ii) $K^{0} \rightarrow \pi^{\pm} e^{\mp} \nu$

iii) $\Lambda^{0} \rightarrow p e^{-} \nu$

f) Asymmetric Dalitz pairs

Source a) can be removed if all candidates of momentum less than 100 MeV/c are ignored. Sources b) - e) would have to occur within about 0.5 cm. (real space) of the primary vertex for there to be no visible kink or interaction. Both b) and c) would give an extra negative track; events with an odd number of primary tracks were ignored by the scanners. The background due to e) has been calculated and amounts to ~0.09 of an event. The largest source of background comes from asymmetric Dalitz pairs. The number of π^{0} produced in $\bar{p}p$ interactions at 15 GeV/c has been measured [25] and the average number of π^{0} in each topology was found to be given by $\langle n_{\pi^{0}} \rangle = 0.97 + 0.37(n/2)$ where n is the number of charged prongs. Using the topological cross sections (chapter 4, table II), it was estimated that 1.775 π^{0} would be produced per event, averaged over all topologies. 1/80 th of all π^{0} will produce Dalitz pairs [26] giving 166 for the number of events studied here.

Since no candidates for direct electron/positron production with an associated strange particle remain, only an upper limit can be given for the $e^{\pm}V^{0}/\pi^{\pm}$ ratio. Taking into account the various scanning efficiencies, measuring efficiency, and the fact that only $e^{\pm}$ of less than ~600 MeV/c can be detected by their spiralling in BEBC, an upper limit (calculated at the 95% confidence level) of 1.4×10^{-3} was calculated for the above ratio.

6.5 Comparison of Inclusive K^o Production in e^+e^- and $\bar{p}p$ Annihilations

Both $\bar{e}e$ and $\bar{p}p$ annihilations have S=Q=B=0 in the initial state and $J^{PC} = 1^{--}$ for $\bar{e}e$ at $s = E^{*2}$ and $J^{PC} = 0^{-+}$ or 1^{--} for $\bar{p}p$ at $s = 4m_N^2$. One might therefore expect $\bar{e}e$ and $\bar{p}p$ annihilations to be the same in the region of $s = 4m_N^2$. However, there is no a priori reason why they should be equivalent at higher energies. It has been noted [27] that there are some remarkable similarities in numbers of prongs and average charged multiplicity distributions. For example the average mean charged topology for $\bar{e}e$ is 4.3 ± 0.1 and for $\bar{p}p$ is 5.46 ± 0.14 at $\sqrt{s} = 4.9$ GeV. Also the total annihilation cross section appears to be related [28]:

$$\sigma(s)^{\bar{e}e \rightarrow \text{hadrons}} \simeq 0.9 \cdot 10^{-6} \sigma(s)^{\bar{p}p \rightarrow \text{hadrons (annih.)}}$$

Since this relation applies at energies above threshold it seems reasonable to compare other cross sections at the same centre of mass energy for both $\bar{e}e$ and $\bar{p}p$ annihilations. A scheme proposed by Bjorken and Kogut, and by Brodsky and Gunion [29] in which hadron production is universal (depends only on $\sqrt{s}$) supports this experimental evidence.

However, if hadron interactions are collisions between the constituent quarks, then $\bar{p}p$ annihilation can be seen as the result of up to three quark-antiquark interactions, each leading to a jet of secondaries. Following a model proposed by Rossi and Veneziano [30] , the relation between the mean charged multiplicities for e^+e^- and $\bar{p}p$ annihilations is of the form

$$\langle n_c(\sqrt{s}) \rangle_{\bar{p}p} = 3 \left\langle n_c\left(\frac{\sqrt{s}}{\eta}\right) \right\rangle_{\bar{e}e} \quad , \text{with } \eta = 3.$$

A more detailed analysis suggests that η should be ~ 4.5 .

The PLUTO collaboration at DESY [31] have published results on inclusive K^o production cross sections in $\bar{e}e$ annihilations from 3.6 to 5 GeV centre of mass energy ($\sqrt{s}$). The K_s^o yield, relative to

$\bar{e}e \rightarrow$ hadrons, shows a sudden increase around 4 GeV, which has been interpreted as a threshold for charmed particle pair production with subsequent decay into strange particles. A group at SLAC [32] have also studied the production of K^0_s in $\bar{e}e$ annihilations for $\sqrt{s}$ between 3.4 and 7.6 GeV and find an increase in the inclusive K^0_s cross section around 4 GeV and structure at 4.028 GeV and 4.415 GeV.

Two variables are defined which represent the K^0 yield per annihilation event :-

$$R_1 = \frac{\sigma(\ \bar{p}p \xrightarrow{\text{annihilation}} K^0_s X\ )}{\sigma(\ \bar{p}p \rightarrow \text{annihilation}\ )}\ ,\quad R_2 = \frac{\sigma(\ e^+e^- \rightarrow K^0_s X\ )}{\sigma(\ e^+e^- \rightarrow \text{hadrons}\ )}$$

These variables are plotted in figure 4 as a function of $\sqrt{s}$, and the estimates of R_1 at various energies from previously published data [33,34] are given in table III. The $\bar{p}p$ data show an increase in R_1 up to $\sqrt{s}$ = 13.76 GeV (the highest energy data available at present). In this experiment, at $\sqrt{s}$ = 4.9 GeV the value of R_1 is found to be 0.129 ± 0.018, which is of the same order of magnitude as the value of R_2 found at neighbouring energies. The values of R_1 do not show the sudden increase found for R_2 [31] . No conclusions can be drawn concerning the presence or absence of structure in R_1 at 4 GeV and 4.4 GeV due to the lack of data in those regions. The data are also shown (figure 5) with R_1 as a function of $\sqrt{s}$ (for $\bar{p}p$) and $3R_2$ as a function of $\sqrt{s}/4.5$ (for $\bar{e}e$). The trend of the data is for a roughly linear increase of the K^0 production cross section with $\eta\sqrt{s}$. However, the mean charged multiplicities in $\bar{p}p$ and $\bar{e}e$ annihilation [27] are not well reproduced using this model [30] .

References

1. G. Goldhaber et al. Phys. Rev. Lett. 37,(1976),255
2. I. Peruzzi et al. Phys. Rev. Lett. 37,(1976),569
3. G. Goldhaber et al. Physics Letters 69B,(1977),503
4. J. Wiss et al. Phys. Rev. Lett. 37,(1976),1531
5. S. Yamada Hamburg Conference 1977
6. E. G. Cazzoli Phys. Rev. Lett. 34,(1975),1125
7. B. Knapp Phys. Rev. Lett. 37,(1976),882
8. Nuclear Physics B 111,(1976),189
9. C. Baltay Phys. Rev. Lett. 31,(1975),1118
10. J. Aubert Phys. Rev. Lett. 35,(1975),416
11. R. Cester Phys. Rev. Lett. 37,(1976),1178
12. R. Carlsson Nuclear Physics B 99,(1975),451
13. J. Canter Aachen Conference, June 1976, and Tufts conf. 1976
14. M. Albrow Nuclear Physics B 114,(1976),365
15. P. Bosetti CERN/EP/PHYS 78-2
16. "Review of Particle Properties" Rev. Mod. Phys. Vol.48, No.2, 1976
17. A. Barbaro-Galtieri et al. Hamburg Conference 1977
18. G. Feldman Physics Reports 33C,(1977)
19. M. K. Gaillard, B. W. Lee, J. L. Rosner Rev. Mod. Phys. 47,No.2,1975
20. J. von Krogh Phys. Rev. Lett. 36,(1976),710
21. J. Blietschau Physics Letters 60B,(1975),207
22. E. Beier Phys. Rev. Lett. 37,(1976),1117
23. K. Winter Physics Letters 57B,(1975),479
24. H. Muirhead CERN/EP/PHYS 77-1
25. T. Kitagaki CERN 74-18 "Antinucleon - Nucleon Interactions"
26. R. H. Dalitz Proc. Phys. Soc. A64,(1951),667
27. H. Muirhead Proc. of Int. Symp. on $\bar{p}p$ Interactions, Loma Kali 1975

R. Ansorge et al. CERN/SPSC 77/97 , CERN/SPSC/P68/Add 1

28. G. Eilam McGill - CIT - LBL preprint, 1975

29. J. D. Bjorken, J. Kogut Phys. Rev. D8,(1973),1341

S. J. Brodsky, J. F. Gunion Phys. Rev. Lett. 37,(1976),402

SLAC-PUB-1937 (1977)

30. G. C. Rossi, G. Veneziano CERN-TH2287 (1977)

G. Veneziano CERN-TH2425 (1977)

31. J. Burmester et al. Physics Letters 67B,(1977),367

32. V. Lüth Physics Letters 70B,(1977),120

33. D. Bertrand et al. Nuclear Physics B128,(1977),365

34. G. Alexander et al. Phys. Rev. 154,(1967),1284

I. M. Gramenitsky Proc. of XVIII Int. Conf. on High Energy Physics Tbilisi (1976)

V. Blobel et al. Nuclear Physics B69,(1974),454

M. A. Jabiol et al. Nuclear Physics B127,(1977),365

D. R. Ward et al. Physics Letters 62B,(1976),238

TABLE I

The upper limits on the inclusive production cross-section times decay branching ratio for D-mesons, D*-mesons and Λ_c-baryons at 95% confidence level.

CHANNEL	σ x BR (μb)
$D^+ \to \bar{K}^o_s \pi^+$	2.4
$D^o \to \bar{K}^o_s \pi^+ \pi^-$	4.5
$D^+ \to \bar{K}^o_s 2\pi^+ \pi^-$	10.0
$D^o \to \bar{K}^o_s 2\pi^+ 2\pi^-$	4.4
$D^+ \to \bar{K}^o_s 3\pi^+ 2\pi^-$	2.0
$D^{*+} \to \bar{K}^o_s \pi^+$	1.5
$D^{*o} \to \bar{K}^o_s \pi^+ \pi^-$	7.0
$D^{*+} \to \bar{K}^o_s 2\pi^+ \pi^-$	6.7
$D^{*o} \to \bar{K}^o_s 2\pi^+ 2\pi^-$	4.9
$D^{*+} \to \bar{K}^o_s 3\pi^+ 2\pi^-$	2.4
$\Lambda_c \to \Lambda \pi^+$	2.9
$\Lambda_c \to \Lambda \pi^+ \pi^+ \pi^-$	5.2
$\bar{\Lambda}_c \to \bar{\Lambda} \pi^-$	2.8
$\bar{\Lambda}_c \to \bar{\Lambda} \pi^- \pi^- \pi^+$	5.3

TABLE II

Upper limits, at 95% confidence level, for the production cross-section times branching ratio of pairs of charmed D mesons and D* mesons for the different $D\bar{D}$ combinations.

REACTION	$\sigma_L \times BR$ (μb)
$D^+D^- + D^-D^+$ $\hookrightarrow \bar{K}^o_S\pi^+ \quad \hookrightarrow K^o_S\pi^-$	1.1
$D^+D^{*-} + D^-D^{*+}$ $\hookrightarrow \bar{K}^o_S\pi^+ \quad \hookrightarrow K^o_S\pi^-$	1.0
$D^{*+}D^- + D^{*-}D^+$ $\hookrightarrow \bar{K}^o_S\pi^+ \quad \hookrightarrow K^o_S\pi^-$	0.9
$D^{*+}D^{*-} + D^{*-}D^{*+}$ $\hookrightarrow \bar{K}^o_S\pi^+ \quad \hookrightarrow K^o_S\pi^-$	1.0
$D^o\bar{D}^o + \bar{D}^oD^o$ $\hookrightarrow \bar{K}^o_S\pi^+\pi^- \quad \hookrightarrow K^o_S\pi^+\pi^-$	1.9
$D^o\bar{D}^{*o} + \bar{D}^oD^{*o}$ $\hookrightarrow \bar{K}^o_S\pi^+\pi^- \quad \hookrightarrow K^o_S\pi^+\pi^-$	1.0
$D^{*o}\bar{D}^o + \bar{D}^{*o}D^o$ $\hookrightarrow \bar{K}^o_S\pi^+\pi^- \quad \hookrightarrow K^o_S\pi^+\pi^-$	0.2
$D^{*o}\bar{D}^{*o} + \bar{D}^{*o}D^{*o}$ $\hookrightarrow \bar{K}^o_S\pi^+\pi^- \quad \hookrightarrow K^o_S\pi^+\pi^-$	0.7
$D^+D^- + D^-D^+$ $\hookrightarrow \bar{K}^o_S2\pi^+\pi^- \quad \hookrightarrow K^o_S2\pi^-\pi^+$	0.4
$D^+D^{*-} + D^-D^{*+}$ $\hookrightarrow \bar{K}^o_S2\pi^+\pi^- \quad \hookrightarrow K^o_S2\pi^-\pi^+$	1.2
$D^{*+}D^- + D^{*-}D^+$ $\hookrightarrow \bar{K}^o_S2\pi^+\pi^- \quad \hookrightarrow K^o_S2\pi^-\pi^+$	1.1
$D^{*+}D^{*-} + D^{*-}D^{*+}$ $\hookrightarrow \bar{K}^o_S2\pi^+\pi^- \quad \hookrightarrow K^o_S2\pi^-\pi^+$	2.2

TABLE II (continued)

$D^0\bar{D}^0 \to \bar{K}^0_S 2\pi^+ 2\pi^-$ + $\bar{D}^0 D^0 \to K^0_S 2\pi^+ 2\pi^-$	0.7
$D^0\bar{D}^{*0} \to \bar{K}^0_S 2\pi^+ 2\pi^-$ + $\bar{D}^0 D^{*0} \to K^0_S 2\pi^+ 2\pi^-$	0.6
$D^{*0}\bar{D}^0 \to \bar{K}^0_S 2\pi^+ 2\pi^-$ + $\bar{D}^{*0} D^0 \to K^0_S 2\pi^+ 2\pi^-$	0.7
$D^{*0}\bar{D}^{*0} \to \bar{K}^0_S 2\pi^+ 2\pi^-$ + $\bar{D}^{*0} D^{*0} \to K^0_S 2\pi^+ 2\pi^-$	1.7
$D^+D^- \to \bar{K}^0_S 3\pi^+ 2\pi^-$ + $D^-D^+ \to K^0_S 3\pi^- 2\pi^+$	1.0
$D^+D^{*-} \to \bar{K}^0_S 3\pi^+ 2\pi^-$ + $D^-D^{*+} \to K^0_S 3\pi^- 2\pi^+$	0.7
$D^{*+}D^- \to \bar{K}^0_S 3\pi^+ 2\pi^-$ + $D^{*-}D^+ \to K^0_S 3\pi^- 2\pi^+$	1.2
$D^{*+}D^{*-} \to \bar{K}^0_S 3\pi^+ 2\pi^-$ + $D^{*-}D^{*+} \to K^0_S 3\pi^- 2\pi^+$	0.7

TABLE III

The inclusive production cross-section of K^o_s in $\bar{p}p$ and pp interactions and R_1, the K^o_s yield per annihilation event, at various energies. When not available the pp cross-section is obtained by extrapolation from surrounding energies.

$\sqrt{s}$ GeV	$\sigma(\bar{p}p \to K^o_s X)$ mb	$\sigma(pp \to K^o_s X)$ mb	$\sigma(\bar{p}p \to \text{annih})$ mb	R_1
3.6	2.27 ± 0.19	0.104 ± 0.014	19.15 ± 2.04	0.113 ± 0.016
4.35	2.05 ± 0.10	0.41 ± 0.10	16.33 ± 0.8	0.100 ± 0.010
4.88	2.14 ± 0.19	0.58 ± 0.02	12.1 ± 0.8	0.129 ± 0.018
6.84	2.24 ± 0.20	1.26 ± 0.03	7.86 ± 0.36	0.125 ± 0.026
7.86	3.1 ± 0.25	1.7 ± 0.2	7.31 ± 0.23	0.192 ± 0.044
13.76	5.2 ± 0.4	4.1 ± 0.3	3.32 ± 0.39	0.331 ± 0.155

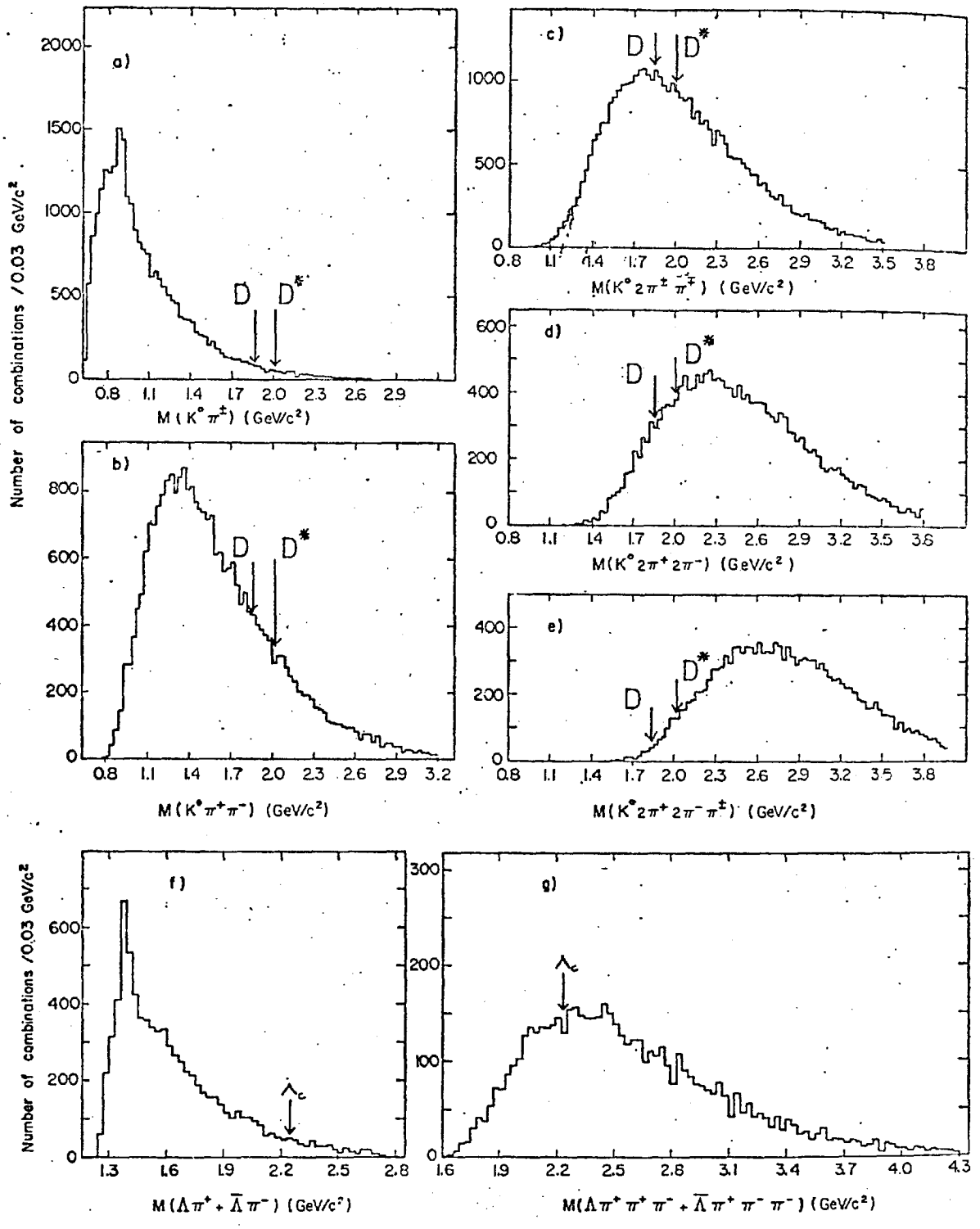


Figure 6.1 : Invariant mass distributions of the $K^0/\bar{K}^0 + n\pi$ (n = 1-5) and $\Lambda^0/\bar{\Lambda}^0 + n\pi$ (n=1,3) systems produced in $\bar{p}p$ interactions at 12 GeV/c.

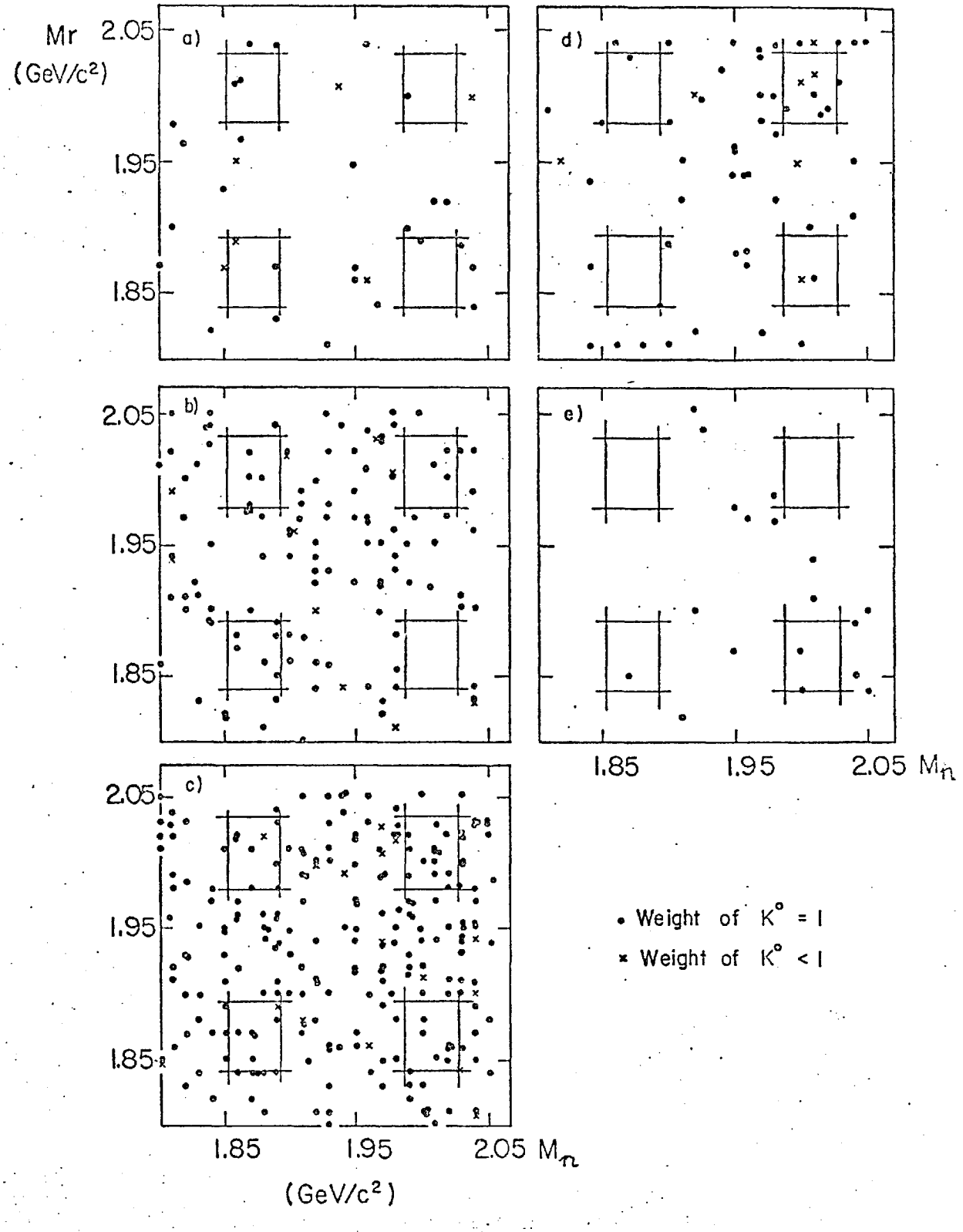


Figure 6.2 : Scatter plots of the invariant mass of $K^0/\bar{K}^0 + n\pi$ versus the recoil mass to that system.

a) n = 1 — $K^0\pi^{\pm}$

b) n = 2 — $K^0\pi^+\pi^-$

c) n = 3 — $K^0\pi^+\pi^-\pi^{\pm}$

d) n = 4 — $K^0 2\pi^+ 2\pi^-$

e) n = 5 — $K^0 2\pi^+ 2\pi^-\pi^{\pm}$

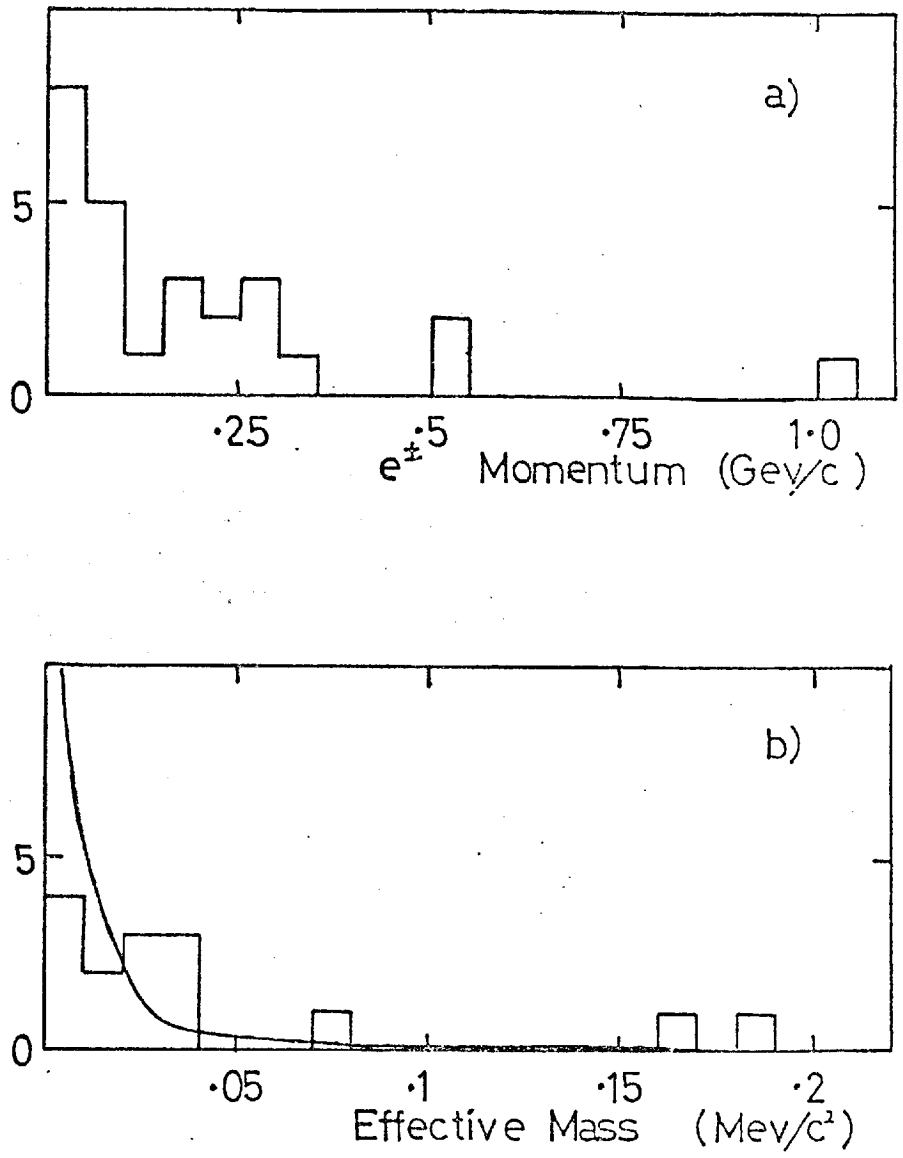


Figure 6.3 : a) Momentum spectrum of $e^{\pm}$.

b) Effective mass of $e^{+}X^{-}$ and $e^{-}X^{+}$ pairs, where $X^{\pm}$ is the track which gives the lowest effective mass. The curve represents the mass spectrum expected from Dalitz pairs.

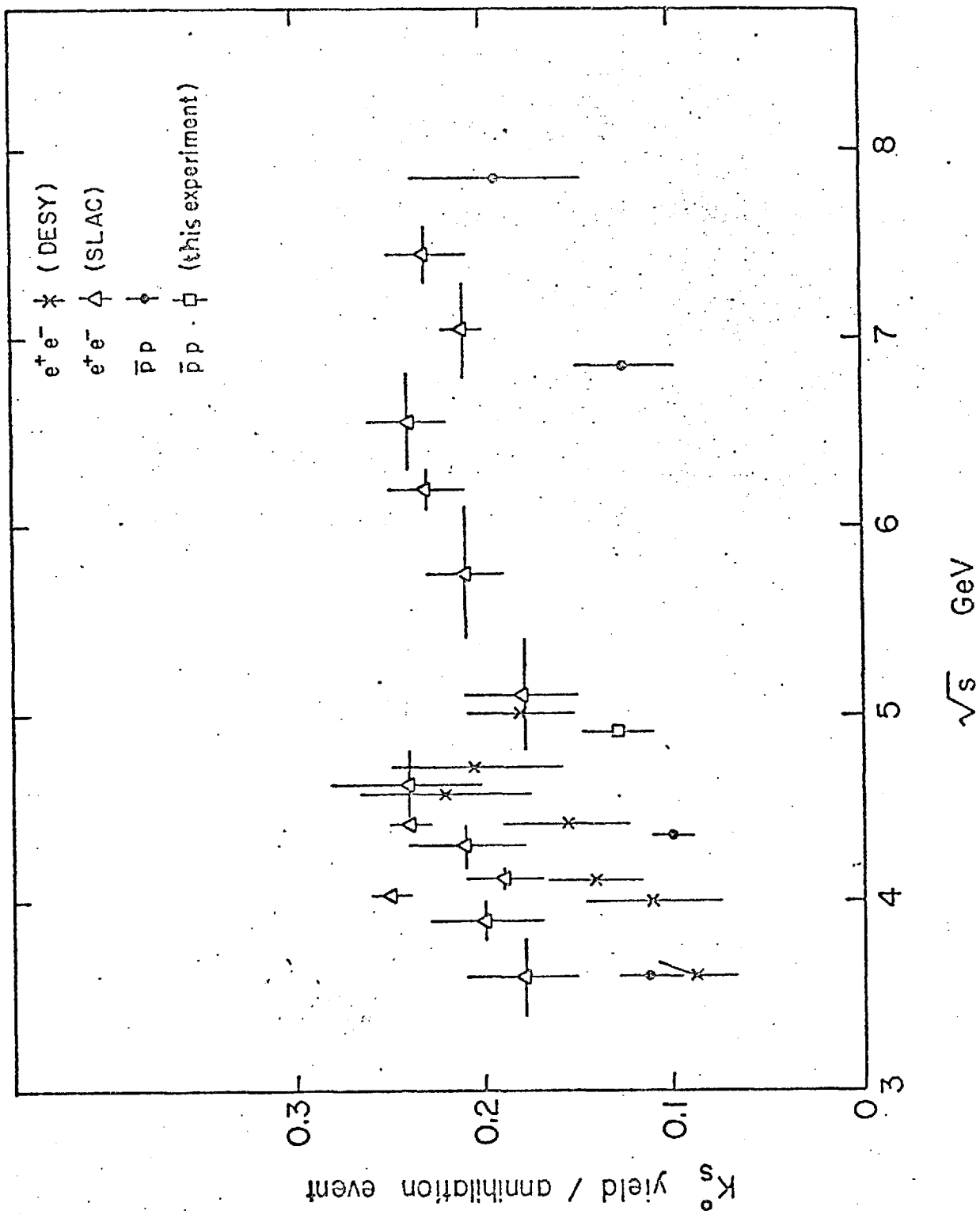


Figure 6.4 : The K^0_s yield in $\bar{p}p$ annihilations as a function of the CM energy $\sqrt{s}$, compared with the K^0_s yield for hadronic events in e^+e^- interactions at the same value of $\sqrt{s}$.

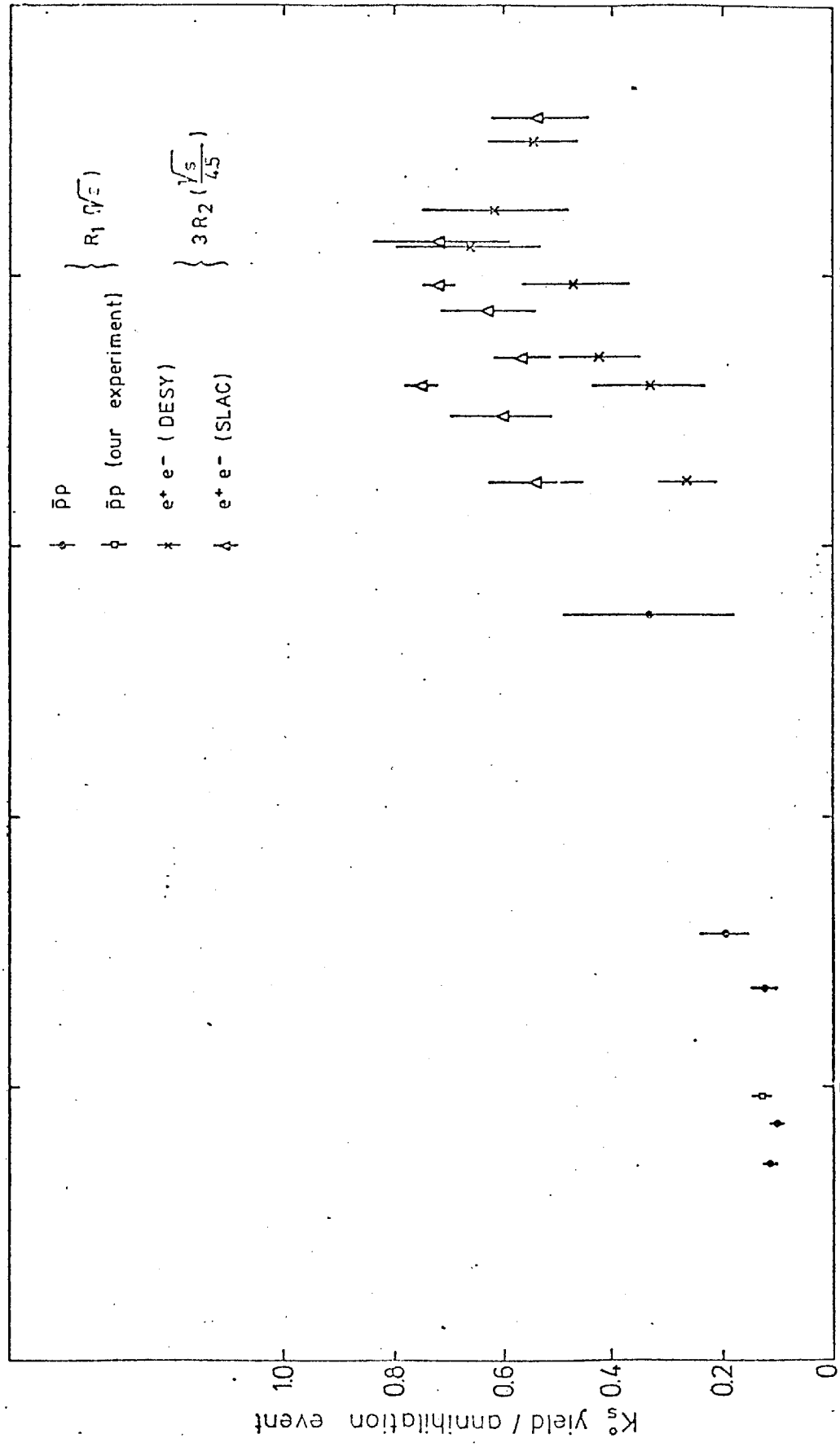


Figure 6.5 : The K^0_s yield in $\bar{p}p$ annihilations as a function of the CM energy $\sqrt{s}$, compared with the K^0_s yield for hadronic events in e^+e^- interactions at a CM energy of $4.5\sqrt{s}$.

Acknowledgements

I would like to offer thanks to all members of the High Energy Nuclear Physics Group at Imperial College and the $\bar{p}p$ Collaboration for the help they have given me over the past few years.

I joined the Group before the experiment had even been thought of, and so was able to participate in all aspects of the experiment including the data taking at CERN, the scanning, measuring and data processing at Imperial College as well as the physics at the end of the chain. An experiment of this size and scale is not a one-person job. The many problems encountered have been eased by the co-operation of the scanning and measuring staff and the expertise of the HPD team at Imperial College. For help in the geometrical and kinematic fitting, my thanks go to Mike Mermikides and Sunanda Banerjee and to Ron Campbell for the REGEOM program. My contributions in this area were the REAM program and general assistance with the geometry and kinematics programs. Data from all laboratories were used for most of the plots shown in Chapters 4 to 6. I would like to thank Agnieszka Jacholkowska (Orsay) for her help with the work on the charm upper limits (6.3) and the Mons team for their contribution to the $e^+e^-/\bar{p}p$ comparison (6.5).

Finally, I wish to thank Professor Ian Butterworth for giving me a place in the group and for acting as my supervisor, and Dr. Don Miller for giving me so much helpful advice. I would also like to thank Dr. Peter Dornan and Dr. Edward Clayton for their support and assistance and the Science Research Council for providing a grant.